University of Southampton

National Oceanography Centre

Arctic Ocean productivity, its ice-free future and application to ice-free oceans

---

Thesis for the degree of Doctor of Philosophy

=

Author:

Jonathan Lawrence

29th January 2019

.

UNIVERSITY OF SOUTHAMPTON

ABSTRACT

FACULTY OF NATURAL AND ENVIRONMENTAL SCIENCES

NATIONAL OCEANOGRAPHY CENTRE

DOCTOR OF PHILOSOPHY

ARCTIC OCEAN PRODUCTIVITY, ITS ICE-FREE FUTURE AND APPLICATION TO ICE-FREE OCEANS

by Jonathan Lawrence

This thesis examines productivity in the Arctic Ocean and its response to a future ice free Arctic. Phytoplankton produce atmospheric oxygen, regulate atmospheric carbon dioxide and underpin ocean ecosystems. Production dynamics and distributions in the Arctic are poorly understood — especially the extent of growth under ice and in prevalent subsurface chlorophyll maxima is unknown — and therefore the perturbation under anthropogenic sea ice retreat is poorly understood. We relate the vertical distribution of production to the ratio of nitrate limitation to light limitation limitation across the Arctic. Depth-integrated production in each water column is then easily related to the vertical distribution because light-governed production rates decrease exponentially with depth. The scaling elucidates under ice and subsurface production magnitudes, and works equally well across the diverse hydrographic (shelves, inflows, central basin) and biogeochemical provinces of the Arctic. Further, the scaling is shown to elucidate biogeochemical transformations of water masses as they transit the Arctic and to be time-invariant. The latter fact is used to predict perturbations to plankton dynamics under anthropogenic ice retreat. Further, unique boundary conditions make the Arctic a powerful place to study general (global) plankton responses to environmental perturbations. We explore this by deriving oceanic photosynthesis across the globe from the theory developed in the Arctic Ocean. The major implication of our results are that oceanic photosynthesis is explicable in terms of a coherent dependence on ocean nutrient and light conditions, and this entails minor productivity increases in an ice-free Arctic Ocean and in the global ocean over the coming century.

Scientific publications

Two scientific papers have been published that accompany the work in this thesis. One is first authored and is presented in a slightly different format here, with the methods (validation) presented in Chapter 3 and the results in Chapter 4. The other is an international collaboration where the thesis author provided a simulation and technical advice, and is a co-author. Both papers appear in Appendix B in their published formats. One further piece of work has been deemed publishable (Chapter 5).

Contents

Abstract . . . . **i**

Contents . . . . **iii**

List of Tables . . . . **vii**

List of Figures . . . . **vii**

Declaration of authorship . . . . **x**

Symbols and abbreviations . . . . **xiii**

1 Extended Summary **3**

2 Introduction **7**

- 2.1 Oceanic photosynthesis: the breathing planet 7
- 2.2 Early phytoplankton production theory 9
- 2.3 The ingredients of photosynthesis 18
  - 2.3.1 Carbon 19
  - 2.3.2 Nitrate and phosphate 19
  - 2.3.3 Iron 20
- 2.4 The kinetics of photosynthesis 21
  - 2.4.1 Nutrient kinetics 21
  - 2.4.2 Light kinetics 23
  - 2.4.3 Temperature and phytoplankton growth rates 24
- 2.5 Arctic Ocean properties 26
  - 2.5.1 Geography and bathymetry 26
  - 2.5.2 Sea ice conditions 26
  - 2.5.3 Potential density and T-S conditions 29

2.5.4 Arctic Ocean circulation 29
2.5.5 Arctic Ocean mixing 33
2.5.6 The wind-driven Arctic Ocean 34
2.5.7 Nutrients 36
2.5.8 Nutrient limitation concepts 39
2.5.9 Nitrate limitation and ocean nitrate transports 41
2.5.10 Maximum annual mixed layer depths 44
2.5.11 Observed productivities by regional sea 45
2.5.12 Ice algae 47
2.5.13 Under-ice production 50

3 Methods 53
3.1 Satellite estimates of Arctic productivity 53
3.1.1 Deriving productivity from space 54
3.1.2 Satellite coverage 56
3.1.3 Surface chlorophyll-*a* and the subsurface maximum 57
3.1.4 The challenges of ongoing productivity changes 60
3.2 Biogeochemical simulations 64
3.2.1 MEDUSA differential equations 66
3.2.2 Ocean physics model 68
3.2.3 Upper ocean physics 70
3.2.4 CMIP climate models 71
3.2.5 CMIP5 Arctic forecasts and uncertainties 73
3.2.6 MEDUSA productivity and chlorophyll-a 75
3.2.7 MEDUSA dissolved inorganic nitrogen 77

4 On the vertical distribution of Arctic Ocean productivity . . 79
4.1 Arctic Ocean boundary nitrate fluxes 80
4.2 Arctic Ocean interior vertical nitrate fluxes 82
4.2.1 Ekman fluxes 82
4.2.2 Diffusive fluxes 83
4.2.3 Entrainment fluxes during winter mixing 84
4.3 Phytoplankton uptake in open water and under ice 85

4.3.1 Open water 85
4.3.2 Under-ice 86
4.3.3 Extension of the Arctic spring bloom under sea ice 89
4.4 Decadal changes in the Beaufort Sea 91
4.4.1 Nitrate dominates current co-limitation 91
4.4.2 Decoupling of chlorophyll maximum from the nitracline . . . 93
4.4.3 The Arctic chlorophyll to carbon phytoplankton ratio 95
4.5 Predicting production's vertical distribution 96
4.6 Phytoplankton response to an ice free Arctic 100
4.7 Discussion 103
4.8 Conclusions 104

5 On the dynamics of productivity in the Arctic Ocean 107
5.1 Photosynthetic kinetics over depth 107
5.2 Nitrate-light conditions and production 111
5.3 Arctic productivity geographical distributions 113
5.4 Future ice-free productivity 115
5.5 Discussion 118
5.6 Implications for global production 120

6 On the dynamics of productivity in the global ocean 123
6.1 Oceanic production and nutrient limitation 124
6.2 Data sources and methods 126
6.2.1 Iron and nitrate data 126
6.2.2 Light data 128
6.2.3 The ratio of nutrient to light limitation 129
6.2.4 Biomes 130
6.2.5 Phytoplankton production data 131
6.3 Numerical model performance 132
6.3.1 Productivity and its vertical distribution 133
6.3.2 Nitrate inventory and photosynthetic light 135
6.3.3 Nitrate and iron limitation 135
6.3.4 Production and nutrient to light limitation ratios 136

6.3.5 Nitrate, silicate and chlorophyll-a transects 137
6.4 Results 141
6.4.1 Phytoplankton productivity distributions 141
6.4.2 Productivity and nutrient to light limitation ratios 141
6.4.3 Invariance and future depth-integrated productivity 144
6.5 Discussion 145
6.5.1 Temperature dependence of photosynthetic rates 146
6.5.2 Future ocean productivity and genetic changes 147

7 Conclusions 151
7.1 Thesis overview 151
7.2 Monitoring ongoing Arctic Ocean changes 152
7.2.1 Arctic Ocean physical nitrate transports 152
7.2.2 The phytoplankton response to an ice-free Arctic 153

Appendices 154

A 155
A1 Data sources 155
A2 Example code 156
A3 MEDUSA partial differential equations 160
A4 MEDUSA functional forms 162
A5 MEDUSA biogeochemical model variables 167

B 173
B1 Media 173
B2 Published papers 173

C 189
C1 Simulated production in Chapter 4 189

References 191

List of Tables

2.1 Phytoplankton representative molecular composition 19

4.1 Estimated Arctic nitrate boundary fluxes 80
4.2 Estimated Arctic interior vertical nitrate fluxes 83
4.3 Arctic plankton parameters and representative values 90

6.1 Global iron fluxes into the ocean 125

A1 MEDUSA biogeochemical 3D model state variables. 167
A2 MEDUSA biogeochemical 2D (benthic) model state variables. . . . 168
A3 MEDUSA phytoplankton process terms 168
A4 MEDUSA miscellaneous process terms 168
A5 MEDUSA zooplankton process terms 169
A6 MEDUSA nutrient process terms 169
A7 MEDUSA detritus process terms 170
A8 Phytoplankton growth parameters 170
A9 Zooplankton parameters 170
A10 Phytoplankton and detritus loss parameters 171
A11 Fast detritus submodel parameters 171
A12 Miscellaneous parameters 171

List of Figures

2.1 Ocean productivity estimate from space 8

2.2 Phytoplankton abundances on the 1899 Plankton Expedition 11
2.3 Sverdrup's critical depth model and map of ocean productivity . . . 14
2.4 Critical depth and critical turbulence conditions 16
2.5 Active phytoplankton growth below the Canadian Arctic mixed layer 17
2.6 Michaelis-Menten kinetics 23
2.7 Temperature dependence of phytoplankton growth rates 25
2.8 Arctic Ocean bathymetric map 27
2.9 Arctic sea ice extent 28
2.10 Potential density, T-S conditions and water classes 30
2.11 Arctic Ocean circulation 31
2.12 Arctic Ocean nutrient distributions 38
2.13 Arctic boundary velocities and nitrate concentrations 43
2.14 Arctic boundary nitrate transports 44
2.15 Arctic winter mixed layer depths 46
2.16 Arctic regional sea environmental conditions and productivities . . 50

3.1 Validation data available for satellites 56
3.2 Satellite vertical profile errors 60
3.3 Satellite regional sea and seasonal errors 61
3.4 Arctic Ocean upper ocean physical conditions 72
3.5 Arctic observation-model chlorophyll-a profiles 75
3.6 Arctic observation-model nitrate transect 76

4.1 Arctic Ocean nitrate budget 81
4.2 Canadian Arctic subsurface chlorophyll-a maxima trends 87
4.3 Northward propogation of under ice blooms 89
4.4 Predicting vertical Arctic production distributions 97
4.5 Model trends in Arctic phytoplankton 101
4.6 Spatial patterns of model Arctic phytoplankton trends 102

5.1 Map of turning point z_r 109
5.2 Arctic productivity related to the ratio of nitrate to light limitation 110
5.3 Nitrate and light dependencies of Arctic productivity 111
5.4 Model patterns of depth-integrated annual production 112

5.5 Geographical patterns of Arctic productivity 113
5.6 Changes in model nitrate and light conditions across the Arctic . . 116
5.7 Productivity in an ice-free Arctic 117

6.1 Oceanic dissolved iron concentrations 128
6.2 Ocean biomes and observed ratio of nutrient to light conditions . . 131
6.3 Normal distribution fit to in-situ production data 133
6.4 Global observed-model productivity, nitrate and light 134
6.5 Patterns of global nitrate and iron limitation 136
6.6 Nutrients, light and vertical phytoplankton structure 137
6.7 Atlantic-Pacific nitrate, silicate and chlorophyll-a transects 138
6.8 Satellite and ^{14}C production data 140
6.9 Productivity and its relationship to the ratio of nutrient to light limitation 142
6.10 Invariance of productivity and limitation relationship 143
6.11 Future limitation and vertical productivity changes 145
6.12 Future vertical and depth-integrated productivity changes 147

C.1 Map of change in model subsurface production 190

Academic Thesis: Declaration Of Authorship

I, Jonathan Lawrence, declare that this thesis and the work presented in it are my own and has been generated by me as the result of my own original research.

Arctic Ocean productivity, its ice-free future and application to ice-free oceans

I confirm that:

1. This work was done wholly or mainly while in candidature for a research degree at this University;
2. Where any part of this thesis has previously been submitted for a degree or any other qualification at this University or any other institution, this has been clearly stated;
3. Where I have consulted the published work of others, this is always clearly attributed;
4. Where I have quoted from the work of others, the source is always given. With the exception of such quotations, this thesis is entirely my own work;
5. I have acknowledged all main sources of help;
6. Where the thesis is based on work done by myself jointly with others, I have made clear exactly what was done by others and what I have contributed myself;
7. Either none of this work has been published before submission, or parts of this work have been published as:
   -**Lawrence J.**, Popova, E., Yool, A., and Srokosz, M., 2015, On the vertical phytoplankton response to an ice-free Arctic Ocean, J. Geophys. Res. Oceans, 120, 8571-8582, doi:10.1002/2015JC011180.

Signed:____

Date:____

Acknowledgements

The genesis of this thesis occurred during OSNAP cruise JR302, from St John's, Canada to the United Kingdom. My thanks go to the Istituto delle Scienze Marine in Venice for hosting me during the analysis and preparation of the thesis. The project was supervised by A. Yool, E. Popova and M. Srokosz.

Symbols and abbreviations

α	Initial slope of photosynthesis-irradiance curve (gC $(\mathrm{gChl})^{-1}$ $(\mathrm{Wm}^{-2})^{-1}$ d^{-1})
K_T	Turbulent diffusivity ($\mathrm{m}^2\mathrm{s}^{-1}$)
K_T^*	Normalised turbulent diffusivity (dimensionless)
ρ	Density ($\mathrm{kg\,m}^{-3}$)
τ	Wind stress (Nm^{-2}); also growing season length (d) and timescale of nutrient exhaustion (d)
C_D	Drag coefficient (dimensionless)
f	Planetary vorticity (s^{-1})
F	Nutrient flux ($\mathrm{mmol\,m}^{-2}\,\mathrm{yr}^{-1}$)
h_l	Depth of ocean light penetration (m)
hf	Photon energy (J)
H	Mixing depth (m)
H^*	Normalised mixing depth (dimensionless)
I	Ambient irradiance ($\mathrm{W\,m}^{-2}$)
J	Light limitation (d^{-1})
k	Nutrient half-saturation constant ($\mathrm{mmol\,m}^{-3}$); also ocean light attenuation coefficient (m^{-1})
m	Phytoplankton cell loss rate (d)
N	Ambient nutrient concentration ($\mathrm{mmol\,m}^{-3}$)
P	Phytoplankton productivity ($\mathrm{gC\,m}^{-3}\,\mathrm{d}^{-1}$)
Q	Activation energy ($\mathrm{J\,mol}^{-1}$); also nutrient limitation (dimensionless)

R	Gas constant ($\mathrm{J\,mol^{-1}\,K^{-1}}$)
T	Temperature (C); also transport (Sv)
t	Time (s)
u_{10}	Wind speed 10 m above the ocean surface ($\mathrm{m\,s^{-1}}$)
U, V, W	Transport components (Sv)
V	Maximum production rate ($\mathrm{d^{-1}}$)
$\boldsymbol{v}$	velocity ($\mathrm{m\,s^{-1}}$)
x, y, z	Rectangluar cartesian coordinates

ACC	Alaskan Coastal Current
BSO	Barents Sea Opening
CDOM	Colored Dissolved Organic Matter
CMIP5	Coupled Model Intercomparison Project 5
DIN	Dissolved Inorganic Nitrogen
DMIZ	Deep Marginal Ice Zone
EGC	East Greenland Current
HadGEM-ES	Hadley Centre Global Environment Model-Earth System component
LIM2	Louvain-la-Neuve Sea Ice Model 2
MEDUSA	Model of Ecosystem Dynamics, Nutrient Utilisation, Sequestration and Acidification
MLD	Mixed Layer Depth
NCC	Norweigan Coastal Current
NEMO	Nucleus for European Modelling of the Ocean
OPA	Ocean Paralllis Model
SCM	Subsurface Chlorophyll Maximum
SMIZ	Shelf Marginal Ice Zone
SPM	Subsurface Production Maximum
SST	Sea Surface Temperature
VGPM	Vertically Generalised Production Model
WSC	West Spitsbergen Current

CHAPTER 1

Extended Summary

The Arctic Ocean is rapidly changing. Retreating sea ice is expected to increase light penetration into the upper ocean, where it may stimulate increased phytoplankton growth. But expected changes in the physical supply of nutrients may limit the extent to which plankton can utilise this extra light.

Photosynthetic dynamics in the Arctic Ocean are thought to be governed by these nitrate and light limitations. But, the extent to which nutrients and light limit growth, and how this may correspond to photosynthetic distributions in a present or future ice-free Arctic, is not known — especially the present extent of growth under ice and in subsurface chlorophyll-a maxima. Possible changes in productivity with sea ice retreat are, therefore, also poorly understood.

It is widely thought that oceanic photosynthesis distributions are restricted to a surface euphotic layer, with lateral changes governed by surface nutrient availability [*Williams and Follows*, 2011]. For example, Nathansohn (1906) posited that oceanic plankton growth is determined by spatial variations in vertical mixing that supplies essential nutrients, alleviating nutrient limitation on plankton growth. Subsequent work suggests that the proximate essential nutrients (on biological timescales) are nitrate [*Tyrrell*, 1999] and iron [*Martin and Fitzwater*, 1988;

Kolber et al., 1994]. Sverdrup (1953) has suggested that the depth of a mixed surface layer may set the amount of light that phytoplankton receive, and therefore the conditions under which net growth can be maintained.

Here we use the Arctic Ocean to show that, contrary to Sverdrup (1953), phytoplankton may grow below the mixed layer when turbulence is low. We explain why the discrepancy between Sverdup's theory and Arctic observations arises, in terms of an existing critical turbulence theory [*Taylor and Ferrari*, 2011].

We then develop a theory that relates the vertical distribution of production to the ratio of nitrate limitation to light limitation across the Arctic Ocean. Depth-integrated production in each water column is then readily related to the vertical distribution because light-governed production rates decrease exponentially with depth. The scaling elucidates under ice and subsurface production magnitudes, and works equally well across the diverse hydrographic (shelves, inflows, central basin) and biogeochemical provinces of the Arctic. Further, the scaling is shown to elucidate biogeochemical transformations of water masses as they transit the Arctic, and to be time-invariant. The latter fact is used to predict perturbations to plankton dynamics under anthropogenic sea-ice retreat. Projected nitrate decreases and light increases are inferred to deepen productivity distributions, combining to give modest production increases of 10% in an ice-free Arctic, occurring at depths >20 m.

Further, conditions unique to the Arctic make it a powerful place to study general (global) plankton responses to environmental perturbations. As the Arctic Ocean transitions to open water it converges on the ice-free state currently experienced in the extra-Arctic oceans. This suggests that the transition from an ice-covered to ice-free Arctic Ocean may provide some clues as to productivity patterns outside the Arctic. We use in situ ^{14}C data to demonstrate the corresponding relationship between nutrient-on-light limitation and production for the global ocean. Further, we use a simulation to indicate that the relationship is invariant in the wider ocean, and entails small global productivity changes (<10%) over the coming century.

Thus the theory advanced for the Arctic Ocean is testable by polar ship measurements of productivity, nitrate and light. By relating production to environmental conditions, the theory also provides a means of monitoring ocean production changes indirectly by means of more readily measurable environmental changes.

The phytoplankton response to an ice-free Arctic Ocean may be monitored in two practical ways. First, nutrient concentrations are reported to be declining in the Atlantic inflow to the Arctic, where ∼78% of nitrate is supplied to the Arctic [*Rey*, 2012]. Models project ongoing decreased nitrate supply to surface Arctic waters [*Vancoppenolle et al.*, 2013], which can be monitored by continued hydrographic surveys and by including nitrate sensors on existing physical arrays around the Arctic boundary [*Tsubouchi*, 2014]. Second, the plankton response to ice retreat and the expected nitrate decrease can be tested. Trends in nutrient and light conditions, and the phytoplankton response can be monitored by direct nitrate, light and production measurements within the Arctic basin. Observations and the model anaylsis presented here suggest that one of the key regions to observe the onset of this response may be the Canada Basin [*McLaughlin and Carmack*, 2010]. In the Canada Basin it will be necessary to untangle the climate trend from strong decadal variabilty in the gyre circulation, that may be responsible for much of the observed current trends [*McLaughlin et al.*, 2011].

CHAPTER 2

Introduction

2.1 Oceanic photosynthesis: the breathing planet

Oceanic photosynthesis has played a central role in the development of Earth and the evolution of life that inhabits it. Using energy from sunlight, ubiquitous single-celled organisms called phytoplankton turn carbon dioxide and dissolved salts in the ocean into organic matter, producing oxygen in the process. This oxygen sustains the metabolism of most complex life on earth. Phytoplankton are also the essential food source for higher organisms in the open ocean.

The earliest phytoplankton evolved at least 2.5 billion years ago [*Summons et al.*, 1999] — one and a half billion years before their terrestrial eukaryotic counterparts [*Strother et al.*, 2011], and two billion years before terrestrial macro-plants [*Chaloner*, 1970; *Kenrick and Crane*, 1997]. Early phytoplankton oxygenation in the ocean was consumed by oxidation of reduced materials, leading to the widespread deposition of banded iron oxide formations [*Kump and Barley*, 2007]. Production of oxygen started to exceed consumption by iron oxidation around 2.4 billion years ago, and oxygen began to enter the atmosphere [*Bekker et al.*, 2004;

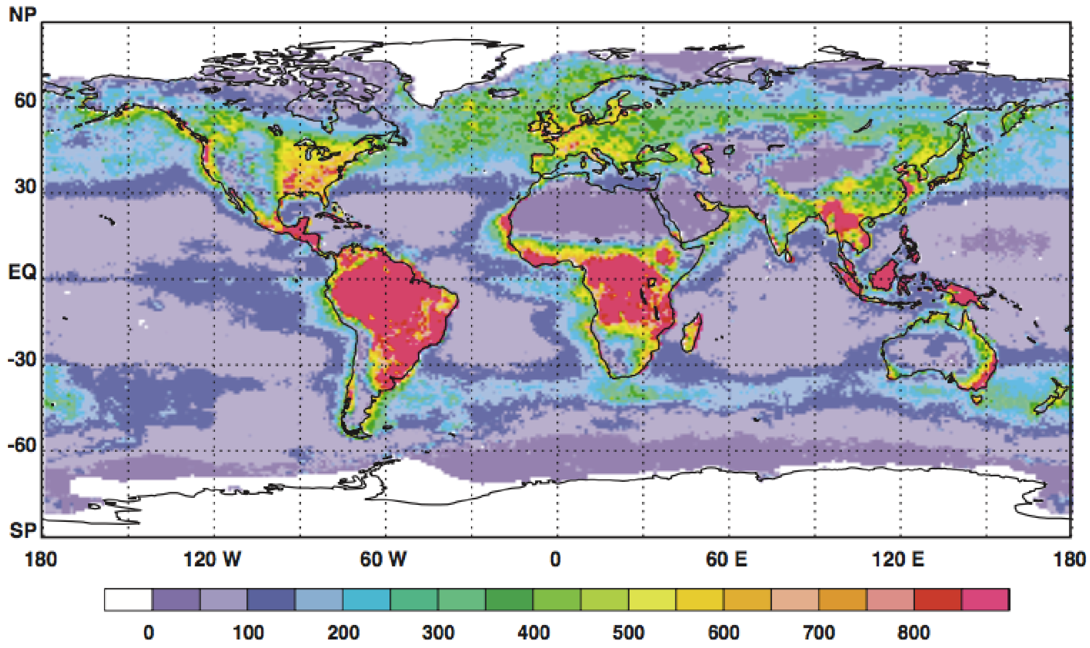

Figure 2.1: Satellite-based estimate of annual biosphere primary production ($gC\,m^{-2}\,yr^{-1}$) [*Field et al.*, 1998]. Global annual production is $104.9\,PgCyr^{-1}$, with 46.2% contributed by the oceans and 53.8% by land.

Canfield, 2005]. High atmospheric oxygen levels are necessary to sustain the higher metabolic rates inherent to complex life, so this increase in atmospheric oxygen was likely central to the subsequent evolution of multi-cellular life, starting around 0.8 billion years ago [*Hedges et al.*, 2004].

Today, oceanic photosynthesis contributes roughly half of global oxygen production (Figure 2.1). Despite equal contributions from the ocean and land, the ocean biosphere is just one percent of the mass of the terrestrial biosphere. Therefore the carbon fixation rate per unit mass is much higher in the ocean than on land. In fact, the average turnover time of the entire ocean phytoplankton community is approximately one week [*Falkowski et al.*, 1998]. Despite these fundamental contributions, it was not until the end of the nineteenth century that ocean phytplankton productivity started to receive attention as an area of scientific study.

2.2 Early phytoplankton production theory (1870–1950)

The beginning of the scientific treatment of ocean phytoplankton may be traced to the Kiel physiologist Victor Hensen who began investigations in the 1870s. Hensen's outlook was that ocean production can be treated analogously to agricultural production on land. He contended that by measuring the abundance of the productive ocean phytoplankton "crop", a general ocean productivity could be estimated, as had been done for crop yields on land [*Hensen*, 1887]. Ocean phytoplankton were considered by Hensen to constitute the key part of the flow of organic matter in the sea. Therefore "to gain an estimate of the plankton production of the sea" [*Hensen*, 1887] would in his view, provide the answer to the general conditions of higher organisms in the seas, including fisheries which were the primary economic revenue of several northern European countries at the time.

Throughout the 1870s and 1880s, Hensen developed techniques to measure phytoplankton standing crop in the Baltic and North Seas [*Hensen*, 1887]. He inferred from these measurements that phytoplankton standing crop is roughly uniformly distributed across the sea [*Hensen*, 1887]. But, at the time, the main plant sources for marine animals was thought to be derived from land, so it was doubted that the enclosed basins of the Baltic and North Seas were representative of the open ocean [*Mills*, 1989]. Concerned that the contended uniformity of standing crop may not be true in the open ocean, Hensen expanded his investigations into the Atlantic Ocean. In 1889, Hensen embarked on a Trans-Atlantic expedition from Germany to Brasil, returning via Ascension, Bermuda and Greenland (Figure 2.2).

The expedition results, in fact showed great variety in phytoplankton abundances. Plankton abundances (by volume) were found to be large in the north-western Atlantic near Greenland, very small in the tropics, and somewhat larger in the equatorial current. But instead of recognising this result, Hensen wrote that "Great evenness is being irrefutably established by the counts along the transect" [*Hensen*, 1892], arguing that deviations from evenness arose from non-representative local circumstances that should be ignored.

Thus, it was left to Karl Brandt (Hensen's assistant at Kiel) to take on the problem of why phytoplankton abundance was not uniform. In Brandt's view this could be best achieved by determining the chemical control of the phytoplankton standing crop. By measuring the chemical composition of phytoplankton, Brandt was able to determine their nutritional requirements [*Brandt*, 1897, 1898].

In particular, Brandt (1901) noted the importance of nitrogen in regulating plankton growth. Nitrogen was known to be present in the chemical composition of phytoplankton, and to be a limiting factor for terrestrial agriculture. Brandt knew that marine bacteria were ubiquitous, and supposed that denitrifying[1] bacteria — like those active in the terrestrial nitrogen cycle — must also be active in the sea. He knew that terrestrial nitrate run-off into the ocean ought, over geological time, to increase seawater nitrate to poisonous levels; but that concentrations in the ocean are in fact low compared to land. He conjectured that low ocean nitrate concentrations are maintained by denitrifying bacteria, removing excess nitrate supplied from the land [*Brandt*, 1901]. The suppression of bacterial denitrification rates at low temperatures then explained high phytoplankton abundances at high latitudes and low abundances at low latitudes. In Brandt's words if "denitrifying bacteria can not perform their functions in cold water, it follows, almost necessarily, that polar seas must be richer in nutrient substances than tropical seas" [*Brandt*, 1901].

At the time of Brandt's hypothesis ocean nitrate measurements were sparse. An increase in measurements through subsequent expeditions presented two fundamental challenges [*Gebbing*, 1909]. First, nitrate concentrations were abundant in the deep ocean, contrary to the distribution expected if nitrogen was terrestrially derived. Second, nitrate concentrations were found to be much higher in the Southern Ocean than the North Atlantic. Brandt's hypothesis that latitudinal nitrate concentrations were temperature regulated implied that nitrate distributions should be high in the Southern Ocean. Instead nitrate concentrations were found to latitudinally asymmetric, with no clear temperature control. These contradictions to Brandt's theory provided an opportunity for an alternative explanation.

---

[1] Denitrification: the use of nitrate as an alternative to oxygen for oxidation of organic matter when oxygen becomes depleted [*Sarmiento and Gruber*, 2006].

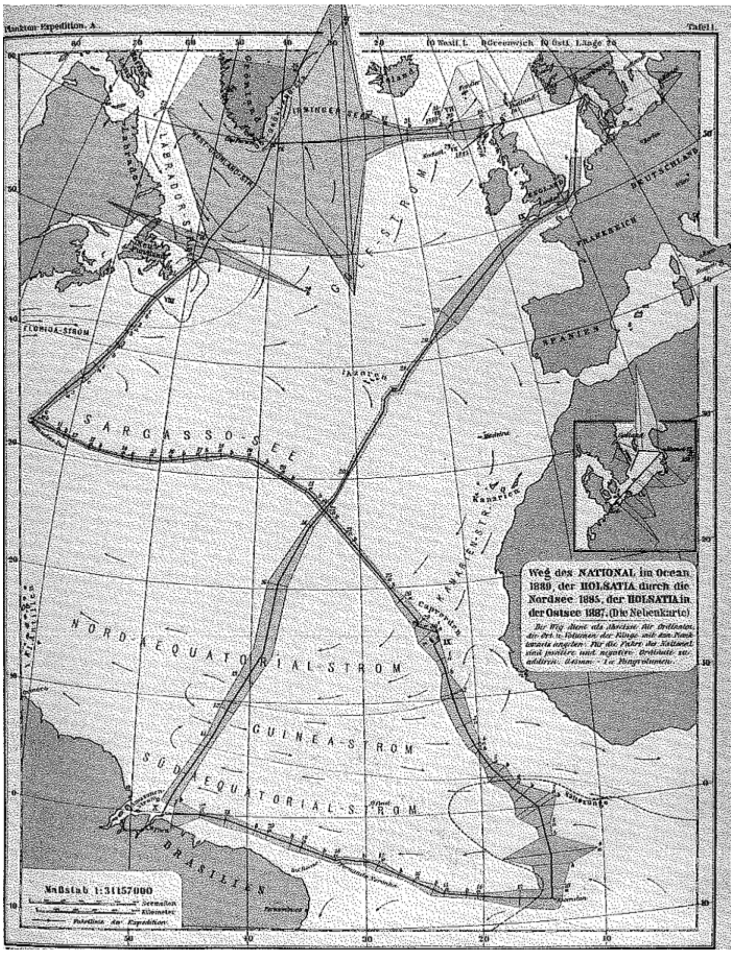

Figure 2.2: Volumetric abundances of plankton measured along the cruise track of the 1889 Plankton Expedition in the Atlantic Ocean [*Hensen*, 1892]. Stations along the cruise track are marked by numbers. Reproduced from Mills (1989).

Alexander Nathansohn — influenced by hydrographic work recently underway in Scandinavia — provided another model in 1906. In his model nutrients are transported to the surface through vertical exchange of water masses; balanced by export of organic matter to the deep ocean. Nathansohn (1906) noted a common pattern in the North Atlantic and Mediterranean Sea. Where vertical mixing is strong — such as in the Straits of Messina, where Polar Water meets Atlantic Water, and along the divergence between the North Equatorial Current and Guinea Current — nutrients are replete and phytoplankton abundance is high [*Nathansohn*, 1906]. In the gyres, observed mixing is weak and phytoplankton abundances are low.

Brandt remained unconvinced. He argued that the latitudinal asymmetry in nitrate arose from hydrographic heterogeneity [*Brandt*, 1915], and sought a relationship between temperature and nitrate independent of latitude. Brandt argued at length for such a relation [*Mills*, 1989], seemingly failing to notice that it would not distinguish between the biological (Brandt) and physical (Nathansohn) hypotheses: cold waters may be rich in nitrate because denitrification is low, or through vertical exchange with nutrient-rich deep waters.

Further sampling by Nathansohn in Monaco demonstrated that phytoplankton also respond to changes in vertical mixing throughout the seasonal cycle [*Nathansohn*, 1908]. Phytoplankton blooms were observed following cooling events in Autumn, January and March, and when vertical water mass exchanges were frequent and large, phytoplankton abundances in the surface water were higher [*Nathansohn*, 1908]. Yet Nathansohn's explanations of the mechanisms that connected circulation and phytoplankton abundance were often incorrect. For example he invoked offshore winds when explaining phytoplankton abundances near the coast, despite Ekman's (1905) contemporary work on perpendicular wind-driven transports. He also invoked implausible connections between water column stability and phytoplankton blooms, such as dilution of the surface waters by precipitation too minor to be significant [*Nathansohn*, 1908].

A greater elucidation of circulation controls took form in the context of the boreal spring bloom. The first breakthrough was made by Haakon Hasberg Gran in his doctoral thesis (1902). Gran (1902) knew that diatom abundance in the Norwegian Sea peaked in March-April and September-November and that similar observations implied this phenomenon was widespread. The spring bloom, he noted, is "such a universal phenomenon that it must have universally acting causes" [*Gran*, 1902]. Gran was aware that light, nutrients and temperature may control photosynthetic growth. He knew that light could account for the start of the spring bloom, but not the end when light was still increasing. He also knew that temperate and Arctic species declined simultaneously at the end of the bloom, ruling out a temperature control on termination of the bloom. From this, Gran hypothesised that light increases allowed overwintering diatoms to grow rapidly in spring. This growth rapidly depletes nutrients and diatom abundances decline until nitrifying[2] bacteria

---

[2] Nitrification: the microbially facilitated conversion of ammonium to nitrate [*Sarmiento and*

become active in summer. Bacterial nitrification in summer, he suggested, then supplies additional nutrients that may stimulate a second (autumnal) bloom.

Working independently of Gran, an American George Whipple (1899) noted that diatom abundances in reservoirs in Massachusetts peaked twice a year in spring and fall, both associated with prior vertical circulation that renewed nutrients from deep water. When Whipple's work reached Europe in 1910, Gran promptly noted its significance, inferring that both the spring and autumnal bloom in the Norweigan Sea could be explained by light and vertical nutrient supply, with no need for recourse to nitrification.

By 1930, the synthesis of ocean biology and physics was such that Gran opined "the theory of Brandt—that phosphates and nitrate can be and often are the limiting factors of the production of the sea—and that of Nathansohn—that these salts accumulate in the depth of the sea and circulate by upwelling of deep water and in winter by the temperature convection—have been confirmed by a series of newer investigations" [*Gran*, 1930].

Gran was aware that if seasonal cycles in standing stock were analogous to geographical differences, then studying the seasonal cycle would provide general information about the control on ocean plankton abundance. He reasoned that plankton organisms are distributed within a euphotic top layer where growth occurs in the daytime, but destruction (respiration) occurs throughout the water column during both day and night [*Gran*, 1930]. Summarising, Sverdrup (1953) noted that "Gran and Braarud [Gran's assistant at Oslo] have suggested that production by photosynthesis cannot exceed destruction of organic matter by respiration if a deep mixed top layer exists". By assuming that phytoplankton are evenly distributed over this mixed later, Sverdrup reasoned that there must be some critical depth, such that blooms can only occur when the mixed layer is shallower than this depth. He showed that it was possible to compute this critical depth, and applied weather ship data from the North Atlantic to show that the "recorded amounts of phytoplankton... confirm these conclusions" (Figure 2.3a). Sverdrup (1955) also updated Nathansohn's theory with a more complete understanding of mixing patterns, sketching out a hypothetical map of phytoplankton productivity based on

---

Gruber, 2006].

global mixing patterns (Figure 2.3b).

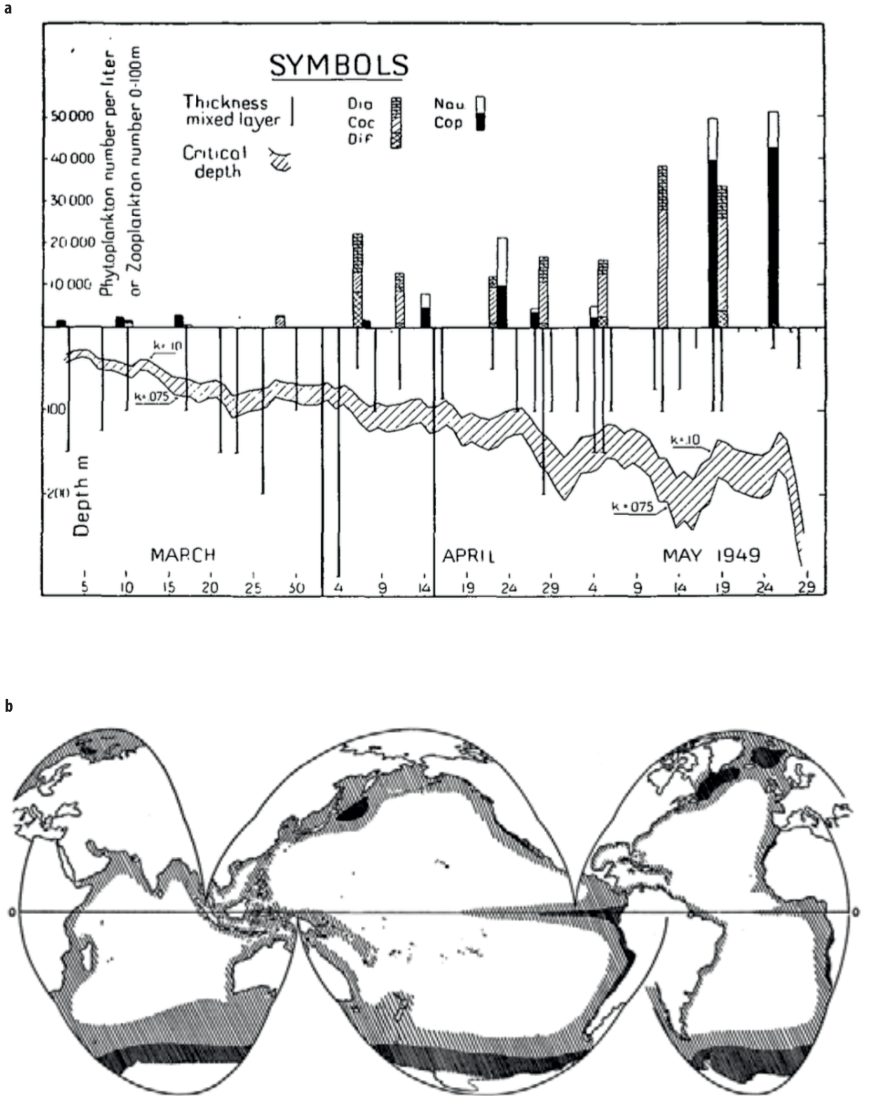

Figure 2.3: **(a)** Observations at Weather Ship ‘M’ (66°N, 2°E) used by Sverdrup (1953) to support the hypothesis that the vernal phytoplankton blooms occur when mixed layers are less that a critical depth. The symbols are explained in the graph. **(b)** Sverdrup’s (1955) estimate of relative phytoplankton productivity based on internal physical processes of vertical convection, upwelling and turbulent diffusion. Dark hatching: high production; mild hatching: moderate production; open: low production.

Sverdrup’s (1953) ‘critical depth’ model has faced a number of subsequent challenges. We will focus on one that is particularly applicable to the Arctic Ocean. Sverdrup’s critical depth model predicts that blooms are initiated when the water column becomes stratified, increasing average light available to phytoplankton

[*Taylor and Ferrari*, 2011]. But blooms have been observed in the absence of water column stratification [*Townsend et al.*, 1992].

Sverdrup's critical depth model considers a thoroughly mixed surface layer bounded at the base by a density gradient that prevents mixing with the layers below. Phytoplankton in this surface layer are thoroughly mixed such that they are then evenly distributed (cell division rates are much lower than mixing rates). For evenly distributed phytoplankton, the light level available to them is the average over the mixed layer. However, if the rate of mixing in the upper layer is reduced then phytoplankton cell division rates are no longer much lower than mixing rates and phytoplankton cells are not equally exposed to light. Phytoplankton near the surface will be exposed to more light than those at the base. As the mixing rate decreases, a bloom at the top of this surface layer becomes more readily possible irrespective of mixed layer depths.

Thus, either reducing the mixed layer depth or the mixed-layer turbulence may cause phytoplankton to bloom (Figure 2.4). Below a critical turbulence it is possible to maintain a steady plankton population in an arbitrarily deep mixing layer. Below a critical mixed-layer depth, a steady plankton population can be maintained for arbitrarily high turbulence values (light incident on cells approaches the mixed-layer average as turbulence increases, Sverdrup's solution).

Taylor and Ferrari (2011) derive a normalised turbulence and mixing depth and show the conditions under which positive phytoplankton populations can be maintained. Normalised mixing depth is given by, $H^* = H/h_l$, where H is the mixing depth (m) and h_l is the e-folding depth of light penetration (m). Normalised turbulent diffusivity is, $K_T^* = K_T/mh_l^2$, where K_T is turbulent diffusivity (m^{2}s^{-1}) and m is the loss rate of phytoplankton cells (d). The Arctic Ocean (interior of the Atlantic inflow) has low turbulence throughout the year. For typical Arctic basin values,

$$H^* = \frac{H}{h_l} = \frac{50}{10} = 5 \tag{2.1}$$

and

$$K_T^* = \frac{K_T}{mh_l^2} = \frac{10^{-3}}{10^{-5} \cdot 10^2} = 1. \tag{2.2}$$

Mixing depth H is from Steele *et al.* (2001), light penetration depth h_l is from Sakshaug (2004), phytoplankton loss rate m is from Taylor and Ferrari (2011), and turbulent diffusivity K_T is from Bourgault *et al.* (2011). It can be seen (Figure 2.4) that the Arctic Ocean is generally in the domain where a positive phytoplankton population can be maintained irrespective of the mixing layer depth. This may not matter if light penetration depth is less than mixing layer depths ($H^* > 1$, Equation 2.1). In this case it is too dark for growth below the mixing layer. But, when mixing layer depths are very shallow and light penetration is deep enough ($H^* < 1$), we should expect that phytoplankton can grow below the mixing layer. Light penetration deeper than mixing layers occur in the interior of

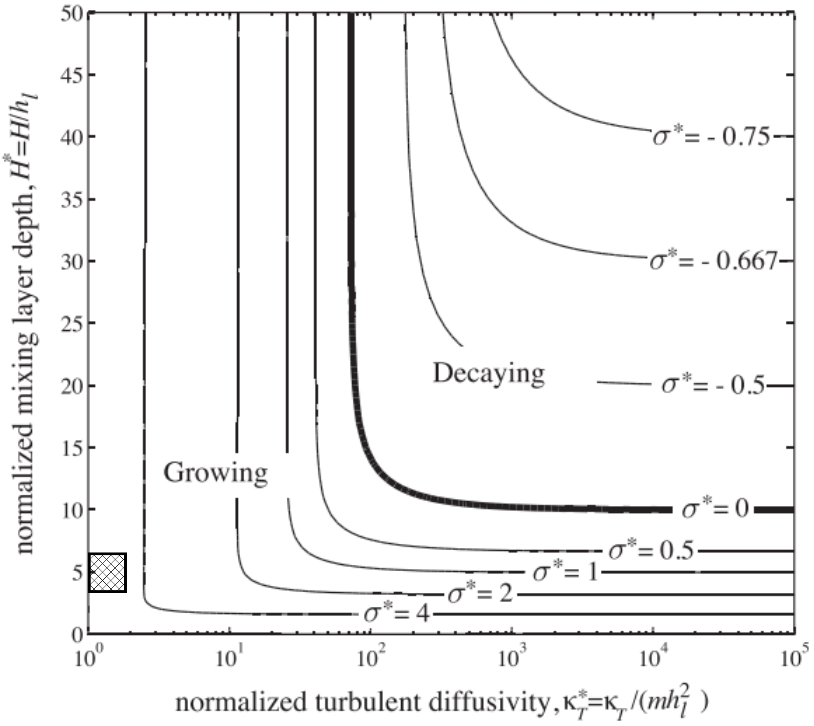

Figure 2.4: Normalized maximum growth rate as a function of turbulent diffusivity and mixing-layer depth, according to by Taylor and Ferrari (2011). The hatched box indicates typical Arctic conditions. Mixing layer depth and turbulent diffusivity are defined in Equations 2.1 and 2.2. Maximum growth rate (σ, d) is normalised by the constant loss rate (m), $\sigma* = \sigma/m$.

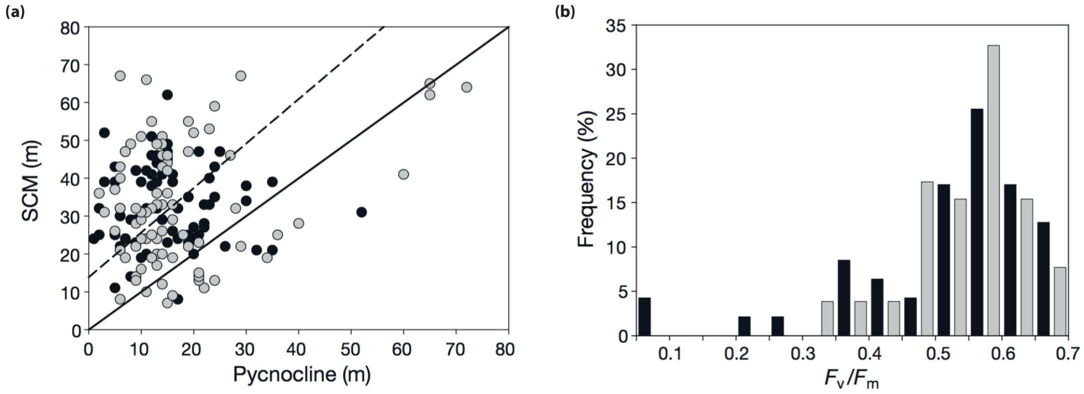

Figure 2.5: **(a)** Relationship between depth of the subsurface chlorophyll maximum (SCM) and the pycnocline in 2005 (black circles) and 2006 (gray circles) from Martin *et al.* (2010). Solid line indicates 1:1 match; and dashed line the linear regression between SCM and pycnocline depths (y = 1.18x + 13.86; $r^2 = 0.04$). **(b)** Frequency distribution of F_v/F_m, a measure of photosynthetic competence of the cell [*Martin et al.*, 2010], at the surface (black) and at subsurface chlorophyll maximum (gray). High F_v/F_m indicates that cells are healthy and well acclimated to grow at the respective irradiance and nutrient conditions.

the Arctic in summer [*Steele et al.*, 2001; *Matrai et al.*, 2013]. This may explain why phytoplankton growth below the pycnocline is widespread in the Canadian Arctic, as demonstrated by observations of phytoplankton chlorophyll-a and cell photosynthetic competence (Figure 2.5).

The Canadian Arctic example suggests that Arctic Ocean phytoplankton may grow on dissolved nutrients below the mixed layer. In this case the light or nutrients available to plankton cells are not determined by the mixed-layer average. Instead in this thesis we will explicitly consider how light and nutrients are distributed over depth.

From the formation of the Kiel school in the 1870s to Sverdrup's formalisations of the link between vertical circulation and phytoplankton abundances in the 1950s, a general theory that linked nutrient distributions to photosynthesis developed. Hensen, Brandt and the Kiel school emphasised the correspondence between production on the land and in the sea. They elucidated how phytoplankton, by acting as the autotrophic energy source for marine life, could be used to assess the health of the seas. They also introduced the hypothesis that nitrate concentrations play a central role in setting phytoplankton abundances.

Brandt sought to explain patterns in phytoplankton abundance in terms of denitrification losses of nitrate. Higher abundances at high latitudes were enabled, he supposed, by temperature-inhibition of denitrifying bacteria. Nathasohn instead, explained phytoplankton abundance patterns in terms of the vertical supply of nutrients. Locations where the vertical supply of nutrients was great could support higher abundances. Nathasohn's theory was developed by Gran, Braarud and Sverdrup to explain the temperate spring bloom and later combined with Sverdrup's knowledge on ocean mixing to map out spatial patterns in production.

Theory on critical turbulence combined with observations from the Canadian Arctic, indicate that positive phytoplankton populations are widespread below the mixed layer depth in the Canadian Arctic, aided by turbulence levels that are orders of magnitude below other oceans. This entails that mixed-layer nutrient and light budgets will not be adequate to elucidate Arctic Ocean production dynamics.

2.3 The ingredients of photosynthesis

Photosynthesis proceeds by a kinetic reaction that converts inorganic nutrients into organic compounds according to

$$6CO_2 + 6H_20 \rightleftharpoons C_6H_{12}O_6 + 6O_2, \tag{2.3}$$

where carbon dioxide (CO_2) is reduced to glucose ($C_6H_{12}O_6$). The rate at which the reaction can proceed depends on the supply of photon energy (hf) and the reactants carbon dioxide and water (H_20). The reverse reaction where glucose is oxidised to carbon dioxide is respiration.

Phytoplankton also require a host of macronutrients and micronutrients to build machinery and perform metabolic functions within the cell. Assessment of the chemical composition of phytoplankton cells shows that these basic building blocks are the macronutrients C, N, P, O (Table 2.1). Plankton also require micronutrients (Fe, Co and Zn...) as structural elements and to catalyse reactions [*Williams and*

Metabolite	Elemental Composition	% cell
Protein	$C_{3.83}H_{6.05}O_{1.25}N$	54.4
Carbohydrate	$C_6H_{10}O_5$	25.5
Lipid	$C_{40}H_{74}O_5$	16.1
Nucleic acid	$C_{9.625}H_{12}O_{6.5}N_{3.75}P$	4.0

Table 2.1: Representative molecular compositions of major cell components and average contributions by dry weight, as evaluated by Anderson *et al.* (1995).

Follows, 2011].

2.3.1 Carbon

The diffusion rate of carbon dioxide (CO_2) in water and the dehydration kinetics of bicarbonate to CO_2 place constraints on marine phytoplankton [*Reinfelder*, 2011]. Biocarbonate ions in the ocean may dehydrate to form CO_2, equilibrating changes that occur in dissolved CO_2 concentrations. Ocean photosynthetic algae have generally overcome constraints on carbon availability by evolving carbon concentrating mechanisms, found in nearly all marine phytoplankton [*Reinfelder*, 2011]. These mechanisms work by concentrating carbon inside the cell around the carbon-fixing enzyme RuBisCO, such that the enzyme can work at a higher efficiency. Because of this mechanism for transporting carbon into the cell, carbon is not generally thought to limit oceanic photosynthesis [*Reinfelder*, 2011].

2.3.2 Nitrate and phosphate

Nitrogen and phosphorus are also required by plankton: to build metabolic machinery, as energy transduction molecules and as the basis of DNA (Table 2.1). Cell uptake of nitrogen and phosphorus occurs in an average stoichiometry of 16:1 [*Redfield*, 1934; *Klausmeier et al.*, 2004], so ocean waters that contain one nutrient in excess of this ratio will become depleted in the other under growth. Measurements across the ocean show that nitrate generally runs out slightly before phosphorus, implying that biological growth in the ocean is limited by nitrate [*Tyrrell*, 1999].

But oceanic nitrate and phosphorus have different sources. Phosphate in the ocean is continentally sourced, whereas nitrate can be supplied by oceanic nitrogen-fixing bacteria. When ocean nitrate levels are low, plankton with nitrogen-fixing capacity can grow where plankton that require dissolved nitrate cannot. This superior growth of nitrogen fixers adds nitrate to the ocean and the balance between nitrogen and phosphorus is restored. The phytoplankton community can thus regulate its environment by restoring the stoichiometric nitrate:phosphorus balance according to the external supply of phosphate, whose variation over long timescales may ultimately limit production in the ocean [*Tyrrell*, 1999].

2.3.3 Iron

Since early ocean expeditions it has been known that nitrate concentrations are elevated in the Southern Ocean [*Gebbing*, 1909]. Excess nitrate should not occur if it limits growth, since the photosynthetic reaction should continue until nitrate is exhausted. This phenomenon of regions with excess macro-nutrients but low growth (termed ‘high-nutrient low-chlorophyll’ regions) has also been observed in the equatorial Pacific and subarctic Atlantic and Pacific [*Martin and Fitzwater*, 1988; *Kolber et al.*, 1994; *Achterberg et al.*, 2013].

Besides nitrate, phytoplankton also require iron: as an electron transporter in photosynthesis, as structural elements of proteins, and in nitrogen fixing enzymes [*Morel and Price*, 2003]. Measured iron concentrations in high-nutrient low-chlorophyll regions are extremely low [*Gordon et al.*, 1982], suggesting iron limits phytoplankton growth in these regions. Subsequent enrichment experiments have show that adding iron increases growth, confirming this hypothesis [*Martin and Fitzwater*, 1988; *Behrenfeld et al.*, 1996].

2.4 The kinetics of photosynthesis

2.4.1 Nutrient kinetics

Photosynthesis proceeds as a kinetic reaction (i.e. at a rate that depends on reactant concentrations). The reaction is catalysed by enzymes, without which the reactions would proceed very slowly or not at all. These enzymes are not consumed in the reaction so they are returned to be used for subsequent reactions.

Michaelis and Menten (1913) consider this process as a simple two step reaction where (1) a molecule binds to an enzyme and reacts to form a product (2) the product is released and the enzyme is free to bind to a new molecule (the derivation here follows [*Williams and Follows*, 2011]). For molecule A binding to enzyme E to form product C the reaction is

$$A + E \rightarrow A \cdot E \rightarrow E + C. \tag{2.4}$$

The rate of production of C depends on the rate that A binds to enzymes to form $A \cdot E$

$$\frac{d[C]}{dt} = k_p[A \cdot E], \tag{2.5}$$

where square brackets denote concentrations ($\mathrm{mmol\,m^{-3}}$) and k_p ($\mathrm{s^{-1}}$) is the rate constant of product formation. We are interested in how the rate of production of $[C]$ depends on the concentration of nutrient $[A]$ rather than $[A \cdot E]$ so we need to know the relationship between $[A]$ and $[A \cdot E]$. To make this conection consider the rate of change of the enzyme-substrate complex $A \cdot E$. This complex increases in concentration when the substrate binds to a free enzyme but decreases when the product C is formed

$$\frac{d[A \cdot E]}{dt} = k_f[A][E] - k_p[A \cdot E], \tag{2.6}$$

where k_f is the rate constant of the forward reaction $[A] + [E] \rightarrow [A \cdot E]$ in units of $(\mathrm{mmol\,m^{-3}})^{-1}\,\mathrm{s^{-1}}$.

If the reaction runs to equilibrium, where the amount of complexed enzyme is unchanging, $d[A \cdot E]/dt = 0$, then

$$[A \cdot E] = \frac{k_f}{k_p}[A][E]. \tag{2.7}$$

If the total available enzyme concentration is also fixed $[E_T]$, defined as the sum of the free and complexed forms, then

$$[E_T] = [E] + [A \cdot E]. \tag{2.8}$$

Equations 2.7 and 2.8 can be combined to give

$$[A \cdot E] = \frac{[E_T][A]}{(k_p/k_f + [A])}. \tag{2.9}$$

By combining Equations 2.5 and 2.9, the rate of production of C can now be expressed in terms of A

$$\frac{d[C]}{dt} = k_p[E_T]\frac{[A]}{k_p/k_f + [A]}. \tag{2.10}$$

This enzymatic reaction asymptotes to a maximum production rate $d[C]/dt = k_p[E_T]$ as the substrate concentration $A \to \infty$. The substrate that supports half the maximum production rate is $A = k_p/k_f$. Therefore, the reaction is usually expressed as

$$\frac{d[C]}{dt} = V\frac{[A]}{k_A + [A]}. \tag{2.11}$$

where $V = k_p[E_T]$ is the maximum production rate and $k_A = k_p/k_f$ is the nutrient concentration that supports half the maximum production rate. This relationship is applicable to a wide variety of data for enzymatic reactions (an example is plotted in Figure 2.6).

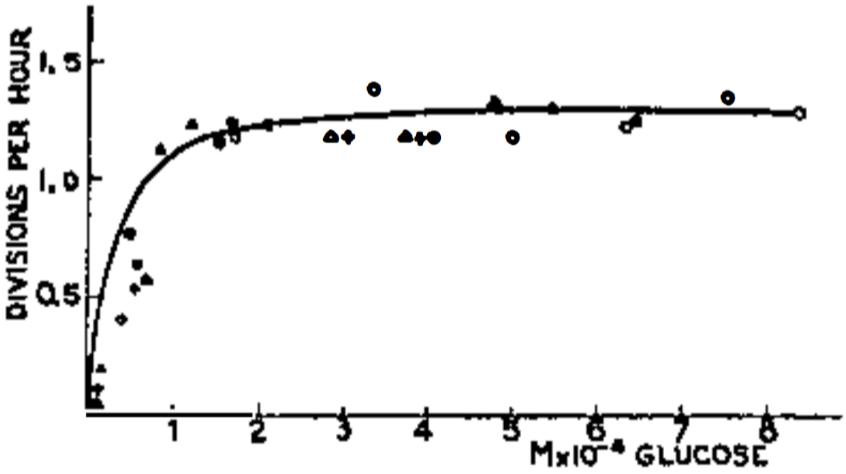

Figure 2.6: Growth rate of *E. coli* in a synthetic medium as a function of glucose concentration. Solid line is drawn to Equation (11) with $V = 1.35$ divisions per hour, and $k_A = 0.22$ Mx10^{-4}. Temperature was fixed at 37 °C. Reproduced from Monod (1949).

2.4.2 Light kinetics

Photosynthesis proceeds using photon energy derived from the sun. Light-harvesting pigments absorb photons which they handle for a certain time (about 10^{-10} s [*Lodish et al.*, 2001]) before energy is then transferred to other areas of the cell and additional photons can be absorbed. The role of pigments in these two steps is analogous to enzyme handling in the nutrient kinetic model above.

Thus, following *Baly* (1935), we may consider the two steps where (1) a photon is absorbed into the cell by a light-harvesting pigment (2) the photon energy is transferred to activate a set of light-independent reactions that form organic compounds, and the pigment is released to absorb a new photon. Let light-harvesting pigment A (mmol m^{-3}) absorb photon I (mmol m^{-3}) to form $A \cdot I$. Let $A \cdot I$ then react with C (mmol m^{-3}) to form product D (mmol m^{-3}), releasing A to take up another photon. We can write this as

$$A + I + C \rightarrow A \cdot I + C \rightarrow A + D. \tag{2.12}$$

The rate of the first reaction is set by the uptake of photons I, to form $A \cdot I$. This uptake rate is determined by available pigments $(A - x)$ where A is total pigments and x are the pigments already bound to photons. The rate of the second reaction depends on the reactant C and temperature [*Baly*, 1935]. As per Baly (1935) we express the temperature-dependence using the Arrenhius terms temperature (T), activation energy (Q) and the gas constant (R) . If the reactions run to equilibrium, then the reaction rate r ($\mathrm{mmol\,m^{-3}\,s^{-1}}$) can be expressed as

$$r = k_1 I(A - x) = k_2 C x e^{-Q/RT}, \tag{2.13}$$

where k_1 and k_2 ($(\mathrm{mmol\,m^{-3}})^{-1}\,\mathrm{s^{-1}}$) are the rate constants of the reactions. Dividing through by $k_1 I x$ gives

$$\frac{r}{k_1 I x} = \frac{A - x}{x} = \frac{k_2 C}{k_1 I} e^{-Q/RT}, \tag{2.14}$$

and

$$\log \frac{r}{K - r} = \log \frac{k_2 C}{k_1 I} - Q'/T \tag{2.15}$$

where $K = k_1 I A$ and is the initial rate of photosynthesis, and Q' = Q/2.303R.

Pigment uptake of a photon $[A \cdot I]$ is analogous to a molecule bonding to an enzyme $[A \cdot E]$, where photon uptake is regulated by pigment concentration. The second step releases the pigment of its photon, leaving it free to repeat photon uptake. This model for light kinetics fits the observed photosynthetic response to light well [*Warburg*, 1919].

2.4.3 Temperature and phytoplankton growth rates

In Figure 2.7, phytoplankton growth rates are plotted against temperature for a suite of cultures grown in variable light and nitrate conditions. At replete light

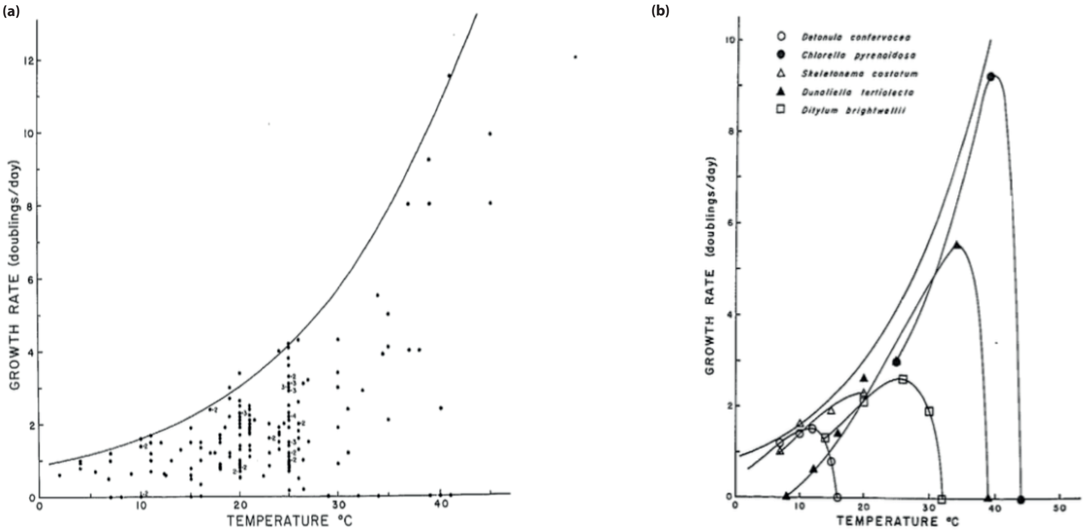

Figure 2.7: **(a)** Variation in the specific growth rate of photoplankton with temperature, from laboratory cultures [*Eppley*, 1972]. The line is the community maximum expected growth rate, $V = V_0 \cdot 1.066^T$. Small numbers by points indicate the number of values which fell on the point. **(b)** Growth rate vs. temperature curves for five unicellular algae with different temperature optima. Reproduced from Eppley (1972).

and nutrient conditions, the growth rate tends to V (d^{-1}). Therefore, by assuming that replete conditions are indicated by the upper bound of the graph, V may be determined by this bound as $V = V_0 \cdot 1.066^T$, where V_0 is the growth rate at $T = 0$°C (Figure 2.7). This is a hypothetical (not directly measured) maximum growth rate for the phytoplankton community, comprising growth rates of individual phytoplankton that are adapted to specific temperature ranges (Figure 2.7b). To determine the actual phytoplankton community growth rate the maximum expected growth rate must be adjusted for light and nutrient limitation.

So far we have introduced the role of oceanic photosynthesis, some of the early development of ocean productivity theory, and the general kinetics of photosynthesis. Now we turn to consider the conditions of the Arctic Ocean.

2.5 Arctic Ocean properties

2.5.1 Geography and bathymetry

The Arctic Ocean is surrounded by continental landmasses. This continental barrier limits the connectivity of the Arctic Ocean with the Pacific and Atlantic Oceans to narrow gateways that are typically a few hundred metres in depth, but reach intermediate ocean depths (2700 m) at their deepest point in the Fram Straits (Figure 2.8). In the interior, wide shallow shelves stretch around the boundaries. These are typically 100-1500 km across and 100 m deep, and are substantially wider on the Eurasian than Amerasian side. The shelves bound four central basins. The Canada Basin is the largest. It is separated from the Makarov Basin by the Alpha Cordillera, and from the Amundsen and Nansen Basins by the Lomonosov Ridge, which runs from Russia to Greenland roughly under the North Pole. Water depths in the basins are typically 3000–4000 m deep. The deepest point is in the Eurasian Basin at 5450 m.

Bathymetry influences Arctic Ocean properties. Gateways into the Arctic (<2700 m) restrict the depths of Atlantic and Pacific water that enter (Atlantic and Pacific basins are up to 6 km deep). Atlantic and Pacific water properties vary with depth so the restriction influences the ocean properties that are fluxed through the Arctic boundary. For example, deep waters that contain the highest nutrient concentrations occur at greater depths than Arctic gateways (> 2 km), preventing the highest nitrate waters from entering the Arctic. Accordingly, nitrate concentrations in the deep Atlantic may reach 30–40 mmol m^{-3} but do not generally exceed 15 mmol m^{-3} in the deepest points of the Arctic.

2.5.2 Sea ice conditions

The Arctic is the only ocean that retains sea ice throughout the year. Sea ice extent and thickness are maximum in March and minimum in September (Figure 2.9) [*Laxon et al.*, 2013]. Ice thickness varies from 0–5 m and is thickest in winter in the Canadian Arctic, north of Greenland and in the Canadian Arctic Archipelago

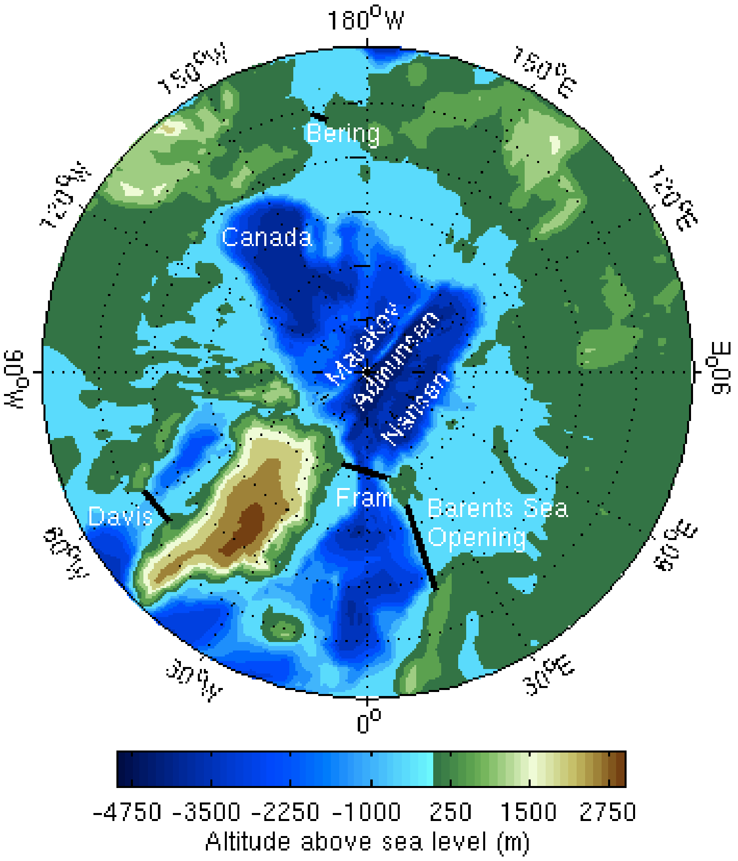

Figure 2.8: Arctic Ocean bathymetric map showing the principal basins and four straits connecting the Arctic with the lower latitude oceans.

[*Laxon et al.*, 2013].

Sea ice extent is zonally asymmetric. It extends to below the Arctic circle in the Pacific sector and east and west of Greenland, but only into the Barents Sea in the eastern Atlantic Sector (Figure 2.9a). This asymmetry likely arises because of differences in ocean circulation and heat transport between the Pacific and eastern Atlantic sectors [*Årthun et al.*, 2012; *Onarheim et al.*, 2015]. The Atlantic Ocean inflow is warmer, with larger heat transports than the Pacific inflow: the Barents Sea Opening (Atlantic) summer heat flux is estimated as 86±19 TW, compared to 13±2 TW through the Bering Straits (Pacific) [*Tsubouchi et al.*, 2012]. Sea ice extends further south on the east and west sides of Greenland (Figure 2.9) because ocean currents and atmospheric wind patterns drive sea ice export out of the Arctic here [*Rampal et al.*, 2009].

The Arctic sea ice cover is also reducing in extent each year (Figure 2.9c). The September minimum is decreasing $11\%\,\mathrm{yr}^{-1}$ on average, although the decrease is

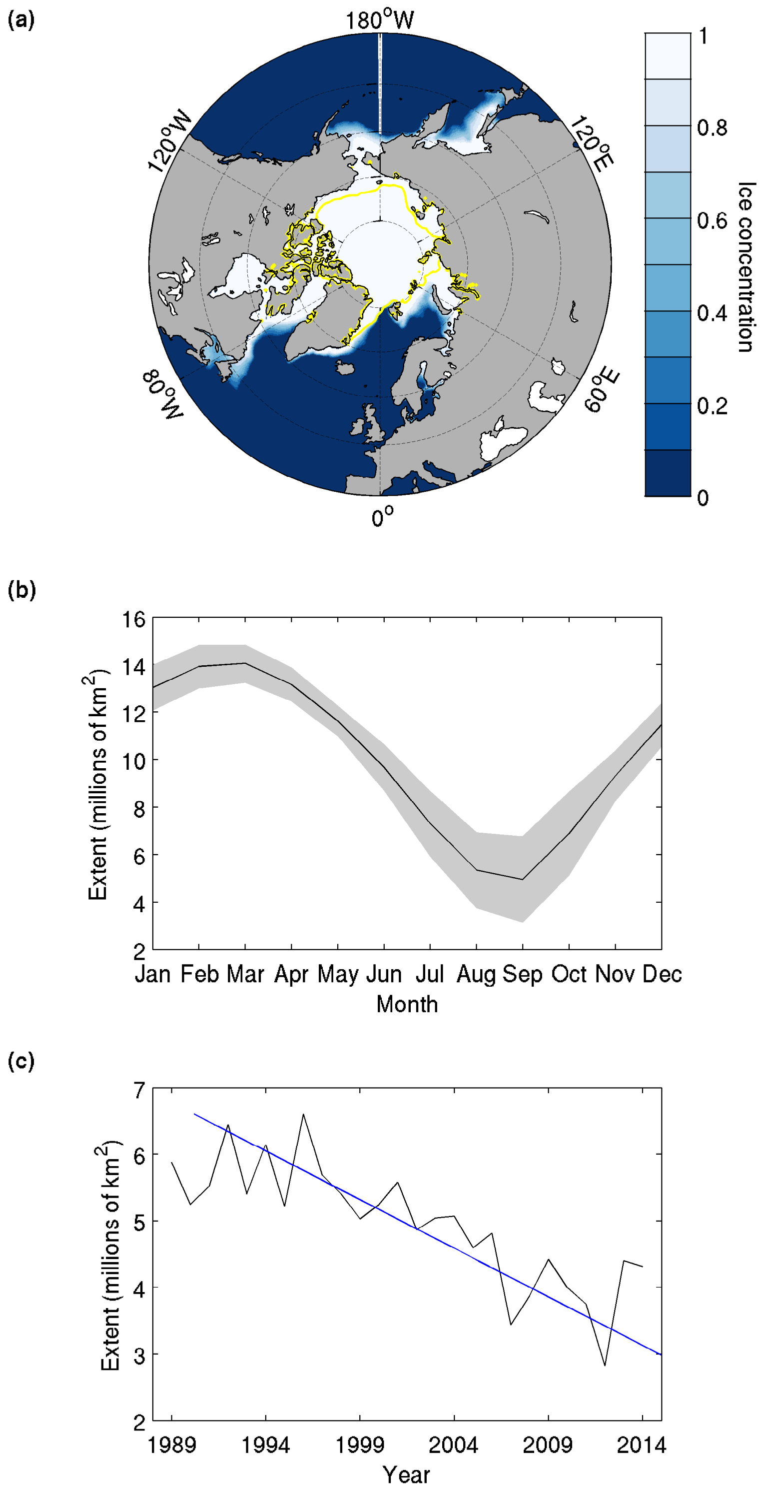

Figure 2.9: **(a)** Map of Arctic sea ice at its maximum (March) and minimum extent (September, yellow contour), averaged over 1989–2014. **(b)** Seasonal cycle of Arctic sea ice extent (1989–2014 average; ±1S.D.). **(c)** Declining trend in minimum sea ice extent over 1989–2014. Data are from Meier *et al.* (2015).

both non-linear and non-monotonic. Both thermodynamic and dynamic processes contribute to this decrease, including: the size and fragility of the preconditioned winter ice pack, increasing atmospheric and ocean temperatures, and changes in wind patterns that drive export of sea ice [*Zhang et al.*, 2008].

2.5.3 Potential density and T-S conditions

Arctic Ocean waters are cold but fresh, and potential density is low across the Arctic (Figure 2.10a). At the surface, mixing of precipitation, sea-ice melt-water and river outflow with Arctic Ocean surface waters produces cold, fresh waters (Figure 2.10c). Sea surface temperature changes are small, and the density structure (stratification) is set by variations in salinity (Figure 2.10c). Particularly-buoyant surface waters are located along the Siberian Shelf and in the Beaufort Gyre (Figure 2.10a), arising from large inputs of freshwater from Siberian rivers [*Morison et al.*, 2012], and the wind-driven circulation in the Beaufort Gyre [*Proshutinsky et al.*, 2002], respectively .

Denser, warmer conditions are found at intermediate depths, particularly in dense, salty Atlantic Water (Figure 2.10c). Atlantic Water (AW) is separated from surface Mixed Layer Waters (MLW) by Upper and Lower Halocline Waters (UHW, LHW) that prevent mixing between the two end members (Figure 2.10c). This separation is of particular climatic importance because it prevents the transfer of heat trapped in Atlantic Water from reaching the surface mixed layer, where it may melt sea ice [*Lique*, 2015]. Lower intermediate water (LIW) and deep water (ADW) are cold and salty (Figure 2.10c).

2.5.4 Arctic Ocean circulation

General circulation dynamics in the Arctic Ocean are complicated by the small Rossby deformation radius [*Nurser and Bacon*, 2013], flow recirculations [*von Appen et al.*, 2014], bifurcations [*Weingartner et al.*, 2005], and ageostrophy [*Woodgate et al.*, 2001]. Typical studies may rely on plausible model scenarios [*Aksenov et al.*, 2010b], or omit the Arctic entirely [*Ganachaud and Wunsch*, 2000]. Based on syn-

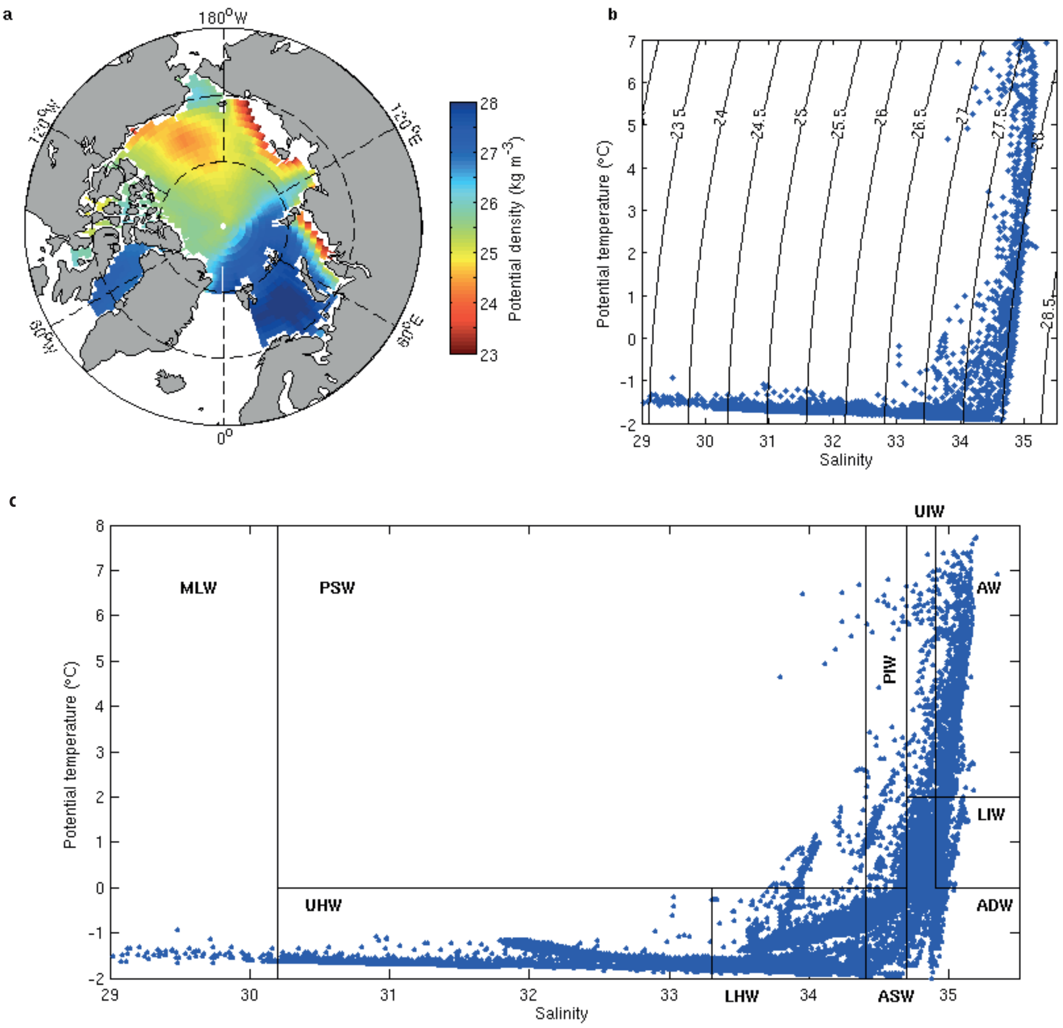

Figure 2.10: **(a)** Winter (February) potential density (kg m^{-3}) at 10 m based on the PHC climatology [*Steele et al.*, 2001]. **(b)** Potential temperature-salinity at 10 m with density contours. **(c)** Potential temperature-salinity for six Arctic Ocean depths (10 m, 75 m, 200 m, 500 m, 900 m, 1300 m). Conventional water masses are indicated based on Aksenov *et al.* (2010). MLW: Mixed Layer Water. PSW: Polar Surface Water. UHW: Upper Halocline Water. Lower Halocline Water. ASW: Arctic Surface Water. PIW: Polar Intermediate Water. UIW: Upper Intermediate Water. LIW: Lower Intermediate Water. AW: Atlantic Water. ADW: Arctic Deep Water.

thesising models with sparse hydrographic measurements, schematics of the general Arctic Ocean circulation have emerged that consider four vertically-arranged water classes as follows [*Bluhm et al.*, 2015].

Surface waters flow into the Arctic Ocean through the Barents Sea Opening, in the West Spitsbergen Current on the east side of Fram Strait, and through the

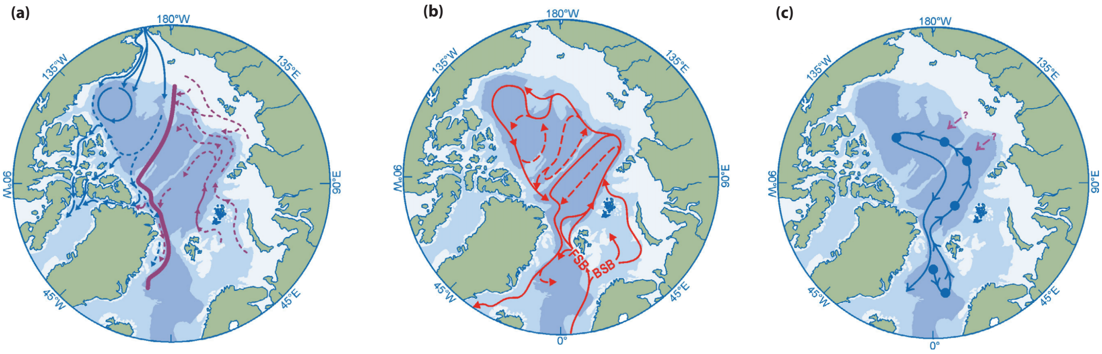

Figure 2.11: Schematic of Arctic Ocean circulation from Bluhm *et al.* (2015). **(a)** Halocline sources, flows and associated fronts (blue: Pacific-origin; maroon: Atlantic-origin; thick maroon line: front between them). **(b)** Arctic Circumpolar Boundary Currents derived from Atlantic Intermediate Water. **(c)** Deep water exchange (Aagaard *et al.*, 1985). BSB: Barents Sea Branch. FSB: Fram Strait Branch. Reproduced from Bluhm *et al.* (2015).

Bering Straits (Figure 2.11a, 2.13a). Water exits the Arctic Ocean through Fram Straits and Baffin Bay. In the interior, waters entering from the Atlantic and Pacific circulate cyclonically (anticlockwise) around the boundary in the topographically-steered Arctic Boundary Current. Strong topographic-steering occurs both around the shelf slope and along the trans-Arctic ridges [*Bluhm et al.*, 2015]. Annual-mean flows in this Boundary Current are weak (1–5 $\mathrm{cm\,s^{-1}}$, [*Woodgate et al.*, 2001]). Anticyclonic wind patterns over the Beaufort Sea drive the anticyclonic Beaufort Gyre, an important storage of freshwater in the Arctic Ocean [*Giles et al.*, 2012] that is clearly seen in the surface potential density field (Figure 2.10a). Surface waters are also driven across the Arctic in the Transpolar Drift by the sea level pressure gradient from the Pacific to the Atlantic [*Proshutinsky and Johnson*, 1997].

Cold, fresh surface waters are separated from denser deep waters by a fresh halocline layer (5–120 m depth) [*Steele and Boyd*, 1998]. This layer comprises water of both Pacific and Atlantic origins, which meet at an Arctic-wide front (Figure 2.11a), the position of which moves substantially between years [*Steele and Boyd*, 1998]. The cold halocline layer is likely to form through a mixture of advective and convective processes, and is sustained through weak vertical diffusivity in the Arctic Ocean (e.g. [*Fer*, 2009]). In the convective model, salt rejection when sea ice is formed leads to saline surface waters that are convectively unstable. The resulting halocline is subsequently capped by freshwater [*Rudels et al.*, 1996]. In the advective model, cold salty waters from the shelf interleave below cold fresh surface waters and above warm salty intermediate waters of Atlantic origin [*Aagaard et al.*, 1981]. The two processes may be diagnosed separately in T-S space because in the convective case, halocline waters will be at the freezing point temperature (whereas advected waters may be warmer). Analysis of hydrographic data suggests both processes occur [*Woodgate et al.*, 2001].

Arctic Intermediate Water pathways are restricted by gateway depths (Figure 2.11b). Water may enter the Arctic from the Atlantic, but not the Pacific, and can only exit through Fram Strait (because additional density is accrued through cooling in the Barents Sea Branch [*Aksenov et al.*, 2010b]). Pathways of Atlantic water through the Arctic may be traced across the Arctic by the anomalously warm temperature signal [*McLaughlin et al.*, 1996] or the conservative geochemical tracer ^{129}I [*Karcher et al.*, 2012]. ^{129}I is an isotope produced by nuclear processing in the north east Atlantic, with no Pacific origin, making it a unique tracer of Atlantic waters. By combining observed distributions of ^{129}I concentrations in the Arctic interior with numerical models of ocean transports, Karcher *et al.* (2012) have attempted to piece together Atlantic Intermediate Water pathways. They broadly conclude that entering water flows either side of Svalbard, in the Barents Sea Branch and Fram Strait Branch. On entering the Eurasian Basin, waters are topographically steered by the shelf slope and transverse ridges, before exiting through Fram Straits (Figure 2.11).

Deep waters may only enter and exit the Arctic through Fram Straits (≤ 2700 m). They may also be formed within the Arctic by modification of intermediate waters entering through the Barents Sea Opening, or density flows down the continental slope [*Jones et al.*, 1995]. It is likely that waters entering through Fram Straits are augmented by additional salinity within the Arctic [*Aagaard et al.*, 1981], but the details are far from clear. Since we are concerned with photosynthesis which is restricted to surface layers, the lack of understanding concerning deep circulation in the Arctic Ocean will not affect us here.

2.5.5 Arctic Ocean mixing

Turbulent mixing in the Arctic Ocean is low — typically one to two orders of magnitude below mid-latitudes [*Levine et al.*, 1985; *D'Asaro and Morison*, 1992; *Plueddemann*, 1992; *Pinkel*, 2005] — arising from weak tides and ocean wind stress. Sea ice isolates the ocean from wind-driven mixing, acting to dampen inertial motions through its strong rigidity. Tides are generally weak in the Arctic Ocean, as it is north of the critical latitude of diurnal tides (74.5°N).

Low mixing rates imply that mixing does not play a strong role in the distribution of oceanic properties or evolution of Arctic water masses. This may change with a declining sea ice cover. Micro-structure measurements indicate enhanced internal wave energy in ice-free waters [*Rainville and Woodgate*, 2009]. Enhanced mixing with sea ice loss would then imply a stronger exchange of properties. Of particular relevance is the heat stored at intermediate depths in the Arctic Ocean, separated from surface waters by stratification. Heat content of intermediate waters is adequate to melt all sea ice in the Arctic [*Lique*, 2015], so mixing of this heat to the surface would have profound consequences. At present, turbulent diffusivity is elevated near the surface, but rapidly decreases to background values of order $K_b = 10^{-5}$–$10^{-6}\,m^2s^{-1}$ at the intermediate depths where heat gradients are large [*Fer*, 2009]. Present heat fluxes are therefore very modest (0.05–0.3 Wm^{-2}) [*Padman and Dillon*, 1987; *Fer*, 2009; *Lenn et al.*, 2009]. Vertical gradients in turbulent diffusivity also have consequences for nitrate supply to the surface. In the Admunsen Gulf, Bourgault *et al.* (2011) measured high diffusivities at 10 m (K_{max} = 3 x $10^{-3}\,m^2s^{-1}$), but diffusivity decreased exponentially with depth to a background value K_b = 3 x $10^{-6}\ m^2s^{-1}$ by 50 m. The nitracline was observed at 62 m depth so the mean diffusive nitrate flux across the nitracline was low (0.5 $mmolm^{-2}d^{-1}$).

Pan-Arctic dissipation measurements indicate that areas of enhanced turbulent kinetic energy are related to longitude and topography. Mixing rates are enhanced over rough topography [*Rippeth et al.*, 2015], which is thought to cause the breaking of internal waves and dissipation of energy through turbulence (i.e. diapyncal mixing) [*Ferrari and Wunsch*, 2008]. Tides (not winds) are identified as the main energy source of this enhanced dissipation [*Rippeth et al.*, 2015].

Internal wave energy is enhanced in ice-free waters [*Rainville and Woodgate*, 2009], which suggests higher turbulent dissipation in an ice-free Arctic Ocean. But present pan-Arctic dissipation rates are insensitive to ice conditions [*Rippeth et al.*, 2015]. Rippeth *et al.* (2015) suggest that increased transfer of momentum from the atmosphere to ocean as Arctic sea ice declines will instead lead to an expansion in mixing hotspots centred around rough topography. Measurements made in the Canada Basin in the low-ice and stormy summer of 2012 show enhancement of internal wave energy associated with increased momentum transfer; but increased mixing at intermediate depths was not seen away from topography [*Lincoln et al.*, 2016]. This supports Rippeth *et al.*'s (2015) implication that the presence of topography may be central to overcoming stratification and increasing vertical mixing under declining ice cover [*Lincoln et al.*, 2016].

2.5.6 The wind-driven Arctic Ocean

Two time-dependent wind-driven circulation regimes exist in the Arctic Ocean. When high pressure systems sit over the Arctic, east-to-west (anticyclonic) winds occur over the Siberian Seas, driving an anticyclonic ocean circulation [*Proshutinsky and Johnson*, 1997]. This wind pattern moves the trajectories of cyclones towards land, increasing river runoff; and induces colder Arctic surface temperatures, that lead to thicker and more extensive Arctic sea ice cover [*Proshutinsky and Johnson*, 1997]. When low pressure around Iceland (the Icelandic Low) forms into a tongue that extends north towards the Arctic, cyclonic winds develop in the Arctic. These anticyclonic and cyclonic modes alternate every 5–7 years [*Proshutinsky and Johnson*, 1997].

Anticyclonic winds drive Ekman convergence over the Beaufort Gyre and weaken the transpolar drift [*Proshutinsky et al.*, 2002]. This causes an increase in potential energy in the gyre, and a downwards deformation of the salinity field, as light freshwater piles up over the gyre [*Proshutinsky et al.*, 2002]. Freshwater storage in the Arctic is also enhanced during the anticyclonic mode by increased ice growth and reduced ice drift out of the Arctic [*Proshutinsky and Johnson*, 1997]. In the cyclonic mode, winds drive ocean divergence and the gyre is weaker. A weaker gyre increases leakage of freshwater and export of ice into the Greenland Sea [*Proshutinsky et al.*, 2002].

Wind-driven freshwater storage in the Beaufort Gyre has important consequences for the adjacent North Atlantic. The transition from an anticyclonic mode to a cyclonic mode releases freshwater from the Arctic into the North Atlantic where it may interact with the Thermohaline Circulation by modulating buoyancy forcing of high-latitude sinking waters [*Hátún et al.*, 2005]. This release mechanism could have been responsible for the Great Salinity Anomaly in the North Atlantic [*Dickson et al.*, 1988; *Proshutinsky et al.*, 2002].

Recent satellite measurements in the Beaufort Gyre show sea surface height has increased at 1–2 $\mathrm{cm\,yr^{-1}}$ under increasingly anticyclonic winds (1995–2010) [*Giles et al.*, 2012]. Freshwater storage increased (8,000 ± 2,000 $\mathrm{km^3}$) over the same period [*McPhee et al.*, 2009; *Rabe et al.*, 2011]. There is also a clear distinction in the satellite data, prior to and after 2002. Reanalysis-derived (NCEP/NCAR) winds are more or less consistent in both periods, but sea surface height decreases $-0.59\pm0.13\,\mathrm{cm\,yr^{-1}}$ prior to 2002 and increases $1.88\pm0.09\,\mathrm{cm\,yr^{-1}}$ afterwards [*Giles et al.*, 2012]. This indicates that the wind is more effective at spinning up the gyre since 2002: the efficiency of momentum transfer from the atmosphere to the ocean increased. Further, an increased ice drift speed has been observed from 2004 onwards, which cannot be fully explained by changes in wind speed [*Comiso et al.*, 2008]. Buoy observations also show a larger ice deformation rate in summer 2007 compared with 1979-2006 [*Rampal et al.*, 2009]. These higher ice deformation rates and drift speeds suggest the mechanical strength of the ice is decreasing, making it easier for the wind to move it, driving ocean motions beneath [*Giles et al.*, 2012]. This interpretation is consistent with declining Arctic sea-ice extent and thickness: larger areas of open-water and the lower mechanical strength of thinner ice are likely to increase the efficiency of momentum transfer.

Depression of the isopycnal field by wind-driven Ekman convergence has implications for the availability of nitrate in the gyre. Nitrate-rich Pacific-origin waters enter the gyre along isopycnals at subsurface depths (typically 40 m; [*McLaughlin and Carmack*, 2010]). To reach euphotic surface waters, nitrate rich waters must be mixed with the fresher surface waters above; isopycnal deepening and increased stratification both make this more difficult. Between 2003-2009, gyre convergence and stratification increased and the depth of the nitracline increased accordingly, from 50 m to 70 m between 2007–2009 [*McLaughlin and Carmack*, 2010].

The phytoplankton response to nitrate changes is indicated by the depth of the subsurface chlorophyll maxima (SCM) that commonly develops around the nitracline [*Martin et al.*, 2010]. The Canada Basin average chlorophyll-maximum deepened between 2003–2009, from 46–60 m, in response to a deeper nitracline [*McLaughlin and Carmack*, 2010]. Between 2003–2006 this increased the amount of nitrate available at the SCM; but from 2006–2009, available nitrate decreased. This decrease in available nitrate likely arose because 2007–2009 deepening of the SCM (from 56 to 66 m) did not keep pace with deepening of the nitracline (from 50 to 70 m).

The phytoplankton response to a deepening nitracline is subtle, depending on the interplay between a deepening nitracline, reduced light at depth, and increased average water column light with the reduced sea ice cover. This balance speaks to wider Arctic phytoplankton challenges under changing nitrate and light conditions and will be developed throughout the thesis. We will analyse the trade-off in nutrients and light with depth and discuss the consequences (Chapter 4); it will also motivates us in our approach to explaining current and ice-free Arctic photosynthesis (Chapters 5, 6).

2.5.7 Nutrients

Arctic Ocean nutrient distributions observed at the surface and 200 m are given in Figure 2.12. Because of low data coverage, all months and years are plotted together to improve the spatial coverage: masking seasonal and multi-year variability. Data are heavily biased towards summer when shipboard sampling is easier, and sampling has also been greatest in the decades of the 1970s and the 2000s-present [*Bluhm et al.*, 2015]. This bias towards summer indicates that these measurements generally reflect different stages of summer nutrient limitation of phytoplankton growth, not the winter nutrient supply.

Nitrate, phosphate and silicate

The Arctic Ocean is strongly oligotrophic, with surface nitrate concentrations in the range 0–10 mmolm^{-3} at the surface, and 10–15 mmolm^{-3} at 200 m (Figure 2.12a–b). (In the North Atlantic nitrate concentrations are 20–30 mmolm^{-3} at 200 m depth [*Hansell and Follows*, 2008].) Higher nitrate concentrations (4–10 mmolm^{-3}) occur in the Atlantic sector: in the Greenland and Norweigan Seas, and East Baffin Bay. These extend into the Eurasian basin, approximately up to the Lomonosov Ridge, perhaps reflecting the position of the halocline front where nitrate-rich Atlantic Water subducts below nitrate-poor Pacific Water (Figure 2.11a).

Most Arctic shelves are shallower than 200 m so data coverage is restricted to the basins (Figure 2.12). At this depth nitrate concentrations are more homogenous between the Atlantic inflow and interior Arctic. This likely relates to the fact that Arctic winter mixed layer depths and summer euphotic depths (where light is 1% of the value at the ocean surface) are shallower than 200 m (except in the Atlantic inflow) [*Hill et al.*, 2013], so nitrate concentrations are less influenced by biological uptake or mixing with deplete surface waters.

Phosphate concentrations across the surface Arctic are variable, 0–2 mmolm^{-3} (Figure 2.12b–c). There is widespread exhaustion of phosphate on the Siberian shelves, but phosphate is generally not exhausted in the inflows and the Central Basin (0.5–2 mmolm^{-3}). Phosphate has similar values at 200 m as the surface, but is generally more uniformly distributed. The exception to this is the Canada Basin where phosphate levels are elevated at 200 m (1.25–2 mmolm^{-3}).

Measurements of silicate in the Arctic Ocean have more complete coverage than either phosphate or nitrate (Figure 2.12e–f). Silicate is low in the Atlantic inflow, Kara Sea and Beaufort Sea (0–5 mmol m^{-3}). Silicate concentrations are generally replete (10–40 mmol m^{-3}) in the Eurasian Basin and along the East Siberian Shelf.

Iron

Arctic Ocean surface iron concentrations are low (0.5–3 nmol m^{-3}), with a surface minimum that reflects biological uptake [*Klunder et al.*, 2012]. There is not, how-

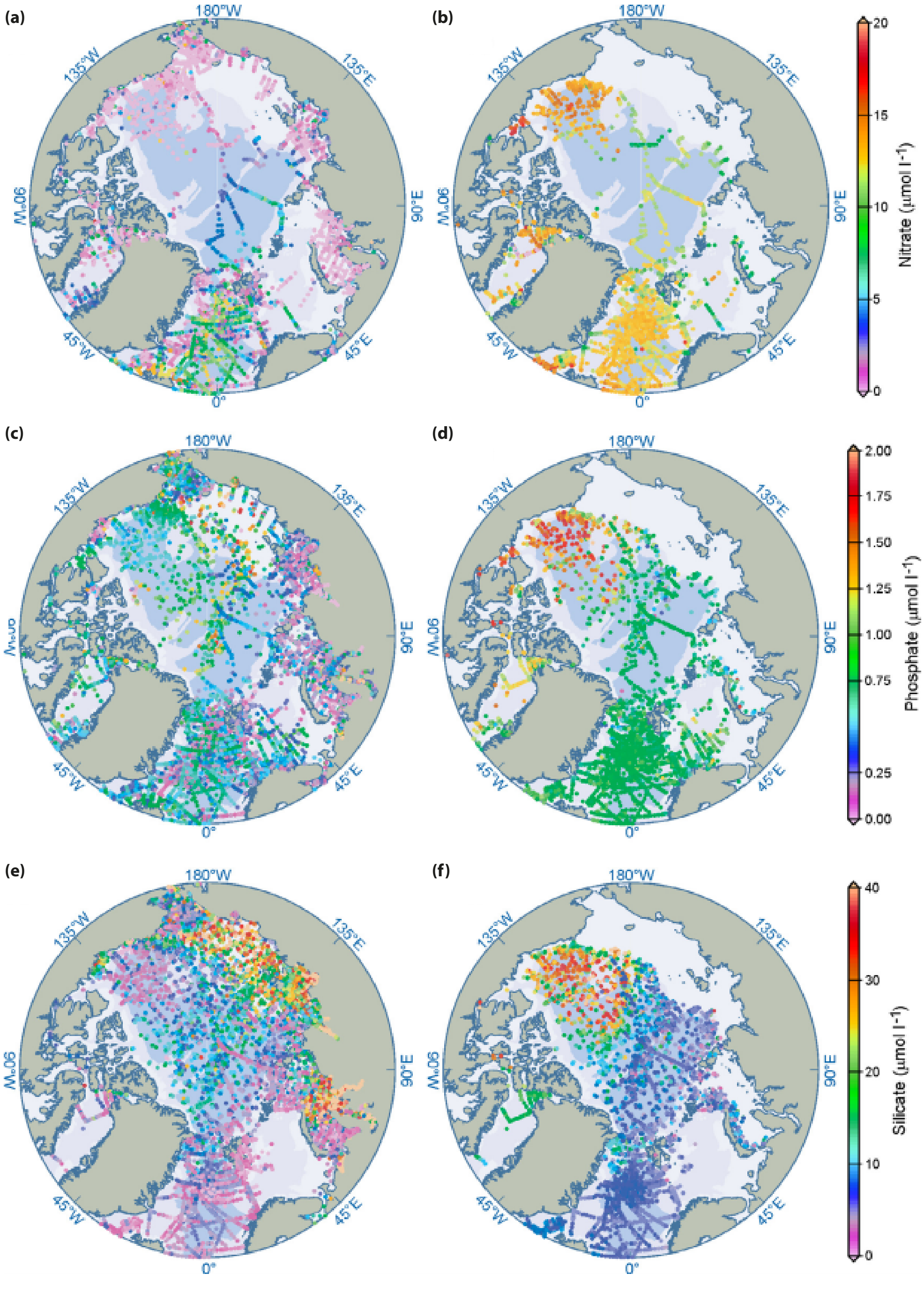

Figure 2.12: Arctic macro-nutrient concentrations at the surface (left) and at 200 m depth (right) from Bluhm *et al.* (2015). **(a)** surface nitrate **(b)** nitrate at 200 m **(c)** surface phosphate **(d)** phosphate at 200 m **(e)** surface silicate **(f)** silicate at 200 m. Reproduced from Bluhm *et al.* 2015.

ever, widespread exhaustion of iron across the Arctic, as in the case of nitrate [*Klunder et al.*, 2012]. The fact that iron concentrations rarely reach zero indicates that iron is not a strongly limiting nutrient for growth at the pan-Arctic Ocean scale. However, there are few iron measurements in the Arctic Ocean, and this picture may change as coverage improves.

Iron and low-salinity generally correlate ($r^2 = 0.6$, $p < 0.001$) on the Eurasian side of the Arctic, suggesting an important riverine source for iron [*Klunder et al.*, 2012]. On the Amerasian side no such correlation is found, and a more complex pattern implicates the interplay of a number of processes including sea-ice melt, biological uptake, remineralisation, and scavenging in setting iron distributions [*Klunder et al.*, 2012].

2.5.8 Nutrient limitation concepts

Leibig limitation

Several concepts of phytoplankton nutrient limitation exist. The simplest, usually called Leibig's Law, posits that a single factor limits growth. The principle is derived from agriculture where it was noted in the early 19th Century that low nitrogen conditions limited the crop yield. In this theory, growth is only stimulated by addition of the limiting nutrient. Increases in other factors, such as light, temperature or another nutrient, will not stimulate further growth because the limiting nutrient is not available. The growth rate μ (d^{-1}) according to Leibig's Law may be expressed as

$$\mu = min\left(\frac{V[S_1]}{k_1 + [S_1]}, \frac{V[S_2]}{k_2 + [S_2]} ... S_n\right) \tag{2.16}$$

for limiting substrates $S_1...S_n$ ($\mathrm{mmol\,m^{-3}}$). The maximum growth rate is V (d^{-1}) and $k_1...k_n$ are the half saturation constants ($\mathrm{mmol\,m^{-3}}$).

Blackman limitation

Another concept of nutrient limitation is that of Blackman (1905). This concept states that several factors may co-limit photosynthetic growth. Each limiting factor is related experimentally to its impact on photosynthesis, and normalised to the maximum growth rate obtained in the experiment (the saturation growth rate V). The impact of the multiple limiting factors are then combined multiplicatively to give a growth rate μ that depends on all limiting substrates $\mathrm{S}_1 ... \mathrm{S}_n$ according to

$$\mu = V \frac{[S_1]}{k_1 + [S_1]} \cdot \frac{[S_2]}{k_2 + [S_2]} ... S_n. \tag{2.17}$$

Factors that are not limiting equal unity so the terms will drop out. This allows the flexibility of not prescribing limiters *a priori*. Instead all potentially limiting terms can be added and non-limiting terms that equal unity then drop out.

However, the interactive influences of light and nutrients cannot be captured by Blackman limitation. If this were the case, then the impact of, say, increasing light-dependent growth rates would be to linearly increase the total growth rate (μ), independent of nutrient conditions.

There is evidence instead that cells dynamically regulate their responses to nutrient and light conditions simultaneously. For example, at low nutrient conditions cells reduce their pigmentation-per-unit biomass [*Williams and Follows*, 2011]. Presumably this is because there is no incentive for the cell to support pigments that produce photosynthate which cannot be used (because of the lack of inorganic nutrients).

Here, phytoplankton alter aspects of their light-dependent growth to accommodate changes in nutrient uptake rates. This is not a scenario that the classical Blackman function captures.

One way to replicate these inter-dependencies has been advanced by Geider *et al.* (1997, 1998). In their model, pigmentation is determined by the ratio of energy supply from light absorption and photosynthetic energy conversion, to the energy demand for growth. If energy supply exceeds demand then the cell is supporting more pigments than is strictly efficient, and pigmentation is regulated downwards. If energy demand exceeds supply then additional pigmentation is added.

More complicated co-limitation

Saito *et al.* (2008) list three types of observed co-limitation in their review (1) independent nutrient co-limitation (2) biochemical substitution co-limitation (3) biochemically dependent co-limitation. In the first case both limiting elements (e.g. N and P) are below the sea water concentrations that support maximum growth rates. Since each nutrient limits a different processes within the cell (the limitations are biochemically mutually exclusive), addition of both nutrients is required to achieve maximum growth rates.

In the second case, two elements (e.g. Co and Zn) can substitute for the same biochemical role within the organism. Here, either of the two elements functions effectively within the same enzyme (or there are two enzymes that carry out the same function, each utilising a different element). Thus, addition of either element will alleviate growth.

In the third case, limitation by one element inhibits the ability of a phytoplankton cell to acquire another element. Here the two limitations are not independent, so the assumption in Blackman limitation that limiters are independent and multiplicative would not strictly be true. For example, the ability of phytoplankton to acquire carbon may be dependent on sufficient supply of zinc, because the metabolic machinery used to acquire carbon requires adequate zinc levels to function [*Morel et al.*, 1994].

Yet ocean distributions of cobalt and zinc do not correspond to large scale ocean phytoplankton patterns (in the way that nitrate and iron do) [*Williams and Follows*, 2011], so the applicability of more complicated co-limitation remains unclear.

2.5.9 Nitrate limitation and ocean nitrate transports

Nitrate concentrations are near-zero across the surface Arctic Ocean (Figure 2.12). This pattern appears to extend across variable ice conditions, from open water into the central Arctic where ice may be several metres thick. These low concentrations, combined with the nutrient kinetics outlined above, indicate that nitrate will limit photosynthetic growth across the Arctic in summer, including under ice. This is contrary to the historical assumption that cold water, a short growing season and sea ice cover would prevent photosynthetic growth in the Central Arctic Ocean [*Wheeler and Gosselim*, 1996]. Because nitrate limits growth across the surface Arctic Ocean, productivity patterns may reflect the distribution of physical nitrate supply.

Quasi-synoptic hydrographic and hydrochemical surveys around the boundary of the Arctic Ocean give an indication of the distribution of ocean nitrate transports into the Arctic. Volume and nitrate transports are provided in Tsbouchi *et al.* (2012) and Torres-Valdes *et al.* (2013) respectively, and are reviewed here.

The hydrographic velocity field indicates that waters enter the Arctic through the Barents Sea Opening (2.6±0.9 Sv), the Bering Straits (1.0±0.2 Sv) and the West Spitsbergen Current (3.8±1.3 Sv) in Fram Straits (Figure 2.13a). Waters exit the Arctic in the East Greenland Current (5.4±2.1 Sv) on the western side of Fram Straits, and through Davis Straits (3.1±0.7 Sv). Nitrate profiles along the boundary show typical depleted conditions in the surface and increases with depth (Figure 2.13b). This likely reflects biological uptake of nutrients in the surface and their remineralisation at depth.

The horizontal oceanic nitrate transport is given by the product of the tracer concentration and the volume transport

$$T_n = \sum_{j=1}^{N} \Delta x_j \int_{bottom}^{surface} v_j c_j dz \tag{2.18}$$

where j is the station pair index and x_j is the station spacing (m). For each station pair j, the velocity profile $v_j(z)$ and corresponding nitrate concentration profile $c_j(z)$ are integrated over depth. Thus the transport is the summation of horizontal transports per station pair, integrated from the maximum observation depth up to the surface across the pan-Arctic boundary.

Nitrate transports across the Arctic boundary reflect patterns in volume transports (Figure 2.14). Major nitrate additions to the Arctic occur through the Barents Sea Opening (~34 kmol s^{-1}) and secondarily through Bering Straits (~ 9 kmol s^{-1}). These inputs are balanced by export through Davis Strait (~ 31 kmol s^{-1}) and to a lesser extent by export through Fram Straits (~10 kmol s^{-1}). The smaller

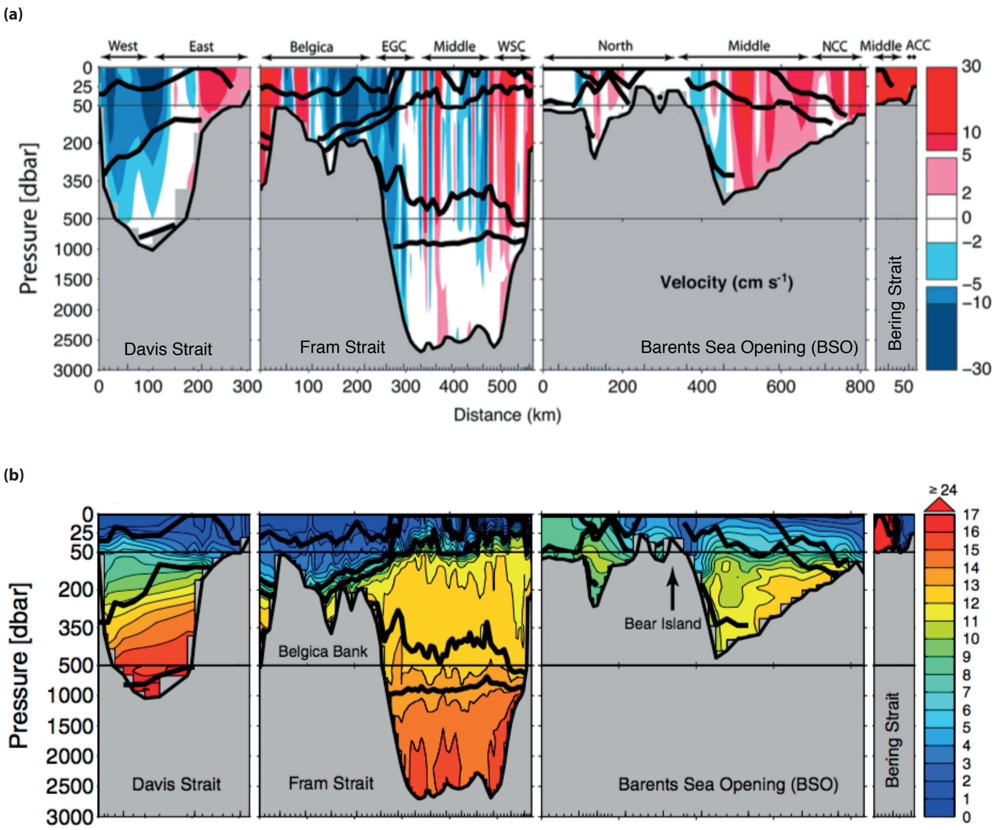

Figure 2.13: **(a)** Inverse model velocity section across the main Arctic Ocean gateways from Tsubouchi *et al.* (2012). Velocity units are in cm $\mathrm{s^{-1}}$; negative indicates outputs and positive indicates inputs. **(b)** Nitrate section (μmol $\mathrm{L^{-1}}$) across the main Arctic Ocean gateways from Torres-Valdes *et al.* (2013). Bold black lines in (a) and (b) show water mass boundaries as defined in Tsubouchi *et al.* (2012) (not used here). Note the depth scale is expanded from 0–50, 50–500, and 500–3000 m. Data used were collected during the summer: Davis Strait (September 2005), Fram Strait (August–September 2005), Barents Sea Opening (April and June 2002), and Bering Strait (August 2005). EGC: East Greenland Current; WSC: West Spitsbergen Current; NCC: Norwegian Coastal Current; ACC: Alaskan Coastal Current.

net export through Fram Straits arises from the near balance between large export in the East Greenland Current ($\sim$63 kmol $\mathrm{s^{-1}}$) and import in the West Spitsbergen Current ($\sim$52 kmol $\mathrm{s^{-1}}$).

In summary, the major nitrate import to the Arctic Ocean is from the Atlantic through the Barents Sea Opening and the major export is into the North Atlantic through the Davis Strait. Large local nitrate transports in the Fram Straits almost

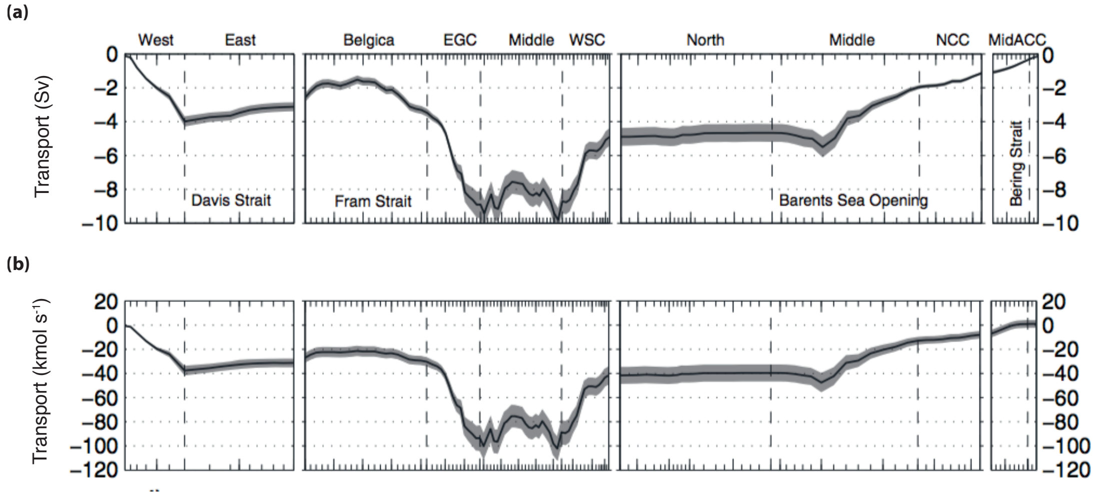

Figure 2.14: **(a)** Accumulated volume transport (Sv; ±1 S.D.) **(b)** Accumulated nitrate transport calculated from Equation 2.18 (kmol s^{-1}; ±1 S.D.). EGC: East Greenland Current; WSC: West Spitsbergen Current; NCC: Norwegian Coastal Current; ACC: Alaskan Coastal Current. Reproduced from Torres-Valdes *et al.* (2013).

balance when summed across the Straits.

Nitrate concentrations are low in surface waters along the pan-Arctic boundary (Figure 2.13b). Deplete conditions extend over typical Arctic boundary euphotic depths (50 m) [*Hill et al.*, 2013], so euphotic-zone nitrate supply requires vertical exchange. Further, inert chemical tracers indicate that advective timescales into the Arctic are of the order of several years (waters take around a decade to reach the North Pole from the Barents Sea Opening) [*Smith et al.*, 2011]. Because nitrate is annually exhausted across most of the Arctic (Figure 2.12), nitrate in surface waters must be used locally before lateral advection is able to spread it around at the scale of the Arctic Basin.

2.5.10 Maximum annual mixed layer depths

Mixing exchanges nitrate-rich deep waters with nitrate-deplete surface waters. This brings nitrate-rich waters into the euphotic zone, inducing growth. Outside of the Arctic there is some indication that deep winter mixed layer depths enhance productivity. Entrainment of iron into surface waters by mixing is thought to support annual productivity in the sub-Arctic Pacific and Southern Ocean [*Nishioka et al.*, 2011; *Tagliabue et al.*, 2014b]; mixing in the low latitude Atlantic and Pacific taps nutrient rich thermocline waters [*Sarmiento et al.*, 2004a]. But exceptions to this patterns occur, such as in areas of the wind-driven gyres where the nutricline is sufficiently depressed by wind-driven convergence that mixing does not penetrate the nutricline [*Sarmiento et al.*, 2004b]. Changes in mixed layer depths are then not mixing over a substantial nitrate gradient and thus only weakly influence surface nitrate concentrations. This failure of winter mixing to recharge surface nitrate also occurs in the Arctic Ocean Beaufort Gyre [*Codispoti et al.*, 2013], where typical winter mixing depths (33 m) [*Peralta-Ferriz and Woodgate*, 2015] are shallower than the nutricline (50 m) [*McLaughlin and Carmack*, 2010].

Arctic maximum annual mixed layer depths and the month in which they occur are shown in Figure 2.15. These are calculated from the Polar Hydrographic Climatology — a global climatology with a high quality Arctic [*Steele et al.*, 2001] — using a density difference criteria of $0.03\,\mathrm{kg\,m^{-3}}$ [*de Boyer Montégut et al.*, 2004]. Arctic Ocean mixed layer depths are much shallower than other oceans (0-40 m).

Mixing is deepest in the Atlantic Sector (Figure 2.15a), both in the Arctic outflow region of Baffin Bay (west of Greenland), and in the Atlantic inflow (Greenland, Norweigan and Barents Seas). Mixed layer depths are only a few tens of meters in the interior Arctic Ocean basin and shelves, indicative of the strong stratification. Export of freshwater in the East Greenland Current extends low mixed layer depths southwards into the Greenland Sea here [*Tsubouchi et al.*, 2012]. The time of year in which mixed layer depths are at their maximum is fairly coherent across the Arctic: mixed layer depths are deepest in winter between January and March (Figure 2.15b).

2.5.11 Observed productivities by regional sea

Estimates of Arctic regional sea productivities are available from nutrient inversions [*Codispoti et al.*, 2013], synthesis of in-situ chlorophyll-a and ^{14}C data [*Sakshaug*, 2004; *Hill et al.*, 2013], satellites [*Arrigo et al.*, 2008; *Pabi et al.*, 2008] and numerical models [*Popova et al.*, 2010]. These diverse estimates broadly agree on the spatial

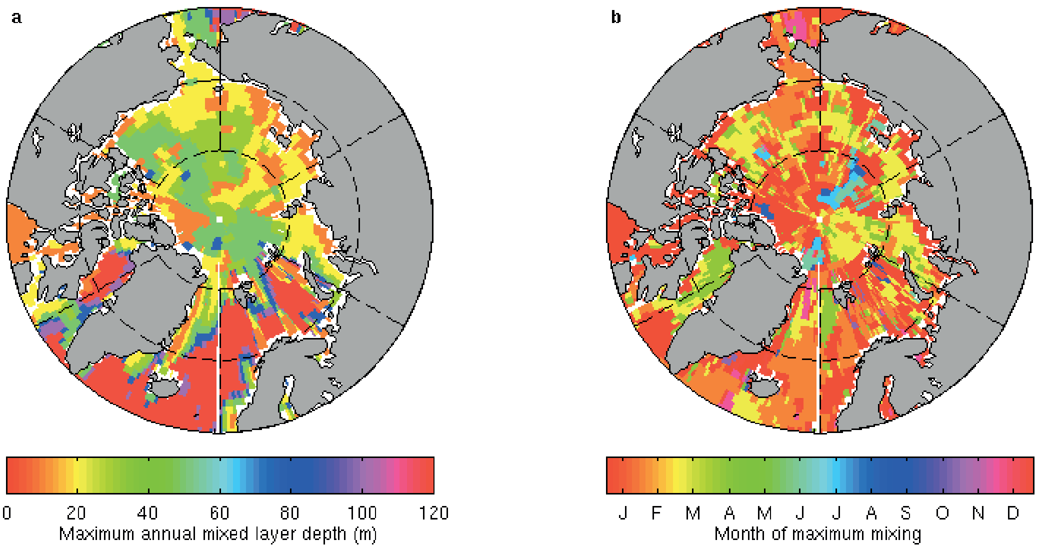

Figure 2.15: **(a)** Arctic winter maximum mixed layer depths (m), calculated from the PHC climatology using a 0.03 kg m^{-3} difference criteria [*Steele et al.*, 2001]. The axis is restricted to 0–100 m to show variations in the Arctic interior. **(b)** Month of year in which maximum mixed layer depths occur.

distributions of production in the Arctic (Figure 2.16b). Production is higher near the periphery, in the Barents Sea, Bering Sea, Greenland Sea, Nordic Sea and Baffin Bay. Production is lower on the interior shelves in the Chukchi Sea, East Siberian Sea, Laptev Sea and Kara Sea. Production is especially low in the Beaufort Sea. (These patterns are also true for regional sea per-unit-area productions.) In the Central Basin area-integrated production is moderate because of the larger size of the region (Figure 2.16a), but per-unit area production rates are very low (33±50 mgCm^{-2}d^{-1}) [*Fernández-Méndez et al.*, 2015], comparable to the Beaufort Sea (24–96 mgCm^{-2}d^{-1}) [*Gradinger*, 2009]. (The methods used to arrive at these pan-Arctic productivity estimates are examined in the next chapter.)

These patterns in production tend to correspond to patterns in sea ice extent (light) and physical nitrate supply (Figure 2.16). Production is high in the open water inflows, where maximum annual mixed layers (in winter) are deep and summer light is replete; and lower in the ice-covered interior where maximum annual mixed layers are shallow and summer light is deplete. Further, nitrate transports are larger and the sea-ice edge further northward in the Atlantic than Pacific sector: the September ice edge extends into the Kara Sea in the Atlantic sector but only into the southern Chukchi Sea in the Pacific sector (Figure 2.16a). This zonal asymmetry in sea ice extent and lateral ocean nitrate transports accounts for greater depth-integrated production in the Atlantic sector than the Pacific (Figure 2.16b). In the Beaufort Sea wind-driven convergence suppresses surface nitrate supply [*McLaughlin and Carmack*, 2010; *Giles et al.*, 2012; *Codispoti et al.*, 2013; *Davis et al.*, 2014], and correspondingly observed productivities are some of the lowest in the Arctic Ocean (Figure 2.16b).

The correspondence between productivity and sea-ice extent and nitrate supply implies that nitrate and light conditions exert a firm control on productivity in the Arctic Ocean. The correspondence also suggests that sea ice can be used as a proxy for phytoplankton growth since patterns of nitrate supply and light both covary with ice cover. For this reason, numerical models of Arctic productivity that adequately simulate the ice field manage to simulate productivity equally well, irrespective of whether model phytoplankton limitation is due to nitrate or light [*Popova et al.*, 2012]. However, these models diverge when the sea ice declines in the forecast [*Vancoppenolle et al.*, 2013]. In models where light limits, removing the ice increases productivity; but in models where nitrate already limits, additional light is of little benefit and productivity decreases with decreasing nitrate supply. Thus, using ice as a proxy for productivity will not tell us about the response of productivity to ice loss. Instead we will need to relate productivity directly to nitrate and light conditions.

2.5.12 Ice algae

Photosynthetic growth in the Arctic Ocean also occurs within sea ice. The sea ice acts as a substrate that supports the algal cells, which grow on nutrients dissolved in sea water that percolates through the ice [*Gradinger*, 2009]. This determines a vertical structure of algal growth within the ice that is often focussed towards the base of the ice (typically within the bottom 10 cm of ice), where nutrients are more readily available [*Lavoie et al.*, 2005].

The seasonal cycle of ice algal growth is initiated when light becomes adequate in the spring, and is curtailed when the ice substrate melts, although production rates may be inhibited by nutrient limitation before this [*Lavoie et al.*, 2005; *Boetius et al.*, 2013]. At small scales, snow cover may also play an important role in ice-algal growth [*Rózanska et al.*, 2009]. Snow cover can act to dampen production rates, but this can also prolong the length of the bloom because the ice substrate melts slower [*Lavoie et al.*, 2005]. In the fall, growing ice enhances convection of water through the basal (∼2 cm) layer in the ice, enhancing nitrate supply to ice algae [*Lavoie et al.*, 2005].

Many ice algae are unique to sea ice and do not occur in the pelagic ocean. One dominant species is the diatom *Melosira arctica* which grows on the underside of sea ice. It is thought to be important for organic matter export to benthic commuities [*Boetius et al.*, 2013], but the genetic variations of sub-populations are unknown and whether any of these strains can adapt to a seasonally ice-free Arctic is unclear (Klaus Valentin comm.).

Ice algae export of organic carbon to benthic communities occurs in large events [*Boetius et al.*, 2013]. This flux has been observed supporting benthic growth at depths of 3500-4500 m [*Boetius et al.*, 2013]. It may thus also be an important Arctic Ocean carbon sink. Sediment traps moored in the Admunsen Basin in the 1990s measured an export of around 1 $\mathrm{gCm^{-2}yr^{-1}}$ (>1500 m), with a peak input of sub-ice algae in August of up to 28% [*Fahl and Nöthig*, 2007]. Repeated measurements over the sea-ice minimum 2005–2007 showed an increased carbon flux of 6.5 $\mathrm{gCm^{-2}yr^{-1}}$ (>850 m) with an average peak in July. The earlier ice retreat shifted peak flux earlier in the year [*Lalande et al.*, 2009].

Different estimates place ice algal growth as <25% and <10% of Arctic primary production [*Legendre et al.*, 1992; *Pabi et al.*, 2008]. Given the small volume in which ice-algal growth occurs, it is perhaps unlikely the contribution is this high. Further, because ice algae grow on ocean nitrate, estimates of production based on ocean nutrient inversions capture ice-algal growth within the total productivity estimate [*Codispoti et al.*, 2013], whereas other techniques based on satellites and direct ocean chlorophyll and ^{14}C production do not [*Sakshaug*, 2004; *Pabi et al.*, 2008; *Arrigo et al.*, 2008; *Hill et al.*, 2013]. Small discrepancies in estimated total

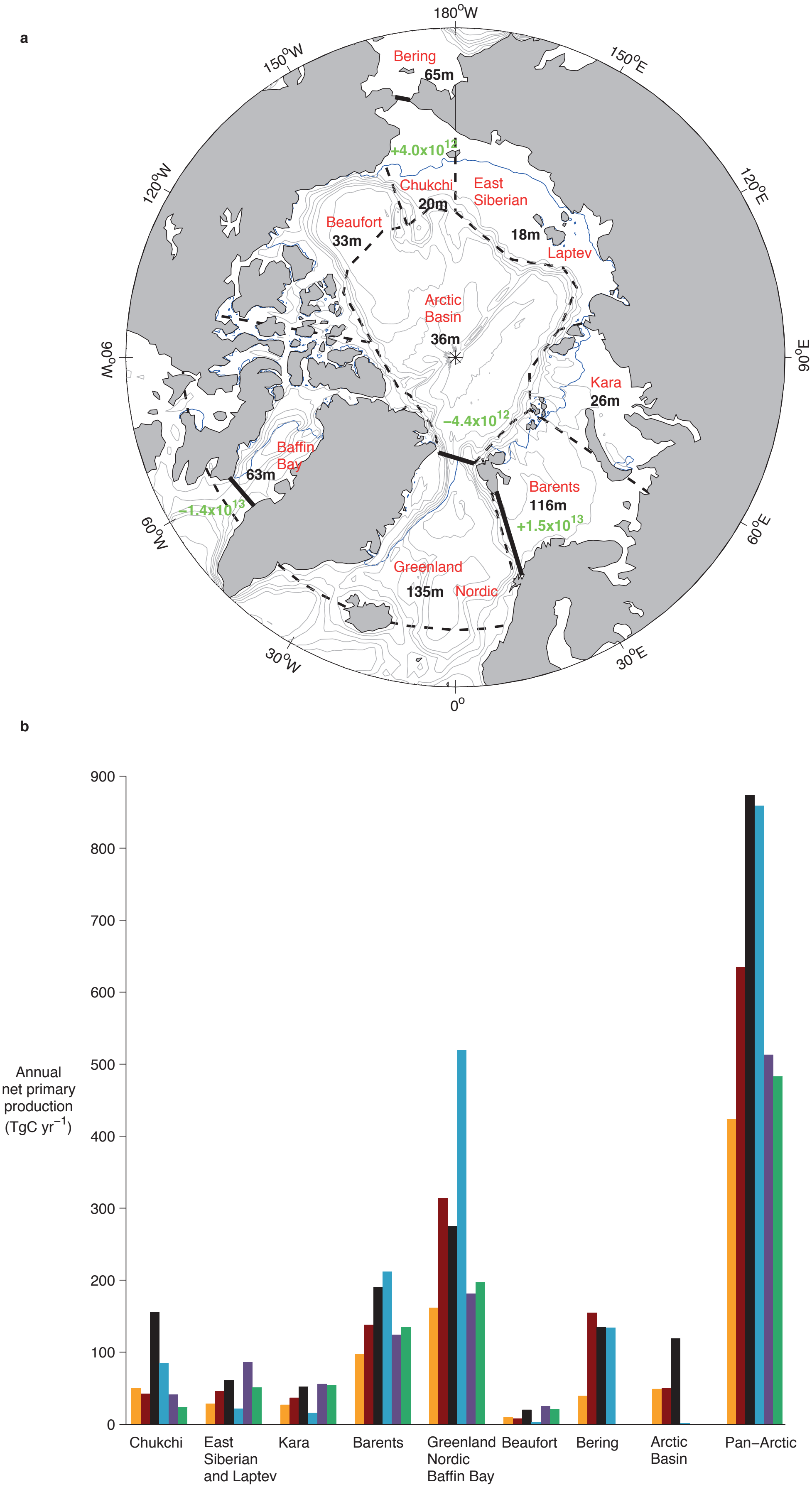
a
180°W
150°W
150°E
120°W
120°E
90°W
90°E
60°W
60°E
30°W
30°E
0°
Bering
65m
+4.0x10^12
Chukchi
20m
East
Siberian
18m
Laptev
Beaufort
33m
Arctic
Basin
36m
Kara
26m
−4.4x10^12
Baffin
Bay
63m
−1.4x10^13
Barents
116m
+1.5x10^13
Greenland
135m
Nordic
b
Annual net primary production (TgC yr^−1)
900
800
700
600
500
400
300
200
100
0
Chukchi
East Siberian and Laptev
Kara
Barents
Greenland Nordic Baffin Bay
Beaufort
Bering
Arctic Basin
Pan−Arctic

Figure 2.16: **(a)** Some observed Arctic Ocean conditions. Regional seas (red text, dash black line) with climatological maximum-annual mixed layer depths (black text), summer lateral ocean nitrate transports (green text, thick black line; $\mathrm{gN\,yr^{-1}}$), and 2000s-average September ice extent (15% concentration threshold, blue line) [*Steele et al.*, 2001; *Torres-Valdés et al.*, 2013; *Meier et al.*, 2015]. **(b)** Arctic regional productivity ($\mathrm{TgC\,yr^{-1}}$) from five different methodologies: thesis model (orange), ^{14}C measurements (red) [*Sakshaug*, 2004], nitrate inversion (black) [*Codispoti et al.*, 2013], Chl and ^{14}C synthesis (blue) [*Hill et al.*, 2013], and satellite algorithms (purple, green) [*Arrigo et al.*, 2008; *Pabi et al.*, 2008]. Reported satellite estimates omit the ice-covered Arctic Basin and Bering Sea. The subArctic Bering Sea is omitted from pan-Arctic totals.

production by studies that do, and do not, include ice algae indicate the relatively small role played by ice algae in total Arctic Ocean production (Figure 2.16b).

2.5.13 Under-ice production

The large areal extent of sea ice in the Arctic suggests that under-ice production may constitute an important part of total Arctic productivity. But this depends on under ice production rates, which are reported to be highly variable.

In the summer Chukchi Sea phytoplankton carbon fixation rates are as high as $3.7\,\mathrm{gCm^{-2}d^{-1}}$ and growth rates are as high as $1.6\,\mathrm{d^{-1}}$ [*Arrigo et al.*, 2014]. In a 1994 transect of the Arctic, growth rates varied from $2.57\,\mathrm{gCm^{-2}d^{-1}}$ in the Chukchi Sea to $0.521\,\mathrm{gCm^{-2}d^{-1}}$ in the Nansen Basin and $0.073\,\mathrm{gCm^{-2}d^{-1}}$ in the Marakov Basin [*Gosselin et al.*, 1997]. In the Canada Basin, summer phytoplankton growth rates under ice have been measured across the range 20 to $178\,\mathrm{mgCm^{-2}d^{-1}}$ [*Lee et al.*, 2010].

Measurements of under-ice nitrate concentrations in the Chukchi Sea suggest that phytoplankton may be able to strip surface waters of nitrate before the seasonal retreat of sea ice here [*Arrigo et al.*, 2012]. Analysis of historical data from the Canadian Arctic suggests this nitrate-depletion phenomenon may be widespread [*Matrai and Apollonio*, 2013]. Annual production in the and under sea-ice in the

Canadian Arctic may be as high as $30\,\mathrm{gCm^{-2}yr^{-1}}$, and contribute 50% of net community production on the shelf and 90% in the Canada Basin [*Matrai and Apollonio*, 2013]. As Arctic annual sea-ice cover thins, light penetration to the surface ocean increases [*Nicolaus et al.*, 2012]. Reduction in sea ice thickness, and the proliferation of melt ponds, is likely to enhance production under ice in the future [*Palmer et al.*, 2014].

In this chapter we have sought to provide a summary of known Arctic Ocean conditions that we will draw on throughout the thesis. We have noted two unique Arctic Ocean characteristics in particular. First, low turbulence means that phytoplankton are not vertically homogeneous (well-mixed) and production can occur predominantly below the mixed-layer. We will therefore look directly at vertical profiles of nutrients and light in this thesis. Second, the correspondence between sea ice and productivity is little use in forecasting the response under ice loss: we will need to look at the light and nutrient conditions directly.

From here, the thesis is developed from the basic kinetic relationships summarised in Blackman (1905) and Michaelis and Menten (1913), and derived above. The kinetics are contextualised with observations in the Canadian Arctic. We perform some simple calculations on these observations to relate the vertical photosynthetic response to nitrate and light conditions. This insight is then developed to show how the contradictory impacts of Arctic sea ice retreat on productivity (via nitrate and light) are readily resolvable (Chapter 4).

We then turn to a more robust understanding of contemporary Arctic phytoplankton dynamics (Chapter 5). For this we use the insight that phytoplankton dynamics are independent of sea ice. On this basis, a relationship between vertical productivity and the ratio of nitrate limitation to light limitation is advanced, and it is demonstrated how this relates to depth-integrated production and its geographical distributions across the Arctic Ocean. The relationship is shown to be invariant, applying equally well in an ice-free Arctic Ocean. Last, we use ice-free observations of photosynthetic rates, nutrients and light to confirm the existence of this relationship in the extra-Arctic oceans (Chapter 6). This should give us some confidence that the ice-free Arctic Ocean solution presented in Chapter 5 may be correct. We close with some immediate practical recommendations (Chapter 7). These focus on international monitoring efforts of the Arctic Ocean as it transitions to an ice-free state.

CHAPTER 3

Methods

To get a handle on Arctic Ocean productivity and ongoing changes we need methods that directly determine production at the pan-Arctic scale contemporaneously. In this chapter we explore the two available methods, satellites and numerical models. We introduce how both methods work, draw out some of the shortcomings inherent with each method, and discuss how some of these are exacerbated in the Arctic Ocean. We finish by assessing the performance of the simulation used in this thesis in the Arctic Ocean.

3.1 Satellite estimates of Arctic productivity

The Arctic is the most severely under-sampled ocean on the planet, and spatial and temporal variability of both physical and biological parameters is poorly constrained. Satellite ocean colour imaging and the development of algorithms to retrieve depth-integrated primary production from surface chlorophyll has enabled satellite-derived pan-Arctic primary production estimates, which may be compared with the sparse in situ record [*Hill et al.*, 2013]. Satellite estimates allow sampling at temporal and spatial resolutions higher than in situ data coverage. For example, Pabi et al. (2008), compared primary production across different ecological provinces and found that it is generally highest in the shelf zone and the marginal ice zone over the continental shelf (SMIZ) and lower in the pelagic zone and the marginal ice zone over deep water (DMIZ). They also suggests that SMIZ primary production peaks later (around June–July) than DMIZ (which generally peak around May). Satellite estimates also allow for a more continuous pan-Arctic time-series to be developed, making inter-year comparisons and estimates of secular trends possible; for example, reported increases in primary productivity between 1998–2006 were largest in the pelagic zone (43 $\mathrm{Tg\,C\,yr^{-1}}$, 32% increase), followed by the shelf zone (38 $\mathrm{Tg\,C\,yr^{-1}}$, 63% increase [*Pabi et al.*, 2008]).

3.1.1 Deriving productivity from space

Satellite estimates of production are based on the retrieval of the photosynthetic pigment chlorophyll-*a*. Chlorophyll-*a* has characteristic absorption peaks (440 nm, 665 nm) and troughs (550 nm). Thus reflectance ratios that contrast the peak and trough ($\mathrm{R}_r s(440)/\mathrm{R}_r s(550)$) capture the impact of chlorophyll-*a* on the light returned to the satellite, from which surface ocean chlorophyll-a concentrations may be derived [*Kirk*, 1994].

The light that this reflectance value captures originates (90%) from above the depth z_{90}, where z_{90} is calculated as the reciprocal of the diffuse attenuation coefficient ($1/k_d$) [*Gordon and McCluney*, 1975]. z_{90} is 10–20 m in the Arctic Ocean in summer. The vertical chlorophyll-*a* profile cannot be directly measured (based on the single retrieved surface value), so an assumption must be made about its shape. Typically, in the Arctic it has been assumed that chlorophyll-*a* is fixed (homogenous) at the surface value over the mixed layer, and decreases exponentially below [*Arrigo et al.*, 2011; *Hill et al.*, 2013]. This assumes that mixing rates are much faster than growth rates in the mixed layer, such that chlorophyll is mixed faster than vertical differences in growth rates can introduce inhomogeneities. As noted in Chapter 2, at the low turbulences found across the Arctic this is not valid. Some algorithms empirically relate vertical structure to surface chlorophyll concentrations ([*Ardyna et al.*, 2013] and therein). But these empirical algorithms have performed poorly in recent tests on new data sets in the Arctic Ocean (Bouman personal correspondence).

Photosynthetic rates per unit chlorophyll-a are then derived from incident light, daylength and sea surface temperature (e.g [*Behrenfeld and Falkowski*, 1997]). Many algorithms exist based on this central framework, that utilise different temperature functional forms [*Friedrichs et al.*, 2009], resolve light wavelengths, or attempt to infer depth-dependencies [*Saba et al.*, 2011].

More recently, an alternative algorithm based on phytoplankton biomass has also been proposed [*Westberry et al.*, 2008]. Light backscattered to satellites by ocean particles (at 443 nm) is used to estimate phytoplankton carbon biomass (through a linear empirical scaling factor). Phytoplankton growth rates are then calculated from irradiance and the carbon:chlorophyll ratio (chlorophyll being derived as above).

Algorithm comparison to in situ data suggests that the largest satellite algorithm errors arise in optically complex (Case 2) waters near coastlines [*Saba et al.*, 2011]. Here non-chlorophyll-a constituents may comprise a large part of reflectance, ruining the chlorophyll-a signal. Optical in situ measurements in the Arctic show that Chromophoric Dissolved Organic Matter (CDOM) dominates (90%) of the reflectance at 443 nm, the dominant retrieval band for chlorophyll-a [*Matsuoka et al.*, 2007]. (CDOM is a poorly chemically defined mixture of humic and fulvic acids, e.g. Miller and Moran, 1997; it is also commonly defined based on its absorption spectra, e.g. Nelson *et al.*, 1998.) Therefore, raw reflectance values over-estimate chlorophyll-a and productivity. Arctic Ocean satellite algorithms have been adjusted by constant factors to try and correct for non-chlorophyll reflectance [*Arrigo et al.*, 2011], but CDOM varies independently from chlorophyll-a [*Wang et al.*, 2005] so a constant factor does not remove the error [*Nelson et al.*, 1998]. Satellite-derived surface chlorophyll-a consequently captures less than 20% of the variance in measured Arctic Ocean values [*Matrai et al.*, 2013].

The data available for validation of satellite algorithms are, however, extremely limited in the Arctic Ocean (Figure 3.1). In situ chlorophyll-a data are more widely available (48,004) than ^{14}C production data (20,453). In particular, chlorophyll-a

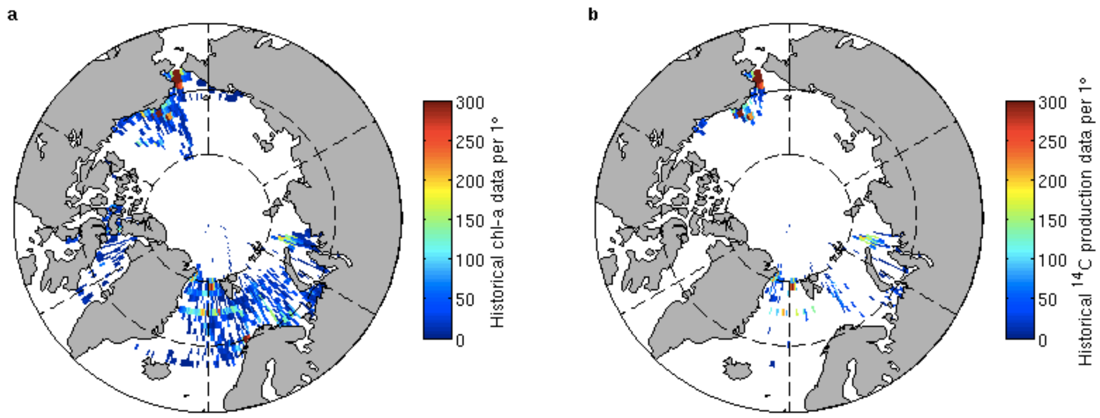

Figure 3.1: Historical data available for validation of satellite algorithms in the Arctic Ocean for **(a)** chlorophyll-a and **(b)** ^{14}C phytoplankton productivity. All years and months are shown together.

data are available in the Baffin Bay and the Canadian Archipelago, where production data are not (Figure 3.1). Both production and chlorophyll-a data are restricted to the peripheral areas of the Arctic, with very poor coverage of the interior shelves, or perennially ice-covered Central Basin. Historical data coverage is also generally very low in any given location. Therefore, seasonal and interannual coverage is generally absent [*Hill et al.*, 2013].

Satellite estimates of Arctic primary productivity thus have a series of attendant limitations. Recognition of these limitations is crucial in interpreting satellite-derived variability and trends. These limitations come in three broad classes: satellite coverage, systematic biases in surface chlorophyll retrieval and vertical chlorophyll profiles, and ongoing changes in the Arctic Ocean. We now discuss each of these three classes in turn.

3.1.2 Satellite coverage

Frequent Arctic fog, cloud and sea-ice cover reduce chlorophyll-a retrieval. The high albedo of sea-ice may also result in data from adjacent pixels being irretrievable. Typically, it is assumed that primary production ceases when ice-coverage is above 10% because of light limitation [*Pabi et al.*, 2008], despite the fact that productivity may be high in the remaining sub-pixel open water areas where alleviation of light limitation has recently occurred. Furthermore, ice-algal and under-ice primary production may be important. The former is perhaps moderate (Chapter 2), but the latter may be as high as 40% of annual pan-Arctic production [*Mundy et al.*, 2009; *Arrigo et al.*, 2012; *Jin et al.*, 2016] and will likely increase with future shifts from multi-year to single year ice, because thinner single year ice results in higher under-ice irradiance [*Greenfeld and Maykut*, 1977; *Frey et al.*, 2011]. All but the largest polynyas and leads are unresolvable by current satellite measurements. Although per-unit-area primary productivity in polynyas is typically very high, large individual polynyas contribute minimally to pan-Arctic primary production [*Sakshaug*, 2004]. There is greater uncertainty in contributions by smaller polynyas, melt ponds and ice leads. The upper bound may be as high as 30% of annual pan-Arctic primary production but is more likely ∼5% [*Sakshaug*, 2004].

Low solar angles and long polar winters also inhibit satellite retrieval — typically restricted to March–September — although it may be assumed that light limitation is effective in reducing primary productivity to minimal amounts outside of this window. Areas of riverine discharge are highly turbid and pose a severe problems for satellite chlorophyll-a retrieval. Absorption and backscattering by suspended non-organic particulate matter introduce substantial error into satellite estimates of surface chlorophyll-*a*. Pixels that are known to be contaminated by river plumes are discarded in pan-Arctic studies [*Pabi et al.*, 2008].

3.1.3 Surface chlorophyll-*a* and the subsurface chlorophyll maximum

Satellite algorithms estimate surface chlorophyll-*a* concentrations from measured spectral ratios that arise through wavelength-dependent absorption and backscattering by sea water and its optical constituents (photosynthetic and protective pigments, CDOM and non-organic particulate matter). Primary productivity is then calculated from surface chlorophyll-*a* concentrations by assuming a certain vertical profile, to give total primary production throughout the water column (Figure 3.2).

Most satellite productivity estimates therefore suffer from two significant biases: overestimation of surface chlorophyll-*a*, which is propagated through the water column, and neglect of subsurface chlorophyll maxima (Figure 3.2). (Note some algorithms now attempt to deal with the second of these problems, see [*Ardyna et al.*, 2013] and refs. therein.)

High riverine discharges and in situ production result in high pan-Arctic CDOM concentrations [*Stedmon et al.*, 2011], enhancing absorption of light which is perceived by the algorithm to be due to enhanced surface chlorophyll-a. Further, phytoplankton are capable of varying both their carbon:chlorophyll-a ratio and the proportion of auxiliary pigments. Typically, high pigment packaging (high chlorophyll-a:carbon) is adopted at lower light conditions (such as the base of the euphotic zone) and corresponds to a lower specific absorption (absorption per pigment) due to greater self-shading of pigments. Phytoplankton pigment packaging in the Arctic during the growing season is high, resulting in lower specific absorption due to self-shading by pigments [*Matsuoka et al.*, 2009]. The effect of this is to reduce the primary productivity per unit chlorophyll-a, resulting in an over-estimate bias of primary productivity from satellite estimates. Arctic CDOM concentrations and pigment packaging both vary seasonally [*Matsuoka et al.*, 2011], currently unrepresented in satellite algorithms.

Subsurface chlorophyll maxima develop in the Arctic in summer in areas where surface nutrients have been exhausted and light penetration is deeper [*Ardyna et al.*, 2013], making phytoplankton growing conditions at depth more optimal than at the surface [*Hickman et al.*, 2010]. They primarily occur on inflow and outflow shelves under partial ice cover [*Hill et al.*, 2013], being most pronounced in the Bering, Chukchi, Barents and Beaufort Seas [*Arrigo et al.*, 2011; *Ardyna et al.*, 2013] where summer sea-ice cover is lower and inflowing waters are sufficiently nutrient charged to maintain productivity at depth [*Brown and Arrigo*, 2012]. Subsurface chlorophyll maxima cannot be directly observed by satellites, so the extent to which they introduce errors into satellite productivity estimates depends on how well the assumed vertical production profile matches up with the actual profile (Figure 3.2). Thus, errors in satellite-based estimates of pan-Arctic primary production vary seasonally and spatially as a result of seasonal and spatial variability in subsurface chlorophyll maxima.

Errors as a percentage of primary production in the corresponding time or region bin (relative errors) are largest in January–March and smallest in July–September (Figure 3.3c). They are large in the Chukchi, Beaufort, and Kara sectors and smaller in the Barents, Baffin and Greenland sectors (Figure 3.3f).

The SCM contribution to annual pan-Arctic primary production errors are small in winter when there is no subsurface chlorophyll maximum and pan-Arctic primary production is low (0.2%) and larger in summer (16%) when subsurface chlorophyll maxima are more pronounced and pan-Arctic primary production higher [*Arrigo et al.*, 2011; *Ardyna et al.*, 2013]. Errors are largest on inflow and outflow shelves where subsurface chlorophyll maxima are most pronounced and primary production is highest, suggesting that absolute errors due to neglect of subsurface chlorophyll maxima may be large.

Errors introduced by overestimation of surface chlorophyll-*a* values and neglect of the subsurface chlorophyll maximum are of the opposite sign and so, to some degree, mask one another [*Arrigo et al.*, 2011]. The extent to which they do so depends on the distribution of errors (Figure 3.2) and the spatial and temporal scales these errors are aggregated over (Figure 3.3). In total (by season and sector), 18/35 subsurface-surface error-pairs are of opposite sign, no better than random.

There is significant disagreement in the literature over the total error for satellite-based pan-Arctic estimates of annual primary productivity. Arrigo et al. (2011) who calculate errors arising from neglect of subsurface chlorophyll maxima and surface chlorophyll-*a* alone suggest that the error is <1%, whereas Hill et al. (2013) argue for an error of 40–75%, based on comparison to in situ data. The latter would bring satellite-based annual productivity estimates up to those made using ^{14}C and nutrient-based estimates (Figure 2.16). Coincident in situ primary productivity measurements are limited (Figure 3.1) , but agreement is very poor for available matches in the interval 1997–2007 ($r^2 = 0.11$)[*Matrai et al.*, 2013].

Future community shifts, both to smaller sizes [*Daufresne et al.*, 2009] and in species composition [*Li et al.*, 2009], may necessitate recalibration of current algorithms. For example, larger phytoplankton cells have a higher package effect [*Matsuoka et al.*, 2009].

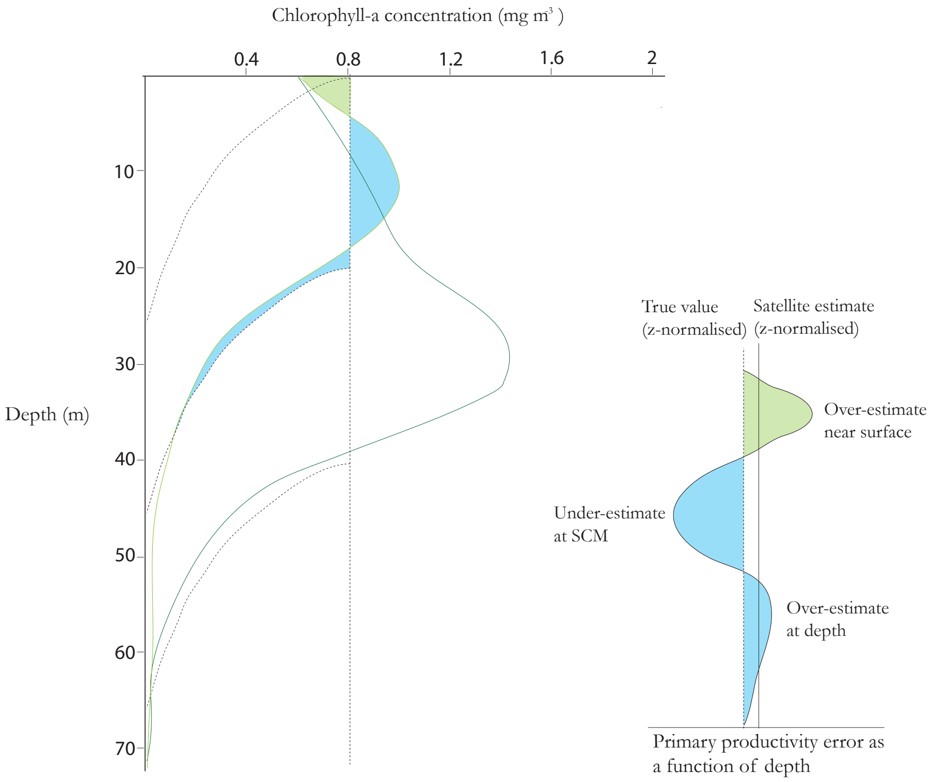

Figure 3.2: Representative chlorophyll-a profiles for shallow (light green) and deep (dark green) subsurface chlorophyll maxima. Different satellite algorithms are shown (dashed black lines) which assume an exponential decrease from the surface, an exponential decrease below homogenous 20 m (most common, e.g. [*Arrigo et al.*, 2008] and [*Pabi et al.*, 2008]) and 40 m mixed layers; and chlorophyll-a confined to a single homogenous mixed layer 100 m deep. Compensation of overestimation due to surface chlorophyll errors (green shading) by net underestimation due to subsurface chlorophyll errors (blue shading) is hypothesised to lead to satellite productivity estimates near the true value (inset).

3.1.4 The challenges of ongoing productivity changes

Projected changes in the Arctic physical environment will induce changes in phytoplankton bloom timing, productivity and export. Contemporary phytoplankton productivity can be largely (88%) accounted for by changes in mean summertime irradiance at the sea surface and the maximum depth of winter mixing [*Popova et al.*, 2010] which affect the open water area and growing season length, and the amount of nutrients available for photosynthesis respectively.

Earlier retreat of sea-ice will generally result in earlier blooms: in peripheral

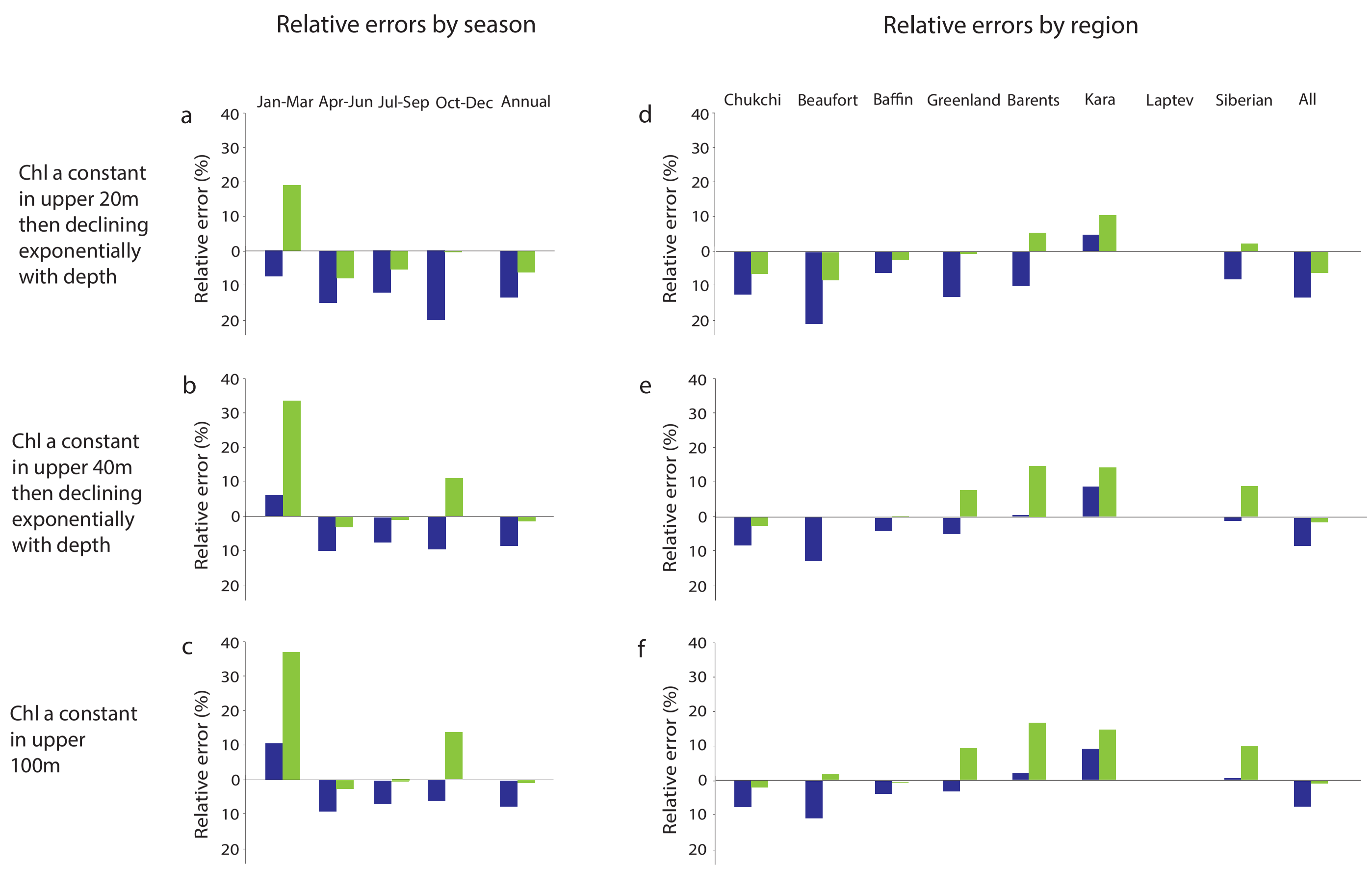

Figure 3.3: The degree of masking when neglecting primary productivity in the subsurface chlorophyll maximum (blue) by overestimating surface chlorophyll-a (green). **(a–c)** By season **(d–f)** by region under different assumed chlorophyll depth profiles (corrected for a satellite chlorophyll-a bias of $0.21\,\mathrm{mgm^{-3}}$) [*Arrigo et al.*, 2011]. In total 18/35 subsurface-surface error-pairs are of opposite sign, no better than random. Data are replotted from Arrigo *et al.* (2011).

areas of the Arctic Ocean bloom peaks are reported to have advanced up to 50 days earlier over the period 1997–2009, primarily due to alleviation of light limitation, but warming upper ocean temperatures may also be important [*Kahru et al.*, 2011]. Changes in timing of the spring bloom may result in mismatch between peak phytoplankton biomass and zooplankton grazing, increasing export of phytoplankton and pelagic-benthic coupling [*Wassmann and Reigstad*, 2011], but changes in timing may be detrimental to higher trophic levels whose development is predicated on a consistent bloom timing. Copepod development is timed such that its larval and juvenile stages coincide with the ice-algal and and phytoplankton blooms respectively. In turn, Arctic mammals are dependant on copepods as a source of fat, laid down for the leaner winter months. Therefore, the effects of changes in the timing of ice-algal and phytoplankton will propagate up through the ecosystem due to strong trophic ties. Determining exact phytoplankton bloom initiation and peak dates in the Arctic by satellite is compounded by low data coverage which may bias estimates by ∼30 and ∼15 days, or more, respectively [*Cole et al.*, 2012]. It is also difficult to differentiate between true phenological shifts and apparent shifts arising because earlier ice retreat makes more of the under-ice bloom visible to satellites [*Matrai and Apollonio*, 2013].

Nutrients are presently exhausted over 75% of the surface Arctic Ocean (0–10 m) by the end of the growing season [*Tremblay and Gagnon*, 2009] and continually low Greenland Sea and Baffin Bay net primary production under increasing growing season length is attributable to nutrient limitation [*Brown and Arrigo*, 2012]. Future changes in the magnitude of annual pan-Arctic primary production will depend on nutrient supply [*Tremblay and Gagnon*, 2009]. Nutrient supply to the euphotic zone is restricted by the strong Arctic halocline and occurs primarily through winter mixing and episodic upwelling events [*Pickart et al.*, 2013]. Therefore, future nutrient supply will vary regionally, depending on spatial variability of winter mixed layer depth and episodic upwelling events and circulation patterns of inflowing nutrient rich Pacific and Atlantic waters. Increased sea-ice melt will both strengthen the halocline through its fresh water contribution (aided by increased riverine flux) but also weaken it through increased surface wind-stress. The relative dominance of these factors is largely unknown and likely to vary spatially.

Satellite algorithms that have recently been applied to the Arctic assumed homogeneous primary production throughout a mixed layer of constant depth and exponential decrease below (Figure 3.2) [*Arrigo et al.*, 2008; *Pabi et al.*, 2008]. Two main problems arise from these assumptions. Firstly, the mixing layer depth is not constant: it varies throughout the growing season in response to wind-driven mixing, sea-ice melting and riverine inputs, and may change under sea-ice decline. Secondly, primary production is not homogenous throughout the mixed layer [**?**] and observed photosynthetically-competent SCM occur below the mixed layer, probably due to a shortage of inorganic nitrogen in the upper euphotic zone [*Martin et al.*, 2010].

These changes relate to the potential success and limitations of future satellite-based estimates of Arctic primary productivity in a number of ways.

Changes in export, important both for assessment of carbon sequestration and pelagic-benthic coupling, cannot be directly assessed by satellites which estimate depth-integrated primary production not export production, for which an export ratio must be measured in situ or assumed. Hypothetically, gross primary production[1] may increase with increased irradiance and temperature without additional nutrient supply through enhanced recycled production[2]. Under this condition gross (but not net) primary production increases without any additional carbon export. This situation may be realised in a future Arctic where sea-ice retreat results in nutrient limitation, compensated for by the restructuring of the phytoplankton community to decrease the net community export ratio, and adapted to by more species with shorter generation times or better physiological tolerances which use and recycle nutrients more efficiently [*Wassmann and Reigstad*, 2011].

---

[1] Primary production is the net uptake of carbon dioxide by phytoplankton, which is equal to the gross primary production (photosynthesis) minus phytoplankton respiration. The term net community production is used to refer to primary production minus the respiration by heterotrophs as well [*Sarmiento and Gruber*, 2006].

[2] Recycled production is that attributable to nutrients that are supplied either by recycling of organic matter within the surface ocean. New production is that attributable to nutrients supplied from external sources, mostly by upwelling or upward mixing of nutrients from the thermocline. Export production is the large-scale export of organic matter from the surface [*Sarmiento and Gruber*, 2006].

Changes in subsurface chlorophyll maxima locations, magnitudes and timings are also likely under changing nutrient and light conditions. CDOM volume fluxes, distribution, lability and relative dominance of sources and sinks important in distribution and seasonal cycling will also likely change in the future [*Stedmon et al.*, 2011]. Projected increased Arctic riverine fluxes will bring more CDOM into the Arctic, likely complemented by increased in situ CDOM production due to near surface water temperature increases and offset by increased photodegredation with reduced sea-ice [*Stedmon et al.*, 2011]. This will impact the magnitude of errors, and the extent to which subsurface-chlorophyll-maxima-induced and CDOM-induced errors mask one another in satellite estimates of primary productivity.

A decade-long Arctic primary productivity trend has been inferred by regressing primary productivity to sea-ice cover [*Arrigo et al.*, 2008]. Extrapolation of this trends is highly uncertain. Nutrients and light are currently both coupled to sea-ice, making the regression possible [*Popova et al.*, 2012]. But nutrients and light may have opposing effects on production in the future: production may increase (light control) or decrease (nutrient control) with ice retreat [*Vancoppenolle et al.*, 2013]. Primary production trends have also generally been linearly fitted to historical data sets [*Arrigo et al.*, 2008; *Pabi et al.*, 2008; *Brown and Arrigo*, 2012] but it is unclear how primary production relates to accelerating (non-linear) ice loss or abrupt changes in ice cover [*Holland et al.*, 2006; *Wang and Overland*, 2009; *Perovich*, 2011].

3.2 Biogeochemical simulations

Numerical simulations can be used to bridge theory and sparse observations by illustrating the predictions theory makes and comparing them to observations. To do this we must check that the numerical simulation provides a realistic representation of observations.

In this thesis we use output from the biogeochemical Model of Ecosystem Dynamics, nutrient Utilization, Sequestration and Acidification (MEDUSA), developed in Southampton. MEDUSA computes finite difference solutions to solve for a set of state variables. The model has been developed for several purposes, making several of the variables extraneous to the work here. Since the thesis here is restricted to phytoplankton production, which we will derive from nitrate and light conditions, we will restrict ourselves to the relevant parts of the model for clarity. The basic model architecture is also run at a variety of resolutions, for varied time scales, and with varied forcing to produce several simulations. For this thesis we restrict ourselves to a single simulation. Full details of the model are available in Yool *et al.* (2013) and this simulation in Yool *et al.* (2015).

The biogeochemical model (MEDUSA) is embedded within a general circulation model (NEMO) that comprises ocean (OPA) [*Madec*, 2008] and ice (LIM2) [*Timmermann et al.*, 2005] components. The simulation is run for 1975–2099, at a global-average resolution of 1/4°. (We used 1/4°because it was the highest resolution we had available.) It starts from a prior simulation that was run over 1860–1975 at 1 °resolution [*Yool et al.*, 2015]. The grid is non-linear and resolution increases toward the poles: for example, resolution at 60°N is 16.8 km. The model is forced at the ocean surface and continental margins with output from the Earth System model HadGEM2-ES [*Collins et al.*, 2011] which was run under Representative Concentration Pathway 8.5 [*Riahi et al.*, 2011].

Productivity is partitioned between two phytoplankton classes: "large" and "small" phytoplankton. "Large" phytoplankton are assumed to be synonymous with diatoms and "small" phytoplankton are assumed to be synonymous with nanophytoplankton [*Yool et al.*, 2015]. The classes have slightly different physiological coefficients for nutrient and light uptake efficiencies to reflect the competitive advantage of "small" phytoplankton in surface to volume area, and the diatom requirement for silicate. MEDUSA includes nitrogen, silicon, and iron nutrients (and the elemental cycles of carbon and oxygen). Phytoplankton carbon and oxygen are factored in through the Redfield C:N:O_2 ratio of 106:16:-151 (derived from Anderson (1995) and Redfield (1958)). The two classes also contribute differently to export rates and other model aspects that are beyond the scope of this thesis (further details are in [*Yool et al.*, 2015]). Production is calculated in the same way for both classes. This is done by modulating a temperature-dependent theoretical maximum production rate, as per Eppley (1972), by Michaelis-Menten nutrient limitation and hyperbolic light limitation terms (below). Photo-acclimation is factored in through a chlorophyll-specific initial slope of the photosynthesis-irradiance curve. For total production, we recombine the productivity of the two classes, taking the average light and nutrient uptake constants accordingly.

3.2.1 MEDUSA differential equations

The following partial differential equations describe the conservation of chemical matter in phytoplankton in MEDUSA. The full model partial differential equations and associated terms, that incorporate nutrients, phytoplankton, zooplankton and detritus are given in Appendix A. Here, we focus on the model aspects that are most pertinent to primary productivity.

The model considers the rate of change of biomass and chlorophyll in two phytoplankton classes, non-diatoms (Pn, Chl_{Pn}) and diatoms (Pd, Chl_{Pd}), according to

$$\begin{aligned}
\frac{\partial Pn}{\partial t} &= PP_{Pn} \cdot Pn - G\mu_{Pn} - Gm_{Pn} - M1_{Pn} - M2_{Pn}, && (3.1)\\
\frac{\partial Pd}{\partial t} &= PP_{Pd} \cdot Pd - Gm_{Pd} - M1_{Pd} - M2_{Pd}, && (3.2)\\
\frac{\partial Chl_{Pn}}{\partial t} &= \frac{\theta_{Pn}^{Chl}}{\xi}\left(R_{Pn} \cdot PP_{Pn} \cdot Pn - G\mu_{Pn} - Gm_{Pn} - M1_{Pn} - M2_{Pn}\right), && (3.3)\\
\frac{\partial Chl_{Pd}}{\partial t} &= \frac{\theta_{Pd}^{Chl}}{\xi}\left(R_{Pd} \cdot PP_{Pd} \cdot Pd - Gm_{Pd} - M1_{Pd} - M2_{Pd}\right), && (3.4)\\
\frac{\partial Pd_{Si}}{\partial t} &= PP_{PdSi} \cdot Pd_{Si} - Gm_{PdSi} - M1_{PdSi} - M2_{PdSi} - DS_{PdSi}. && (3.5)
\end{aligned}$$

Phytoplankton production rates for non-diatom and diatoms are calculated according to ambient nutrients, light and temperature. Phytoplankton response to light is determined by

$$\theta_{Pn}^{Chl} = \frac{Chl_{Pn} \cdot \xi}{Pn}, \quad \theta_{Pd}^{Chl} = \frac{Chl_{Pd} \cdot \xi}{Pd} \tag{3.6}$$

$$\hat{\alpha}_{Pn} = \alpha_{Pn} \cdot \theta_{Pn}^{Chl}, \quad \hat{\alpha}_{Pd} = \alpha_{Pd} \cdot \theta_{Pd}^{Chl} \tag{3.7}$$

θ_{Pn}^{Chl} and θ_{Pd}^{Chl} ($\mathrm{gChl\,gC^{-1}}$) are the non-diatom and diatom scaled chlorophyll-to-biomass ratios, which are converted from nitrogen (Pn, $\mathrm{mmolN\,m^{-3}}$) to carbon units using the conversion factor $\xi = 0.01257$ molN(gC)$^{-1}$. $\hat{\alpha}_{Pn}$ and $\hat{\alpha}_{Pd}$ ((W m^{-2})$^{-1}$ d^{-1}) scale the (constant) initial slope of the photosynthesis-irradiance curve, α (gC (gChl)$^{-1}$ (W m^{-2})$^{-1}$ d^{-1}) by this ratio so that phytoplankton with elevated chlorophyll respond more sensitively to irradiance.

Photoacclimation is incorporated into the biogeochemical model using the photoadaptation model advanced by Geider *et al.* (1997). Geider *et al.*'s model assumes that energy supply is matched to demand by a cell efficiently allocating resources between energy storage and light harvesting. At low light, resources are allocated to light-harvesting over storage and chlorophyll is synthesised, increasing the chlorophyll-to-carbon ratio.

$$R_{Pn} = \frac{\theta^{Chl}_{max,Pn}}{\theta^{Chl}_{Pn}} \cdot \frac{PP_{Pn}}{\hat{\alpha}_{Pn} \cdot I}, \tag{3.8}$$

$$R_{Pd} = \frac{\theta^{Chl}_{max,Pd}}{\theta^{Chl}_{Pd}} \cdot \frac{PP_{Pd}}{\hat{\alpha}_{Pd} \cdot I}. \tag{3.9}$$

Here R is the proportion of photosynthesate that is directed towards chlorophyll biosynthesis. R is set by the ratio of achieved to maximum potential photosynthesis. This is determined by the maximum chlorophyll-to-biomass ratio that the cell can sustain at low light (θ^{Chl}_{max}, gChl gC^{-1}), the instantaneous light harvesting capacity of the cell ($\theta^{Chl}\hat{\alpha}I$) and the achieved photosynthetic rate (PP, mmolN m^{-3} d^{-1}).

If the achieved photosynthetic rate exceeds the light harvesting capacity (PP/θ^{Chl} $\hat{\alpha}I > 1$) then R increases (Equations 3.8 and 3.9) and more chlorophyll is synthesised (Equations 3.3 and 3.4). More chlorophyll can be added (under increasingly low light) until $\theta^{Chl} \rightarrow \theta^{Chl}_{max}$. If the light harvesting capacity exceeds the achieved photosynthetic rate ($PP/\theta^{Chl}\hat{\alpha}I < 1$) then R will decrease and less chlorophyll will be synthesised (Equations 3.3 and 3.4).

The maximum phytoplankton growth rate (V_T) is calculated as an exponential function of temperature (T) and base growth rate at 0°C (V_0) [*Eppley*, 1972]

$$V_T = V_0 \cdot 1.066^T. \tag{3.10}$$

Given the initial slope of the photosynthesis-irradiance curve ($\hat{\alpha}$) and maximum phytoplankton growth rate (V_T), realised growth rate at ambient irradiance, I (Wm^{-2}) is given by

$$J = \frac{V_T \cdot \hat{\alpha} \cdot I}{\sqrt{V_T^2 + \hat{\alpha}^2 \cdot I^2}}. \tag{3.11}$$

Nutrient limitation of phytoplankton growth is implemented with Michaelis-Menten (1913) terms that use ambient nutrient concentrations and constants for the concentration at which phytoplankton growth is half its theoretical maximum (k_i)

$$Q_N = \frac{N}{k_N + N}, \tag{3.12}$$

$$Q_F = \frac{F}{k_F + F}. \tag{3.13}$$

Light and nutrient modulation are brought together with the (temperature-dependent) theoretical maximum growth rate to determine the realised local growth rate

$$P = J \cdot Q_N \cdot Q_F. \tag{3.14}$$

3.2.2 Ocean physics model

Biogeochemical tracers in the MEDUSA model are advected and mixed by an underlying physical model. The physical model used is version 3.4 of NEMO. This physical model comprises a general ocean circulation model, OPA9 [*Madec*, 2008], coupled to a sea-ice model, Louvain-la-Neuve Ice Model version 2 (LIM2) [*Timmermann et al.*, 2005]. The physical model is resolved at approximately 1/4° horizontal resolution (1440 x 1021 grid points), with a focussing of resolution around the equator (to improve the representation of equatorial upwelling), and at high northern latitudes. The grid cell resolution varies from 6.0–27.8 km globally, with an average resolution of 12.5 km (6.8–15.4 km) in the Arctic (poleward of 70°). Vertical space is divided into 75 levels, with increasing thickness with depth, from 1 m at the surface to approximately 200 m at 6000 m. Partial-level thicknesses are used for bottom topography to improve the representation of deep water circulation. Vertical mixing is parameterised using the turbulent kinetic energy scheme of Gaspar *et al.* (1990), with subsequent modifications by Madec (2008).

The sea-ice submodel (LIM2) is based on a three-layer thermodynamic framework (two layers of sea ice, one layer of snow), and a viscous-plastic rheology. Model sea ice is coupled to the ocean through a non-linear quadratic drag law based on the shear between the sea ice and ocean surface velocities. Freshwater exchange between sea ice and the ocean is calculated from precipitation and ice formation and melting, with sea-ice salinity fixed at 4 PSU and precipitation assumed to be fresh. The heat flux between the ocean and sea ice is proportional to the friction velocity at the ice-ocean interface and the temperature deviation from the salinity-dependent freezing point. Solar radiation can penetrate sea ice not covered by snow, and is dissipated by brine pockets within the ice.

The ocean-ice submodels are forced by output from a physical climate model simulation (HadGEM2-ES). HadGEM2-ES is an Earth System model (ocean-atmosphere-terrestrial), that includes representations of the climatically-important terrestrial and oceanic carbon cycles, and atmospheric chemistry and aerosols [*Collins et al.*, 2011]. HadGEM2-ES ran from start-1860 to end-2005 under historical atmospheric pCO2 concentrations, and then from start-2006 to end-2099 under Representative concentration pathway (RCP) 8.5 pathway. RCP 8.5 is a scenario in which CO_2 emissions rise throughout the 21st century, leading to an $8.5\,\mathrm{W\,m^{-2}}$ increase in radiative forcing by the end of the century. The output from HadGEM2-ES was processed into forcing fields with variable frequencies to reduce computational cost. Precipitation is monthly, radiation is daily and turbulent variables are 6-hourly (air, temperature, humidity and wind velocity).

Because of the high computational cost associated with 1/4° resolution, the biogeochemical simulation was initialized in year 1975 from a regridded physical and biogeochemical state from a 1° instance of NEMO (that was itself initialised off the above HadGEM2-ES run) [*Yool et al.*, 2015]. (Details of the 1°simulation are given in Yool *et al.*, 2015.) To decrease drift in NEMO, sea surface salinity (SSS) was relaxed (with a time scale of 30 days) toward that from HadGEM2-ES. The simulation's freshwater budget was also corrected for imbalances between forced (downward) precipitation and calculated (upward) evaporation.

3.2.3 Upper ocean physics

The Polar Science Center Hydrographic Climatology (PHC) provides monthly 1° gridded salinity and temperature climatological fields [*Steele et al.*, 2001], which can be used to assess the realism of simulated surface salinity, temperature and mixed layer depths. Here we compare sea surface temperature, sea surface salinity, and the corresponding surface mixed layer depth for the month of February. We select February as illustrative because it is commonly the month of maximum annual mixing (Figure 2.15), when nitrate is entrained for growth in the following summer [*Tremblay and Gagnon*, 2009].

Simulated sea surface temperatures capture the broad observed pattern (Figure 3.4a,b). Elevated temperatures are restricted to the subpolar Atlantic and its inflow, which dominates heat fluxes into the Arctic Ocean [*Årthun et al.*, 2012]. The model captures the bifurcation of the Barents Inflow and the Fram Strait Branch around Spitsbergen [*Aksenov et al.*, 2010b], but appears to over-estimate how far warm surface waters propagate into the Arctic along both of these branches. Elsewhere waters are homogenously cold and salinity changes dominates density (Chapter 2).

Simulated sea surface salinity captures the broad highs in the salty Atlantic and (lesser) Pacific inflows, and lows in the Beaufort Gyre and along the Siberian Shelf (Figure 3.4c,d). The position of the front between the salty Atlantic inflow and fresher interior waters is also captured. However, Arctic surface salinity patterns are less homogenous than surface temperature, and more poorly represented in the model. Low salinity in the Beaufort Gyre extends too far in towards the Marakov Basin (North Pole) in the model. There is also poor representation of the actual distribution of salinity lows along the Siberian Shelf, in particular in the East

Siberian Sea, where very fresh waters are not represented in the model at all.

Discrepancies in model sea surface salinity along the Siberian Shelf could arise from errors in Siberian river fluxes, that dominate freshwater input here [*Morison et al.*, 2012], or in the strength of cross-shelf mixing of this freshwater with saltier basin waters. In the Beaufort Gyre, the salinity low arises from wind-driven convergence that leads to the storage of freshwater [*Proshutinsky et al.*, 2002; *Giles et al.*, 2012]. Therefore, model leakage of low salinity waters out of the Canada Basin likely arises from the deficiencies in model convergence patterns (including ice-ocean drag).

Upper ocean surface temperature and salinity patterns set the upper ocean density structure. Here we define the mixed layer depth using a common density criteria ($0.03\,\mathrm{kg\,m^{-3}}$) [*de Boyer Montégut et al.*, 2004], and we saturate the color scale at 100 m to focus on patterns in the Arctic Ocean (where maximum mixed layers are of the order of 60 m; Chapter 2), rather than the subpolar inflow. There is a clear difference between deep mixed layers in inflows and shallow mixing in the colder, fresher, ice-covered interior, as captured by the simulation. There is also a clear difference in observations and simulation between deep mixed layer depths in the Atlantic and shallow mixed layer depths in the Pacific; the latter constrained by the shallow bottom (typically ∼50 m). Beyond this, fine-scaled spatial patterns differ. Deep mixing in the model is too widespread in the Atlantic and Pacific inflows: it extends too far in the model Pacific inflow, westwards along the Chukchi-East Siberian shelf break, and in the model Atlantic inflow, into the Nansen Basin. Model mixing is generally not patchy enough, as exhibited in the discrepancy between observed and modelled mixed layers in the Canada Basin and Marakov Basin — likely a consequence of 1/4° model resolution being inadequate to resolve finer scale mixing processes.

3.2.4 CMIP climate models

The Coupled Model Intercomparison Project (CMIP) convenes the running of a suite of Earth System Models under a common protocol that imposes certain procedural specifications and boundary conditions. Here we focus on models run under

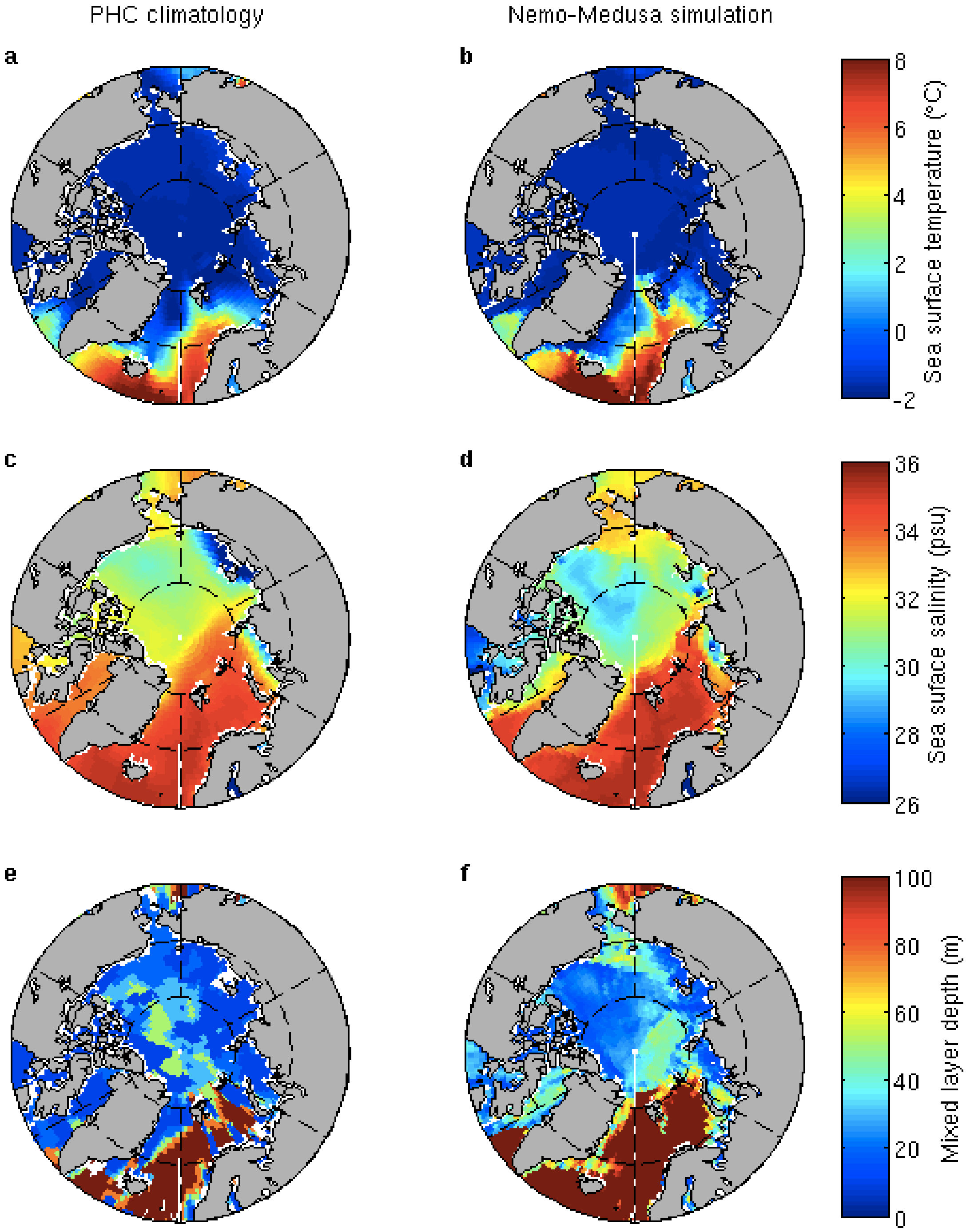

Figure 3.4: Arctic Ocean February upper ocean physical conditions from the PHC climatology (left) and model simulation (right). **(a-b)** sea surface temperature (°C), **(c-d)** sea surface salinity (PSU) and **(e-f)** mixed layer depth (m).

the most recent (fifth) iteration: CMIP5. These models comprise multiple (ocean, atmosphere, terrestrial) modules, of which ocean-ice-biogeochemistry is one component. Because of the additional computational cost associated with the extra modules, simulations are conducted at lower resolutions than ocean-only models.

Ocean horizontal resolution varies from 0.5–2°[*Vancoppenolle et al.*, 2013], which is inadequate to resolve crucial physical ocean processes, including eddies and the high-latitude Rossby deformation radius. The number of vertical levels vary from 31–59.

Model-ensembles are run under 4 Representative Concentration Pathways (RCPs 2.6, 4.5, 6, 8.5) that are defined as the cumulative measure of human emissions of greenhouse gases from all sources (units Wm^{-2}). Since each model architecture, submodel suite, selection of paramaterisations and so forth has risen historically with no imposed design protocol, models vary too widely in their form and dynamics to discuss exhaustively. They do, however, share some similarities.

Briefly, biogeochemical models are based on the nutrient-phytoplankton-zooplankton-detritus framework [*Riley*, 1946]. The simplest models use a single phytoplankton class and one limiting nutrient. Intermediate models have several limiting nutrients and one has an additional phytoplankton class (HadGEM2-ES). The most complicated models have >20 tracers, with several phytoplankton and zooplankton classes, and limiting nutrients. Some have variable nutrient requirements across phytoplankton groups. Other biogeochemical differences also exist in how nitrogen fixation, atmospheric and riverine fluxes, and benthic remobilisation are treated.

Sea ice is assumed to be opaque in several CMIP5 models (no light penetrates), and therefore light which penetrates through the ocean surface linearly increases with simulated open water fraction. This is highly unrealistic because observed under-ice bloom production is comparable with open-water rates [*Arrigo et al.*, 2012]. This omission biases the model forecasts where sea ice declines (over-estimating the consequent light increase).

3.2.5 CMIP5 Arctic climate models: forecasts and uncertainties

Phytoplankton productivity in the CMIP5 ensemble has been assessed based on the controls exerted by sea ice cover and nitrate limitation [*Vancoppenolle et al.*, 2013]. Validation of the appropriate model output (even baseline means) is challenged by the paucity of data. Observed sea ice concentrations are readily available from satellite (Figure 2.9), but nitrogen and productivity measurements are scarce (Figures 3.1, 3.6). Therefore, this previous analysis was conducted based on annual mean nitrate, with no distinction between (winter) physical supply and (summer) phytoplankton uptake [*Vancoppenolle et al.*, 2013]. Model-mean contemporary productivity is realistic in its magnitude ($511 \pm 12\,\mathrm{TgCyr}^{-1}$) and spatial distribution, but the inter-model spread is large ($\sigma = 198\,\mathrm{TgCyr}^{-1}$, 40% of the mean) [*Vancoppenolle et al.*, 2013]. Inter-model spread is also large for nitrate (mean = 4.4 mmolm^{-3}; $\sigma = 2.4$ mmolm^{-3}, 55% of the mean), and there is little inter-model agreement in either regional productivity or nitrate distributions. The large inter-model spread in productivity arises because of disagreement between model nitrate and sea-ice (light) conditions [*Vancoppenolle et al.*, 2013].

This is exacerbated in the model forecast. The decline in sea-ice concentration drives increases in productivity through improved light conditions, but the extent to which inter-model productivity increases depends on the degree of initial nitrate limitation and the magnitude of the decreasing nitrate trend in each model [*Vancoppenolle et al.*, 2013]. Models therefore, do not even agree on whether future productivity increases or decreases; a result that has also been found in a separate model ensemble analysis [*Popova et al.*, 2012].

Analysis of the CMIP5 model ensemble ties nitrate reductions to shoaling mixed layer depths, and reduced ocean nitrate transports into the Arctic Ocean from the Atlantic and Pacific [*Vancoppenolle et al.*, 2013]. Reductions in subpolar nitrate concentrations have been reported from several independent model intercomparison studies, and have been tied to weaker convective mixing in a warming ocean [*Bopp et al.*, 2013; *Steinacher et al.*, 2010]. A linear correlation analysis indicates that (annual-mean) mixed-layer depths within the Arctic explain 60% of the variance in nitrate reductions. But this is based on an ensemble-mean mixed-layer depth reduction of 25 m (2080–2099 minus 1980–1999), less than the present inter-model spread (σ=43 m). It is also based on 7 of 11 models. The 4 other models are omitted from this correlation analysis by the authors. (This omission was necessary because a failure to save the appropriate model output meant that mixed layers are reconstructed for each model, which was not possible for 4 of the models,

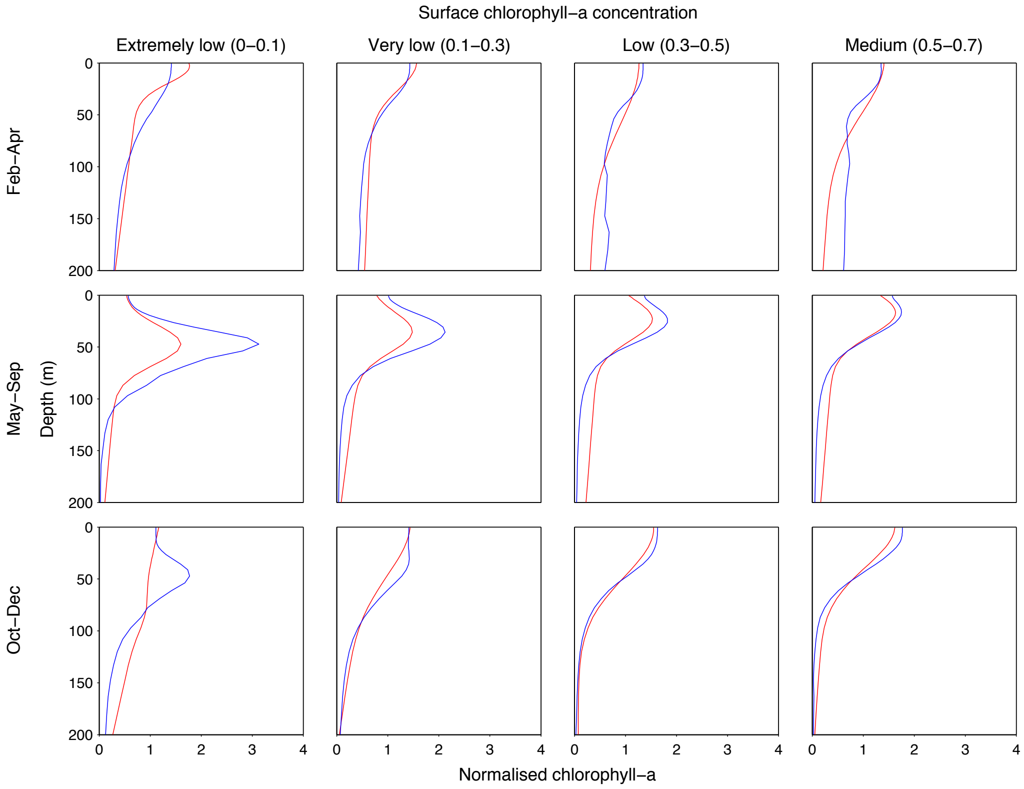

Figure 3.5: Observed (red) and simulated (blue) Arctic normalized chlorophyll-*a* profiles, sorted by season and surface chlorophyll concentration. Observations (n = 2403 profiles) span 1954–2007, whereas simulated profiles span 1990–2009. Locations where water depths are <50 m are omitted. Observations cover variable ice conditions but are biased toward open water and summer months; details of the observations can be found in Ardyna *et al.* (2013).

including HadGEM2-ES used here [*Vancoppenolle et al.*, 2013]. This shortcoming also precludes useful model mixed-layer comparison with the PHC climatology.)

Several CMIP5 models also presume zero-light, zero phytoplankton growth conditions under ice. Sea-ice decline then necessarily drives productivity increases in these models; contrary to observations that indicate massive phytoplankton growth already occurs under-ice [*Arrigo et al.*, 2012].

3.2.6 MEDUSA productivity and chlorophyll-a

To use the MEDUSA simulation we first need to check that the numerical simulation is a realistic representation of available observations. The simulated depth-

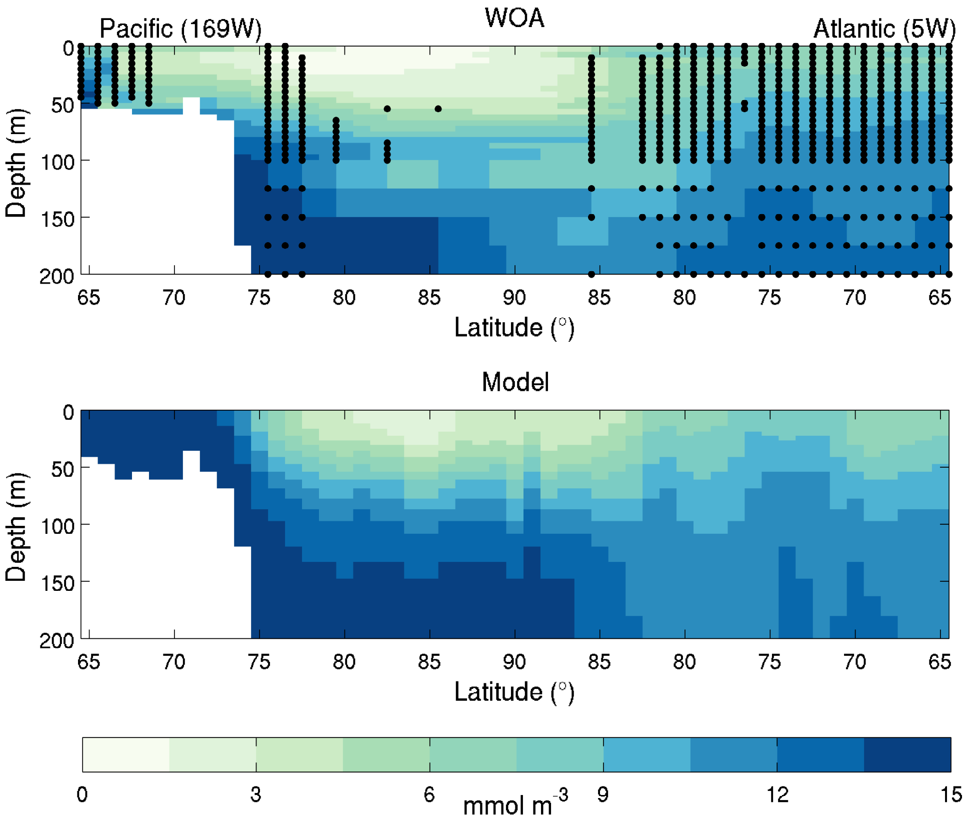

Figure 3.6: Transect of annual mean (top) observed [*Garcia et al.*, 2014] and (bottom) simulated Arctic dissolved inorganic nitrogen (mmol m^{-3}). The transect runs from Bering Straits to Fram Straits (65°N–90°N at 169°W and 5°W). Grid squares containing observations are shown by black dots in the top of the figure (number of observations = 5923). Observation distribution is biased toward lower latitudes.

integrated production field was given in Chapter 2 with satellite and in situ estimates (Figure 2.16). The spatial pattern of production in the simulation agrees well with the spatial pattern inferred using diverse techniques.

The simulation also reproduces observed Arctic Ocean seasonal chlorophyll distributions (Figure 3.5). Seasonal increases in light stimulate a spring bloom in nitrate replete surface waters with chlorophyll profiles decreasing with depth according to attenuation of light in the water column (top row). In more oligotrophic waters, surface nitrate depletion by the spring bloom promotes the subsequent development of subsurface chlorophyll maxima. The subsurface chlorophyll maxima that develop are more pronounced and occur deeper in more oligotrophic waters, a feature captured by the simulation (middle row). In autumn, increased mixing replenishes surface nitrate, and chlorophyll maxima return to surface waters (bottom row), accompanied in ice-free waters by a second bloom [*Ardyna et al.*, 2014]. Deviation of the simulation from observed chlorophyll profiles is restricted to areas with extremely low surface chlorophyll where the model overestimates the strength of summer subsurface chlorophyll maxima (middle left panel) and insufficiently homogenizes the vertical chlorophyll distribution during winter mixing (bottom left panel).

3.2.7 MEDUSA dissolved inorganic nitrogen

We also compare simulated annual-average dissolved inorganic nitrogen (DIN) to the World Ocean Atlas 2013 (WOA) [*Garcia et al.*, 2014] along a Pacific-Atlantic transect that traverses the central Arctic (Figure 3.6). Surface DIN is broadly higher at lower latitudes (toward 65°N) where supply to the Arctic Ocean occurs [*Torres-Valdés et al.*, 2013] and decreases interiorward as nutrients are removed from surface waters by biological uptake and inflowing waters subduct below the halocline [*Hioki et al.*, 2014]. The simulation broadly captures observed DIN concentrations along the transect, with the exception of the Chukchi shelf where simulated upstream concentrations advected in from the Pacific are too high, and observational biases toward summer may also bias the comparison [*Brown et al.*, 2015]. Note that few DIN observations are available for the central Arctic. In Appendix B we provide a second model-WOA transect to demonstrate that we have not inadvertently selected a misrepresentative transect here.

CHAPTER 4

On the vertical distribution of Arctic Ocean productivity

We start this chapter by considering the physical nitrate supply to the Arctic Ocean euphotic zone. Some simple calculations indicate that this supply is dominated by entrainment during winter mixing, as reported for other ocean basins [*Nishioka et al.*, 2011; *Tagliabue et al.*, 2014b]. Then, by scaling the ratio of nitrate limitation to light limitation, we show how nitrate limitation acts to pull production towards depth, and light limitation acts to pull production towards the surface. We show that the annual vertical distribution of production is then predictable from nitrate entrained in winter, and light available the following summer. We apply this to the transition of the Arctic Ocean to an ice-free state to indicate how expected light increases (with sea ice loss) and decreases in physical nitrate supply impact the vertical distribution of production; this is lastly related to changes in depth-integrated production across the Arctic Ocean.

4.1 Arctic Ocean boundary nitrate fluxes

Consideration of a nitrate budget for the Arctic Ocean, based on fluxes reported in the literature, indicates that nitrate available for new production in the Arctic Ocean is supplied though ocean transports from adjacent basins (Figure 4.1). External sources to the ocean, from the atmosphere [*Beine et al.*, 2003] and river outflow [*Emmerton et al.*, 2008; *Tremblay et al.*, 2011; *Le Fouest et al.*, 2013] are thought to be negligible at the pan-Arctic scale and small at the regional scale. The hydrographic data discussed in Chapter 2 indicates that ocean nitrate transports occur through the (Pacific) Bering Straits and (Atlantic) Barents Sea Opening (Figure 2.14). Estimates of nitrate fluxes across the Arctic Ocean boundary are given in Table 4.1.

The observed nitrate distributions around the Arctic boundary, discussed in Chapter 2 (Figure 2.13), indicate that surface waters entering the Arctic are deplete in nitrate ($< 3\,\mathrm{mmol\,m^{-3}}$), with high nitrate concentrations largely restricted to sub-euphotic depths ($> 60\,\mathrm{m}$). This implies that recharging of surface nitrate in the Arctic interior must be supported by vertical exchanges. Several lines of

Arctic Ocean boundary nitrate flux	Magnitude ($\mathrm{gN\,yr^{-1}}$)
Ocean transports	
Bering Straits	4.0×10^{12}
Barents Sea Opening	1.5×10^{13}
Fram Straits	-4.4×10^{12}
Davis Straits	-1.4×10^{13}
Atmospheric transfer	
Deposition	~ 0
Denitrification	-6.2–29×10^{12}
River inflow	1.1×10^{11}

Table 4.1: Estimated Arctic nitrate boundary fluxes. Oceanic transports are from Torres-Valdes *et al.* (2013), river transports are from Le Fouest *et al.* (2013), atmosphere-ocean fluxes are from Beine *et al.* (2003), and ocean-atmosphere denitrification fluxes are from Chang and Devol (2009).

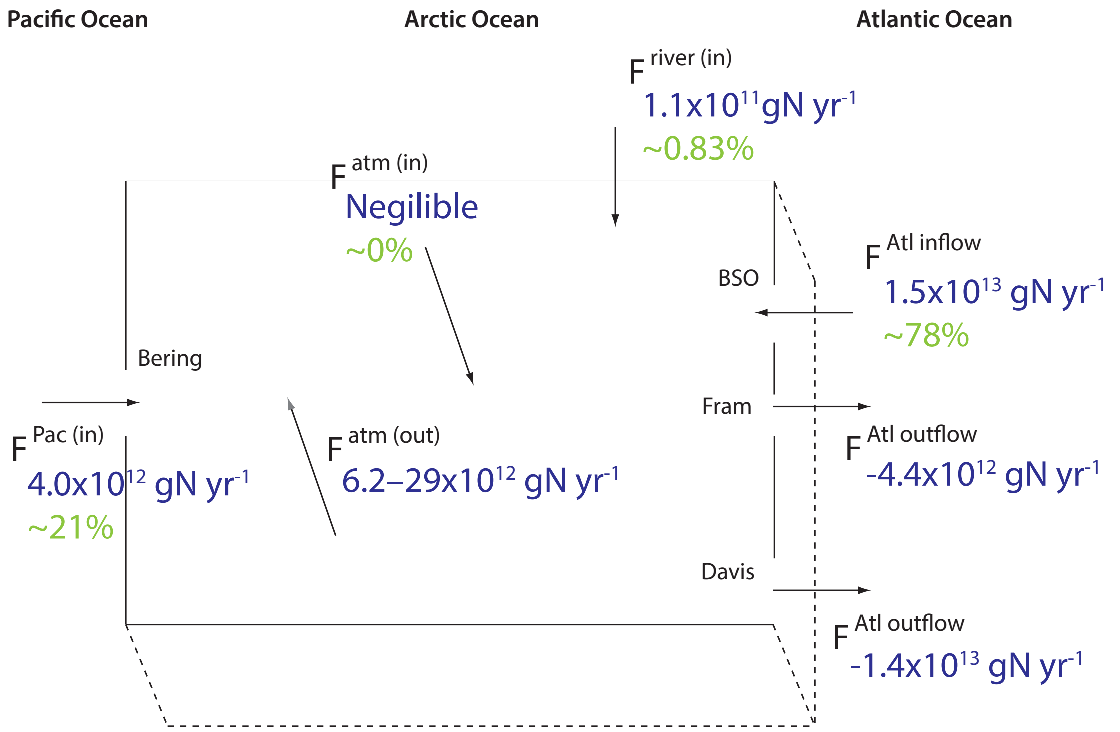

Figure 4.1: An Arctic nitrate budget indicating fluxes (blue, gN yr^{-1}) and their estimated contribution to pan-Arctic new primary production (green). Contributions to productivity are calculated using the pan-Arctic primary production estimate of Sakshaug (2004) and scaled to achieve a closed budget (100%). BSO: Barents Sea Opening. Atl: Atlantic. Pac: Pacific. Atm: atmosphere. Oceanic transports are from Torres-Valdes *et al.* (2013), river transports are from Le Fouest *et al.* (2013), atmosphere-ocean fluxes are from Beine *et al.* (2003), and ocean-atmosphere denitrification fluxes are from Chang and Devol (2009).

evidence support this. First, density and nitrate are strongly positively correlated in the Arctic [*Tremblay et al.*, 2011; *Pickart et al.*, 2013]. Second, lateral advection timescales are longer than one growth season [*Popova et al.*, 2013], the timescale over which surface nitrate is exhausted [*Codispoti et al.*, 2013]. Therefore, surface nitrate is exhausted before it can be advected over significant distances. Third, nitrate-rich Atlantic inflow water can be traced in the Arctic using the inert isotope tracer ^{129}I (the isotope has no Pacific Ocean sources so acts as a unique tracer of Atlantic Ocean waters). Observed and modelled distributions of the tracer indicate that nitrate-rich Atlantic water in the Arctic interior subducts below Pacific halocline waters [*Karcher et al.*, 2012]. To supply these nitrate-rich waters to the surface then requires vertical exchange.

4.2 Arctic Ocean interior vertical nitrate fluxes

We consider three processes by which nitrate may be exchanged vertically: Ekman pumping, diffusive fluxes and entrainment in the mixed layer (pre-charging) during winter mixed layer deepening. We now calculate the size of each flux to assess their relative importance in sustaining Arctic production.

4.2.1 Ekman fluxes

In the Arctic, polar easterlies drive a northward Ekman transport which induces shelf-break edge upwelling [*Carmack and Chapman*, 2003]. A vertical Ekman velocity (w_{ek}) is given by

$$w_{ek} \sim \frac{\partial V_{ek}}{\partial y} = \frac{\partial}{\partial y}\left(\frac{\tau_s^x}{\rho_0 f}\right) \tag{4.1}$$

where V_{ek} is the meridional Ekman transport velocity, τ_s^x is the zonal wind stress, ρ_0 is the ocean reference density and f is the Coriolis parameter at Arctic latitudes [*Williams and Follows*, 2011]. A typical wind speed (u_{10}) [*Pickart et al.*, 2013] and drag coefficient (C_D) [*Kara et al.*, 2007] during upwelling gives a wind stress (τ_s^x) of

$$\begin{aligned}\tau_s^x = C_D \rho_{air} u_{10}^2 &= 1.3 \times 10^{-3} \cdot 1.2\,\mathrm{kg\,m^{-3}} \cdot 6^2\,\mathrm{m\,s^{-1}} && (4.2)\\ &= 0.056\,\mathrm{N\,m^{-2}} && (4.3)\\ &\sim 0.05\,\mathrm{N\,m^{-2}}, && (4.4)\end{aligned}$$

driving a meridional Ekman transport velocity of

$$V_{ek} = -\left(\frac{\tau_s^x}{\rho_0 f}\right) \sim \frac{0.05\,\mathrm{N\,m^{-2}}}{10^3\,\mathrm{kg\,m^{-3}} \cdot 10^{-4}\,\mathrm{m\,s^{-1}}} = 0.5\,\mathrm{m^2 s^{-1}}. \tag{4.5}$$

A typical Ekman upwelling velocity is then

Vertical nitrate flux	Approximate magnitude ($\mathrm{mmol\,m^{-2}\,yr^{-1}}$)	Proportion of total flux
Ekman	350	25%
Diffusive	47	3%
Winter entrainment	1000	70%

Table 4.2: Estimated Arctic Ocean interior vertical nitrate fluxes. Calculated in the text.

$$w_{ek} \sim \frac{\partial V_{ek}}{\partial y} \sim \frac{0.5\,\mathrm{m^2 s^{-1}}}{10^5\,\mathrm{m}} = 5\times 10^{-6}\,\mathrm{m\,s^{-1}}, \tag{4.6}$$

where $\partial y = 10^5\,\mathrm{m}$ is the width of the ice-free shelf during upwelling [*Carmack and Chapman*, 2003]. Upwelling event frequency is typically $10\,\mathrm{yr^{-1}}$ with an average duration of 8 d [*Pickart et al.*, 2013], giving an annual Ekman upwelling velocity of

$$w_{ek} \sim 10\,\mathrm{yr^{-1}} \cdot 8\,\mathrm{d} \cdot 86400\,\mathrm{s\,d^{-1}} \cdot 5\times 10^{-6}\,\mathrm{m\,s^{-1}} \sim 35\,\mathrm{m\,yr^{-1}}. \tag{4.7}$$

Multiplying this by a typical nitrate concentration at the base of the Ekman layer $[N]_w$ [*Tremblay et al.*, 2008], gives a vertical Ekman nitrate flux

$$\begin{aligned} F_N^{Ek} = w_{ek} \cdot [N]_w &\sim 35\,\mathrm{m\,yr^{-1}} \cdot 10\,\mathrm{mmol\,m^{-3}} && (4.8)\\ &= 350\,\mathrm{mmol\,m^{-2} yr^{-1}}. && (4.9)\end{aligned}$$

4.2.2 Diffusive fluxes

A typical vertical diffusive flux of nitrate across the nitracline is given by [*Giering et al.*, 2014]

$$\begin{aligned} F_N^{dif} = K_T \frac{\Delta N}{\Delta z} &= 10^{-5}\,\mathrm{m^2 s^{-1}} \cdot 0.15\,\mathrm{mmol\,m^{-3} m^{-1}} && (4.10)\\ &= 1.5\times 10^{-6} \mathrm{mmol\,m^{-2} s^{-1}} && (4.11)\\ &\sim 47\,\mathrm{mmol\,m^{-2} yr^{-1}} && (4.12)\end{aligned}$$

where K_T is a typical Arctic Ocean diffusivity [*Shaw and Stanton*, 2014] and $\Delta N/\Delta z$ a typical vertical nitrate gradient [*Martin et al.*, 2012].

4.2.3 Entrainment fluxes during winter mixing

A simple consideration of entrainment (pre-charging) during enhanced mixing in winter (neglecting detrainment) gives a nitrate supply of

$$F_N^{ent} = [N]_w \cdot z_w = 10\,\mathrm{mmol\,m^{-3}} \cdot 100\,\mathrm{m} \tag{4.13}$$

$$= 1000\,\mathrm{mmol\,m^{-2}yr^{-1}} \tag{4.14}$$

where $[N]_w$ is the typical change in nitrate concentration brought about by maximum annual mixing [*Codispoti et al.*, 2013] and z_w is the respective mixed depth [*Steele et al.*, 2001]. Detrainment is neglected here because observations demonstrate that productivity happens below the mixed layer in the summer Arctic Ocean [*Martin et al.*, 2010].

The calculated vertical fluxes are tabulated in Table 4.2. They suggest that vertical nitrate supply is dominated by pre-charging during winter mixing (~70%). Ekman pumping is also significant (~25%), but diffusive mixing is minor (~3%). Consequently, this implies that ~70% of production is sustained through pre-charging and ~30% by nitrate mixed up throughout the growing season, explaining why patterns of Arctic primary production regress well to winter mixed layer depth [*Popova et al.*, 2010]. The dominance of entrainment in nutrient supply is similar to that found in the oceanographically diverse waters of the Southern Ocean [*Tagliabue et al.*, 2014b] and Western Subarctic Pacific [*Nishioka et al.*, 2011].

4.3 Phytoplankton uptake in open water and under ice

Nitrate fluxed upwards into the euphotic zone is taken up by phytoplankton growth. The rate at which dissolved nitrate is depleted is given by the difference between the rate of vertical supply and phytoplankton uptake rate. When vertical nitrate fluxes are greater than or equal to phytoplankton uptake rates, surface nitrate remains replete and surface-intensified growth is favoured by higher light in surface waters. If vertical nitrate fluxes are lower than growth rates then surface production will become nitrate limited, and phytoplankton growth will occur at subsurface depths where there is adequate nitrate to grow on.

Bloom duration and the subsequent subsurface production that may develop under oligotrophic conditions are considered for open water areas first. Then under ice areas are shown to exhibit the same dynamics but with faster depletion rates and shorter depletion durations.

4.3.1 Open water

The depletion rate of nitrate in open water is given by the difference between vertical supply and phytoplankton uptake rates. Taking typical Arctic phytoplankton growth rates $F_N^P \sim 4.0\,\mathrm{mmolN\,m^{-2}d^{-1}}$ [*Matrai et al.*, 2013] and the Ekman and diffusive fluxes (F_N^{Ek}, F_N^{dif}) from above (noting pre-charging does not supply nitrate *during* the summer growth season), gives the nitrate depletion rate

$$
\begin{aligned}
F_{depl} &= F_N^P - F_N^{Ek} - F_N^{dif} && (4.15)\\
&\sim 4.0\,\mathrm{mmol\,m^{-2}d^{-1}} - 0.96\,\mathrm{mmol\,m^{-2}d^{-1}} - 0.13\,\mathrm{mmol\,m^{-2}d^{-1}} && (4.16)\\
&= 2.9\,\mathrm{mmol\,m^{-2}d^{-1}}. && (4.17)
\end{aligned}
$$

Bloom duration

Given typical Arctic nitrate concentrations at the start of the growing season of $[N]_w \sim 10\,\mathrm{mmol\,m^{-3}}$ [*Codispoti et al.*, 2013], and typical nitrate depletion to 20 m during the bloom [*Tremblay et al.*, 2006], then the depletion time τ_{exh} is given by

$$\tau_{exh} = \frac{[N]_w \cdot z}{F_{depl}} = \frac{10\,\mathrm{mmol\,m^{-3}} \cdot 20\,\mathrm{m}}{2.9\,\mathrm{mmol\,m^{-2}d^{-1}}} \sim 69\,\mathrm{d}. \tag{4.18}$$

This lies within the range of observed bloom durations of ∼60 to 80 days [*Tremblay et al.*, 2006, 2008].

Depth of production

Assuming a typical growing season length of τ ∼150 d [*Martin et al.*, 2010], the depth at which production occurs at the end of a growing season (Z_{mig}) is given by the depth to which nitrate is depleted

$$Z_{mig} = \frac{F_{depl} \cdot \tau}{[N]_w} = \frac{2.9\,\mathrm{mmol\,m^{-2}d^{-1}} \cdot 150\,\mathrm{d}}{10\,\mathrm{mmol\,m^{-3}}} \sim 44\,\mathrm{m}. \tag{4.19}$$

The observed depth is ∼40 m [*Bergeron and Tremblay*, 2014]. Note that these data from the Beaufort Sea (provided by *Bergeron and Tremblay* and plotted in Figure 4.2) are for chlorophyll-*a*, but florescence data confirm that deep chlorophyll maxima in the Beaufort Sea reflect active growth [*Martin et al.*, 2010].

4.3.2 Under-ice

Observations of primary production and nitrate under ice imply the same vertical distribution of production as in open water: an initial bloom depletes surface nitrate, after which subsurface maxima develop [*Mundy et al.*, 2009; *Lee et al.*, 2010; *Matrai and Apollonio*, 2013]. We can check whether the same nitrate and production dynamics occur under ice as in open water with some straightforward calculations.

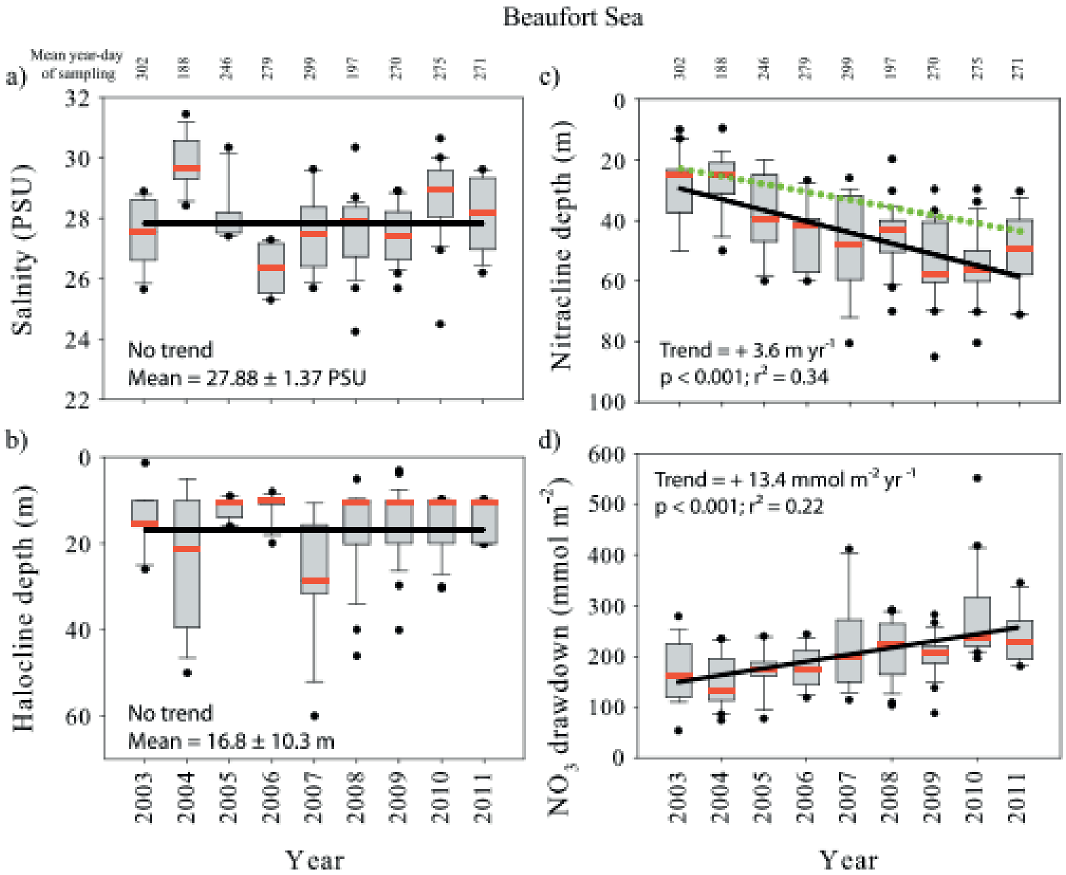

Figure 4.2: Observed changes in the Beaufort Sea between 2003–2011 from Bergeron *et al.* (2014). **(a)** Salinity. **(b)** Halocline depth. **(c)** Nitracline (black) and chlorophyll-maximum (green) depths. **(d)** Nitrate drawdown. The year day of sampling is given on the top axis. No net freshening is observed yet the nitracline and chlorophyll-maxium have deepened, the latter more slowly, resulting in an increasing decoupling. Note the offset between the nitracline and chlorophyll maximum by 2011 is $\sim 15\,\mathrm{m}$, at $\sim 40\,\mathrm{m}$ depth. Reproduced from Bergeron *et al.* (2014); where sampling locations are also given.

Depth of production

Observed under-ice nitrate concentrations prior to the growing season ($[N]_w$) are variable. We can account for this variability by using the observed upper and lower bounds [*Matrai and Apollonio*, 2013], and determine if the depth to which nitrate is depleted for the respective growing season lengths are correct in both cases.

1. Lower bound: $[N]_w = 1\,\mathrm{mmol\,m^{-3}}$

   Typical under ice production rates are 1/4 of open water ($0.25\,\mathrm{gC\,m^2d^{-1}}$)

[*Mundy et al.*, 2009]. With an initial nitrate concentration 10 times lower than open water, the nitrate depletion rate is 2.5 times as fast. Open water drawdown rates are $\sim 3\,\mathrm{md}^{-1}$, so under ice rates are $\sim 7.5\,\mathrm{md}^{-1}$. This drawdown rate over the respective under-ice growth period $\tau \sim 10\,\mathrm{d}$ [*Matrai and Apollonio*, 2013] gives the depth of production at the end of the growth season as

$$Z_{mig} = \frac{F_{depl} \cdot \tau}{[N]_w} = 7.5\,\mathrm{md}^{-1} \cdot 10\,\mathrm{d} \sim 75\,\mathrm{m}, \tag{4.20}$$

consistent with the observed depth to which nitrate is depleted of 75 m [*Matrai and Apollonio*, 2013].

2. Upper bound: $[N]_w = 3.33\,\mathrm{mmol\,m}^{-3}$

   At observed pre-growth nitrate concentrations 3 times lower than open water, nitrate depletion is 3/4 as fast. This gives an under-ice nitrate depletion rate of $\sim 2.25\,\mathrm{m\,d}^{-1}$. This depletion rate over the respective under-ice growing period $\tau \sim 34\,\mathrm{d}$ [*Matrai and Apollonio*, 2013] gives the depth of production at the end of the growth season as

$$Z_{mig} = \frac{F_{depl} \cdot \tau}{[N]_w} = 2.25\,\mathrm{md}^{-1} \cdot 34\,\mathrm{d} \sim 75\,\mathrm{m}, \tag{4.21}$$

   again consistent with the observed depth to which nitrate is depleted of 75 m [*Matrai and Apollonio*, 2013].

For both the high and low pre-charged nitrate concentrations, nitrate is depleted to a similar observed depth (75 m), presumably bounded by the euphotic depth. But in the second case where the initial nitrate inventory is higher, nitrate depletion takes longer (i.e. growth is sustained over a longer season, 34 d vs 10 d).

We have suggested the vertical profile of primary production is governed by the balance between nitrate supply and depletion rates. Arctic Ocean vertical nitrate fluxes are lower than phytoplankton uptake rates so net depletion occurs over the growing season [*Tremblay et al.*, 2006], resulting in the observed widespread nitrate exhaustion across the surface Arctic Ocean in summer [*Codispoti et al.*, 2013].

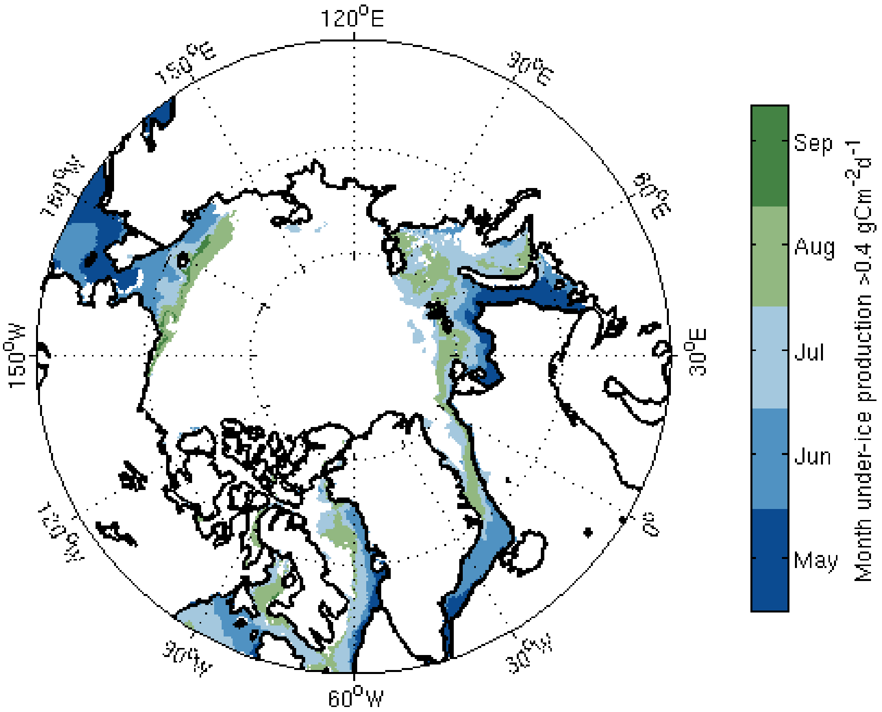

Figure 4.3: Month in which production exceeds 0.4 $\mathrm{gC\,m^{-2}\,yr^{-1}}$ under Arctic sea ice (>10% ice cover). May ice margin thick black line.

Nitrate depletion results in the development of subsurface production following the surface bloom [*Martin et al.*, 2010; *Wassmann and Reigstad*, 2011].

Determining the rate at which nitrate is exhausted, produces bloom durations and end-of-season production depths that agree well with observations. This is the case both in open water and under ice, suggesting that seasonal phytoplankton dynamics are coherent across variable sea-ice conditions. We will use this coherence to derive a single set of phytoplankton dynamics later in the thesis, which seems to be applicable to all sea ice conditions.

4.3.3 Extension of the Arctic spring bloom under sea ice

One straightforward implication of this continuity between phytoplankton nitrate uptake in open water and under ice is that the seasonal northward propagation of the spring bloom occurs continuously across the sea ice margin. This bloom propagation is seen across the Norwegian marginal ice zone in spring [*Strass and Nöthig*, 1996]. It is also seen in the Chukchi Sea, where reported under-ice phyto-

Symbol	Parameter	Derivation notes	Value
V	Max. phytoplankton growth rate	$V = V_0 * 1.066^T, V_0 = 0.515 (d^{-1})$	
α	Initial slope of the P-I curve	$\alpha = \alpha_p \cdot (Chl/C)$, $\alpha_p = 12$ $\mathrm{gC\,(gChl)^{-1}\,(W\,m^{-2})^{-1}\,d^{-1}}$, $\frac{\mathrm{Chl}}{\mathrm{C}} = \frac{1}{90}\ \mathrm{gChl\,(gC)^{-1}}$.	$0.133\ (\mathrm{W\,m^{-2}})^{-1}\mathrm{d}^{-1}$
I	Irradiance at SCM	$I_z = I_0 \cdot I_z/I_0$, $\mathrm{I_0} = 250\ \mathrm{Wm^{-2}}$, $\frac{\mathrm{I_z}}{\mathrm{I_0}} = 0.05$.	$12.5\,\mathrm{Wm^{-2}}$
k	Nitrate half saturation constant		$0.75\,\mathrm{mmolN\,m^{-3}}$
N	Nitrate concentration at SCM		$1.5\,\mathrm{mmolN\,m^{-3}}$

Table 4.3: Nitrate, light and physiological parameter symbols and the corresponding typical Arctic Ocean values. The relationships needed to derive Arctic Ocean values are also given. Data sources are α [*Pabi et al.*, 2008; *Yool et al.*, 2013], I [*Martin et al.*, 2010, 2013], V_0 [*Yool et al.*, 2013], k [*Yool et al.*, 2013], and N and T [*Martin et al.*, 2010].

plankton blooms are equal in size to the North Atlantic spring bloom [*Arrigo et al.*, 2012].

To give a sense of what this phenomenon may look like at the Arctic basin scale, the month in which production under ice exceeds 0.4 $\mathrm{gCm^{-2}yr^{-1}}$ is plotted in Figure 4.3 using the numerical model (0.4 is a typical mid-range Arctic bloom rate [*Matrai et al.*, 2013], selected to qualitatively show the propagation). Phytoplankton growth under ice (>10% cover) contributes 40% of annual Arctic production, with blooms propagating northwards well inside the ice margin (Figure 4.3), consistent with available in situ observations [*Strass and Nöthig*, 1996; *Arrigo et al.*, 2012]. This is clearly problematic for satellite productivity estimates that neglect productivity under ice [*Arrigo et al.*, 2008; *Pabi et al.*, 2008]. With production rates under the seasonal ice cover reaching rates in open water areas [*Arrigo et al.*, 2012], it may also explain the reported 23% increase in Arctic Ocean productivity with 23% loss in sea-ice extent between 2003–2007 [*Arrigo et al.*, 2008].

4.4 Decadal changes in the Beaufort Sea

4.4.1 Nitrate dominates current co-limitation

The limitation status of current subsurface production indicates how it may respond to future oceanographic changes. If nitrate is currently limiting then we may expect phytoplankton to migrate deeper under a longer growing season (with earlier ice retreat) or a reduced nitrate inventory. However, if light is limiting then phytoplankton may already be restricted by the euphotic depth.

We assume for simplicity that the physiological parameters are constant (the half saturation k_N and the initial slope of the photosynthesis-irradiance curve α), and fix them at typical Arctic values at the subsurface chlorophyll maxima (Table 4.3). We make the further simplifying assumption that temperature effects are not important, such that $V = 1$. Scaling the light limitation on nutrient limitation terms gives

$$L = \frac{J}{Q_N} = \frac{\dfrac{\alpha \cdot I}{\sqrt{V^2 + \alpha^2 \cdot I^2}}}{\dfrac{N}{k_N + N}} \sim \frac{\dfrac{\frac{2}{15} \cdot 12.5}{\sqrt{1 + \frac{4}{225} \cdot 156.25}}}{\dfrac{1.5 \times 10^{-3}}{0.75 \times 10^{-3} + 1.5 \times 10^{-3}}} = 1.3. \tag{4.22}$$

At $L < 1$ light limitation is stronger than nitrate limitation. Here, $L > 1$ indicating that nitrate limitation is stronger than light limitation. The fact that L is not much greater than unity, suggests that typical SCMs are moderately well balanced in their trade off of light (from above) and nitrate (from below).

To consider whether nitrate limitation dominates across a realistic range of Arctic Ocean temperatures we can evaluate L at T = *-2°C* and T = *8°C*. Noting that $V = V_0 \cdot 1.066^T$, for T = *-2°C*, we arrive at

$$L = 1.45, \tag{4.23}$$

and at T = *8°C*,

$$L = 1.3. \tag{4.24}$$

Therefore across a realistic range of observed Arctic temperatures (e.g. [*Steele et al.*, 2001]), nitrate limitation is likely to dominate over light limitation, at the environmental conditions chosen.

The robustness of nitrate limitation at SCM depths can be checked by taking the bounds of maximum nitrate and minimum light.

1. Maximum nitrate: SCM nitrate concentrations vary between 0–10 $\mathrm{mmol\,m^{-3}}$ [*Martin et al.*, 2010]. Taking 5 $\mathrm{mmol\,m^{-3}}$, gives $L = 0.99$. Note that 5 $\mathrm{mmol\,m^{-3}}$ is in the top quintile of observed nitrate concentrations at subsurface chlorophyll maxima [*Martin et al.*, 2010].
2. Minimum light: Using a minimum irradiance $I_z/I_0 = 0.01$ [*Martin et al.*, 2010], gives $L = 0.47$. Note that 0.01 is is in the bottom quintile of observed irradiance at Arctic subsurface chlorophyll maxima [*Martin et al.*, 2010].

These calculations indicate that SCMs at the most extreme (nitrate favourable) conditions observed in the Canadian Arctic Archipelago by Martin *et al.* 2010 are light-limited, but that average conditions are nitrate-limiting ($L > 1$). This implies that increased nitrate limitation is expected to deepen SCM, consistent with observed deepening of subsurface chlorophyll maxima with nitracline deepening in the Beaufort Sea (Figure 4.2). Therefore, subsurface chlorophyll maxima are expected to continue to deepen under a longer growing season, or if future per-unit-area vertical nutrient fluxes decrease. Here we have used data from the Beaufort Sea because these are the data that are publicly available. Below, we show the general applicability of this insight using the numerical model.

Once again we may evaluate the effects of temperature on the nitrate and light sensitivities listed here. If we consider the extreme case of high nitrate conditions (5 $\mathrm{mmol\,m^{-3}}$) and low light conditions ($I_z/I_0 = 0.01$), we find that at $T = -2°C$,

$$L = 0.89. \tag{4.25}$$

Similarly, at $T = 8^{\circ}C$,

$$L = 0.54. \tag{4.26}$$

At both ends of the temperature range, L <1 and light limitation exceeds nutrient limitation. This is reasonable as we would expect to see a shift to phytoplankton light limitation as light decreases and nutrients increase.

4.4.2 Decoupling of the nitracline and subsurface chlorophyll maximum

Subsurface chlorophyll maxima have been reported at nitracline depths across the Beaufort Sea (2003–2009) [*Martin et al.*, 2010]. However, the multi-year trend in the Beaufort Sea (2003–2011) demonstrates that the nitracline and subsurface chlorophyll maxima can decouple (Figure 4.2), either due to deepening of the nitracline [*McLaughlin and Carmack*, 2010] or a longer growing season [*Bergeron and Tremblay*, 2014].

As phytoplankton grow deeper in the water column, they incur an increasing cost of reduced light. At a certain depth, the reduction in light will no longer permit further increases in the depth of phytoplankton growth with the nitracline, causing the SCM and nitracline to decouple. We may expect this decoupling depth to be set by the depth at which light requirements start to dominate nitrate requirements ($L < 1$). We assume that phytoplankton photoacclimate to offset the reduced light at depth, by increasing the chlorophyll:carbon ratio to 1/30 (from 1/90 as given in Table 4.3). Note; 1/30 is near the maximum of the reported Arctic Ocean range of 1/25–1/100 [*Platt et al.*, 1982; *Sakshaug*, 2004]. With this new chlorophyll:carbon ratio substituted into Equation 4.22, $L < 1$ when light at the subsurface chlorophyll maxima satisfies $I < 2.2\,\mathrm{W\,m^{-2}}$.

Therefore, decoupling of growth from the nitracline is expected when the nitracline reaches the depth at which irradiance is $2.2\,\mathrm{W\,m^{-2}}$. Irradiance attenuates exponentially with depth in the ocean according to [*Kirk*, 1994]

$$I = I_0 e^{-kz}, \tag{4.27}$$

where k can be found by noting that at the euphotic depth $I/I_0 = 0.01$

$$k = \frac{4.6}{z_{eu}} = \frac{4.6}{40} \sim 0.115, \tag{4.28}$$

where a typical Beaufort Sea euphotic depth, z_{eu} =40 m, is given by Hill *et al.* (2013). Substituting k into Equation 4.27 and using a typical surface irradiance I_0 = 250 Wm^{-2} (Table 4.3), gives the decoupling depth, z_{th}

$$I = I_0 e^{-kz} \Rightarrow z_{th} = -\frac{1}{k} ln\left(\frac{I}{I_0}\right) \sim -\frac{1}{0.115} ln\left(\frac{2.2}{250}\right) = 41\,\text{m}. \tag{4.29}$$

Bergeron et al. (2014) observe decoupling in the Beaufort Sea as the nitracline deepens through ~30–40 m (Figure 4.2).

The study site of Bergeron *et al.* has shallower euphotic depths than the Canada Basin. In the Canada Basin,

$$z_{eu} = 50\,\text{m} \tag{4.30}$$

$$\Longrightarrow \; z_{th} \sim 51\,\text{m} \tag{4.31}$$

where the Canada Basin euphotic depth (z_{eu}) is given by Hill *et al.* (2013). Decoupling in the Canadian Basin is observed at ~55 m by McLaughlin *et al.* (2010), slightly deeper than this calculation.

Scaling nitrate and light limitation indicates that at average Arctic SCM conditions nitrate limitation dominates (Equation 4.22). This implies that under a longer growing season, or reduced per-unit-area vertical nitrate supply, the fraction of production in the subsurface will intensify. Further, as phytoplankton growth occurs at greater depths, they receive less light and decoupling from the nitracline may occur. As the nitracline deepens, nitracline depths become increasingly light limited, and the depth offset between the nitracline and chlorophyll maxima increases (with phytoplankton trading-off higher light for less nitrate to minimise limitation). This decoupling is seen in recent trends in the Beaufort Sea (Figure 4.2). We now demonstrate that the same response occurs in the numerical model as the Arctic transitions to an ice-free state and loses nitrate.

4.4.3 The Arctic chlorophyll to carbon phytoplankton ratio

In the above discussion, we simplified the calculations of phytoplankton limitation status by approximating the phytoplankton chlorophyll-to-carbon (*Chl:C*) ratio with a representative Arctic value of $1/90\,\mathrm{gChl(gC)^{-1}}$ (Table 4.3). In reality, the *Chl:C* ratio is a dynamic variable, as phytoplankton alter their pigmentation per unit biomass in response to environmental constraints on growth.

Phytoplankton increase their *Chl:C* ratio at low irradiance and at high temperatures under nutrient replete conditions (Geider *et al.* 1997 and refs. therein). At high irradiance the *Chl:C* ratio decreases, with a more pronounced decrease at low temperatures and low nutrient availability.

These behaviours can be considered as phytoplankton regulation of energy supply to match energy demand for growth *Geider et al.* [1997]. When light is low but temperatures and nutrients are favourable for growth, inadequate light is preventing growth and phytoplankton account for this by increasing pigmentation. Conversely, when light availability exceeds the growth rates possible at ambient temperatures and nutrient conditions, phytoplankton reduce pigmentation to prevent surplus photon uptake. In this way phytoplankton do not waste additional resources capturing photons that are not required to fuel growth.

In the Arctic, physical conditions that affect light availability such as sea ice cover, cloudiness and waters depths should be expected to alter phytoplankton *Chl:C* ratios.

Although measurements of *Chl:C* are limited in the Arctic, there is some evidence that at increasing water depths and ice cover, Arctic phytoplankton increase *Chl:C* ratios to compensate for lower light *Platt et al.* [1982]; *Sakshaug* [2004].

However, it is interesting to note that recent observations in northern Baffin

Bay show that subsurface biomass maxima (SBM) can also coincide with the SCM *Martin et al.* [2010]. At increasing water depths, phytoplankton may be expected to increases *Chl:C* ratios to compensate for lower light, and the SCM would be deeper than the SBM. As the Baffin Bay measurements indicate, this does not always appear to be the case *Martin et al.* [2010]. Here, the very low ambient nutrient concentrations may inhibit phytoplankton energy demand for growth, removing the need for additional pigmentation and photon energy supply. But without additional measurements, this remains speculative.

4.5 Predicting production's vertical distribution

A composite of observational time series suggests a consistent seasonal cycle of vertical production distributions across the Arctic Ocean. Supply of nitrate to the euphotic zone across the Arctic Ocean is dominated by entrainment in the winter mixed-layer [*Sundfjord et al.*, 2007, 2008; *Tremblay and Gagnon*, 2009; *Codispoti et al.*, 2013; *Randelhoff et al.*, 2015; *Janout et al.*, 2016]. Because temperatures are cold and exhibit relatively small vertical variability across the Arctic Ocean [*Steele et al.*, 2001], vertical changes in phytoplankton nitrate uptake rates during the following growing season are expected to be determined by light. Therefore, seasonal nitracline deepening rates across the Arctic Ocean may depend on the surface nitrate inventory at the time of maximum mixed layer depths and solar radiation dose the following summer.

Phytoplankton respond to nitracline deepening by more growth in the water column occurring at depth [*Martin et al.*, 2010; *McLaughlin and Carmack*, 2010; *Bergeron and Tremblay*, 2014]. Therefore, the vertical distribution of production over an annual cycle may be determined by the winter-entrained nitrate inventory and summer solar radiation dose. The subsurface fraction of production (P_2/P) is then expected to be higher where the nitrate inventory is lower or solar radiation dose is higher: such as in the Beaufort Gyre and Admunsen Gulf, where stratification and Ekman convergence prevent entrainment of nitrate into surface waters [*Martin et al.*, 2010; *McLaughlin and Carmack*, 2010] and a substantial pro-

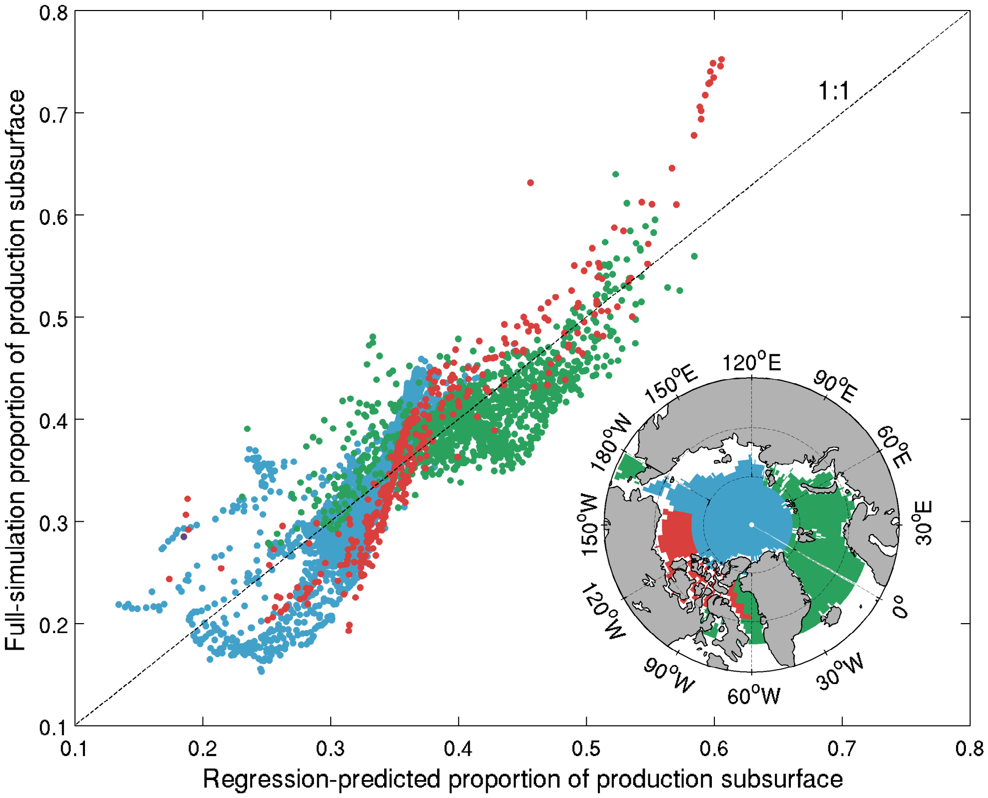

Figure 4.4: The simulated (2000s) proportion of annual production occurring subsurface (below 20 m) plotted against that predicted by a linear regression model based on the winter (max. mixed layer depth) nitrate inventory (N) and summer (July–September, integrated 400–700 nm) light (I). The linear regression model regresses N and I to the proportion of production at depth ($P_2/P = 0.000430\,I$ - $0.00120\,N + 0.355$, $R^2 = 0.73$, p $<$0.01). Data are grouped into three geographical regions: inflows, Central Arctic and the Canadian Arctic, as shown on the inset map. Baffin Bay is split between the Canadian Arctic Outflow to the west and West Greenland Current and Hudson Bay influenced waters to the east and South. Water depths <50 m are masked to prevent bias of the subsurface production fraction.

portion of annual production happens in subsurface chlorophyll maxima [*Tremblay et al.*, 2008; *Mundy et al.*, 2009; *Martin et al.*, 2010]. Conversely, in low light areas, subsurface production is expected to be low. We can test this by building a multi-linear regression model based on co-located entrained nitrate inventory (N) and solar radiation dose (I, Figure 4.4). The regression model is of the form

$$\frac{P_2}{P} = aI - bN + c, \tag{4.32}$$

where c is a constant.

Let us assume that the solar radiation dose that phytoplankton receive (I) is set by the amount of photosynthetically active light in the summer months (integrated July–September and 400–700 nm). Let us also assume that nitrate available for phytoplankton growth (N), is set by entrainment of nitrate in the winter mixed layer. To compare the availability of nitrate and light with vertical structure, we will compare the fraction of annual phytoplankton growth below a fixed depth (P_2/P, 20 m), with the nutrients and light available above this depth. To do this we will integrate the available light (I) and nitrate (N) over the depth 0-20 m.

Applying these simplifying assumptions to the regression model gives

$$\frac{P_2}{P} = 0.000430\, I - 0.00120\, N + 0.355, R^2 = 0.73, p < 0.01 \tag{4.33}$$

This regression model captures 73% of the simulated variance in the subsurface fraction of annual production. The regression model suggests that the contribution phytoplankton growth at depth makes to depth-integrated annual production is predictable from co-located nitrate inventory and summer light (where the subsurface fraction is taken as >20 m, which will be discussed below).

To examine the spatial variability of simulated vertical production distributions we split the Arctic Ocean into three geographic regions (Figure 4.4). First, we delineate inflows as waters exterior of main gateways and the Central Arctic Ocean as interior waters. A third region is then used to show the transformation of water masses as they transit across the Canadian Arctic from the Pacific inflow to their outflow along the west side of Baffin Bay [*Curry et al.*, 2014]. This region encompasses the Canadian shelf and basin (up to 78°N) and western Baffin Bay. Baffin Bay is split between the Canadian Arctic Outflow to the west, and the West Greenland Current and Hudson Bay influenced waters to the east and south. These three regions have distinct vertical production distributions, which can be explained in terms of ice distributions and physical nitrate supply. Around the edge of the Arctic Ocean, ice-free (high-light) conditions enable substantial production at depth (Figure 4.4). Conversely, in the Central Basin and the Chukchi inflow extensive ice cover (low light) prevents substantial production at depth. Summer light and the subsurface fraction increase towards the inflows where ice cover is reduced. As water masses transit from the Pacific inflow across the Canadian Arctic Ocean they experience nitrate depletion due to phytoplankton uptake [*Tremblay et al.*, 2008] and denitrification [*Yamamoto-Kawai et al.*, 2006; *Chang and Devol*, 2009]. (This transit probably takes around 5 years [*Popova et al.*, 2013].) Depletion of the nitrate inventory drives deepening of production maxima, resulting in an increasing subsurface fraction of production as waters move across the Canadian Arctic Ocean (Figure 4.4).

The numerical simulation demonstrates that reduced nitrate inventories cause deepening of production distributions. A higher proportion of annual growth then occurs at depth (>0.5) where light-dependent growth rates are lower. However under thicker ice, summer light is too low to support net growth at depth so the subsurface fraction is low (<0.3) [*Codispoti et al.*, 2013].

The vertical structure relates to depth integrated production. In the first case depth-integrated production is low because nitrate depletion necessitates phytoplankton grow at depth where light is lower. In the second case depth-integrated production is low because ice cover reduces light over the entire water column. Therefore, depth-integrated production decreases towards low and high subsurface fractions of production, being maximum at intermediate subsurface fractions. In our simulation intermediate subsurface fractions correspond to inflows, where observed depth-integrated production is highest (Figure 2.16).

An ensemble of models run as part of the Coupled Model Intercomparison Project 5 (CMIP5) consistently project reductions in winter nitrate inventory and summer light increases as sea ice cover decreases [*Vancoppenolle et al.*, 2013]. The insights from the regression model suggest reductions in winter nitrate inventory may cause deepening of production distributions. The impact of increased light over the water column on depth-integrated production would then be offset by reduced light experienced by deeper growth. We now demonstrate this response in the numerical simulation.

4.6 Phytoplankton response to an ice free Arctic

The Arctic Ocean is expected to be ice free by the end of the century [*Boé et al.*, 2009], and perhaps as early as 2054–2058 [*Liu et al.*, 2013]. The CMIP5 ensemble indicates that physical nitrate supply to surface waters is expected to decrease as Arctic sea ice retreats and light increases [*Vancoppenolle et al.*, 2013].

This simulation gives the onset of a seasonally ice free Arctic Ocean in the 2050s and a modest reduction in maximum annual mixed layer depth from the present day to 2099 (Figure 4.5a). Unrealistic fluctuations in simulated maximum annual mixed layer depth arise from localized over-mixing in the model south of Fram Strait and do not impact the Arctic-average nitrate inventory (Figure 4.5b). Reducing surface nitrate induces the expansion of low surface nitrate waters (Figure 4.6a). Deepening of the nitracline and increased light induces deepening of geographically co-located chlorophyll and production maxima (Figure 4.5c, 4.6c) as phytoplankton adjust to the perturbed nitrate and light conditions. Phytoplankton maxima deepen more slowly than the nitracline (Figure 4.5c), resulting in increasingly offset depths which reflect increasing light limitation with depth. This is in agreement with the observed phytoplankton response to low light at depth in oligotrophic conditions discussed above [*McLaughlin and Carmack*, 2010; *Bergeron and Tremblay*, 2014]. Reductions in the nitrate inventory occur in both Pacific and Atlantic inflows but extremely low inventories ($<50\,\mathrm{mmol\,m^{-2}}$) are only reached in the Atlantic inflow because the decreasing trend starts from a lower present day inventory here. Nitrate inventory decreases in the inflows because nitrate supply that originates in the subpolar North Atlantic and Pacific decreases in the coming century, in agreement with most CMIP5 models [*Vancoppenolle et al.*, 2013].

Simulated depth-integrated production changes reflect the ability of summer light increases to compensate reduced nitrate inventories (Figure 4.6d). As the ice retreats and the nitrate inventory diminishes, summer light increases over the water column are offset by reduced light experienced by deeper phytoplankton growth. We broadly simulate decreasing production in open water and increasing production within the present ice zone, in agreement with ensemble projections [*Steinacher et al.*, 2010; *Vancoppenolle et al.*, 2013]. This broad pattern is mod-

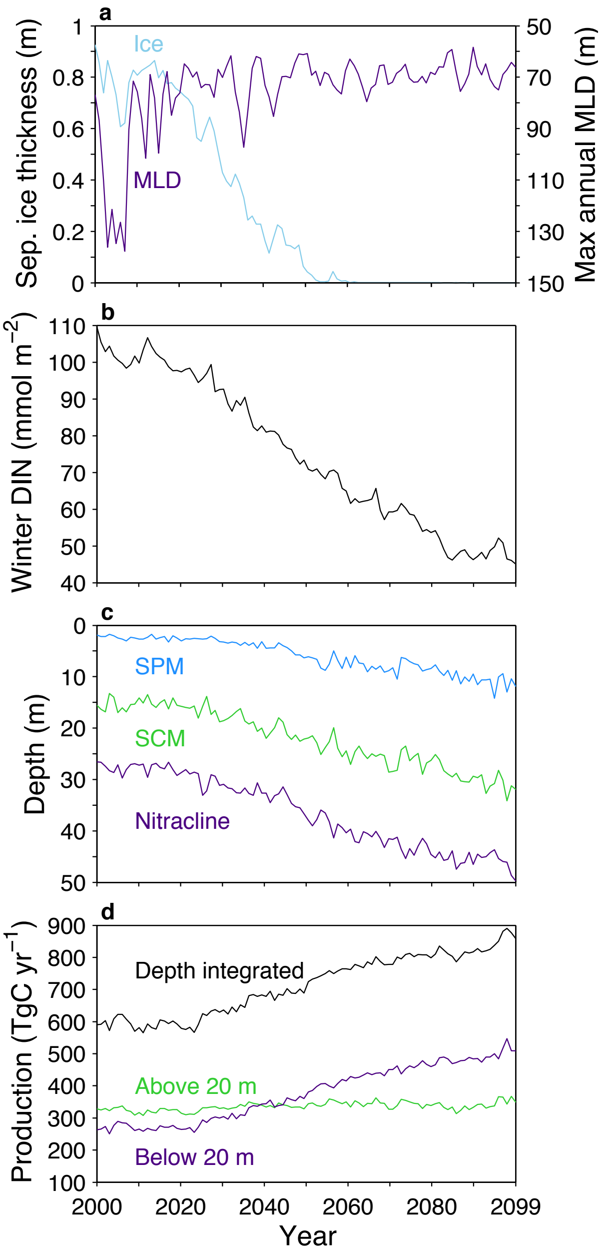

Figure 4.5: Arctic-average (> 65°N) simulated 21st century trends in **(a)** September ice thickness (ice) and maximum annual mixed layer depth (MLD, m), **(b)** winter dissolved inorganic nitrogen (DIN) inventory (mmol m^{-2}), **(c)** September subsurface production maxima (SPM), subsurface chlorophyll maxima (SCM) and nitracline depths (m), **(d)** annual surface, subsurface and total production (TgC yr^{-1}).

ulated by regional differences in nitrate supply. Light increases do not lead to increased production in the Beaufort Sea because of a decreased nitrate inventory. Further downstream in the Admunsen Gulf, where present day ice cover is thinner

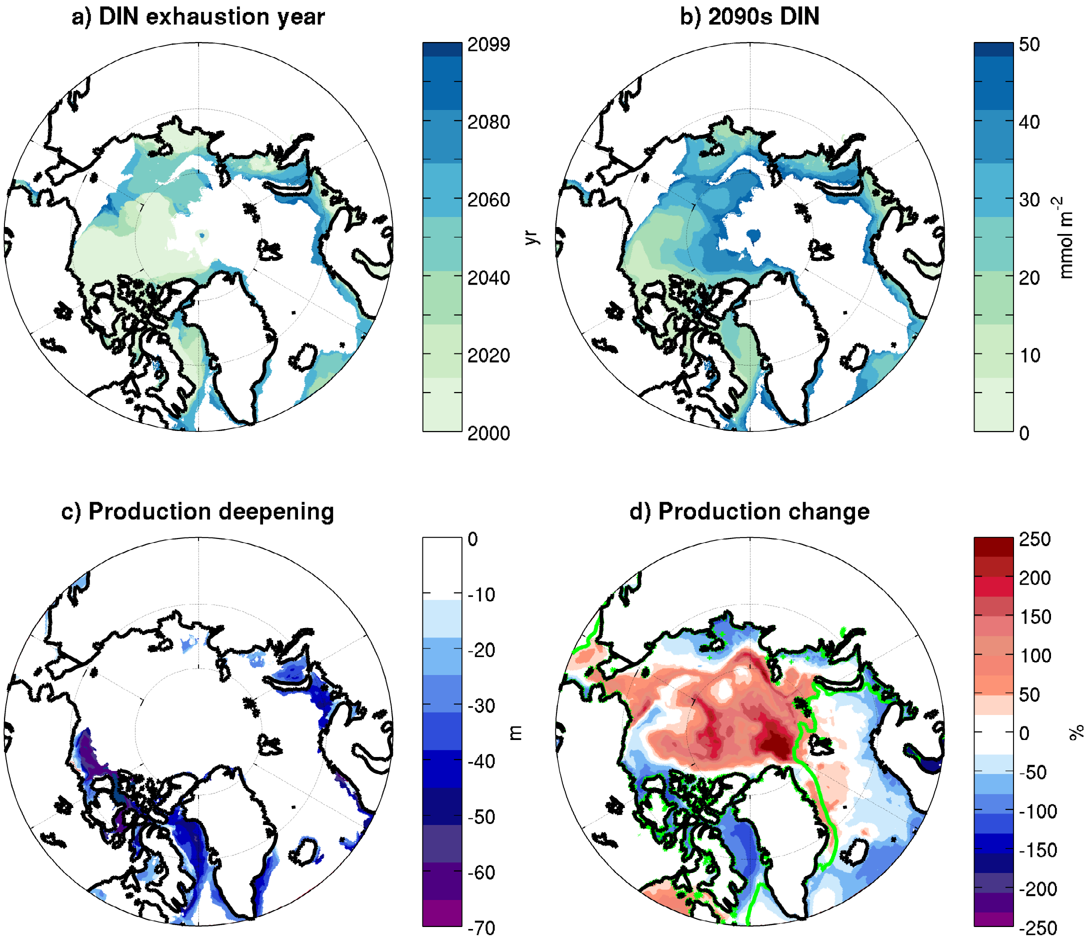

Figure 4.6: 21st century changes in simulated dissolved inorganic nitrogen and primary production. **(a)** Onset year at which the nitrate inventory first drops below 50 mmol m^{-2} (masked areas do not reach this threshold). **(b)** 2090s nitrate inventory (mmol m^{-2}), masked to only show locations where the inventory is below 50 mmol m^{-2}. **(c)** 2090s - 2000s change in September production maxima depth (m) (negative values indicate deepening). **(d)** 2090s-2000s change in annual depth-integrated production (%) with 2000s winter-average (Jan–Mar) 95% ice cover contour (green line).

and less extensive, reductions in the nitrate inventory exceed light increases and production therefore decreases. Reduced advective nitrate supply to the Siberian shelves exceeds modest summer light increases here.

Simulated production increases in a future Arctic Ocean are 10% at the onset of a seasonally ice free Arctic Ocean, and 30% by the end of the century (using the differences between the respective decade averages of 2000s, 2050s and 2090s). Increases primarily occurring at depths >20 m (Figure 4.5d).

4.7 Discussion

We have shown that vertical production distributions across the Arctic Ocean appear to be governed by local balances in nitrate inventory and summer light. Nitrate-light balances that result in low or high subsurface fractions of production lead to low depth-integrated annual production. Nitrate reductions act to deepen production distributions where light-dependent growth rates are lower, provided light at depth is sufficient to support net growth (Figure 4.4). Therefore, CMIP5 projections of reducing nitrate inventories [*Vancoppenolle et al.*, 2013] can be expected to deepen future production distributions such that increases in summer light due to ice retreat are offset by lower light levels experienced at greater depth (Figures 4.5, 4.6).

In the simulation low nitrate inventory waters are found over the Beaufort Gyre (Figure 4.6b). Simple process models suggest sea ice decline will increase Beaufort Gyre convergence [*Davis et al.*, 2014]. Recent convergence has reduced the nitrate inventory [*McLaughlin and Carmack*, 2010], suggesting that increased convergence under ice retreat may play a role in future nitrate inventory reductions in the Beaufort Sea and downstream Canadian Archipelago. Our simulation shows such a change, with some of the largest relative reductions in production arising from convergence in the Beaufort Sea and downstream low nitrate waters (Figure 4.6d).

Large Arctic Ocean production decreases are co-located with September production maxima deepening, except on the Siberian shelves where water depths are too shallow (Figure 4.6c, d). Production maxima deepening does not occur across the Arctic Ocean but is localized to extremely low nitrate inventory waters. This occurs because production maxima correspond to the depth of minimal nitrate-light co-limitation. Since light attenuates exponentially with depth, light limitation increases rapidly with depth and extremely low nitrate concentrations are required to deepen production maxima. For this reason, simulated production maxima deepening are co-located with extremely low surface nitrate concentrations (Figure 4.6b, c). This correspondence happens at $<2.5\,\mathrm{mmol\,m^{-3}}$ because of the non-linear production-nitrate function, as discussed in future chapters.

We have predicted the vertical distribution of contemporary Arctic production by defining the proportion of production at depth as that below 20 m. The general insights presented here are not sensitive to this depth, but at extreme reference depths one of nitrate or light limitation dominates and we end up with the trivial results that occur at the limits. For example, if we chose a very deep reference depth and define summer light and nitrate inventory as being integrated from the surface to the reference depth then light limitation will dominate at all locations in the Arctic Ocean. Conversely, if we chose a very shallow reference depth then nitrate limitation dominates. With shallow reference depths the proportion of production at depth tends towards 1 and with deep reference depths towards 0. Therefore, with deep reference depths we arrive at the result that light limitation dominates so growth is restricted to above the reference depth. At shallow reference depths nitrate limitation dominates so growth occurs below the reference depth. From this it can be seen that whilst all reference depths produce consistent and physically sound results, choosing the right reference depth is necessary to see the full impact of nitrate and light limitation on the vertical distribution of Arctic Ocean production.

Models within the CMIP5 ensemble agree on a reduction in the Arctic Ocean surface nitrate inventory contemporary with ice retreat, yet disagree on the sign of future production changes [*Vancoppenolle et al.*, 2013]. The simulation used here replicates the declining nitrate trend (Figure 4.5b) and suggests why the current ensemble production projections diverge. Divergence may arise because the model hindcasts generally fail to reproduce both contemporary winter nitrate inventories and summer light inadequately [*Vancoppenolle et al.*, 2013], shown here to be central features of Arctic Ocean production dynamics. In particular, several models fail to account for production under ice [*Vancoppenolle et al.*, 2013], likely substantial across the ice-covered Arctic Ocean [*Arrigo et al.*, 2012; *Matrai and Apollonio*, 2013; *Arrigo et al.*, 2014].

4.8 Conclusions

In this chapter we have used a numerical simulation, that reproduces observed chlorophyll and nitrate distributions (Figures 3.5, 3.6), to show that phytoplankton respond to reductions in winter nitrate inventories and summer light increases by deepening of production distributions. Spatial patterns of vertical production distributions are thus related to local nitrate and light conditions (Figure 4.4). Because nitrate decreases and light increases deepen production distributions, CMIP5 ensemble projections of reduced nitrate supply concomitant with ice retreat can be inferred to deepen future production distributions (Figure 4.5). Light increases due to ice retreat are offset by lower light experienced by deeper production distributions. Resulting Arctic Ocean production increases are modest, 10% in a seasonally ice free Arctic and 30% by the end century, and occur at depth (Figure 4.5d).

CHAPTER 5

On the dynamics of productivity in the Arctic Ocean

In the last chapter we used a regression model to indicate that the vertical distribution of annual production can be predicted from nitrate and light conditions over the seasonal cycle; and we used the numerical model to illustrate the consequences of this for a future Arctic. Here we consider Arctic Ocean production over depth as a function of ambient nitrate and light conditions. We produce a relationship between nitrate and light conditions, vertical production structure, and depth-integrated production

5.1 Photosynthetic kinetics over depth

Laboratory biochemical kinetic studies give the photosynthetic rate as a function of nitrate [*Michaelis and Menten*, 1913] and light [*Baly*, 1935] according to

$$P(N) = \frac{N}{k_N + N}, \qquad P(I) = \frac{\alpha I}{\sqrt{V^2 + \alpha^2 I^2}}. \tag{5.1}$$

where k is the half-saturation constant and α is the initial-gradient of the photosynthetic-light relation. The extent to which light and nitrate inhibit productivity may be quantified by the ratio of their limitations

$$L_{x,y,z,t} = \frac{\dfrac{\alpha I}{\sqrt{V^2+\alpha^2 I^2}}}{\dfrac{N}{k_N+N}}, \tag{5.2}$$

where L increases with stronger nitrate limitation and weaker light limitation. At the surface nitrate limitation is stronger and at depth light limitation is stronger. Therefore there is a depth at which conditions turn from nitrate to light limiting, which occurs at

$$P(N) = P(I) \tag{5.3}$$

Let this depth be z_r and the fraction of production that occurs below this depth be P_2/P. Above this depth, nitrate limitation is stronger; and below light limitation is stronger. Therefore, we should expect the fraction of total production that occurs below this depth (P_2/P) to increase with the ratio of nitrate limitation to light limitation (L)

$$\frac{P_2}{P} \approx \frac{\dfrac{\alpha I}{\sqrt{V^2+\alpha^2 I^2}}}{\dfrac{N}{k_N+N}} + c \approx L + c, \tag{5.4}$$

where I and N are averaged over the depth 0-z_r and c is a constant. This returns two scalar values for a given water column that describe its limitation state (L) and vertical production distribution (P_2/P). In Chapters 5 and 6 we will ignore the effects of temperature, which is assumed to be 10.38 degrees, such that V= 1.

The last chapter showed that the annual cycle in vertical production distributions can be approximated by ambient nitrate concentrations at maximum annual mixing and summer light (July–September average, integrated across 400–700 nm). These terms capture 73% of Arctic variability in annual vertical production distributions, adequate for our purposes here. We can therefore substitute these approximations for N and I into Equation 5.4.

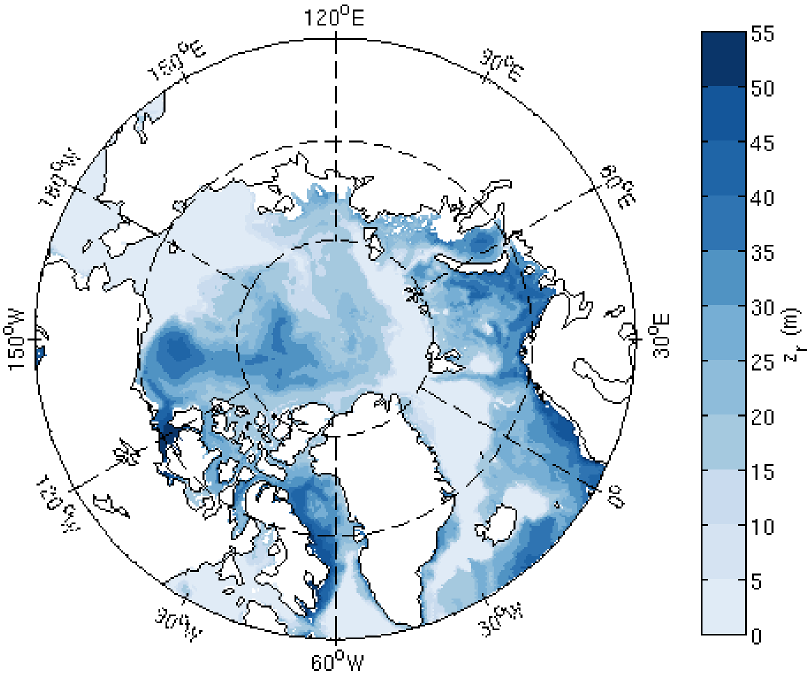

Figure 5.1: Map of turning point z_r (m), diagnosed from the model using Equation 5.3.

The turning point, z_r, is diagnosed from Equation 5.3. It depends on ambient nitrate and light conditions that vary laterally. It is deeper where nitrate concentrations are low and light is replete. Plotting z_r therefore traces out patterns such as low-nitrate in the Beaufort Gyre [*McLaughlin and Carmack*, 2010] and in western Baffin Bay (Figure 5.1). To compare water columns across the Arctic we fix z_r at the average for the Arctic Ocean domain, 20 m.

We can now plot Equation 5.4, using output from the numerical model, to test for the expected covariance (Figure 5.2). Each point in the figure is an Arctic Ocean water column; the ordinate gives the annual vertical production structure; and the abscissa gives the environmental conditions experienced by phytoplankton, in terms of surface nitrate and light. Production is deeper for stronger nitrate limitation and reduced light limitation across the Arctic Ocean.

To help interpretation of the relationship, we provide two example water columns plotted as Hovmöllers (Figure 5.2). At location (1) in the North Chukchi Sea, high Pacific-Arctic ocean nitrate transports mean nitrate is replete, and ice cover cover is low (Figure 2.16a). Production rates are high under these conditions (Figure 2.16b), and light is more limiting than nitrate so most production happens in near-surface waters above z_r (72%). At location (2) in the Admunsen Gulf, surface

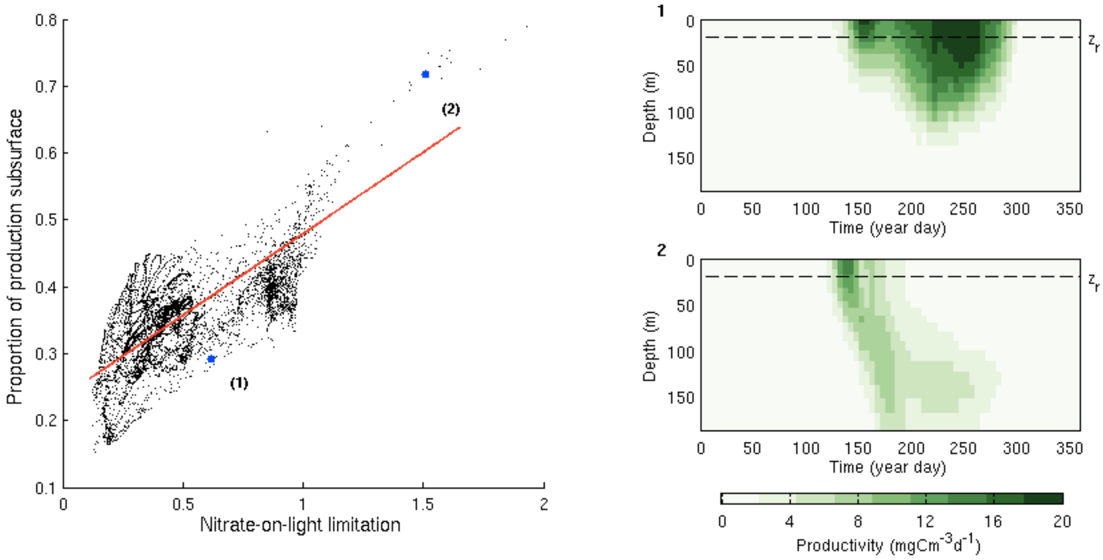

Figure 5.2: Model subsurface production proportion plotted against the ratio of nitrate limitation to light limitation (2000s). The linear least-squares fit (red line) is $P_2/P = 0.294L + 0.236$ (Equation 5.4, r^2=0.67, p<0.01). Water depths < 50 m are omitted. On the right hand side, annual productivity is plotted for example water columns (blue dots) in (1) the North Chukchi Sea (73.0°N, 169.0°W) and (2) the Admunsen Gulf (71.0°N, 120.0°W). z_r is the turning point, 20 m.

nitrate concentrations are very low and waters are seasonally ice-free in summer [*Martin et al.*, 2013]. Nitrate conditions are inadequate to sustain phytoplankton growth at the surface after a short bloom, and production must migrate to depth, enabled by deep summer light penetration. Annual production is therefore low and little of the annual production occurs above z_r (28%).

The relationship that arises demonstrates that phytoplankton respond coherently to nitrate-light condition across the Arctic Ocean. The proportion of production at depth increases with the ratio of nitrate limitation to light limitation; where low nitrate conditions prevents growth at the surface and increased light enables more production at depth. Interestingly, this means that phytoplankton are responding coherently to nitrate and light across variable sea ice conditions, as our preliminary calculations in Chapter 4 suggested. Therefore, we should expect the relationship to hold as the Arctic transitions to an ice free state.

In the rest of this Chapter we will use this relationship to elucidate what governs production distributions in the contemporary Arctic Ocean, and its transition to an ice free state. Because we use the same relationship, the underlying dependencies

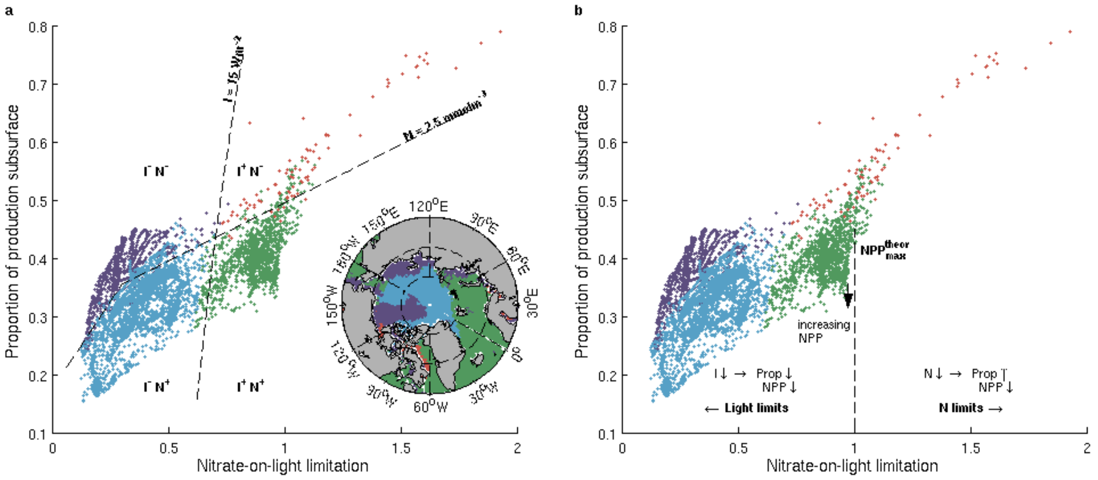

Figure 5.3: Model subsurface production proportion plotted against the ratio of nitrate limitation to light limitation (2000s). Water columns are coloured by surface winter nitrate inventory and summer light. Green = I $\geq$ 15 Wm^{-2}, N $\geq$ 2.5 mmolm^{-3}. Blue = I <15 Wm^{-2}, N $\geq$ 2.5 mmolm^{-3}. Purple = I <15 Wm^{-2}, N <2.5 mmolm^{-3}. Red = I $\geq$ 15 Wm^{-2}, N <2.5 mmolm^{-3}. These values are the light threshold along the model ice-edge ($I = 15$ Wm^{-2}) and the point of maximum curvature in the model photosynthesis-nitrate curve ($N = 2.5$ mmolm^{-3}). **(a)** Annotated with light-nitrate domains and the boundaries between domains (black dash) for comparison with figures below **(b)**. Annotated with the depth-integrated dependencies expected from theory. NPP: Depth-integrated productivity. Prop: P_2/P. N: Nitrate inventory. I: Light inventory.

do not change. We therefore introduce these generic dependencies first, and then show how these govern changes in production across the Arctic Ocean.

5.2 Nitrate-light conditions and production

The general relationship states that Arctic production occurs more deeply in the annual-average when nitrate is more limiting and light less limiting (Figure 5.2). Here, low light acts to pull production towards the surface, whereas low nitrate acts to pull production towards depth. High light conditions then occur towards the right of the graph and lower nitrate conditions occur towards the top of the graph; as illustrated in Figure 5.3.

Physically, we can interpret this in the following way. At low light production is restricted to near the surface, and with increasing light more production may

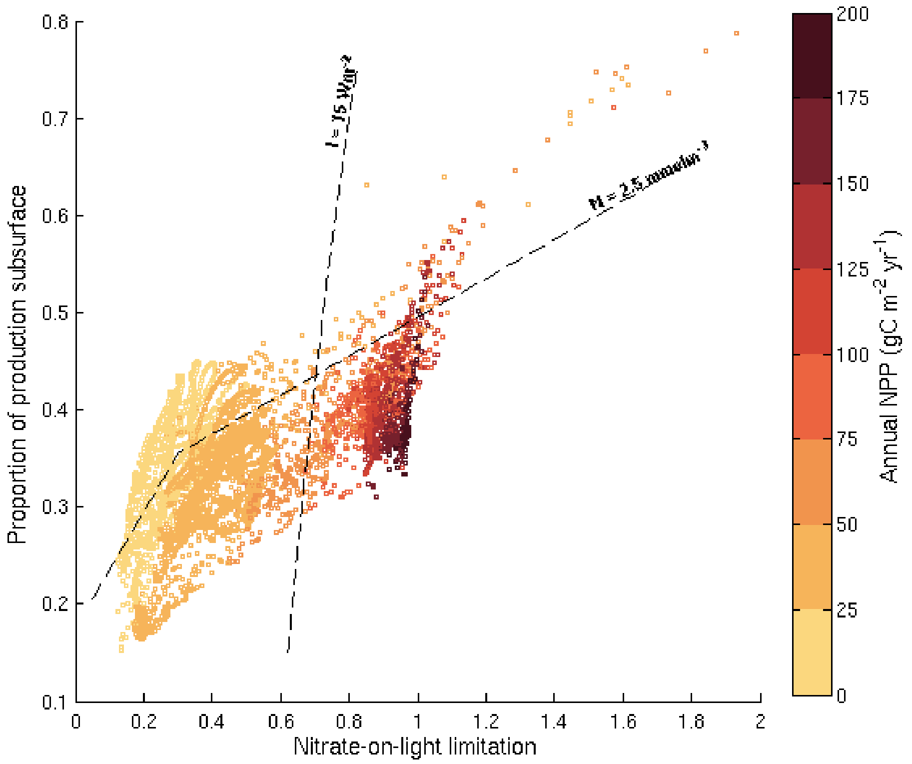

Figure 5.4: Model Arctic Ocean depth-integrated production as a function of the ratio of nitrate limitation to light limitation and vertical production structure.

happen at depth. But for the deep fraction of production to dominate, high light conditions must be complemented by low surface nitrate inventories (Figure 5.3a).

This can then be related to depth-integrated production by noting that its magnitude depends on the severity of nitrate and light limitation: strong limitation by either nitrate or light is expected to result in low depth-integrated production (Figure 5.3b). If depth-integrated production is reduced by low light, then productivity will be pulled towards the surface (low P_2/P). But if depth-integrated production is reduced by low nitrate, then productivity will be pulled towards depth (high P_2/P).

Therefore, depth-integrated production is expected to be largest around $L = 1$ (Figure 5.3b), decreasing to the left (right) as light (nitrate) becomes limiting. Further, at equal L, depth-integrated production is expected to decrease when production is pulled towards depth and P_2/P is higher (Figure 5.3b). This arises because high subsurface proportions require low nitrate inventories; and when L is

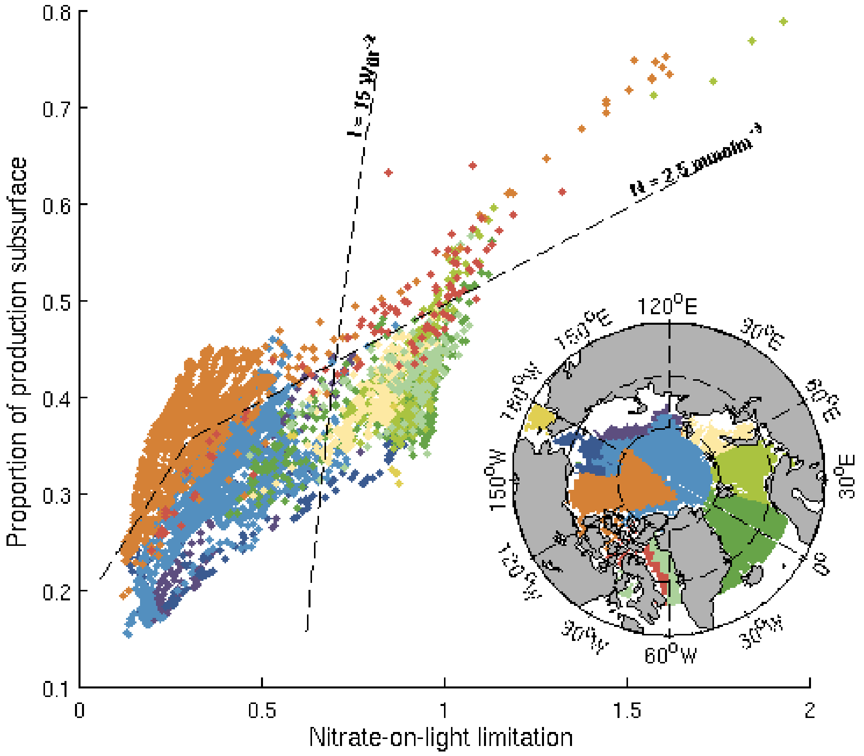

Figure 5.5: Model subsurface production proportion plotted against the ratio of nitrate limitation to light limitation (2000s). Water columns are coloured by regional sea (inset map). As far as possible, regional sea boundaries match observation studies (Figure 1a). These boundaries are modified in our study to account for the Beaufort Gyre [*Giles et al.*, 2012] and West Baffin Bay outflow [*Curry et al.*, 2014]. Water depths $< 50\,\mathrm{m}$ are omitted (inset map).

equal, low nitrate entails low light (Equation 5.2), so depth-integrated production is low. Depth-integrated productivity is then highest in areas of the Arctic Ocean where nitrate and light are replete, as expected (Figure 5.3b). Plotting depth-integrated production for each Arctic water column confirms these expectations: productivity is largest around $L = 1$ and, at equal L, decreases with P_2/P as production is pulled towards depth (Figure 5.4).

5.3 Arctic productivity geographical distributions

We can extend these insights into nitrate and light controls on productivity by mapping the location of water columns in the Arctic Ocean onto L vs P_2/P space

(Figure 5.5). This indicates how how measured production rates summarised in the introduction to this thesis are produced by environmental constraints. Prompted by the nitrate-light conditions, we elucidate each quadrant in turn.

High nitrate-light conditions and productivity map on to inflow seas (Figure 5.5), where ocean nitrate transports are large and waters are generally ice free in summer (Figure 2.16a). Productivity is higher in the Atlantic sector than the Pacific sector (Figure 5.5), in agreement with observed productivities and the Atlantic-Pacific zonal asymmetry in nitrate transports and ice cover (Figure 2.16).

High-nitrate low-light conditions are found in the ice-covered interior seas (Figure 5.5). Here productivity is low and orientated towards the surface, because perennial ice-cover means that euphotic depths are shallow and little production is supported at depth.

Low-nitrate low-light conditions are found in the interior Beaufort Gyre (Figure 5.5). Low nitrate conditions arises in the gyre because convergence suppresses surface nitrate supply (as discussed in the introduction). Light is also low because of strong ice cover. However, because nitrate concentrations in the surface 20 m are vanishingly low [*McLaughlin and Carmack*, 2010], a high fraction of production must occur at depth. Correspondingly productivity is low and the subsurface fraction is high.

Low-nitrate high-light conditions are found as waters transit the Canadian Archipelago and western Baffin Bay (Figure 5.5). As waters leave the Arctic through the Canadian Archipelago, they flow out from under ice cover and the increase in light supports a higher fraction of production at depth [*Tremblay et al.*, 2008; *Martin et al.*, 2010].

Certain changes in water-mass nitrate and light conditions can also be traced as water masses transit the Arctic Ocean (Figure 5.6).

Pacific waters enter the Arctic Ocean through Bering Straits, flowing into the Chukchi Sea and under ice (Figure 5.6a), reducing the light available for phytoplankton growth [*Arrigo et al.*, 2014]. As these waters flow across the Beaufort Gyre convergence reduces the surface nitrate inventory [*McLaughlin and Carmack*, 2010; *Giles et al.*, 2012], giving low nitrate and light conditions. Outflow of these waters into the North Atlantic through Baffin Bay, out from under ice cover then increases light availability, encouraging more production at depth.

As waters transit across the Arctic Ocean from the Pacific to the Atlantic, nitrate concentrations decrease, P_2/P increases and depth-integrated production decreases (Figure 5.6a). The excess phosphate that exits the Arctic Ocean is thought to support ~16% of nitrogen fixation in the North Atlantic [*Yamamoto-Kawai et al.*, 2006].

In the Atlantic sector the Barents inflow occurs in ice-free waters (Figure 2.16a). In the simulation, light is therefore replete and there is some biological nitrate depletion interiorwards (Figure 5.6a). Adjacent to this inflow, sea ice is exported out of the Arctic along the east coast of Greenland in the East Greenland Current (Figure 2.16a). Phytoplankton in this outflow therefore experience increased light as waters flow out from under ice (Figure 5.6b).

Here we have used a few examples to show how the relationship in Equation 5.4 can be used to elucidate the observed Arctic Ocean properties discussed in the introductory chapter. Further, by providing the dynamic underpinning to understand why these properties arise — as part of a coherent response by phytoplankton to lateral changes in environmental conditions — we can extend the insights to areas where observations are absent. This relation between productivity and environmental conditions may then be applied to environmental perturbations that occur as the Arctic Ocean transitions towards an ice-free state.

5.4 Future ice-free productivity

Arctic sea ice retreat is expected to perturb productivity [*Arrigo et al.*, 2008], but the impact of ongoing changes in the Arctic Ocean is unknown. Numerical simulations are inconsistent on the sign of future production changes because of diverging projections of ocean physics and sea ice which are coupled to nutrient and light diagnostics [*Vancoppenolle et al.*, 2013]. Despite this, a reduction in physical nitrate supply is consistently predicted over the coming century across all CMIP5 simulations and several other independent models [*Steinacher et al.*, 2010; *Slagstad et al.*, 2011; *Popova et al.*, 2012; *Vancoppenolle et al.*, 2013]. Light available for

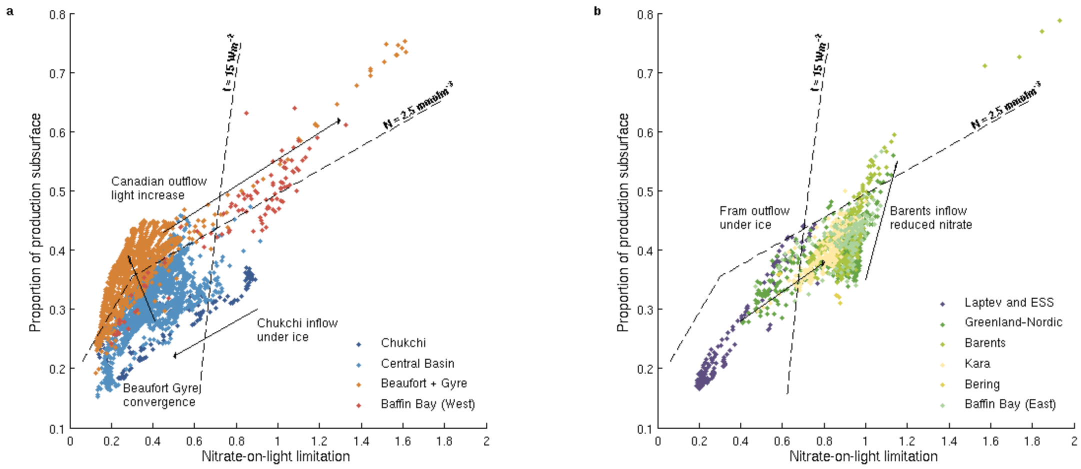

Figure 5.6: **(a)** Changes in model nitrate and light conditions between waters entering the Arctic Ocean from the Pacific Ocean and exiting into the Atlantic Ocean **(b)** Changes in model nitrate and light conditions in the Alantic Inflow and East Laptev and Siberian Seas. Trajectories discussed in the text are annotated (black text and arrows). Regional sea boundaries and nitrate-light domain boundaries are the same as Figure 5.5

photosynthesis also increases across all models, in line with reducing sea ice cover.

For the expected perturbations of nitrate (negative) and light (positive), Equation 5.4 indicates that we should expect the subsurface fraction of production to increase linearly with temporal increases in L. To test this we take the numerical-model means of L and P_2/P for each regional sea (2000s) and plot them with the corresponding means in the 2090s: production distributions vary linearly with the ratio of nitrate limitation to light limitation, and deepen across all Arctic seas over the coming century (Figure 5.7a). Deepening is not equal across all seas, yet seas where L tends to 1 have the largest productivities, and productivity decreases at $L = 1$ with the subsurface fraction (Figure 5.7a), as expected from the dynamics elucidated above.

In a seasonally ice-free Arctic Ocean (2090s) light is replete everywhere and deeper production distributions arise from reduced nitrate inventories. Reduced nitrate inventories entail lower depth-integrated production, so depth-integrated production decreases with the fraction of production at depth in the 2090s (Figure 5.7c).

The exact projected changes by regional-sea are particular to the numerical

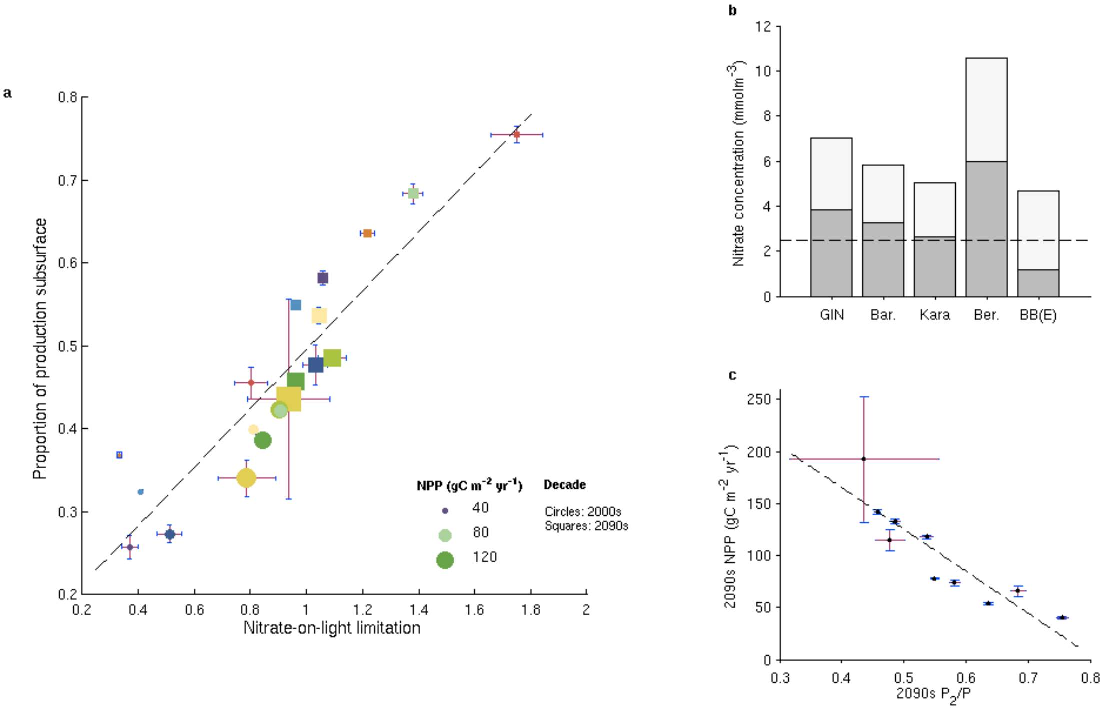

Figure 5.7: **(a)** Regional-sea-average model subsurface production proportion and the ratio of nitrate limitation to light limitation for the 2000s (circles) and 2090s (squares). Symbol sizes are depth-integrated production (NPP, $\text{gCm}^{-2}\text{yr}^{-1}$). The linear least-squares fit (black line) is given by $P_2/P = 0.402L + 0.121$ (Equation 5.4, r^2=0.90, $p<0.01$). Regional seas (colours) are the same as Figure 5.5. **(b)** Average model nitrate concentrations (mmolm^{-3}) in the Greenland-Icelandic-Nordic (GIN), Barents (Bar.), Kara, Bering (Ber.) and East Baffin Bay (BB(E)) Seas in the 2000s (light grey) and 2090s (dark grey). The dashed line is the point of maximum curvature (2.5 mmolm^{-3}) in the nitrate-production relationship (Equation 5.1). **(c)** Regional-sea average 2090s subsurface production proportion plotted against depth-integrated production (NPP, $\text{gCm}^{-2}\text{yr}^{-1}$). The linear fit is NPP = $-402P_2/P + 326$ ($r^2 = 0.89$, $p<0.01$).

model here, so should be treated in concert with other lines of evidence. Accordingly, we elucidate three first order patterns which have independent support.

At end century the Pacific and Atlantic inflows remain nitrate replete (N >2.5 $\text{mmol}\,\text{m}^{-3}$), across the entire IPCC ensemble [*Vancoppenolle et al.*, 2013] and in the simulation used in this thesis (Figure 4.6b). This occurs despite a reduction over the twenty-first century because contemporary nitrate concentrations are adequately high, such that the decreasing trend does not bring nitrate below 2.5 $\text{mmol}\,\text{m}^{-3}$(Figure 5.7b). Because nitrate remains replete in the Greenland-

Icelandic-Nordic (GIN), Barents, Bering and Kara Seas, changes in the limitation states are small and depth-integrated production stays high (Figure 5.7a). (Production remains high under reducing nitrate conditions because of the non-linearity in the kinetic relationship, Equation 5.1.)

The exception to this pattern of peripheral seas is East Baffin Bay (Figure 5.7a). Here simulated nitrate becomes deplete (Figure 5.7b). This increases L, so the proportion of production at depth increases and depth-integrated production decreases, 20% (Figure 5.7a). Hydrographic data collected in the Atlantic inflow since the 1990s suggest the declining nitrate transports into the Arctic Ocean, that underpin these trends, may already be underway [*Rey*, 2012].

Convergence in the Beaufort Gyre and advection of the resultant depleted nitrate signal through the Canadian Arctic Archipelago results in prevalent subsurface maxima here in the present day [*Martin et al.*, 2010; *Torres-Valdés et al.*, 2013]. In the last chapter, we showed that increased gyre convergence over the coming century may drive a reduction in nitrate in the gyre and downstream Canadian Arctic Archipelago. Here, the same result can be seen in the deepening production distributions from 2000s to 2090s (Figure 5.7a).

Satellite observations indicate that convergence has increased in the Canada Basin since 2002 [*Giles et al.*, 2012]. This process of increased convergence and nitrate depletion, and the phytoplankton vertical response, can be observed in current trends in the Beaufort Sea (as discussed in the last chapter) [*McLaughlin and Carmack*, 2010; *Bergeron and Tremblay*, 2014].

Last, melting of perennial sea ice in the interior Arctic Ocean alleviates light limitation, acting to increase depth-integrated production (P_2/P increases and L increases towards 1, Figure 5.7a).

5.5 Discussion

Regional sea production estimates, derived from different methods now agree in their spatial distributions (Figure 2.16a). In the remarks in the introductory chapter we noted that regional-sea productivies intuitively relate to Arctic sea ice cover, but that using sea ice as a direct proxy for growth limitation is problematic.

First, the ice edge does not accurately demark productivity, which extends under ice [*Arrigo et al.*, 2012; *Matrai and Apollonio*, 2013]. Second, sea ice retreat has two distinct effects on productivity (via nitrate and light), and the impacts can be independent and opposite [*Popova et al.*, 2012].

Here, we have sought instead to explain productivity distributions in terms of fundamental nitrate-light limitations on phytoplankton growth. We started from the observation that Arctic phytoplankton depth distributions reflect the vertical partitioning of nitrate limitation (at the surface) and light limitation (at depth). First, phytoplankton distributions deepen through the growing season as surface light increases and nitrate decreases [*Martin et al.*, 2010; *Ardyna et al.*, 2013; *Randelhoff et al.*, 2015]. Second, distributions are deeper in more oligotrophic regions [*Ardyna et al.*, 2013]. Third, distributions have deepened in the Beaufort Sea, between 2003–2011, in response to light increases and nitrate decreases [*McLaughlin and Carmack*, 2010; *Bergeron and Tremblay*, 2014].

We have developed a scaling that captures this response, based on depth-resolved ambient nitrate and light fields and their photosynthetic biochemical dependencies. The scaling relates ambient nitrate and light to the vertical structure of production (Equation 5.4). Surface nitrate decreases and light increases deepen production (Figure 5.2). Locations with a low fraction of production at depth have low depth-integrated production as light limits; locations with deeply-distributed production have low depth-integrated production as nitrate limits (Figure 5.4).

We then map the scaling analysis on to the geography of the Arctic Ocean (Figure 5.5). This reveals a relation between productivity and environmental limitations that agrees with observed Arctic Ocean physical conditions and productivity distributions (discussed in the introduction), and works across variable sea ice conditions.

The phytoplankton productivity response to an ice-free Arctic Ocean is currently highly uncertain. Numerical simulations even disagree on the sign of future change [*Steinacher et al.*, 2010; *Slagstad et al.*, 2011; *Popova et al.*, 2012; *Vancoppenolle et al.*, 2013]. But these numerical simulations do consistently forecast reduced physical nitrate supply and increased light as sea ice retreats over the next century.

Applying these two environmental changes to our analysis entails increased L

and deeper production (Figure 5.7a), where water columns with deeper production at end century have lower depth-integrated production (Figure 5.7c). For the nitrate and light conditions projected by the numerical model used here, Arctic-average production increases 10% by an ice-free Arctic Ocean and 30% by end century, occurring below 20 m — as noted in the previous chapter.

5.6 Implications for global production

The relationship between production and nutrient-light condition introduced here may be extendible to other oceans. Because the scaling is developed from laboratory studies of general photochemical and enzyme kinetics [*Blackman*, 1905; *Michaelis and Menten*, 1913] that are routinely applied across the global ocean [*Williams and Follows*, 2011], it may be anticipated to work globally. This is supported by the fact that well-lit nutrient-deplete subtropical biomes have more deeply distributed production and lower depth-integrated production, than poorly-lit nutrient-replete subpolar biomes [*Platt et al.*, 1991; *Antoine et al.*, 1996] — the same covariances as here. In the next Chapter we will explore whether the relationship developed in this Chapter ($P_2/P \sim L$) can be applied to the problem of global production.

CHAPTER 6

On the dynamics of productivity in the global ocean

In the last chapter, we discussed a relationship between productivity and the ratio of nitrate limitation to light limitation that occurs across ice conditions, in the present Arctic Ocean, and extends into the simulated 2090s seasonally ice-free Arctic. As the Arctic Ocean loses sea ice, it starts to correspond to the ice-free state of other (extra-Arctic) oceans. This suggests that the Arctic may provide some insights into observed productivity patterns in the extra-Arctic ocean. In this chapter we use the Arctic results to investigate phytoplankton dependence on nutrient and light conditions outside of the Arctic Ocean.

We introduced global productivity with a brief discussion of observed global patterns of production, in particular noting that large areas of the extra-Arctic Ocean are limited by iron. We then look at the performance of the simulation across the global ocean. To conduct the analysis, we use ^{14}C productivity data, GEOTRACES and WOA nutrient data, and MODIS light data, to relate phytoplankton growth to ocean nutrient and light conditions. Finally, we demonstrate the same relationship in the validated simulation and show that the relationship is invariant in the simulation — elucidating what this implies for future oceanic phytoplankton growth.

6.1 Oceanic production and nutrient limitation

Productivity estimates are now routinely made over the ice-free ocean using satellites. These maps show that annual production is particularly elevated in northern mid-latitudes, equatorial regions, along western boundaries, and along the Southern Polar Front. Low production is prevalent in the subtropical gyres, Arctic Ocean and Southern Ocean (Figure 2.1).

These patterns broadly correspond to the distributions sketched out by Sverdrup (1955) based on an inferred relationship between physical processes and surface nutrient supply (Figure 2.3b). Sverdrup reasoned that deeper mixing would tap further into the nutricline, providing higher macro-nutrient concentrations and productivity. Highly productive northern latitudes are areas of strong mixing, driven by seasonal convective overturning. Divergence and upwelling sustain production in the western boundaries, the equatorial band and the Southern Polar Front. On the other hand, stratification and downwelling prevent nutrient supply in the subtropical gyres.

But in certain areas macro-nutrient concentrations are high, but chlorophyll and productivity are low. These High-Nutrient Low-Chlorophyll (HNLC) regions — the Southern Ocean, Equatorial Pacific Ocean, and sub-Arctic — are now known to arise because the micro-nutrient iron limits productivity [*Martin and Fitzwater*, 1988; *Kolber et al.*, 1994; *De Baar et al.*, 1995].

Iron is supplied to the ocean from continental and oceanic sources (Table 6.1). Transports from the continents by fluvial, glacial and erosional processes are large (59–72% of total iron supply to the ocean). But the iron is predominantly in particulate form (81–92%) — which is readily adsorbed onto sinking particles and removed in the near-shore environment [*Morel and Price*, 2003] — so these iron fluxes are thought to rarely reach the open ocean [*Jickells et al.*, 2005]. It has been suggested that the Greenland Ice Sheet may be an important exception [*Bhatia et al.*, 2013]. But the ocean circulation near south-east Greenland is unlikely to transport this iron source into the subArctic Atlantic where phytoplankton growth is iron limited [*Hopwood et al.*, 2015]. In the Arctic Ocean, river discharge may be high enough that fluvial fluxes provide iron to phytoplankton in the central Arctic

Source	Flux (Tg yr^{-1})
Fluvial particulate total iron	625–962
Fluvial dissolved iron	1.5
Glacial sediments	34–211
Coastal erosion	16
Atmospheric	450
Hydrothermal	14
Authigenic (sediment diagenesis)	5

Table 6.1: Global iron fluxes (Tg yr^{-1}) to the ocean. Reproduced from Jickells *et al.* (2005). Fluvial particulate and dissolved fluxes are provided separately, as per the original table.

[*Klunder et al.*, 2012].

Atmospheric, hydrothermal and authigenic sources of iron reach the ocean regardless of iron phase. The largest of these sources is atmospheric deposition of continental dusts (27–39%). Approximately 45% is deposited in the North Atlantic, 25% in the Indian Ocean and 15% in the North Pacific (adjacent to African, Arabian and Asian desert sources respectively) [*Jickells et al.*, 2005]. The paucity of continental dust sources in the Southern Hemisphere means that atmospheric deposition in the South Atlantic (4%), South Pacific (6%) and Southern Ocean (6%) are low [*Jickells et al.*, 2005] — exacerbating phytoplankton iron limitation here [*Tagliabue et al.*, 2017].

Iron is also supplied to the ocean from mid-ocean tectonic ridges. Hydrothermal iron supply is strongest in the Southern Hemisphere, where it may mitigate low atmospheric fluxes [*Tagliabue et al.*, 2010]. Iron added to the deep ocean can be transported over 2000 km before it is ventilated into euphotic waters [*Resing et al.*, 2015], so it's influence on the iron inventory may be relevant at the basin scale (including away from ridges) [*Tagliabue et al.*, 2014a]. Because hydrothermal fluxes vary on longer timescales than atmospheric fluxes, they may act to buffer the ocean iron inventory from short term changes in atmospheric deposition [*Tagliabue et al.*, 2010].

Last, redox processes in sediments along the continental margin remobilise iron into the water column. This flux has been identified as an important source in the iron-limited North Pacific [*Lam and Bishop*, 2008] and the equatorial Pacific [*Slemons et al.*, 2010], and it may also contribute to phytoplankton blooms observed downstream of Southern Ocean islands [*Planquette et al.*, 2007]. Its broader role in the global iron inventory and carbon export may also be far more extensive than is currently recognised [*Conway and John*, 2014; *Tagliabue et al.*, 2014a].

6.2 Data sources and methods

6.2.1 Iron and nitrate data

Global dissolved iron concentrations have been collated into a database consisting of 18,653 discrete observations under the GEOTRACES program [*Tagliabue*, 2016]. The database spans 1978–2014 and covers all ocean basins (Figure 6.1). Observed concentrations vary from 0–80 nM, but are typically low (<1 nM). Dissolved ocean nitrate data are available from the World Ocean Atlas climatology [*Garcia et al.*, 2014], as used in the last chapter.

Here we assess the potential for nitrate and iron to co-limit the photosynthetic kinetic rate simultaneously [*Blackman*, 1905], using Michaelis-Menten kinetics [*Michaelis and Menten*, 1913]. This can be expressed as

$$Q = \frac{N}{k_N + N} \cdot \frac{Fe}{k_{Fe} + Fe} \tag{6.1}$$

where N, Fe are ambient nutrient concentrations and k_N, k_{Fe} are the respective half saturation constants.

Blackman's formulation allows phytoplankton limitation by both iron and nitrate. If only one nutrient limiter is assumed, as in the case of Liebig limitation, then we may under-estimate nutrient limitation in oceanic conditions where both iron and nitrate concentrations are below optimal values for phytoplankton growth (Figure 6.1c).

Conversely, more complicated co-limitation has been observed than envisioned by Blackman's (1905) original work (see Section 2.5.8). Additions of Fe-Zn and Fe-Co in the Costa Rica upwelling zone have stimulated phytoplankton growth [*Franck et al.*, 2003; *Saito et al.*, 2005]. Manganese cellular requirements are also thought to be in excess of dissolved stoichiometries in the Southern Ocean [*Moore et al.*, 2013], implying that manganese limits phytoplankton growth here.

We do not implement these trace metal co-limitations as their importance is not well understood [*Moore et al.*, 2013], trace metals have poor data coverage [*Morel et al.*, 2003; *Moore et al.*, 2013], and (with the exception of iron) they are not included in the numerical model [*Yool et al.*, 2013]. As data and our understanding of co-limitation expand, improvements may be made on the Blackman formulation (Equation 6.1). Nonetheless, below we derive the expected relationship from this term. We may, therefore, hope that the broad analysis developed here holds as our understanding of nutrient limitation improves. Notably, phytoplankton uptake of trace metals is, as far as we know, governed by Michaelis-Menten kinetics [*Morel et al.*, 1991].

Extracting the climatological nitrate data that matches (in location and month) available iron observations in the surface 50 m enables assessment of the extent to which nitrate and iron co-limit phytoplankton (Figure 6.1c). High nitrate, low iron conditions are clear in the Southern Ocean. But elsewhere there are few clear latitudinal trends. This is perhaps surprising because phytoplankton C/N/P (uptake) ratios have been reported to vary with latitude [*Martiny et al.*, 2013] and these govern ocean nutrient ratios [*Redfield*, 1934; *Weber and Deutsch*, 2012]; yet we find no clear latitudinal patterns in ocean nitrate-iron ratios (Figure 6.1c). Perhaps latitudinal trends in ocean nitrate-iron ratios are absent because latitudinal differences are masked by zonal differences (for example iron is lower in the Equatorial Pacific whereas nitrate is lower in the Equatorial Atlantic, Figure 6.5). Or perhaps macro-nutrient latitudinal patterns do not extend to include iron [*Tagliabue et al.*, 2017].

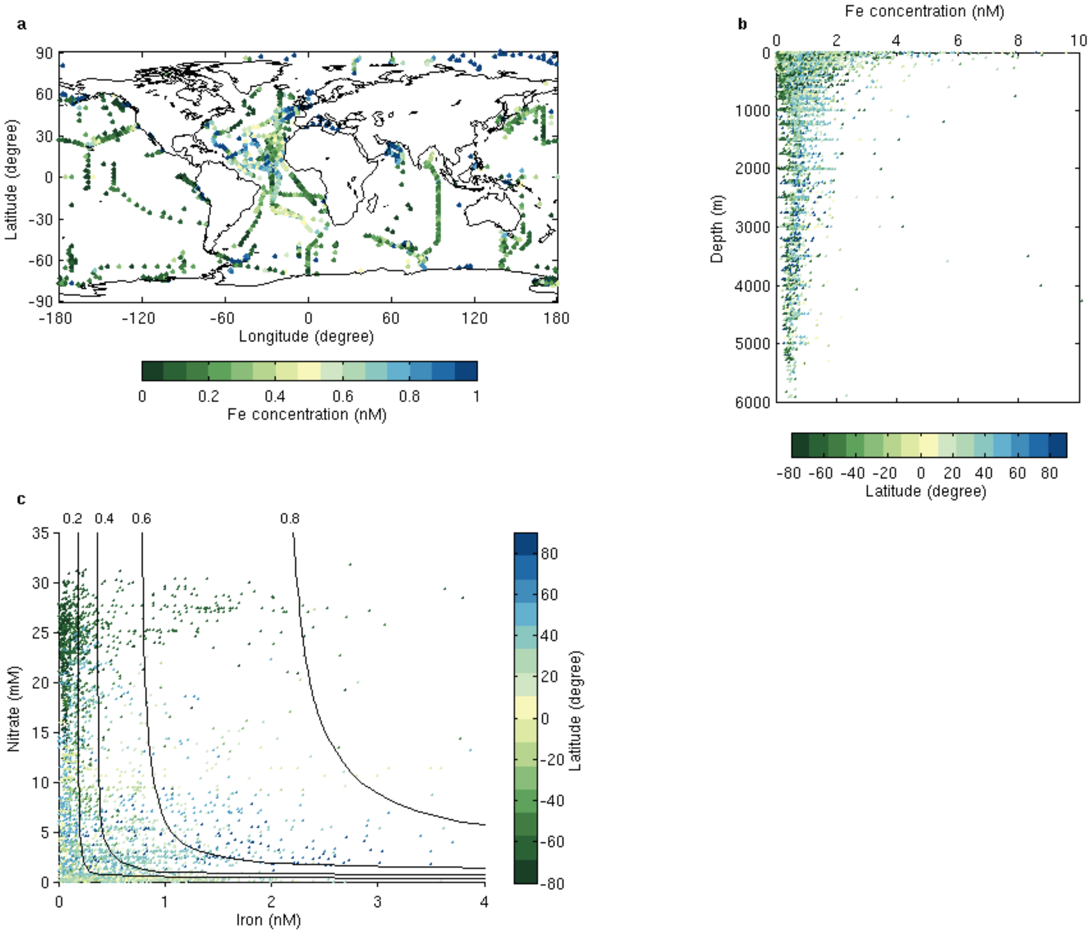

Figure 6.1: **(a)** Ocean surface 50 m iron concentrations (nM) from the hydrographic database (n = 7,378). **(b)** Iron concentrations plotted as a function of depth and latitude (n = 18,653). **(c)** Iron (nM) and nitrate (mM) concentrations in the surface 50 m as a function of latitude (all seasons and locations). Solid lines indicate contours of co-limitation strength (dimensionless values are marked: 0.2, 0.4, 0.6, 0.8). The full observed iron range (0–80nM) has been compressed in (a-c) to differentiate regions of high and low iron (98% of data occurs in the 0–1nM) range).

6.2.2 Light data

The monthly-average solar radiation dose available to phytoplankton was calculated with the Moderate Resolution Imaging Spectroradiometer (MODIS; 2003–2015) monthly sea surface solar irradiance (I_0) using

$$I = \frac{I_0}{k \cdot z_r}(1 - exp(-k \cdot z_r)), \tag{6.2}$$

where z_r is the integration depth (Equation 5.3, $z_r = 77$m), and k is the oceanic light attenuation coefficient. We use a chlorophyll-a dependent attenuation coefficient [*Lee et al.*, 2007]

$$k = \frac{34[Chl]^{-0.39}}{4.6}, \tag{6.3}$$

where $[Chl]$ is the monthly chlorophyll-a concentration from MODIS. A chlorophyll-weighted summer solar radiation dose is then calculated by averaging over the three months of local maximum irradiance (as in Chapter 5).

6.2.3 The ratio of nutrient to light limitation

To calculate the ratio of nutrient to light limitation, we scale the nutrient limitation (Equation 6.1) and light limitation (Equation 5.1) terms

$$\frac{N}{k_N + N} \cdot \frac{Fe}{k_{Fe} + Fe}, \quad \frac{\alpha I}{\sqrt{V^2 + \alpha^2 I^2}} \tag{6.4}$$

as

$$L = \frac{\dfrac{\alpha I}{\sqrt{V^2 + \alpha^2 I^2}}}{\dfrac{N}{k_N + N} \cdot \dfrac{Fe}{k_{Fe} + Fe}} \tag{6.5}$$

The cell response to nitrate (N), iron (Fe) and light (I) conditions is determined by α, the initial gradient of the photosynthesis-irradiance curve, and the half saturation coefficients k_N and k_{Fe}, for nitrate and iron uptake respectively. Constants are selected from observed values as, $\alpha = 13.125$ gC(gchl)$^{-1}$(W m^{-2})$^{-1}$d^{-1}, $k_N = 0.625$ mmolNm^{-3}, and $k_{Fe} = 0.5$ μmolFem^{-3} [*Fasham et al.*, 1990; *Parekh et al.*, 2004].

Light availability (I) is calculated as described above. Nitrate (N) and iron (Fe) concentrations are determined by the average concentration over depth 0-z_r that occurs during maximum annual local mixed layer depths. The month of maximum local mixed layer depths is determined from a mixed layer depth climatology [*de Boyer Montégut et al.*, 2004]. In Chapters 5 and 6 we will ignore the effects of temperature, which is assumed to be 10.38 degrees, such that V= 1.

Here we have an additional term $Fe/(k_{Fe} + Fe)$ in L, compared to Chapters 4 and 5 (Equations 4.22, 5.2, 5.4). This reflects co-limitation of phytoplankton by both iron and nitrate (Equation 6.1); whereas in the Arctic we only considered nitrate limitation (see [*Klunder et al.*, 2012] and the discussion below).

6.2.4 Biomes

Different oceans and regions are characterised by typical patterns in phytoplankton abundance that are persistent. Based on these persistent patterns, Longhurst *et al.* (1995) proposed to divide the ocean into regional biomes, each thought to have a characteristic seasonal cycle of phytoplankton growth, optical field and vertical nutrient transport [*Platt and Sathyendranath*, 1988; *Platt et al.*, 1995].

Here we define biomes based on ocean basin, sea surface temperature (SST) and chlorophyll-a (Figure 6.2a). SST and chlorophyll-a data are retrieved from MODIS. Biomes are constructed by averaging data spanning 2003–2015.

The ocean gyres are defined as areas where chlorophyll-a $<$0.1 mgChlm^{-3}, and divide them by hemisphere and basin into the North and South Atlantic Gyres, North and South Pacific Gyres, and Indian Gyre. The North and South Pacific Gyres are divided along the equator. In the Southern Ocean we define two biomes bounded by the Subtropical Front (SST $<$15°C) and SubAntarctic Front (SST $<$2°C). Between the Subtropical Front and 30°N, eutrophic waters (chlorophyll-a $>$0.1 mgChlm^{-3}) are combined into a Tropics zone. North of this Tropics zone ($>$30°N), the North Atlantic and North Pacific basins are divided (and incorporate their marginal seas). We remove the ice-covered high latitude oceans which have no satellite coverage. Because of limited ^{14}C production measurements in the Indian Gyre we combine the South Pacific and Indian Gyre.

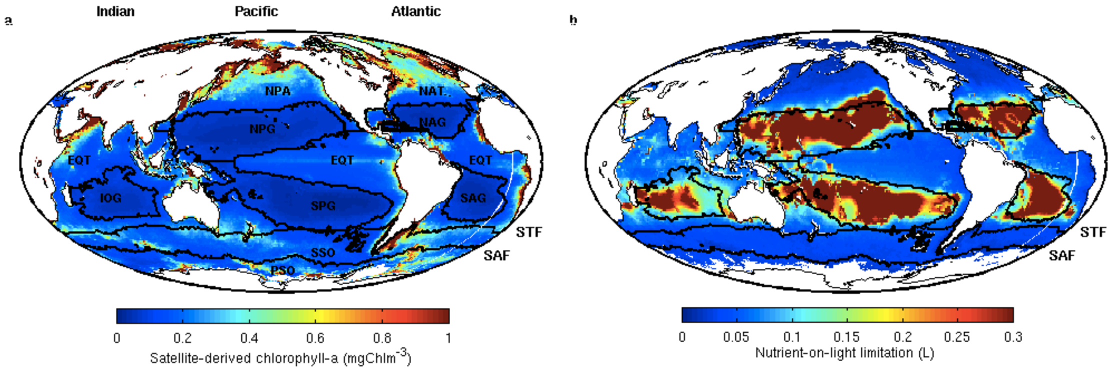

Figure 6.2: **(a)** Ocean biomes (black line) and satellite chlorophyll concentrations (mgChl m^{-3}). Note the tropics (EQT) biome spans all three basins. **(b)** Global map of the ratio of nutrient limitation to light limitation. Black lines: biomes. PSO: Polar Southern Ocean. SSO: Subpolar Southern Ocean. NPA: North Pacific. NAT: North Atlantic. EQT: Tropics Eutrophic Zone. NAG: North Atlantic Gyre. SAG: South Atlantic Gyre. SPG: South Pacific Gyre. NPG: North Pacific Gyre. IOG: Indian Gyre. STF: Subtropical Front. SAF: SubAntarctic Front.

6.2.5 Phytoplankton production data

Phytoplankton production rates are available from in situ ^{14}C radioisotope measurements and satellite algorithms. The ^{14}C in situ database contains 50,050 phytoplankton production data points, with coverage of all major ocean basins [*Buitenhuis et al.*, 2013]. Satellite-based phytoplankton production is calculated using the Vertically Generalised Production Model (VGPM). The VGPM algorithm calculates phytoplankton production as a function of monthly satellite SST, chlorophyll-a, PAR and daylength [*Behrenfeld and Falkowski*, 1997]. Here we use MODIS for consistency.

The vertical shape of production profiles is determined from ^{14}C measurements using the method of Ardyna *et al.* (2013). We extracted 1994 unique profiles from the ^{14}C database. A rigorous quality control was applied to each profile, according to the following three criteria: (1) the uppermost sample had to be collected between the surface and a depth of 10 m; (2) the lowermost sample of the profile had to be collected at a depth of at least 60 m; (3) a minimum of four discrete sampling depths were required. This resulted in 1037 useable profiles.

Next, we visually inspected each profile to check that the vertical sampling resolution was adequate to catch important features such as the depth of maximum production. This resulted in 766 useable profiles.

Each profile was then linearly interpolated at a resolution of 1m and normalised by the average production rate over the profile (Figure 6.3). To determine means from a set of profiles, each profile was weighted equally before averaging across the set. Practically, this ensures that the shape of each profile carries equal weight in determining the shape of the set-average Gaussian distribution. We then fitted Gaussian distributions to each normalised profile according to

$$P(z) = P_{\max} e^{-\left[\left(\frac{z - z_{\max}}{\Delta z}\right)^2\right]}, \tag{6.6}$$

where $P(z)$ is the normalised production rate at depth z. The parameters of the Gaussian distribution are the normalised maximum production rate $P_{\max}$, occurring at depth $z_{\max}$, and with a thickness determined by Δz.

Every Gaussian fit (Equation 6.6) was visually inspected against the in situ data to determine that the fit was adequate; simple correlation statistics for each surface production class illustrate that this is the case (Figure 6.3b). Note that the Gaussian fit improves with the sample size. Based on the visual inspection step, this is likely because in smaller sample sizes a few weaker fits skew the average.

The profiles were sorted into bins according to the surface production rate, using the intervals 0–0.5, 0.5–1, 1–4, and >4 $\mathrm{gCm^{-2}d^{-1}}$. The fraction of production that occurs between z_r and the base of the water column (z_b) was also computed for all profiles

$$\frac{P_2}{P} = \frac{\int_{z_r}^{z_b} P dz}{\int_0^{z_b} P dz}. \tag{6.7}$$

6.3 Numerical model performance

We use the numerical model in concert with observations to look at nutrient and light controls on production. Therefore, we first need to check that the model

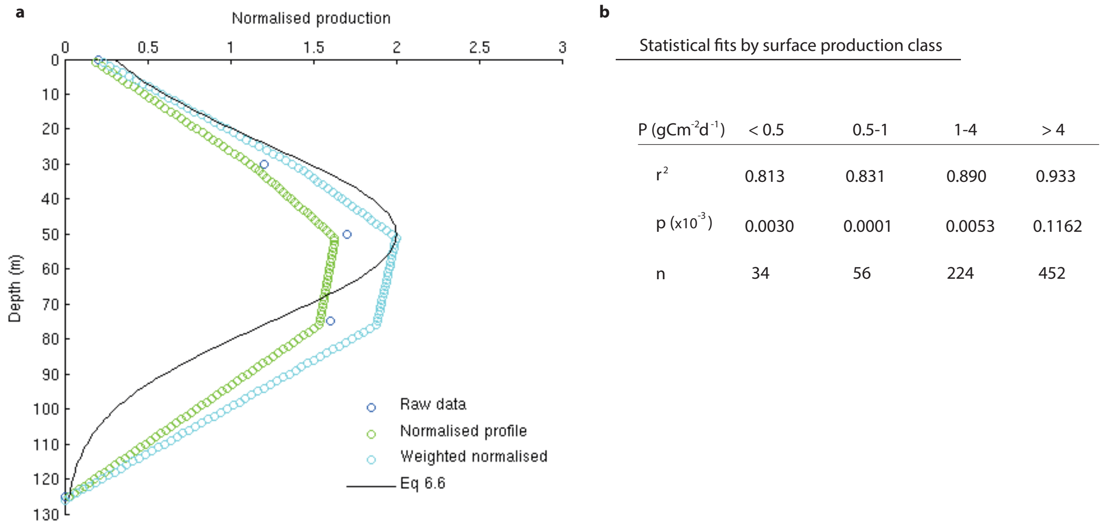

Statistical fits by surface production class

P ($gCm^{-2}d^{-1}$)	< 0.5	0.5-1	1-4	> 4
r^2	0.813	0.831	0.890	0.933
p ($\times 10^{-3}$)	0.0030	0.0001	0.0053	0.1162
n	34	56	224	452

Figure 6.3: **(a)** An example of fitting an in situ profile to Equation 6.6. The fitting method is described in the text. **(b)** Average statistical fits between the normalised in situ data and Equation 6.6 for each surface production class.

provides a realistic representation of observations. Light and nitrate observations are available from the WOA and satellite data [*Bishop and Rossow*, 1991; *Garcia et al.*, 2014]. Depth-integrated production is compared to satellite estimates [*Behrenfeld and Falkowski*, 1997]. The vertical phytoplankton structure is compared using chlorophyll-a observations [*Conkright et al.*, 2002], which provide much better coverage than ^{14}C production measurements. We also test model patterns of limitation by iron and nitrate.

6.3.1 Productivity and its vertical distribution

The model captures the main areas of elevated depth-integrated production discussed above (northern mid-latitudes, equatorial and western boundary upwellings, and along the Southern Ocean Subpolar Front, Figure 6.4a-b). However, Equatorial Pacific Ocean production is over-estimated and North Atlantic Ocean production is under-estimated. Production along the Southern Ocean Subpolar Front is also over-estimated. Higher resolution features, such as Southern Ocean patchiness, hotspots off northern Australia, and a high fidelity North Atlantic drift, are also absent in the model. Model production is lower than satellite estimates around continental margins in the North Pacific Ocean and Arctic Ocean, but satellites

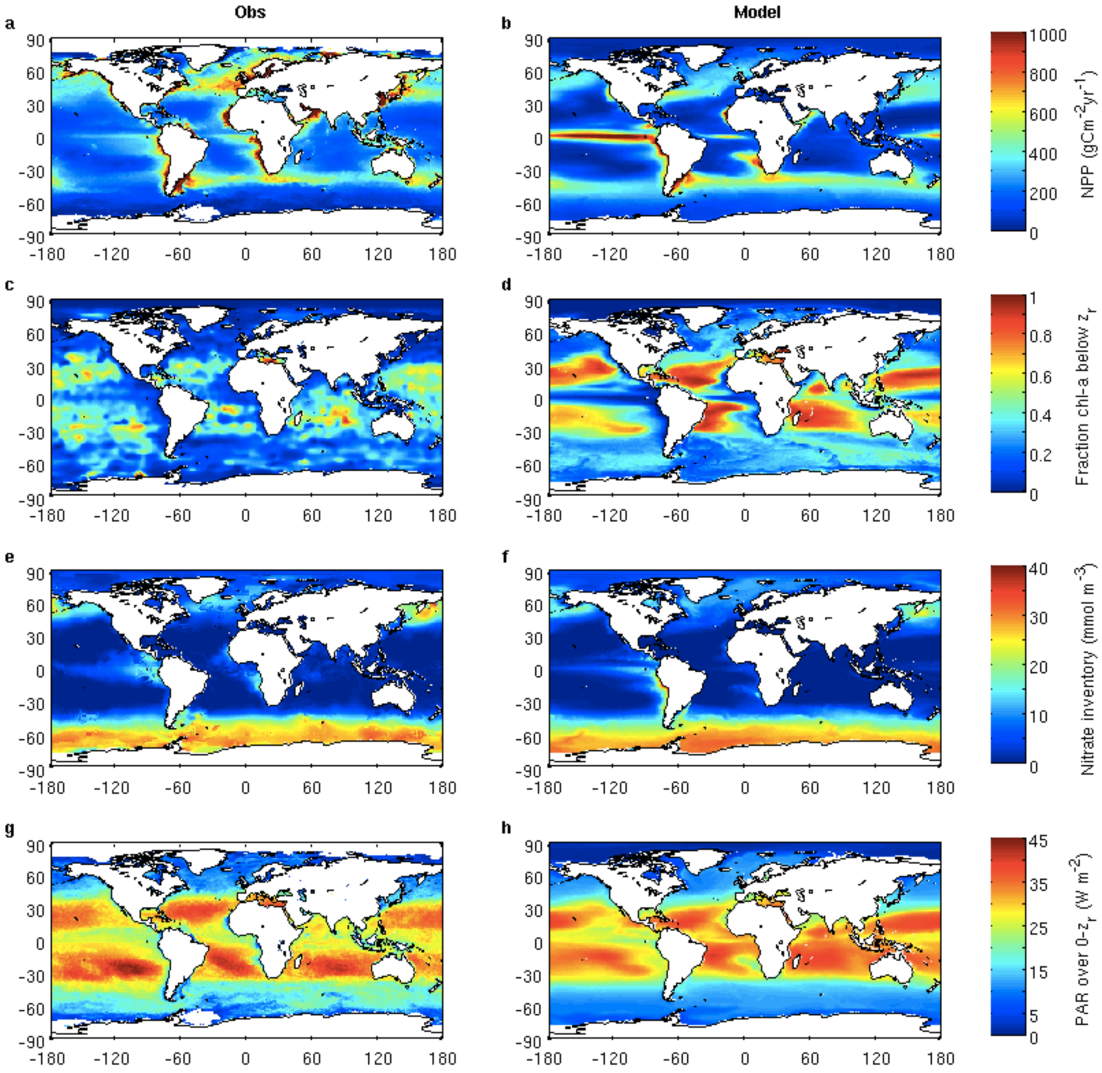

Figure 6.4: **(a)** Global map of satellite-derived (VGPM) annual net primary production (gC m^{-2} yr) [*Behrenfeld and Falkowski*, 1997]. **(b)** Numerical model annual net primary production. **(c)** Observed annual fraction chlorophyll-a below z_r [*Conkright et al.*, 2002]. **(d)** Model annual fraction chlorophyll-a below z_r. **(e)** Observed nitrate inventory (mmolm^{-3}) [*Garcia et al.*, 2014]. **(f)** Model nitrate inventory. **(g)** Satellite-derived (MODIS) PAR integrated over depth 0–z_r [*Bishop and Rossow*, 1991] **(h)** Model PAR integrated over 0–z_r ($z_r = 77$ m).

may over-estimate production here due to non-chlorophyll reflectance [*Matsuoka et al.*, 2007].

Observed deeply distributed phytoplankton in the subtropical gyres is reproduced by the model (Figure 6.4c-d). But values in the simulation are generally more extreme and more homogeneous. Patches of deep phytoplankton chlorophyll-a in the Southern Ocean are not captured by the model.

6.3.2 Nitrate inventory and photosynthetic light

The nitrate inventory is calculated for each degree box as the mean nitrate concentration between 0–z_r, at the time of local annual maximum mixed layer depth. Observed nitrate inventories are calculated using the World Ocean Atlas (2013) nitrate climatology [*Garcia et al.*, 2014] and a mixed layer climatology [*de Boyer Montégut et al.*, 2004]. The model captures areas of high nitrate supply in the sub-Arctic (Figure 6.4e-f). Nitrate inventory is replicated across the western boundaries but is under-estimated in the Benguela Upwelling (South Atlantic) and over-estimated in the Peru Upwelling (South Pacific). Southern Ocean excess nitrate is replicated by the model, but observed patchiness is not captured by the model.

Photosynthetic light is calculated using Equation 6.2 and is mapped in Figure 6.4g. Light penetrates deepest in the observed and modelled subtropical gyres (Figure 6.4g-h). But the model does not capture distinctions between gyres, such as the clearest waters in the South Pacific Gyre [*Morel et al.*, 2007], or latitudinal light increases from North to South across the Atlantic and Pacific Gyres [*Dutkiewicz et al.*, 2015]. The model does capture broad latitudinal gradients in light, but underestimates zonal heterogeneity.

6.3.3 Nitrate and iron limitation

To determine whether nitrate or iron limits phytoplankton growth more strongly we take the model nitrate and iron concentrations at their respective local annual minima and compare to the limitation status diagnosed from enrichment experiments (Figure 6.5). Nitrate limitation dominates in the tropical Atlantic and Indian Oceans where atmospheric iron supply is high [*Jickells et al.*, 2005] and oceanic nitrate supply is low (Figure 6.4e). Nitrate also limits in the subtropical Pacific where oceanic nitrate supply is low and iron is supplied from hydrothermal and dust sources [*Resing et al.*, 2015]. In the Equatorial Pacific, Southern Ocean, and sub-Arctic, iron limitation dominates [*Martin and Fitzwater*, 1988; *Kolber et al.*, 1994; *Behrenfeld et al.*, 1996]; regions where, generally, nitrate supply is large (Figure 6.4e), and dust deposition is low [*Jickells et al.*, 2005]. Iron limitation may be

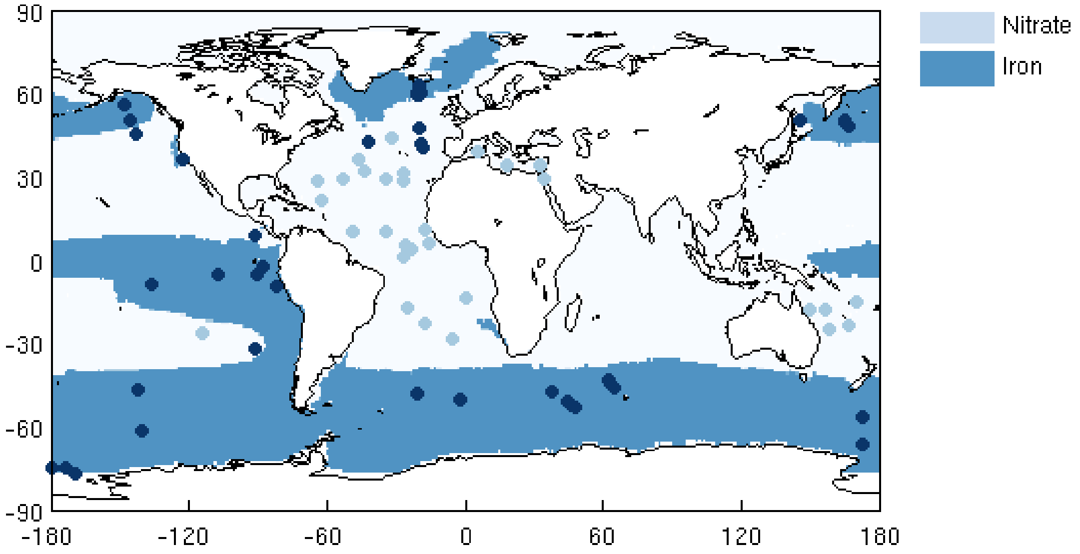

Figure 6.5: Phytoplankton nitrate (light blue) and iron (dark blue) limitation as diagnosed from the model and as determined by enrichment experiments (dots) [*Moore et al.*, 2013]. Note that the extent of iron limitation is most under-constrained by observations in the Indian and Pacific sectors (Figure 6.5).

alleviated locally in these regions by other iron supply mechanisms such as hydrothermal supply [*Tagliabue et al.*, 2010], and iron remobilisation in sediments along continental and island margins [*Planquette et al.*, 2007; *Lam and Bishop*, 2008].

6.3.4 Production and nutrient to light limitation ratios

Phytoplankton nutrient and light limitations are increasing functions of ambient conditions, so they broadly follow the same global patterns (Figure 6.4, 6.6). Strikingly, nutrient and light limitations are the inverse of each other. This arises because low light limitation entails adequate light for phytoplankton to strip supplied nutrients from the surface. Where light is adequate for phytoplankton uptake to keep surface nutrient concentrations near zero, phytoplankton growth must occur at depths where nutrients are available, and a high fraction of growth happens at or below depth z_r. This suggests that a high nutrient limitation to light limitation ratio entails a high fraction of production at depth (this is checked below by scaling nutrient limitation to light limitation and plotting it against the fraction of

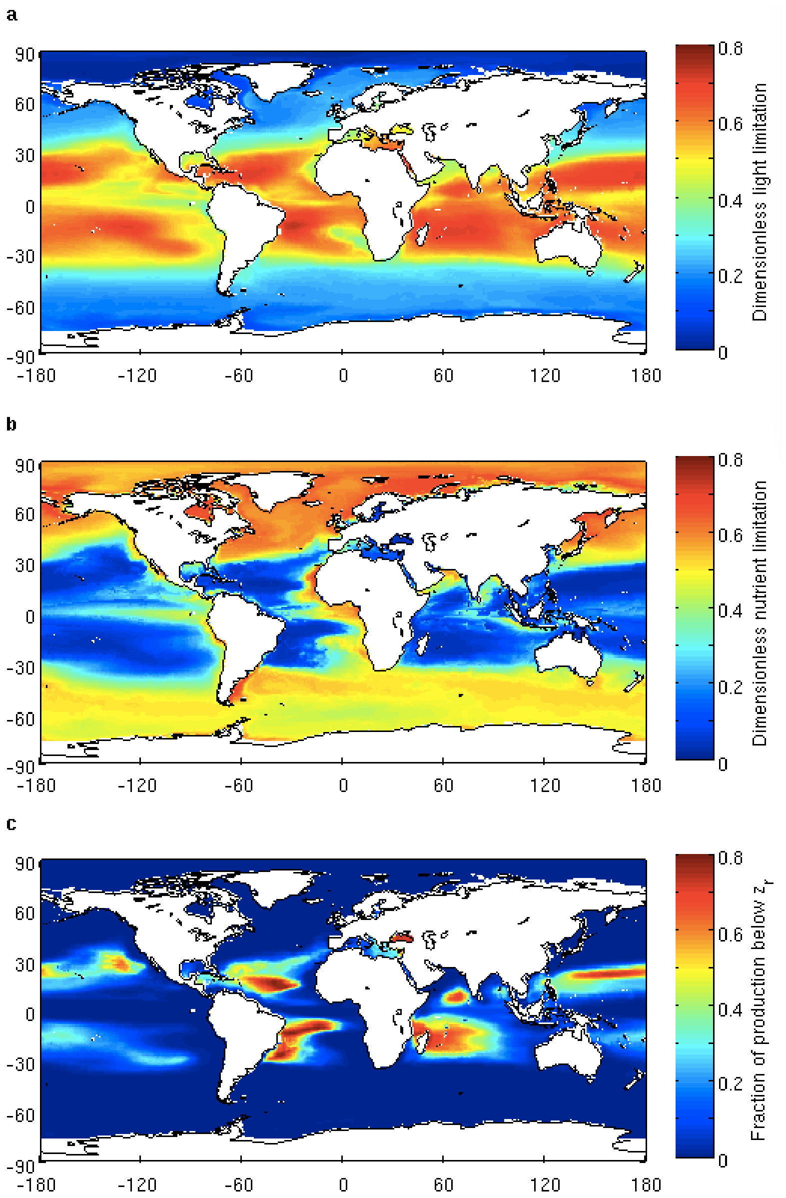

Figure 6.6: **(a)** Model light limitation over the surface layer 0–z_r (Equation 6.1). **(b)** Model nutrient limitation over 0–z_r (Equation 5.1). **(c)** Model fraction of annual production below z_r. Light and nutrient limitation are the inverse, reflecting plankton ability to strip the surface waters of nutrients.

production below z_r).

6.3.5 Nitrate, silicate and chlorophyll-a transects

We also provide model nitrate, silicate and chlorophyll-a transects. In the subpolar North Pacific and North Atlantic, high nitrate and silicate concentrations

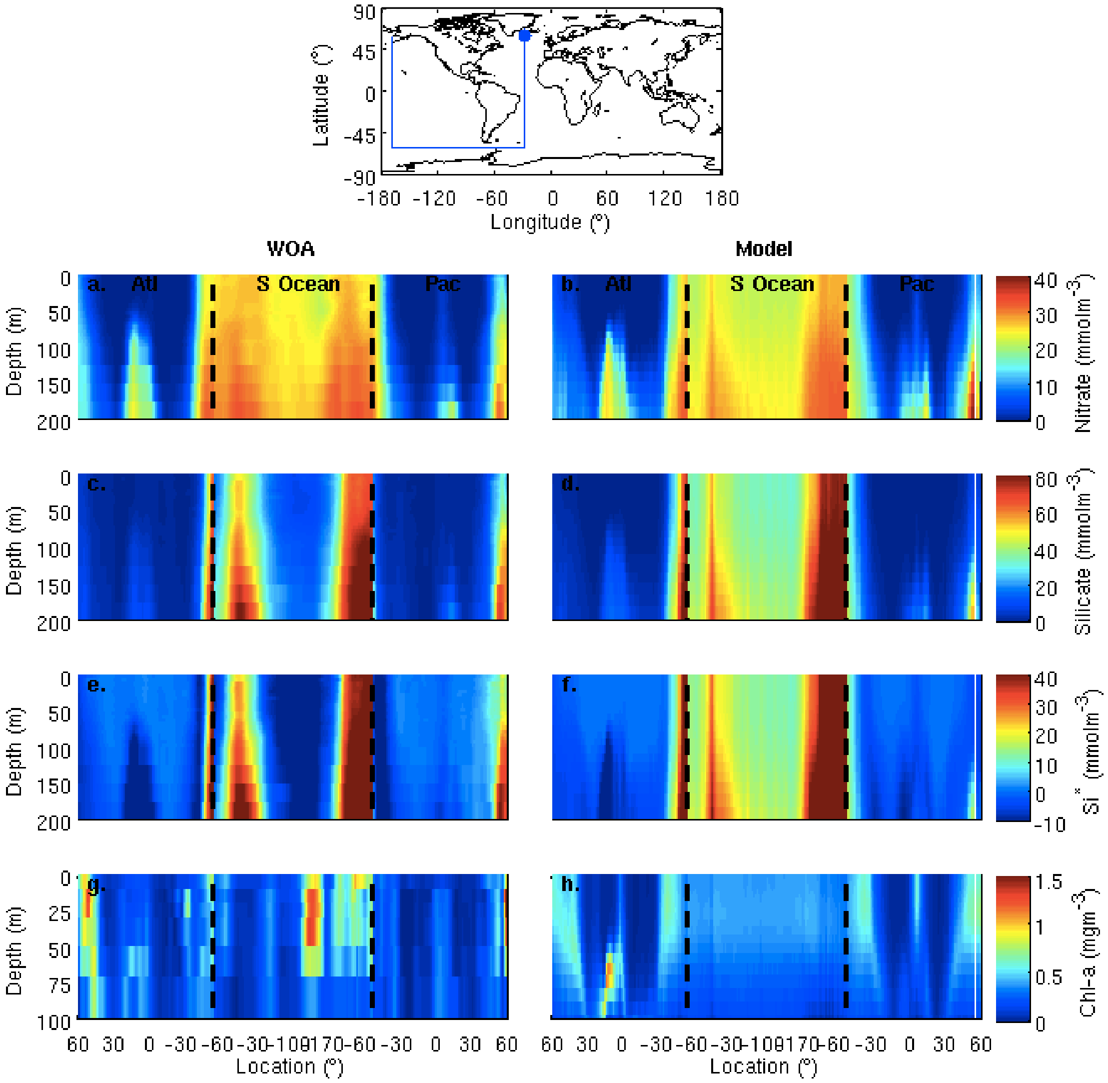

Figure 6.7: Atlantic-Southern Ocean-Pacific upper ocean transects for **(a-b)** nitrate **(c-d)** silicate **(e-f)** Si* and **(g-h)** chlorophyll-a. Data are from the World Ocean Atlas (left) [*Conkright et al.*, 2002; *Garcia et al.*, 2014] and numerical model (right). The transect line is given in the top panel, starting at the dot. Dotted lines (a-h) indicate the three sections of the transect. Atlantic: 60°N–60°S, 25°W; Southern Ocean: 60°S, 30–170°W; Pacific: 60°S–60°N, 170°W. Note (g-h) have a different depth scale.

are found at the surface (Figure 6.7 a,c). In the subtropics elevated concentrations are restricted to depth (>200 m). Near the equator, high nutrients occur nearer the surface (∼50 m). These meridional patterns are captured by the simulation (Figure 6.7 b,d). Subsurface waters (200 m) have higher nutrients in the North Pacific than the North Atlantic (Figure 6.7 a,c). The model captures higher nitrate and silicate in the sub-Arctic Pacific than the sub-Arctic Atlantic (Figure 6.7 b,d).

But it over-estimates nitrate and under-estimates silicate. Why it does this is not clear as the model diatom variables relevant to Si:N ratios were not saved when the model was run. (North Pacific Intermediate Waters (NPIW) are thought to have have higher Si concentrations than anywhere else outside the Southern Ocean because thermocline waters elsewhere are thought to be supplied by subduction and spreading of SAMW, which has low Si concentrations at formation [*Sarmiento et al.*, 2004a]; iron cycle model variables that control Si at formation were not saved, discussed below.)

We can define $Si^* = Si(OH)_4 - NO_3$ to look at the relationship between silicic acid and nitrate. Si^* is positive in regions where silicic acid is in excess of nitrate, and Si^* will be negative where nitrate is in excess. The major phytoplankton group that utilises silicic acid is diatoms, where it is used for the cell wall [*Sarmiento and Gruber*, 2006]. Diatoms growing under healthy ambient conditions are observed to take nitrate and silicic acid up in the ratio 1:1 [*Brzezinski*, 1985]. Therefore, positive Si^* will result in excess ocean silicate under healthy growth, and negative Si^* will result in excess ocean nitrate. However, in low-iron conditions diatoms increase their Si:N ratio, and ocean silicate is more rapidly depleted.

Nutrients decrease northwards across the Antarctic Polar Front (APF), with a more pronounced decrease in silicate than nitrate (Figure 6.7 a,c). A clear band of negative Si^* therefore arises around the Southern Ocean in SubAntarctic Mode Water (SAMW, ∼40-60°S). This band is thought to arise from export of high Si:N diatoms out of SAMW, which depletes SAMW of silicic acid (attributed to low iron availability [*Brzezinski et al.*, 2003]). The northward decrease in nutrients across the APF occurs in the simulation (Figure 6.7 b,d). But negative Si^* values do not occur in simulated SAMW (Figure 6.7f), probably because, whilst the model permits flexible Si:N ratios, these are not tied in any way to low iron concentrations [*Yool et al.*, 2013, 2015].

Chlorophyll-a is low in the subpolar gyres and elevated in subpolar regions and at depth in the equatorial regions, generally reflecting the macro-nutrients described above (Figure 6.7g). Depths of elevated chlorophyll are similar between model and observations in the Atlantic and Pacific (Figure 6.7h). However, patterns differ

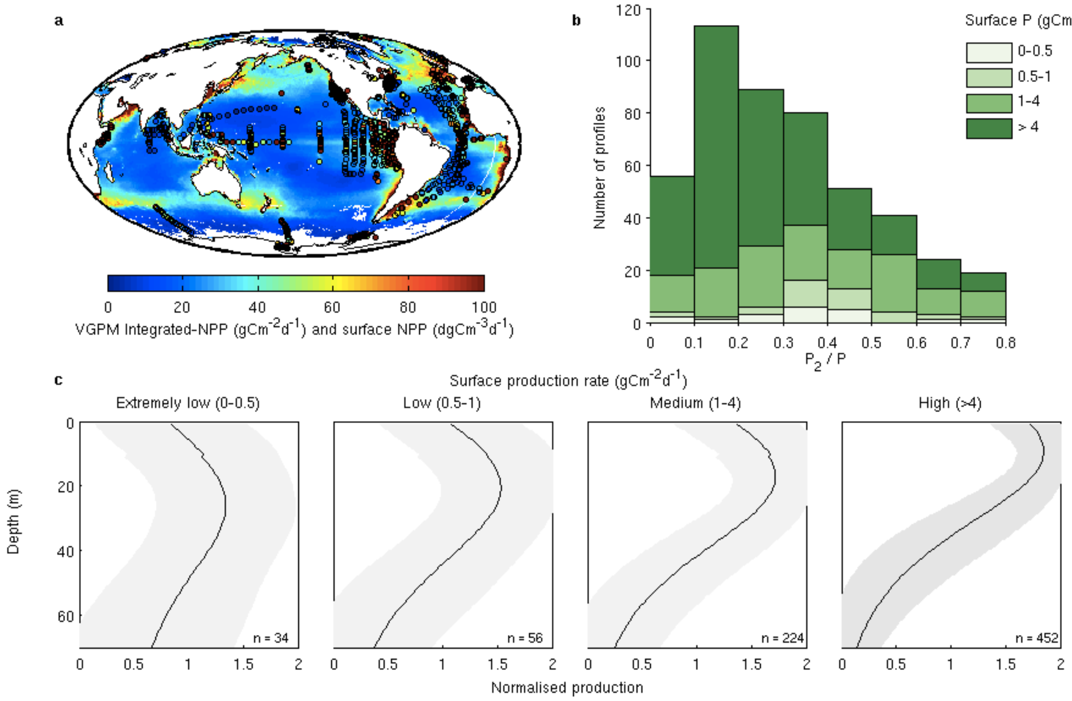

Figure 6.8: **(a)** Satellite-estimated (VGPM) annual depth-integrated phytoplankton production (gC m^{-2} d^{-1}) and in situ ^{14}C observations of surface (0-10m) production rates (dgC m^{-3} d^{-1}; circles; n = 810). **(b)** Frequency distribution of in situ vertical production structure (P_2/P), sorted by surface production rate. **(c)** Normalised production profiles for each surface production rate class (grey shading ±1S.D.).

in the Southern Ocean. Chlorophyll is low in the simulated and observed HNLC Southern Ocean because of iron limitation. But observed chlorophyll increases at the west (right) of the Southern Ocean transect, corresponding to reductions in surface nitrate concentrations (Figure 6.7 a,g), suggesting biological uptake may be depleting nitrate here. This zonal aymmetry in chlorophyll-a the Southern Ocean does not occur in the model (Figure 6.7 h). Again failure to save the relevant model variables precludes competent assessment of Southern Ocean discrepancies.

6.4 Results

6.4.1 Phytoplankton productivity distributions

The vertical structure of production varies systematically with the surface production rate, P_0. At low P_0, the depth of maximum production is high and production depth gradients are weak (Figure 6.8c). For increasing P_0 the depth of maximum production tends towards the surface and depth gradients are larger. A pattern of more production at depth with lower P_0 is also reflected in the fraction of annual production at depth (P_2/P). Phytoplankton profiles with lower fractions of annual production at depth (P_2/P) occur more frequently in the class of high surface production rates (P_0 >4 gCm^{-2}d^{-1}; Figure 6.8b).

This negative relationship between P_0 and P_2/P is explicable in terms of nutrient and light conditions. In nutrient-replete conditions surface productivity (P_0) is high. Light decreases exponentially with depth, so most growth occurs at the surface and P_2/P is low. High P_2/P is achieved when nutrient supply is inadequate to sustain surface production (low P_0) and phytoplankton must grow at depth.

At low P_0 the relationship is less clear (Figure 6.8b). Low P_0 is expected to give high P_2/P; but at low light (low P_0), inadequate light at depth may prevent production at depth (low P_2/P). Low P_0 can therefore entail either low or high P_2/P depending on whether light or nutrients limit. These two separate dependencies can be disentangled by scaling the ratio of nutrient to light limitation (L). Then both high light and low nutrients (increasing L) act to increase P_2/P.

6.4.2 Productivity and nutrient to light limitation ratios

Patterns of the ratio of nutrient to light limitation indicate clear oligotrophic light-replete regions (high L) and eutrophic light-deplete regions (low L), which correspond to the biomes (Figure 6.2b). In the subtropical gyres L and biome-average P_2/P (0.21–0.32) are high. In the more eutrophic biomes (Tropics, North Atlantic, North Pacific), the ratio of nutrient to light limitation (L) is lower and P_2/P (0.17–0.25) is intermediate. In the Southern Ocean biomes low light (low L)

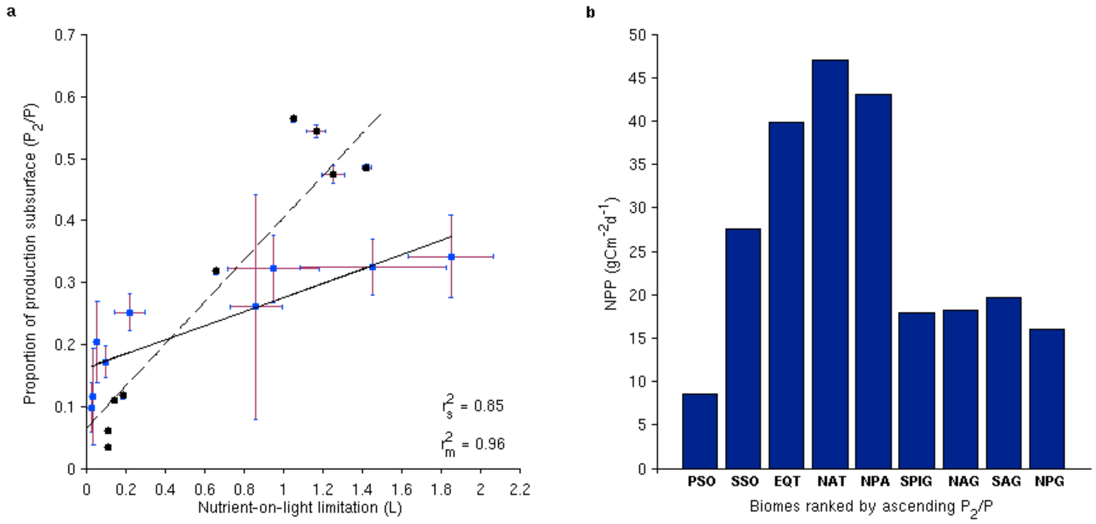

Figure 6.9: **(a)** Observed proportion of production subsurface (P_2/P) versus the ratio of nutrient to light limitation (L) for each biome (blue). Linear best-fit (solid): $P_2/P = 0.134L + 0.156$ ($r_s^2 = 0.85, p < 0.01$). Model P_2/P vs L (black). Linear best-fit (dashed): $P_2/P = 0.384L + 0.04$ ($r_m^2 = 0.96, p < 0.01$). Error bars are 95% confidence intervals. The Indian and South Pacific Gyres are combined due to scarce data. **(b)** VGPM depth-integrated primary production (NPP) for each biome, sorted by ascending P_2/P. Biome abbreviations are given in Figure 6.2. SPIG: combined South Pacific and Indian Gyres.

restricts growth to near the surface and P_2/P is low (0.098–0.12).

Phytoplankton depth distributions thus increase with the ratio of nutrient to light limitation (Figure 6.9). Nutrient depletion (high L) at the surface requires phytoplankton to grow at depth (high P_2/P); and light replete conditions (high L) also entail a higher fraction of growth at depth (P_2/P), by alleviating limitation at depth. By scaling the ratio of nutrient to light limitation we can distinguish between low P_0 that arise because of low nutrients (high P_2/P, e.g. subtropical gyres) and low light (low P_2/P, e.g. North Atlantic). Low nutrients act to pull production towards depth, whereas low light acts to pull production towards the surface.

Plotting biome-average depth-integrated production against its vertical structure indicates that depth-integrated production is maximum at intermediate P_2/P values, and decreases as P_2/P decreases or increases (Figure 6.9b). Maximum production rates occur in mid-latitudes and tropical upwellings, where both nutrients and light are replete and P_2/P is intermediate. In the oligotrophic gyres, nutrients

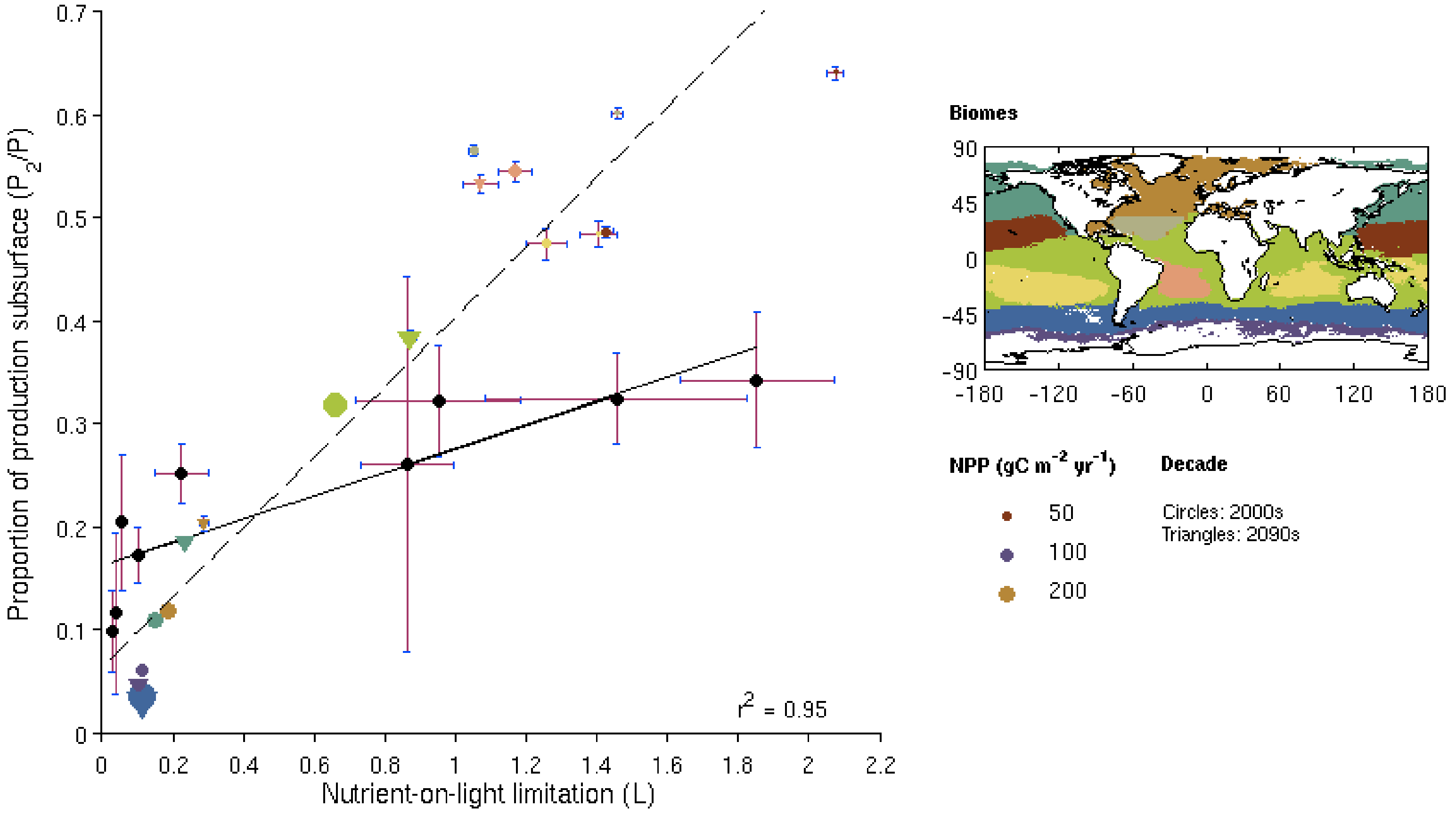

Figure 6.10: Biome-average proportion of production subsurface (P_2/P) versus the ratio of nutrient to light limitation (L) for observations (black), model 2000s (circles) and model 2090s (triangles). Model points are coloured by biomes and the size is scaled by biome-average productivity (gCm^{-2}d^{-1}). The combined model linear regression (dashed) is $P_2/P = 0.402L + 0.121 (r^2 = 0.95, p < 0.01)$. Error bars are 95% confidence intervals. Purple: Polar Southern Ocean. Blue: Subpolar Southern Ocean. Dark Green: North Pacific. Light Brown: North Atlantic. Light Green: Tropics. Grey: North Atlantic Gyre. Pink: South Atlantic Gyre. Dark Brown: North Pacific Gyre. Yellow: South Pacific and Indian Gyres. Model NPP values are also plotted in Figure 6.12.

limit surface production (high P_2/P) and depth-integrated production is low. At high latitudes, inadequate light at depth limits production at depth (low P_2/P) and depth-integrated production is low. (Note these are the same dependencies plotted for the Arctic Ocean in Chapter 5.)

The lower slope in observations than the model seems to arise because observations do not reach high enough P_2/P values at high L (Figure 6.9). This is likely because vertical data sampling was not good enough in columns where production was very deep (which require several measurements below 70 m depth). This resulted in several of these columns not passing basic quality control and others under-estimating the fraction of production at depth (P_2/P).

6.4.3 Invariance and depth-integrated productivity in a future ocean

The relationship between phytoplankton production and the ratio of nutrient to light limitation also occurs in the numerical model (Figure 6.9). Model limitation and vertical productivity patterns across biomes also agree with observations (Figure 6.10). Model P_2/P and L are high in the gyres (L = 1.1-1.4), intermediate in the eutrophic tropics (L = 0.7), and low at mid-high latitudes (L = 0.1-0.2). Model depth-integrated production is low in the gyres (nutrients limit) and at high latitudes (light limits), and high in the eutrophic tropics. The exception to this trend is the Subpolar Southern Ocean biome (Figure 6.10), where the model is over-estimating productivity (compare to observations in Figure 6.9b). Accurate model productivity in this biome (i.e. in agreement with observations) would bring it back into the trend.

Plotting the model 2000s and 2090s together (Figure 6.10) indicates that the relationship between production and the ratio of nutrient to light limitation also occurs at end century (combined $r^2 = 0.95, p < 0.01$). Most biomes show slight increases in L and thus P_2/P over the coming century (Figure 6.10). A warming ocean is expected to strengthen stratification and reduce nutrient supply to the surface, reducing depth-integrated production [*Behrenfeld et al.*, 2006]. But, as pointed out by Lozier *et al.* (2011), physical nutrient supply depends not just on

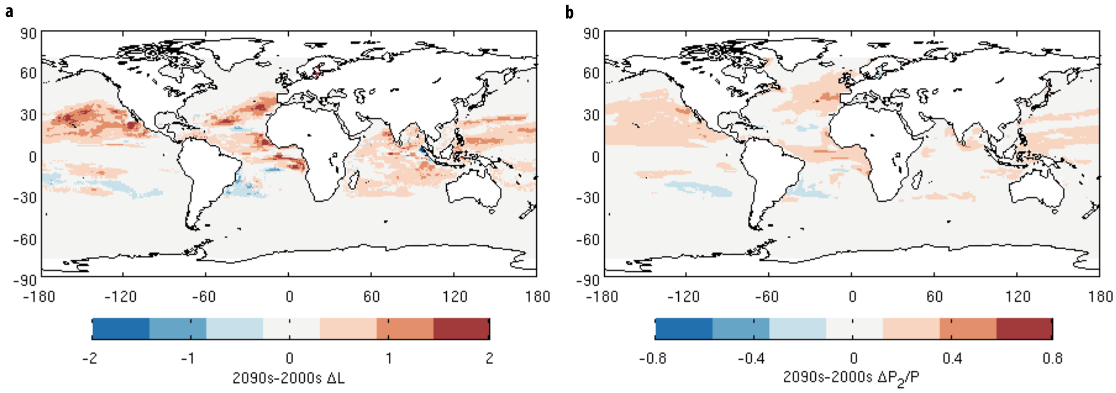

Figure 6.11: Model 21st century (2090-2000s) change in **(a)** L and **(b)** P_2/P.

stratification, but also on the energy available to mix the water column and advective supply. In the numerical model here, warming of the ocean increases the ratio of nutrient to light limitation (L) across the tropics and North Atlantic Ocean (Figure 6.11a). Stronger nutrient limitation requires that local phytoplankton growth horizons deepen to sustain growth, and P_2/P increases in these same locations (Figure 6.11b). At depth light availability is reduced, so with higher model P_2/P we can expect depth-integrated production to decrease. Plotting model depth-integrated production against the fraction that occurs at depth shows this decrease (Figure 6.12). Model depth-integrated production decreases -19% in the North Atlantic Ocean and -9% in the tropics biome, driving most of the global-average decrease of -4% in the simulated coming century (Figure 6.12). Reductions are also large in the North Atlantic Gyre (-22%), and North Pacific Gyre (-25%), but changes in the gyres have a small effect on global production because current gyre productivity is a small share of total global production (Figure 6.12).

6.5 Discussion

To move from the Arctic Ocean in the last chapter to the global ocean in this one we have made two adjustments. First, the turning point z_r is deeper in the global ocean (77 m). This indicates that the global average depth at which light limitation starts to dominate over nutrient limitation is deeper than the Arctic Ocean average (Equation 5.3). It likely reflects the attenuation of light by widespread perennial sea-ice cover in the Arctic Ocean, and the lower ocean irradiance this entails (e.g. [*Frey et al.*, 2011]). Second, we considered both nitrate and iron limitation at the global scale, where we only considered nitrate limitation in the Arctic Ocean [*Codispoti et al.*, 2013; *Tagliabue et al.*, 2017]. This means that we expressed phytoplankton nutrient limitation in the Arctic Ocean as $Q = N/(k_N + N)$, and global ocean limitation as $Q = (N/(k_N + N)) \cdot (Fe/(k_{Fe} + Fe))$. By considering these two changes it can be seen that we have used the same relationship in this chapter as in the last chapter for the Arctic Ocean

$$\frac{P_2}{P} \sim \frac{\dfrac{\alpha I}{\sqrt{V^2 + \alpha^2 I^2}}}{\dfrac{N}{k_N + N} \cdot \dfrac{Fe}{k_{Fe} + Fe}} = L \tag{6.8}$$

where $Fe/(k_{Fe} + Fe) \sim 1$ in the Arctic (Equation 5.4).

6.5.1 Temperature dependence of photosynthetic rates

Photosynthetic rates measured in the laboratory have been inferred to show that temperature directly increases growth within a tolerable temperature range and under optimal resource conditions (Figure 2.7). Higher sea surface temperatures have also been inferred to inhibit growth by stratifying the upper water column and preventing physical nutrient supply [*Behrenfeld et al.*, 2006]. Large scale patterns of phytoplankton growth have thus been hypothesised to depend on ocean temperatures [*Regaudie-de Gioux and Duarte*, 2012].

Indirect effects that change nutrient supply are accounted for in the Michaelis-Menten nutrient limitation term. In the direct case, growth rates may vary with temperature according to its effect on the rate of metabolic processes within the cell. Regaudie-de-Gioux and Duarte (2012) concluded that ocean phytoplankton growth rates have a strong temperature dependence. However, Maranon *et al.* (2014) note that the relationship between phytoplankton and temperature that Regaudie-de-Gioux and Duarte find arises because results were pooled for the entire euphotic zone. Thus, they argue, irradiance is introduced into the analysis as a covarying factor and samples that are from low light conditions near the base

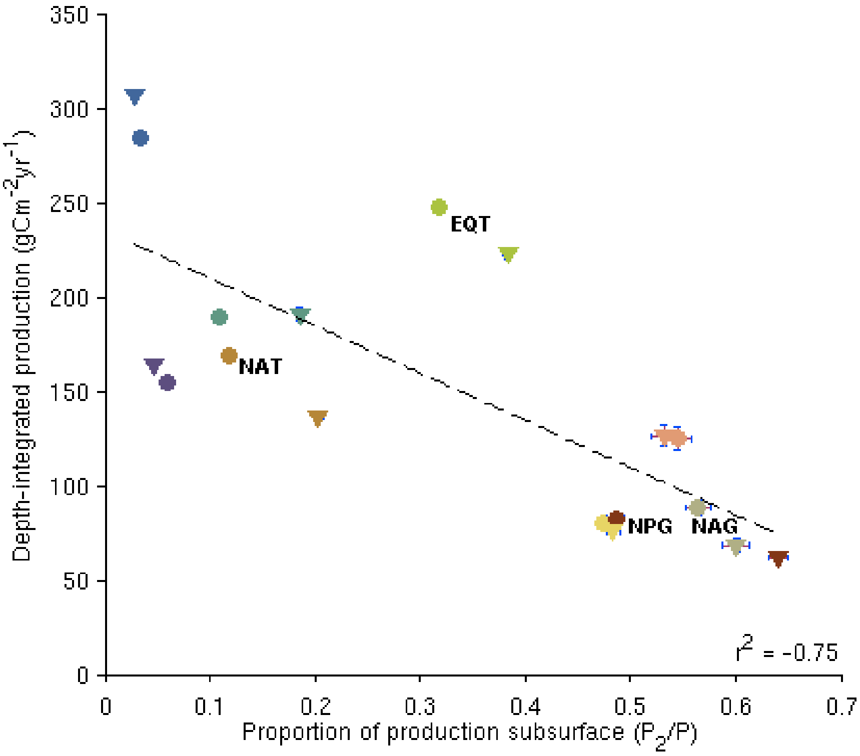

Figure 6.12: Model biome-average 21st century change in P_2/P and depth-integrated productivity, between 2000s (circles) and 2090s (triangles) ($r^2 = 0.75, p < 0.01$). Biomes are indicated by colours as in Figure 6.10. Error bars are 95% confidence intervals (where they are not visible they are smaller than the symbol). NAT: North Atlantic. EQT: Tropics Eutrophic Zone. NAG: North Atlantic Gyre. NPG: North Pacific Gyre.

of the euphotic zone, where temperatures are lower, will necessarily show lower growth rates because of the light dependence. The data provided in Maranon *et al.* (2014) suggest instead that resource supply overrides temperature effects on ocean phytoplankton growth, and they do not find a correlation between higher ocean temperatures and increased phytoplankton growth. [1]

6.5.2 Future ocean productivity and genetic changes

Despite unprecedented rates of environmental change, our results suggest that ocean productivity changes will be small (<10%). Several other studies agree that significant changes in Earth's climate do not necessarily entail large changes

---

[1] It may be that the value of V is important during transient periods where biomass is increasing (such as blooms), but less important during steady-state conditions.

in ocean productivity [*Steinacher et al.*, 2010; *Bopp et al.*, 2013; *Dutkiewicz et al.*, 2013]. Yet, a small productivity change under unprecedented environmental change is perhaps surprising when phytoplankton have been suggested to depend fundamentally on their turbulent environment [*Margalef*, 1978].

Here, we have demonstrated that nutrient and light supply may counteract one another. Low nitrate acts to pull production towards depth, and low light acts to pull production towards the surface; mitigating depth-integrated production changes. We also indicated (in the Arctic Ocean, Figure 4.6) that larger local changes in productivity, may be offset elsewhere in the ocean.

Further, different phytoplankton ecotypes are adversely affected when environmental conditions are unsuitable [*Follows et al.*, 2007; *Thomas et al.*, 2012]. Ambient conditions that cause one ecotype to suffer may favour another more competitive ecotype. The community structure may thus undergo large changes with environment, whilst total productivity is maintained [*Dutkiewicz et al.*, 2013]. Specifically, reductions in productivity in the tropics and North Atlantic Ocean under a warming climate and reduced ocean nutrient supply (Figure 6.11), have been hypothesised to increase diazotroph growth, which is competitively favoured by increasing Fe/N ratios [*Dutkiewicz et al.*, 2014]. Therefore, we may be able to measure phenotype and genetic shifts in the ocean more readily under environmental change that net changes in productivity.

Neutral agent-based models indicate ocean microbe genetic evolution rates exceed dispersal: microbes evolve faster than ocean currents can disperse them, maintaining biogeographical provinces in the face of ocean mixing [*Hellweger et al.*, 2014]. For example, microbes disperse from the Indo-Pacific to Atlantic Ocean across the Aghulas leakage. Populations appear continuous across the barrier at the coarse taxonomic level, but at the genetic level nitrogen conditions within Aghulas rings select for certain genotypes [*Villar et al.*, 2015]. Genetically distinct populations therefore exist in the Indian and Atlantic Oceans [*Villar et al.*, 2015].

Therefore, we may be able to measure phenotype and genetic shifts in the ocean more readily under environmental change than net changes in productivity. Future environmental changes that select for certain genes may remove genes that cannot readily be replaced by dispersal from adjacent biomes. Forecast environmental conditions may thus change patterns of ocean plankton ecotypes and genetic diversity. We suggest that herein — in the genetic markers of biogeography — lies an opportunity for detecting the impact of environmental change on global phytoplankton communities (cf. [*Dutkiewicz et al.*, 2014]).

CHAPTER 7

Conclusions

7.1 Thesis overview

In this thesis we have shown how vertical gradients in nitrate and light can be used to explain the vertical distribution of Arctic Ocean productivity, and how the vertical distribution relates to depth-integrated production (Chapter 4). In Chapter 4 we also elucidated how this insight can be used to untangle the expected opposing effects of light (increase) and nutrients (decrease) on productivity as the Arctic Ocean transitions to an ice-free state. In Chapter 5 we developed this into a simple dynamical relationship which relates Arctic Ocean production distributions to the ratio of nitrate limitation to light limitation. We used a simulation to show how these dynamics relate to observed geographical patterns in Arctic nitrate-light conditions and productivity, and to indicate that the relationship is invariant as the Arctic Ocean transitions to an ice-free state. In Chapter 6, we used ^{14}C productivity observations across the extra-Arctic oceans to show that the same relationship found in the Arctic is also applicable in the wider ocean. Applying the biogeochemical simulation indicates that the relationship in the extra-Arctic is also invariant over the coming century.

Our analysis suggests that, contrary to reported extrapolations [*Arrigo et al.*, 2008], productivity increases in an ice-free Arctic Ocean will be small (10%, RCP 8.5), occurring at depths $> 20\,\text{m}$ (where it is unlikely to be captured by satellites). Our analysis on the extra-Arctic oceans is more preliminary but it also entails small production decreases over the coming century ($< 10\%$, RCP 8.5), in line with studies using model ensembles [*Steinacher et al.*, 2010; *Bopp et al.*, 2013].

7.2 Monitoring ongoing Arctic Ocean changes

Current estimates of Arctic Ocean production are not reliable to within 10% (Chapter 2). Therefore, there is no adequate base line dataset for direct depth-integrated production measurements to be able to capture the expected Arctic Ocean change. Instead, the theory developed in this thesis presents two ways of monitoring ongoing Arctic changes that are commensurable with past successful monitoring regimes and existing monitoring logistics. First, simulations of a future ice-free Arctic are unanimous in projecting reducing surface nitrate over the coming century [*Vancoppenolle et al.*, 2013]. Second, light-on-nitrate increases in the Beaufort Gyre and downstream Canadian Arctic Archipelago have deepened subsurface chlorophyll maxima [*McLaughlin and Carmack*, 2010; *Bergeron and Tremblay*, 2014]; an effect that our analysis indicates will become more widespread and intense in an increasingly ice-free Arctic Ocean. (We stress that this does not diminish the need for an accurate technique to measure basin-scale productivity.)

7.2.1 Arctic Ocean physical nitrate transports

Ocean silicate and nitrate transports into the Arctic Ocean have been declining in the Atlantic inflow [*Rey*, 2012], estimated to provide ~75% of total Arctic Ocean nitrate (Chapter 4). Since 1990 the nitrate transport into the Barents Sea is estimated to have dropped 7% [*Rey*, 2012].

Extant arrays circumnavigating the Arctic Ocean boundary already measure physical transports [*Tsubouchi*, 2014]. These can be readily extended to include lab-on-chip nitrate sensors [*Beaton et al.*, 2012]. Nitrate transports into and out of the Arctic could then be monitored over time, calculated from physical transports and nitrate concentrations; as has been done using quasi-synoptic hydrographic surveys (Chapter 2). These results can be compared with ongoing modelling efforts to confirm that nitrate transports into the Arctic are decreasing as expected, and secondarily to improve model projections of this decrease.

7.2.2 The phytoplankton response to an ice-free Arctic

Past Arctic Ocean monitoring successes have also shown that ice-retreat and reduced physical nitrate supply effect the vertical structure of production by causing production distributions to deepen [*Martin et al.*, 2010; *McLaughlin and Carmack*, 2010; *Bergeron and Tremblay*, 2014; *Randelhoff et al.*, 2015]. Our simulation and theory suggests that the Canadian Arctic will continue to be sensitive to ice retreat, freshwater storage and reduced physical nitrate supply (Chapter 4) — a view supported by recent field campaigns [*McLaughlin et al.*, 2011]. Therefore, targeted campaigns in the Canadian Arctic should be a priority for early detection of future changes in production in response to sea ice retreat (it will be necessary to untangle the long term trend from decadal variability in the Beaufort Gyre).

The theory developed in this thesis derives productivity changes from nitrate and light conditions. These variables are already routinely measured in several international programs (such as the Ocean Observing Initiative [*Cowles et al.*, 2010]), and will be extended with bio-Argo [*Gruber et al.*, 2007]. There, are therefore other locales and dynamics to which it may be applied.

Last, for the more theoretically inclined, our work presents some powerful ways for tackling production problems at any scale of interest. Biological production is posited to relate invariantly to gradients in kinetic rates. We have demonstrated this using a realistic simulation in the Arctic Ocean, and productivity data in the global ocean. Gradients in kinetic rates are readily measurable to arrive at estimates of the temporal evolution of production distributions.

APPENDIX A

A1 Data sources

Ocean physics	
Arctic hydrographic data (T,S)	Steele *et al.* 2001
Arctic sea ice concentration	Meier *et al.* 2015
Mixed layer depth climatology	de Boyer Montégut *et al.* 1997
SeaWiFS surface solar irradiance	Bishop and Rossow 1991
Nutrients	
World Ocean Atlas (2013) nitrate	Garcia *et al.* 2014
World Ocean Atlas (2013) silicate	Garcia *et al.* 2014
Global nutrient enrichment data	Moore *et al.* 2013
Global dissolved iron	Tagliabue [requested]
Phytoplankton	
MODIS surface chlorophyll-a	Carder *et al.* 2004
World Ocean Atlas (2001) chlorophyll-a	Conkright *et al.* 2002
MODIS VGPM productivity	Behrenfeld and Falkowski 1997
^{14}Carbon productivity	Buitenhuis *et al.* 2013

A2 Example code

To illustrate our work flow, some example Matlab code is given below.

```
% The model Arctic Ocean base relationship between vertical productivity
% structure and nitrate-on-light conditions (i.e. P2/P vs L) is calculated from 4
% functions for the selected model decades
dec = 1;
nitMar = nitrate_inv(dec);
parRD = light_inv(dec);
[L Lnorm] = get_L(parRD, nitMar, dec);
[prop Propnorm] = production(dec);

% these functions are...

% ------------------------------------------------------------------
% 1. Nitrate conditions are determined by the function
function [nitMar] = nitrate_inv(dec)
years = linspace(1,91,10);
lattotal = double(1021);
lontotal = double(1442);
depthSurf = 12; % 20 m
depthFilter = 18; % water depth filter (50 m)
months = 12;
dep_roam; depthGrid = roam_dep(:,2); % read in model depth Grid
mask = mask_land; % create land and water depth mask
for i = 1:length(dec)
    startyr = 1999 + years(dec(i));
    endyr = startyr + 9;
    fprintf('Reading model nitrate for decade %d-%d\n', startyr, endyr);
    dnomN = sprintf(['/noc/msm/scratch/medusa/axy/ROAM/DECADE_CLIM/' ...
        'ORCA025-ROAM_1m_CLIM_%d0101_%d1230_ptrc_T_%d-%d.nc'] ...
        ,startyr, endyr, startyr, endyr);
    dnomM = sprintf(['/noc/msm/scratch/medusa/axy/ROAM/DECADE_CLIM/' ...
        'ORCA025-ROAM_1m_CLIM_%d0101_%d1230_grid_T_%d-%d.nc'] ...
        ,startyr, endyr, startyr, endyr);
    nit = ncread(dnomN,'DIN',[1 1 1 1], [lontotal lattotal depthSurf months]);
    nit = nit .* repmat(mask(:,:,depthFilter), [1 1 depthSurf months]); % depth mask
    mld = ncread(dnomM,'somxl010',[1 1 1], [lontotal lattotal months]);
```

```
    [maxmld, monthInd] = max(mld,[],3);
    for y = 1:latend  % nitrate profile at month max mld
        fprintf(’Reading latitude %d\n’,y);
        for x = 1:lontotal
                nitMax(x,y,:) = squeeze(nit(x,y,monthInd(x,y),:));
        end
    end
    nitM = squeeze(nansum(nitMax,3) * (depthGrid(depthSurf)  / depthSurf));
    nitMar(:,:,i) = nitM .* mask(:,:,depthFilter) / 20;
end

% -------------------------------------------------------------------
% 2. Light conditions are determined by the function
function [parRD] = light_inv(dec)
years = linspace(1,91,10);
lattotal = double(1021);
lontotal = double(1442);
depthSurf = 12; % 20 m - surface waters
depthFilter = 18; % water depth filter
months = 12;
dep_roam; depthGrid = roam_dep(:,2); % read in model depth Grid
mask = mask_land; % create land and water depth mask
for i = 1:length(dec)
    startyr = 1999 + years(dec(i));
    endyr = startyr + 9;
    fprintf(’Reading model light for decade %d-%d\n’, startyr, endyr);
    dnomN = sprintf([’/noc/msm/scratch/medusa/axy/ROAM/DECADE_CLIM/’ ...
        ’ORCA025-ROAM_1m_CLIM_%d0101_%d1230_ptrc_T_%d-%d.nc’]...
        ,startyr, endyr, startyr, endyr);
    dnomP = sprintf([’/noc/msm/scratch/medusa/axy/ROAM/DECADE_CLIM/’...
        ’ORCA025-ROAM_1m_CLIM_%d0101_%d1230_diad_T_%d-%d.nc’]...
        ,startyr, endyr, startyr, endyr);
    modchn = ncread(dnomN,’CHN’,[1 1 1 1], [lontotal lattotal depthSurf months]);
    modchd = ncread(dnomN,’CHD’,[1 1 1 1], [lontotal lattotal depthSurf months]);
    chl = modchn + modchd; clearvars modchn modchd;
    chl = chl .* repmat(mask(:,:,depthFilter), [1 1 depthSurf months]);
    ts = ncread(dnomP,’MED_QSR’,[1 latstart 1], [lontotal latend months]);
    totalshortwave = nanmean(ts(:,:,7:9),3);
    rpig = 0.7; xkr0 = 0.225; xkrp = 0.037; xlr = 0.629; % PAR (Levy 2001)
```

```
    xlg = 0.674; xkg0 = 0.0232; xkgp = 0.074; % Attenuation const (Levy2001 Table 3)
    surface_dim = 1;
    zpar = totalshortwave * (0.43 / 2); % Levy2001 eq A23. (Two-band model)
    zpar = reshape(zpar,lontotal,lattotal,surface_dim);
    zparr = zpar; zparg = zpar;
    chl (chl == 0) = realmin; % realmin: smallest +ve: avoid log(zpig=0)
    zpig = chl ./ rpig; % Attenuate due to pigments (Levy2001 A22)
    posz = 2;
    for z = 2:size(zpig,3)
        thick = depthGrid(z)-depthGrid(z-1); % depth box thick
        zkr  = xkr0 + xkrp .* exp(xlr .* log(zpig(:,:,(z-1)))); % r/g atten. coeffs
        zkg  = xkg0 + xkgp .* exp(xlg .* log(zpig(:,:,(z-1)))); % (Levy2001 eqA20,A21)
        zparr(:,:,posz) = zparr(:,:,(z-1)) .* exp( -zkr * thick);% r/g atten.
        zparg(:,:,posz) = zparg(:,:,(z-1)) .* exp( -zkg * thick);% (Levy2001 eqA24,A25)
        parJ = zparr + zparg; % Levy2001 eqA26
        fprintf(’Read level %d\n’, z)
        posz = posz + 1;
    end
    parJ20 = squeeze(nansum(parJ,3) * (depthGrid(depthSurf)  / depthSurf)); % av 0-zr
    parRD(:,:,i) = parJ20 .* mask(:,:,depthFilter);
end


% ---------------------------------------------------------------
% 3. Nitrate-on-light condition (L) is determined by the function
function [L, Lnorm] = get_L(parRD, nitMar, dec)
k = 0.625; % Physiological constants (Yool2013 TPP averages)
alpha = 13.125 * 1/90 * 0.01257; % Yool2013 letting Chl/C = 1/90
V = (0.515 * 1.066) .^ 0; % V = 1 (no T dependence in J)
for i = 1:length(dec)
    fprintf(’Calculating L for decade %d\n’, i);
    Q = nitMar(:,:,i) ./ (k + nitMar(:,:,i));
    J = (V * alpha * parRD(:,:,i)) ./ (sqrt(V .^2 + alpha.^2 * parRD(:,:,i).^2));
    L(:,:,i) = J ./ Q;
    Ln = regridding(L(:,:,i)); % Regrid onto 1 linear grid
    Ln = Ln(155:end,:);
    Lnorm(:,i) = Ln(:);
end
```

```
% ------------------------------------------------------------------
% 4. Productivity vertical structure (P2/P) is determined by the function
function [prop Propnorm NPPnorm SurfProd SubProd] = production(dec)
years = linspace(1,91,10);
lattotal = double(1021);
lontotal = double(1442);
depth = 24; depthSurf = 12;
depthFilter = 18;
months = 12;
dep_roam; depthGrid = roam_dep(:,2); % read in model depth Grid
mask = mask_land; % create land and water depth mask
for i = 1:length(dec)
    startyr = 1999 + years(dec(i));
    endyr = startyr + 9;
    fprintf('Reading model production for decade %d-%d\n',startyr, endyr);
    dnomP = sprintf(['/noc/msm/scratch/medusa/axy/ROAM/DECADE_CLIM/' ...
        'ORCA025-ROAM_1m_CLIM_%d0101_%d1230_diad_T_%d-%d.nc'] ...
        ,startyr, endyr, startyr, endyr);
    prod = ncread(dnomP,'TPP3',[1 1 1 1], [lontotal lattotal depth months]);
    prod = prod * 12.011 * 6.625; % mmolN -> mgC
    prod = prod .* repmat(mask(:,:,depthFilter), [1 1 depth months]); % apply masks
    ProdAn = (nansum(prod,4)) .* (365/months); % creating proportion subsurface
    SurfProd = squeeze(nansum(ProdAn(:,:,1:depthSurf),3)* ...
        (depthGrid(depthSurf)/depthSurf)/1000);
    SubProd = squeeze(nansum(ProdAn(:,:,depthSurf+1:depth),3)* ...
        ((depthGrid(depth)-depthGrid(depthSurf))/length(depthSurf+1:depth))/1000);
    prop(:,:,i) = SubProd ./ (SurfProd + SubProd);
    npp = SurfProd + SubProd;
    propn = regridding(prop(:,:,i));
    propn = propn(155:end,:); Propnorm(:,i) = propn(:);
    nppn = regridding(npp);
    nppn = nppn(155:end,:) NPPnorm(:,i) = nppn(:);
end
```

A3 MEDUSA partial differential equations

The following partial differential equations describe the conservation of chemical matter in MEDUSA between the four main classes: nutrients, phytoplankton, zooplankton and detritus. They are provided here in their full form; but please note that the equations that govern phytoplankton growth (our focus in this thesis), are also given in Chapter 3.

$$\frac{\partial Pn}{\partial t} = PP_{Pn} \cdot Pn - G\mu_{Pn} - Gm_{Pn} - M1_{Pn} - M2_{Pn} \tag{A.1}$$

$$\frac{\partial Pd}{\partial t} = PP_{Pd} \cdot Pd - Gm_{Pd} - M1_{Pd} - M2_{Pd} \tag{A.2}$$

$$\frac{\partial Chl_{Pn}}{\partial t} = \frac{\theta_{Pn}^{Chl}}{\xi} \left(R_{Pn} \cdot PP_{Pn} \cdot Pn - G\mu_{Pn} - Gm_{Pn} - M1_{Pn} - M2_{Pn} \right) \tag{A.3}$$

$$\frac{\partial Chl_{Pd}}{\partial t} = \frac{\theta_{Pd}^{Chl}}{\xi} \left(R_{Pd} \cdot PP_{Pd} \cdot Pd - Gm_{Pd} - M1_{Pd} - M2_{Pd} \right) \tag{A.4}$$

$$\frac{\partial Pd_{Si}}{\partial t} = PP_{PdSi} \cdot Pd_{Si} - Gm_{PdSi} - M1_{PdSi} - M2_{PdSi} - DS_{PdSi} \tag{A.5}$$

$$\frac{\partial Z\mu}{\partial t} = F_{Z\mu} - Gm_{Z\mu} - M1_{Z\mu} - M2_{Z\mu} \tag{A.6}$$

$$\frac{\partial Zm}{\partial t} = F_{Zm} - M1_{Zm} - M2_{Zm} \tag{A.7}$$

$$\frac{\partial D}{\partial t} = M2_{Pn} + M2_{Z\mu} + (1 - D1_{frac}) \cdot M2_{Pd} + (1 - D2_{frac}) \cdot M2_{Zm} \tag{A.8}$$

$$+ (1 - \beta_N) \cdot IN_{Z\mu} + (1 - \beta_N) \cdot IN_{Zm} - G\mu_D - Gm_D - M_D \tag{A.9}$$

$$- \omega_g \cdot \frac{\partial D}{\partial z} \tag{A.10}$$

$$\frac{\partial D_C}{\partial t} = \theta_{Pn} \cdot M2_{Pn} + \theta_{Z\mu} \cdot M2_{Z\mu} + \theta_{Pd} \cdot (1 - D1_{\mathrm{frac}}) \cdot M2_{Pd} \tag{A.11}$$

$$+ \theta_{Zm} \cdot (1 - D2_{frac}) \cdot M2_{Zm} + (1 - \beta_C) \cdot IC_{Z\mu} \tag{A.12}$$

$$+ (1 - \beta_C) \cdot IC_{Zm} - G\mu_{DC} - Gm_{DC} - M_{DC} - \omega_g \cdot \frac{\partial D_C}{\partial z} \tag{A.13}$$

$$\frac{\partial N}{\partial t} = - PP_{Pn} \cdot Pn - PP_{Pd} \cdot Pd + \phi \cdot (G\mu_{Pn} + G\mu_D) \tag{A.14}$$

$$+ \phi \cdot (Gm_{Pn} + Gm_{Pd} + Gm_{Z\mu} + Gm_D) + E_{Z\mu} + E_{Zm} + M1_{Pn} \tag{A.15}$$

$$+ M1_{Pd} + M1_{Z\mu} + M1_{Zm} + M_D + LD_N(k) + BF_N \tag{A.16}$$

$$\frac{\partial S}{\partial t} = - PP_{PdSi} \cdot PdSi + M1_{PdSi} + (1 - D1_{frac}) \cdot M2_{PdSi} + DS_{PdSi} \tag{A.17}$$

$$+ (1 - D2_{frac}) \cdot Gm_{PdSi} + LD_{Si}(k) + BF_{Si} \tag{A.18}$$

$$\frac{\partial F}{\partial t} = - R_{Fe} \cdot \frac{\partial N}{\partial t} + F_{\text{atm}} + F_{\text{ben}} - F_{\text{sca}} + BF_{Fe} \tag{A.19}$$

$$\frac{\partial DIC}{\partial t} = - (\theta_{Pn} \cdot PP_{Pn} \cdot Pn) - (\theta_{Pd} \cdot PP_{Pd} \cdot Pd) \tag{A.20}$$

$$+ (\phi \cdot \theta_{Pn} \cdot G\mu_{Pn}) + (\phi \cdot G\mu_{Dc}) + (\phi \cdot \theta_{Pn} \cdot Gm_{Pn}) \tag{A.21}$$

$$+ (\phi \cdot \theta_{Pd} \cdot Gm_{Pd}) + (\phi \cdot \theta_{Z\mu} \cdot Gm_{Z\mu}) + (\phi \cdot Gm_{Dc}) \tag{A.22}$$

$$+ R_{Z\mu} + R_{Zm} + (\theta_{Pn} \cdot M1_{Pn}) + (\theta_{Pd} \cdot M1_{Pd}) + (\theta_{Z\mu} \cdot M1_{Z\mu}) \tag{A.23}$$

$$+ (\theta_{Zm} \cdot M1_{Zm}) + M_{Dc} + LD_{C}(k) - FD_{CaCO3} + LD_{CaCO3}(k) \tag{A.24}$$

$$+ BF_{C} + ASF_{CO_2} \tag{A.25}$$

$$\frac{\partial ALK}{\partial t} = 2FD_{CaCO3} + 2LD_{CaCO3}(k) + BF_{CaCO3} \tag{A.26}$$

$$\frac{\partial O_2}{\partial t} = (\theta_{nit} \cdot PP_{Pn} \cdot Pn) + (\theta_{nit} \cdot PP_{Pd} \cdot Pd) \tag{A.27}$$

$$- (\theta_{nit} \cdot \phi \cdot G\mu_{Pn}) - (\theta_{nit} \cdot \phi \cdot G\mu_{D}) - (\theta_{nit}\phi \cdot Gm_{Pn}) \tag{A.28}$$

$$- (\theta_{nit} \cdot \phi \cdot Gm_{Pd}) - (\theta_{nit} \cdot \phi \cdot Gm_{Z\mu}) - (\theta_{nit}\phi \cdot Gm_{D}) \tag{A.29}$$

$$- (\theta_{nit} \cdot E_{Z\mu}) - (\theta_{nit} \cdot E_{Zm}) - (\theta_{nit} \cdot M1_{Pn}) - (\theta_{nit} \cdot M1_{Pd}) \tag{A.30}$$

$$- (\theta_{nit} \cdot M1_{Z\mu}) - (\theta_{nit} \cdot M1_{Zm}) - (\theta_{nit} \cdot M_{D}) \tag{A.31}$$

$$- (\theta_{nit} \cdot LD_{N}(k)) + (\theta_{rem} \cdot \theta_{Pn} \cdot PP_{Pn} \cdot Pn) \tag{A.32}$$

$$+ (\theta_{rem} \cdot \theta_{Pd} \cdot PP_{Pd} \cdot Pd) - (\theta_{rem} \cdot \theta_{Pn} \cdot \phi \cdot G\mu_{Pn}) \tag{A.33}$$

$$- (\theta_{rem} \cdot \phi \cdot G\mu_{Dc}) - (\theta_{rem} \cdot \theta_{Pn} \cdot \phi \cdot Gm_{Pn}) \tag{A.34}$$

$$- (\theta_{rem} \cdot \theta_{Pn} \cdot \phi \cdot Gm_{Pd}) - (\theta_{rem} \cdot \theta_{Zu} \cdot \phi \cdot Gm_{Zu}) \tag{A.35}$$

$$- (\theta_{rem} \cdot \phi \cdot Gm_{Dc}) - (\theta_{rem} \cdot R_{Z\mu}) - (\theta_{rem} \cdot R_{Zm}) \tag{A.36}$$

$$- (\theta_{rem} \cdot \theta_{Pn} \cdot M1_{Pn}) - (\theta_{rem} \cdot \theta_{Pd} \cdot M1_{Pd}) \tag{A.37}$$

$$- (\theta_{rem} \cdot \theta_{Z\mu} \cdot M1_{Z\mu}) - (\theta_{rem} \cdot \theta_{Zm} \cdot M1_{Zm}) \tag{A.38}$$

$$- (\theta_{rem} \cdot M_{Dc}) - (\theta_{rem} \cdot LD_{C}(k)) - (\theta_{nit} \cdot BF_{N}) \tag{A.39}$$

$$- (\theta_{rem} \cdot BF_{C}) + ASF_{O2} \tag{A.40}$$

A4 MEDUSA functional forms

Non-diatom limitation and growth

$$\theta_{Pn}^{\mathrm{Chl}} = \frac{\mathrm{Chl}_{Pn} \cdot \xi}{Pn} \tag{A.41}$$

$$\hat{\alpha}_{Pn} = \alpha_{Pn} \cdot \theta_{Pn}^{\mathrm{Chl}} \tag{A.42}$$

$$V_{Pn^T} = V_{Pn} \cdot 1.066^T \tag{A.43}$$

$$J_{Pn} = \frac{V_{Pn^T} \cdot \hat{\alpha}_{Pn} \cdot I}{\sqrt{(V_{Pn^T}^2 + \hat{\alpha}_{Pn}^2 \cdot I^2)}} \tag{A.44}$$

$$Q_{N,Pn} = \frac{N}{k_{N,Pn} + N} \tag{A.45}$$

$$Q_{Fe,Pn} = \frac{F}{k_{Fe,Pn} + F} \tag{A.46}$$

$$PP_{Pn} = J_{Pn} \cdot Q_{N,Pn} \cdot Q_{Fe,Pn} \tag{A.47}$$

Diatom limitation and growth

$$\theta_{Pd}^{\mathrm{Chl}} = \frac{\mathrm{Chl}_{Pd} \cdot \xi}{Pd} \tag{A.48}$$

$$\hat{\alpha}_{Pd} = \alpha_{Pd} \cdot \theta_{Pd}^{\mathrm{Chl}} \tag{A.49}$$

$$V_{Pd^T} = V_{Pd} \cdot 1.066^T \tag{A.50}$$

$$J_{Pd} = \frac{V_{Pd^T} \cdot \hat{\alpha}_{Pd} \cdot I}{\sqrt{(V_{Pd^T}^2 + \hat{\alpha}_{Pd}^2 \cdot I^2)}} \tag{A.51}$$

$$Q_{N,Pd} = \frac{N}{k_{N,Pd} + N} \tag{A.52}$$

$$Q_{Si} = \frac{S}{k_{Si} + S} \tag{A.53}$$

$$Q_{Fe,Pd} = \frac{F}{k_{Fe,Pd} + F} \tag{A.54}$$

$$R_{Si:N} = \frac{Pd_{Si}}{Pd} \tag{A.55}$$

$$R_{N:Si} = \frac{1}{R_{Si:N}} \tag{A.56}$$

$$\text{if} \quad R_{Si:N} \leq R^0_{Si:N} \tag{A.57}$$

$$PP_{Pd} = 0 \tag{A.58}$$

$$\text{else if} \quad R^0_{Si:N} < R_{Si:N} < 3R^0_{Si:N} \tag{A.59}$$

$$PP_{Pd} = J_{Pd} \cdot Q_{N,Pd} \cdot Q_{Fe,Pd} \cdot U_\infty \cdot \frac{R_{Si:N} - R^0_{Si:N}}{R_{Si:N}} \tag{A.60}$$

$$\text{else} \quad PP_{Pd} = J_{Pd} \cdot Q_{N,Pd} \cdot Q_{Fe,Pd} \tag{A.61}$$

$$\text{if} \quad R_{Si:N} < (3R^0_{Si:N})^{-1} \tag{A.62}$$

$$PP_{Pd_{Si}} = J_{Pd} \cdot Q_{Si} \tag{A.63}$$

$$\text{else if} \quad (3R^0_{Si:N})^{-1} \leq R_{Si:N} < (R^0_{Si:N})^{-1} \tag{A.64}$$

$$PP_{Pd_{Si}} = J_{Pd} \cdot Q_{Si} \cdot U_\infty \cdot \frac{R_{N:Si} - R^0_{N:Si}}{R_{N:Si}} \tag{A.65}$$

$$\text{else} \quad PP_{Pd_{Si}} = 0 \tag{A.66}$$

Chlorophyll growth scaling factors

$$R_{Pn} = \frac{\theta^{Chl}_{max,Pn}}{\theta^{Chl}_{Pn}} \cdot \frac{PP_{Pn}}{\hat{\alpha}_{Pn} \cdot I} \tag{A.67}$$

$$R_{Pd} = \frac{\theta^{Chl}_{max,Pd}}{\theta^{Chl}_{Pd}} \cdot \frac{PP_{Pd}}{\hat{\alpha}_{Pd} \cdot I} \tag{A.68}$$

Microzooplankton grazing

$$G\mu_X = \frac{g_\mu \cdot p_{\mu X} \cdot X^2 \cdot Z\mu}{k_\mu^2 + p_{\mu Pn} \cdot Pn^2 + p_{\mu D} \cdot D^2} \text{where X = Pn or D} \tag{A.69}$$

$$IN_{Z\mu} = (1 - \phi) \cdot (G\mu_{Pn} + G\mu_D) \tag{A.70}$$

$$IC_{Z\mu} = (1 - \phi) \cdot (\theta_{Pn} \cdot G\mu_{Pn} + \theta_D + G\mu_D) \tag{A.71}$$

$$\theta_{F\mu} = \frac{IC_{Z\mu}}{IN_{Z\mu}} \tag{A.72}$$

$$\theta^*_{F\mu} = \frac{\beta_N \cdot \theta_{Z\mu}}{\beta_C \cdot k_C} \tag{A.73}$$

$$R_{Z\mu} = (\beta_C \cdot IC_{Z\mu}) - (\theta_{Z\mu} \cdot F_{Z\mu}) \tag{A.74}$$

$$\text{if} \quad \theta_{F\mu} > \theta^*_{F\mu} \tag{A.75}$$

$$F_{Z\mu} = \beta_N \cdot IN_{Z\mu} \tag{A.76}$$

$$E_{Z\mu} = 0 \tag{A.77}$$

$$\text{else} \quad F_{Z\mu} = \frac{\beta_C \cdot k_C \cdot IC_{Z\mu}}{\theta_{Z\mu}} \tag{A.78}$$

$$E_{Z\mu} = IC_{Z\mu} \cdot \left(\frac{\beta_N}{\theta_{F\mu}} - \frac{\beta_C \cdot k_C}{\theta_{Z\mu}} \right) \tag{A.79}$$

Mesozooplankton grazing

$$Gm_X = \frac{g_m \cdot p_{mX} \cdot X^2 \cdot Zm}{k_m^2 + F_m} \text{where X = Pn, Pd, Z}\mu \text{ or D} \tag{A.80}$$

$$F_m = (p_{mPn} \cdot Pn^2) + (p_{mPd} \cdot Pd^2) + (p_{mZ\mu} \cdot Z\mu^2) + (p_{mD} \cdot D^2) \tag{A.81}$$

$$Gm_{Pd_{Si}} = R_{Si:N} \cdot Gm_{Pd} \tag{A.82}$$

$$IN_{Zm} = (1 - \phi) \cdot (Gm_{Pd} + Gm_{Pn} + Gm_{Z\mu} + Gm_{Pd}) \tag{A.83}$$

$$IC_{Zm} = (1 - \phi) \cdot (\theta_{Pd} \cdot Gm_{Pd} + \theta_{Pn} \cdot Gm_{Pn} + \theta_{Z\mu} \cdot Gm_{Z\mu} + \theta_D \cdot Gm_D) \tag{A.84}$$

$$\theta_{Fm} = \frac{IC_{Zm}}{IN_{Zm}} \tag{A.85}$$

$$\theta^*_{Fm} = \frac{\beta_N \cdot \theta_{Zm}}{\beta_C \cdot k_C} \tag{A.86}$$

$$R_{Zm} = \beta_C \cdot IC_{Zm} - \theta_{Zm} \cdot F_{Zm} \tag{A.87}$$

$$\text{if} \quad \theta_{Fm} > \theta^*_{Fm} \tag{A.88}$$

$$F_{Zm} = \beta_N \cdot IN_{Zm} \tag{A.89}$$

$$E_{Zm} = 0 \tag{A.90}$$

$$\text{else} \quad F_{Zm} = \frac{\beta_C \cdot k_C \cdot IC_{Zm}}{\theta_{Zm}} \tag{A.91}$$

$$E_{Zm} = IC_{Zm} \cdot \left(\frac{\beta_N}{\theta_{Fm}} - \frac{\beta_C \cdot k_C}{\theta_{Zm}} \right) \tag{A.92}$$

Plankton loss terms

$$M1_{Pn} = \mu_{1,Pn} \cdot Pn \tag{A.93}$$

$$M1_{Pd} = \mu_{1,Pd} \cdot Pd \tag{A.94}$$

$$M1_{Pd_{Si}} = R_{Si:N} \cdot M1_{Pd} \tag{A.95}$$

$$M1_{Z\mu} = \mu_{1,Z\mu} \cdot Z\mu \tag{A.96}$$

$$M1_{Zm} = \mu_{1,Zm} \cdot Zm \tag{A.97}$$

$$M2_{Pn} = \mu_{2,Pn} \cdot \frac{Pn}{k_{Pn} + Pn} \cdot Pn \tag{A.98}$$

$$M2_{Pd} = \mu_{2,Pd} \cdot \frac{Pd}{k_{Pd} + Pd} \cdot Pd \tag{A.99}$$

$$M2_{Pd_{Si}} = R_{Si:N} \cdot M2_{Pd} \tag{A.100}$$

$$M2_{Z\mu} = \mu_{2,Z\mu} \cdot \frac{Z\mu}{k_{Z\mu} + Z\mu} \cdot Z\mu \tag{A.101}$$

$$M2_{Zm} = \mu_{2,Zm} \cdot \frac{Zm}{k_{Zm} + Zm} \cdot Zm \tag{A.102}$$

$$DS_{Pd_{Si}} = \text{Diss} \cdot Pd_{Si} \tag{A.103}$$

$$M_D = \mu_D \cdot 1.066^T \cdot D \tag{A.104}$$

$$M_{Dc} = \mu_{Dc} \cdot 1.066^T \cdot D_C \tag{A.105}$$

Iron supply and removal

$$F_{\text{free}} = F - F_{\text{ligand}} \tag{A.106}$$

$$F_{\text{ligand}} = L_{\text{total}} - L_{\text{free}} \tag{A.107}$$

$$L_{\text{free}} = 0.5 \cdot \frac{F_1 + \sqrt{F_2}}{k_{\text{FeL}}} \tag{A.108}$$

$$F_1 = k_{\text{FeL}} \cdot (L_{\text{total}} - F) - 1 \tag{A.109}$$

$$F_2 = \max(F_1^2 + (4 \cdot k_{\text{FeL}} \cdot L_{\text{total}}), 0) \tag{A.110}$$

$$F_{\text{sca}} = k_{\text{scav}} \cdot F_{\text{free}} \tag{A.111}$$

Fast detritus production

$$\begin{aligned}
T_N(k+1) &= T_N(k) - LD_N + D1_{frac} \cdot M2_{Pd} && \text{(A.112)}\\
&+ D2_{frac} \cdot M2_{Zm} \cdot \delta z(k) && \text{(A.113)}\\
T_{Fe}(k+1) &= T_{Fe}(k) - LD_{Fe} + R_{Fe} \cdot D1_{frac} \cdot M2_{Pd} && \text{(A.114)}\\
&+ R_{Fe} \cdot D2_{frac} \cdot M2_{Zm} \cdot \delta z(k) && \text{(A.115)}\\
T_C(k+1) &= T_C(k) - LD_C + \theta_{Pd} \cdot D1_{frac} \cdot M2_{Pd} && \text{(A.116)}\\
&+ \theta_{Zm} \cdot D2_{frac} \cdot M2_{Zm} \cdot \delta z(k) && \text{(A.117)}\\
T_{Si}(k+1) &= T_{Si}(k) - LD_{Si} + D1_{frac} \cdot M2_{Pd_{Si}} && \text{(A.118)}\\
&+ D3_{frac} \cdot Gm_{Pd_{Si}} \cdot \delta z(k) && \text{(A.119)}\\
T_{CaCO_3}(k+1) &= T_{CaCO_3}(k) - LD_{CaCO_3} + \theta_{Pd} \cdot D1_{frac} && \text{(A.120)}\\
&+ M2_{Pd} + \theta_{Zm} \cdot D2_{frac} \cdot M2_{Zm} \cdot \delta z(k) \cdot \mathrm{fo}(\Omega_{\mathrm{calcite}}) && \text{(A.121)}\\
\mathrm{fo}(\Omega_{\mathrm{calcite}}) &= (\Omega_{\mathrm{calcite}} - 1)^{\eta} \cdot r_0 && \text{(A.122)}
\end{aligned}$$

Fast detritus remineralisation

$$\begin{aligned}
TC_{bSi} =& T_{Si}(k) \cdot \frac{M_{Si}}{M_{org}} \cdot f_{Si} && \text{(A.123)}\\
TC_{bCaCO_3} =& T_{CaCO_3}(k) \cdot \frac{M_{CaCO_3}}{M_{org}} \cdot f_{CaCO_3} && \text{(A.124)}\\
TC_{\mathrm{protect}} =& TC_{bSi} + TC_{bCaCO_3} && \text{(A.125)}\\
TC_{\mathrm{excess}} =& T_C(k) - TC_{\mathrm{protect}} && \text{(A.126)}\\
TC_{\mathrm{survive}} =& TC_{\mathrm{excess}} \cdot exp\left(-\frac{\delta z(k)}{d_{\mathrm{excess}}}\right) && \text{(A.127)}\\
T_C(k+1) =& TC_{\mathrm{protect}} + TC_{\mathrm{survive}} && \text{(A.128)}\\
LD_C(k) =& \frac{TC_{\mathrm{excess}} - TC_{\mathrm{survive}}}{\delta z(k)} && \text{(A.129)}\\
T_{Si}(k+1) =& T_{Si}(k) \cdot exp\left(-\frac{\delta z(k)}{d_{Si}}\right) && \text{(A.130)}
\end{aligned}$$

$$LD_{Si}(k) = \frac{T_{Si}(k) - T_{Si}(k+1)}{\delta z(k)} \tag{A.131}$$

$$\text{if} \quad z(k) < \text{ lysocline(lat, lon)} \tag{A.132}$$

$$T_{CaCO_3}(k+1) = T_{CaCO_3}(k) \cdot exp\left(-\frac{\delta z(k)}{d_{CaCO_3}}\right) \tag{A.133}$$

$$\text{else} \quad T_{CaCO_3}(k+1) = T_{CaCO_3}(k) \tag{A.134}$$

$$LD_{CaCO_3}(k) = \frac{T_{CaCO_3}(k) - T_{CaCO_3}(k+1)}{\delta z(k)} \tag{A.135}$$

A5 MEDUSA biogeochemical model variables

Table A1: MEDUSA biogeochemical 3D model state variables.

Symbol	**State variable**	**Units**
Pn	Non-diatom phytoplankton biomass	mmol N m^3
Pd	Diatom phytoplankton biomass	mmolN m^3
Pd_{Si}	Diatom phytoplankton biomass (silicate-pool)	mmol Si m^3
Chl_{Pn}	Non-diatom phytoplankton chlorophyll-a concentration	mg chl m^3
Chl_{Pd}	Diatom phytoplankton chlorophyll-a concentration	mg chl m^3
$Z\mu$	Micro-zooplankton biomass	mmol N m^3
Zm	Meso-zooplankton biomass	mmol N m^3
D	Slow-sinking detritus (N)	mmol N m^3
D_C	Slow-sinking detritus (C)	mmol C m^3
N	Nitrogen nutrient	mmol N m^3
F	Iron nutrient	mmol Fe m^3
S	Silicic acid	mmol Si m^3
DIC	Dissolved inorganic carbon	mmol C m^3
ALK	Total alkalinity	meq m^3
O_2	Dissolved oxygen	mmol O$_2$ m^3

Table A2: MEDUSA biogeochemical 2D (benthic) model state variables.

Symbol	**State variable**	**Units**
B_N	Benthic organic nitrogen	$\mathrm{mmol\,N\,m^2}$
B_C	Benthic organic carbon	$\mathrm{mmol\,C\,m^2}$
B_{Si}	Benthic inorganic silicon	$\mathrm{mmol\,Si\,m^2}$
B_{Ca}	Benthic inorganic $CaCO_3$	$\mathrm{mmol\,C\,m^2}$

Table A3: MEDUSA phytoplankton process terms

Symbol	**Variable**
PP_{Pn}, PP_{Pd}	non-diatom and diatom productivity per-unit biomass
PP_{PdSi}	silicate pool productivity per-unit biomass
$G\mu_{Pn}$	micro-zooplankton grazing on non-diatom phytoplankton
Gm_{Pn}, Gm_{Pd}	meso-zooplankton grazing on non-diatoms and diatoms
Gm_{PdSi}	meso-zooplankton grazing on the silicate pool
$M1_{Pn}, M1_{Pd}, M1_{PdSi}$	phytoplankton linear losses
$M2_{Pn}, M2_{Pd}, M2_{PdSi}$	phytoplankton non-linear losses
$\theta^{Chl}_{Pn}, \theta^{Chl}_{Pd}$	non-diatom and diatom chlorophyll : biomass ratios
R_{Pn}, R_{Pd}	non-diatom and diatom chlorophyll-growth scaling factors
θ_{Pn}, θ_{Pd}	phytoplankton C: N ratio
DS_{PdSi}	dissolution of silicate in diatom phytoplankton
$\hat{\alpha}_{Pn}, \hat{\alpha}_{Pd}$	chlorophyll:biomass weighted slope of P-I curve
V^T_{Pn}, V^T_{Pd}	maximum phytoplankton growth rates
T	Temperature
J_{Pn}, J_{Pd}	realised phytoplankton growth rates given local irradiance
I	Irradiance
$Q_{N,Pn}, Q_{Fe,Pn}, Q_{N,Pd}, Q_{Fe,Pd}, Q_{Si}$	nitrogen, iron and silicate limitations of phytoplankton
$R_{Si:N}, R_{N:Si}$	diatom stochiometric silicic acid : nitrate ratio, and inverse

Table A4: MEDUSA miscellaneous process terms

Symbol	**Variable**
FD_{CaCO3}	$CaCO_3$ production
BF_C, BF_{CaCO3}	benthic dissolution (C), benthic dissolution ($CaCO_3$)
ASF_{CO2}, ASF_{O2}	air-sea gas exchange of carbon dioxide, air-sea gas exchange of oxygen
θ_{nit}	O_2 consumption by N remineralisation $\mathrm{mol\,O_2\,(mol\,N)^1}$
θ_{rem}	O_2 consumption by C remineralisation $\mathrm{mol\,O_2\,(mol\,C)^1}$

Table A5: MEDUSA zooplankton process terms

Symbol	Variable
$F_{Z\mu}, F_{Zm}$	total micro-zooplankton grazing, total meso-zooplankton grazing
$Gm_{Z\mu}$	meso-zooplankton grazing on micro-zooplankton
$M1_{Z\mu}, M1_{Zm}$	micro-zooplankton linear losses, meso-zooplankton linear losses
$M2_{Z\mu}, M2_{Zm}$	micro-zooplankton non-linear losses, meso-zooplankton non-linear losses
$R_{Z\mu}, R_{Zm}$	respiration of micro-zooplankton, respiration of meso-plankton
$\theta_{Z\mu}, \theta_{Zm}$	zooplankton C:N ratio
$\theta_{F\mu}, \theta_{Fm}$	zooplankton ingested C:N ratios
$\theta^*_{F\mu}, \theta^*_{Fm}$	ideal C:N ingestion ratios preferred by zooplankton

Table A6: MEDUSA nutrient process terms

Symbol	Variable
$E_{Z\mu}, E_{Zm}$	micro-zooplankton excretion, meso-zooplankton excretion
LD_N, LD_{Fe}	remineralisation of fast-sinking nitrogen and iron detritus
LD_{Si}	dissolution of fast-sinking silicic detritus
LD_C	remineralisation of fast-sinking carbon detritus
LD_{CaCO3}	dissolution of fast-sinking $CaCO_3$ detritus
BF_N, BF_{Fe}, BF_{Si}	benthic remineralisation of N and Fe, benthic dissolution of Si
$F_{\text{free}}, F_{\text{ligand}}$	free iron concentration, and iron concentration bound to ligands
L_{free}	ligand concentration unbound to iron
$F_{\text{atm}}, F_{\text{ben}}, F_{\text{sca}}$	aeolian and benthic iron inputs, iron removed through scavenging
T_N, T_{Fe}, T_C	transfer of sinking nitrogen, iron, carbon across a vertical interface
T_{Si}, T_{CaCO_3}	transfer of sinking silicic acid and $CaCO_3$ across a vertical interface
T_{bSi}, T_{bCaCO_3}	biogenic fractions of silicic acid and $CaCO_3$ transfered
$TC_{\text{protect}}, TC_{\text{excess}}$	fast-sinking detritus protected and not protected from remineralisation
TC_{survive}	portion of excess (non-protected) matter that survives remineralisation

Table A7: MEDUSA detritus process terms

Symbol	**Variable**
$IN_{Z\mu}, IN_{Zm}$	microzooplankton and mesozooplankton nitrogen ingestion
$IC_{Z\mu}, IC_{Zm}$	microzooplankton and mesozooplankton carbon ingestion
$G\mu_D, Gm_D$	microzooplankton and mesozooplankton N detritus ingestion
$G\mu_{DC}, Gm_{DC}$	microzooplankton and mesozooplankton C detritus ingestion
M_D, M_{DC}	remineralisation of nitrogen and carbon detritus
$\mathrm{fo}(\Omega_{\mathrm{calcite}})$	relative quantity of $CaCO_3$ associated with fast-sinking detrital particles
$\Omega_{\mathrm{calcite}}$	saturation state of calcite

Table A8: Phytoplankton growth parameters

Symbol	**Parameter**	**Units**	**Value**
α_{Pn}, α_{Pd}	chl-specific initial slope of P-I curve	$\mathrm{gC\,(gchl)^{-1}(W\,m^{-}2)^{-1}\ d^{-1}}$	15.0, 11.25
ξ	C:N conversion factor	$\mathrm{molN\,(gC)^{-1}}$	0.01257
V_{Pn}, V_{Pd}	max phytoplankton growth rates at 0°C	$\mathrm{d^{-1}}$	0.53, 0.50
$k_{N,Pn}, k_{N,Pd}$	nitrogen half-saturation constants	$\mathrm{mmolN\,m^{-3}}$	0.50, 0.75
$k_{Fe,Pn}, k_{Fe,Pd}$	iron half-saturation constants	$\mathrm{\mu molF\,m^{-3}}$	0.33, 0.67
k_{Si}	silicic acid half-saturation constant	$\mathrm{mmolS\,m^{-3}}$	3.0
$R^0_{Si:N}$	minimum diatom Si:N ratio	$\mathrm{molS\,(molN)^{-1}}$	0.2
$R^0_{N:Si}$	minimum diatom N:Si ratio	$\mathrm{molN\,(molS)^{-1}}$	0.2
U_∞	hypothetical growth ratio at infinite Si:N	–	1.5
$\theta^{Chl}_{max,Pn}, \theta^{Chl}_{max,Pd}$	maximum Chl:C ratios	$\mathrm{gchl\,(gC)^{-1}}$	0.05, 0.05

Table A9: Zooplankton parameters

Symbol	**Parameter**	**Units**	**Value**
g_μ, g_m	maximum zooplankton grazing rate	$\mathrm{d^{-1}}$	2.0, 0.5
k_μ	zooplankton grazing half-saturation constants	$\mathrm{mmolN\,m^{-3}}$	0.8, 0.3
ϕ	zooplankton grazing inefficiency	–	0.2
θ_D	detritus C:N ratio	$\mathrm{molC\,(molN)^{-1}}$	6.625
R_{Fe}	phytoplankton iron to nitrogen uptake ratio	$\mathrm{\mu molF\,(molN)^{-1}}$	30
β_N, β_C	zooplankton N and C assimilation efficiencies	–	0.77, 0.64
k_C	zooplankton net carbon growth efficiency	–	0.80
$\theta_{Z\mu}, \theta_{Zm}$	zooplankton C:N ratios	$\mathrm{molC\,(molN)^{-1}}$	6.625
$p_{\mu Pn}, p_{\mu D}$	microzooplankton grazing preferences	–	0.75, 0.25
p_{mPn}, p_{mPd}	mesozooplankton grazing preferences	–	0.15, 0.35
$p_{mZ\mu}, p_{mD}$	mesozooplankton grazing preferences	–	0.35, 0.15

Table A10: Phytoplankton and detritus loss parameters

Symbol	**Parameter**	**Units**	**Value**
$\mu_{1,Pn}, \mu_{1,Pd}$	phytoplankton loss rates	d^{-1}	0.02, 0.02
$\mu_{1,Z\mu}, \mu_{1,Zm}$	zooplankton loss rates	d^{-1}	0.02, 0.02
$\mu_{2,Pn}, \mu_{2,Pd}$	phytoplankton maximum loss rates	d^{-1}	0.1, 0.1
k_{Pn}, k_{Pd}	phytoplankton loss half-saturation constants	$\mathrm{mmolN\,m}^{-3}$	0.5, 0.5
$\mu_{2,Z\mu}, \mu_{2,Zm}$	zooplankton maximum loss rates	d^{-1}	0.1, 0.2
$k_{Z\mu}, k_{Zm}$	zooplankton loss half-saturation constants	$\mathrm{mmolN\,m}^{-3}$	0.5, 0.75
Diss	diatom frustule dissolution rate	d^{-1}	0.006
μ_D	detrital N remineralisation rate	d^{-1}	0.0158
μ_{Dc}	detrital C remineralisation rate	d^{-1}	0.0127

Table A11: Fast detritus submodel parameters

Symbol	**Parameter**	**Units**	**Value**
$D1_{frac}$	fast-detritus fraction of diatom losses	–	0.33
$D2_{frac}$	fast-detritus fraction of mesozooplankton losses	–	1.00
$D3_{frac}$	fast-detritus fraction of mesozooplankton grazing losses	–	0.80
η	thermodynamic calcification rate power	–	0.81
r_0	$CaCO_3$:POC export rain ratio scalar	–	0.026
M_{Si}	biogenic Si mass : mole ratio, SiO_2	$\mathrm{g(molSi)}^{-1}$	60.084
M_{Org}	organic carbon mass : mole ratio, C	$\mathrm{g(molC)}^{-1}$	12.011
M_{CaCO_3}	calcium carbonate mass : mole ratio, $CaCO_3$	$\mathrm{g(molC)}^{-1}$	100.086
f_{Si}	biogenic Si protection ratio	$\mathrm{gC(gSi)}^{-1}$	0.026
f_{CaCO_3}	calcium carbonate protection ratio	–	0.070
d_{excess}	excess organic carbon dissolution length scale	m	188
d_{CaCO_3}	calcium carbonate dissolution length scale	m	3500
d_{Si}	biogenic Si dissolution length scale	m	2000

Table A12: Miscellaneous parameters

Symbol	**State variable**	**Units**	**Value**
L_{total}	total ligand concentration of seawater	$\mu\mathrm{mol\,m}^{-3}$	1.0
k_{FeL}	dissociation constant for (Fe + ligand)	$\mu\mathrm{mol\,m}^{-3}$	100
k_{scav}	scavenging rate of free (non-ligand bound) iron	d^{-1}	0.001
ω_g	detrital sinking rate	$\mathrm{m\,d}^{-1}$	2.5

APPENDIX B

B1 Media

The Arctic phytoplankton response to an ice-free Arctic reported in this thesis was covered by The Economist; where some of the wider implications of the result are dealt with.

The Arctic Ocean Awakening. Economist Feb 14th 2015 print edition

B2 Published papers

1. On the vertical phytoplankton response to an ice-free Arctic Ocean
The main insight from the numerical results presented in Chapter 4 were published as a paper in Journal of Geophysical Research Oceans, matching a conference talk on the same topic. The paper explores the expected response of phytoplankton to an ice-free Arctic Ocean by considering plankton vertical distribution over the water column. It concludes that Arctic Ocean productivity changes are likely to be small, 10% in a seasonally ice-free Arctic Ocean and increasing to 30% by the end of the century, occurring at depth.

Lawrence, J., Popova, E., Yool, A. and Srokosz, M., 2015. On the vertical phytoplankton response to an ice-free Arctic Ocean. *Journal of Geophysical Research: Oceans*, 120(12), pp.8571-8582. DOI: 10.1002/2015JC011180

2. Net primary productivity estimates and environmental variables in the Arctic Ocean: An assessment of coupled physical-biogeochemical models

This collaboration between several international Arctic Ocean biogeochemical modelling groups assesses the capability of current numerical models and suggests the primary areas that should be focussed on for their improvement

Lee, Y.J.,... Lawrence, J. and others, 2016. Net primary productivity estimates and environmental variables in the Arctic Ocean: An assessment of coupled physicalbiogeochemical models. *Journal of Geophysical Research: Oceans*, 121, pp.1-35, DOI: 10.1002/2016JC011993.

AGU PUBLICATIONS

JGR

Journal of Geophysical Research: Oceans

RESEARCH ARTICLE
10.1002/2015JC011180

Special Section:
Forum for Arctic Modeling and Observational Synthesis (FAMOS): Results and Synthesis of Coordinated Experiments

Key Points:
- We use a 1/4° ocean biogeochemical model to assess Arctic primary production
- Net primary production is linked to nitrate-light conditions
- Application to future production suggests modest increases, occurring at depth

Supporting Information:
- Supporting Information S1

Correspondence to:
J. Lawrence,
jonathan.lawrence@noc.soton.ac.uk

Citation:
Lawrence, J., E. Popova, A. Yool, and M. Srokosz (2015), On the vertical phytoplankton response to an ice-free Arctic Ocean, *J. Geophys. Res. Oceans, 120*, 8571–8582, doi:10.1002/2015JC011180.

Received 31 JUL 2015
Accepted 3 DEC 2015

On the vertical phytoplankton response to an ice-free Arctic Ocean

J. Lawrence[1,2], E. Popova[1], A. Yool[1], and M. Srokosz[1]

[1]National Oceanography Centre, Southampton, UK, [2]National Oceanography Centre, University of Southampton, Southampton, UK

Abstract Rapidly retreating sea ice is expected to influence future phytoplankton production in the Arctic Ocean by perturbing nutrient and light fields, but poor understanding of present phytoplankton distributions and governing mechanisms make projected changes highly uncertain. Here we use a simulation that reproduces observed seasonal phytoplankton chlorophyll distributions and annual nitrate to hypothesize that surface nitrate limitation in the Arctic Ocean deepens vertical production distributions where light-dependent growth rates are lower. We extend this to interpret depth-integrated production changes projected by the simulation for an ice-free Arctic Ocean. Future spatial changes correspond to patterns of reduced surface nitrate and increased light. Surface nitrate inventory reductions in the Beaufort Gyre and Atlantic inflow waters drive colocated production distributions deeper to where light is lower, offsetting increases in light over the water column due to reduced ice cover and thickness. Modest production increases arise, 10% in a seasonally ice-free Arctic Ocean and increasing to 30% by the end of the century, occurring at depth.

1. Introduction

Rapid reductions in Arctic sea ice thickness [*Laxon et al.*, 2013] and extent [*Serreze et al.*, 2007; *Stroeve et al.*, 2012], increased seasonality [*Serreze et al.*, 2007] and shifts from perennial to first year ice [*Stroeve et al.*, 2012], are underway. Reductions in sea ice and changes in seasonality are expected to modify stratification and momentum transfer to the ocean (for example, through internal wave generation [*Rainville and Woodgate*, 2009] and changes in ocean wind stress [*Carmack and Chapman*, 2003; *Davis et al.*, 2014]), which modulates nitrate supply to the euphotic zone [*Popova et al.*, 2006]. Reductions in ice thickness and extent will also impact light available for photosynthesis [*Arrigo et al.*, 2008; *Arrigo and van Dijken*, 2015].

Changes are already underway in the Canada Basin [*McLaughlin et al.*, 2011]. Freshwater accumulation [*Giles et al.*, 2012], probably arising from increased momentum transfer to the ocean [*Giles et al.*, 2012; *Davis et al.*, 2014], has driven a general increase in stratification [*McLaughlin et al.*, 2011]. Convergence and stratification increases have driven concomitant reductions in surface nitrate [*McLaughlin and Carmack*, 2010], deepening summer chlorophyll maxima [*McLaughlin and Carmack*, 2010; *Bergeron and Tremblay*, 2014], and favoring phytoplankton with smaller cell sizes that are more efficient at nutrient uptake [*Li et al.*, 2009]. These changes are likely due to a combination of both long-term sea ice retreat and decadal changes in the wind-driven circulation [*Proshutinsky et al.*, 2002]. For example, freshening of the surface Arctic Ocean arising from climatic changes in precipitation [*Bintanja and Selten*, 2014], runoff, and sea ice cover [*Peterson et al.*, 2006] is exacerbated by increased freshwater storage in the Canadian Arctic Ocean under current decadal wind patterns [*McLaughlin et al.*, 2011; *Giles et al.*, 2012].

Phytoplankton distributions and growth are expected to continue to respond to sea ice retreat but controlling mechanisms across the Arctic Ocean remain unclear [*Arrigo et al.*, 2008; *Tremblay and Gagnon*, 2009; *Codispoti et al.*, 2013; *Brown et al.*, 2015]. Consequently, even the direction of future changes in Arctic Ocean production is highly uncertain [*Steinacher et al.*, 2010; *Popova et al.*, 2012; *Vancoppenolle et al.*, 2013].

In particular, substantial phytoplankton growth can occur under ice [*Arrigo et al.*, 2012; *Matrai and Apollonio*, 2013] and in photosynthetically competent subsurface chlorophyll maxima [*Hill and Cota*, 2005; *McLaughlin and Carmack*, 2010], but the distribution and magnitude of under ice and subsurface production remain unclear [*Arrigo et al*., 2011; *Hill et al*., 2013; *Martin et al*., 2013] because they are not retrievable by satellite [*Smith*, 1980; *Pabi et al*., 2008].

Here we use a simulation that reproduces observed phytoplankton chlorophyll distributions across the Arctic Ocean, including in subsurface chlorophyll maxima and under ice, to elucidate what governs vertical net production distributions over the seasonal cycle. We will then use this generalizable response of Arctic Ocean phytoplankton to nitrate and light conditions to explain simulation-projected changes in depth-integrated net production (hereafter production) in terms of its vertical distribution.

2. Methods

2.1. Simulation Description

For the simulation, an intermediate complexity biogeochemical model (MEDUSA) [*Yool et al*., 2013], embedded within a general circulation model (NEMO) that comprises ocean (OPA) [*Madec*, 2008] and ice (LIM2) [*Timmermann et al*., 2005] components, is run to 2099 at a global-average model resolution of 1/4°. The grid is nonlinear and resolution increases toward the poles. For example, resolution at 60°N is ~16.8 km. The model is forced with output from HadGEM-ES [*Collins et al*., 2011] under representative concentration pathway (RCP) 8.5 [*Riahi et al*., 2011]. Production is calculated for two phytoplankton classes. This is done by modulating a temperature-dependent theoretical maximum production rate, as per *Eppley* [1972], by standard Michaelis-Menten nutrient limitation and hyperbolic light limitation terms. Photoacclimation is factored in through a chlorophyll-specific initial slope of the photosynthesis-irradiance curve. Full details can be found in *Yool et al*. [2013].

2.2. Defining Production, Nitrate, and Light Metrics

Here we consider pan-Arctic Ocean net primary production (hereafter primary production or production): the biological uptake of inorganic nutrients from physical supply in waters north of 65°N. To describe the vertical structure of primary production across the Arctic Ocean, we consider production that occurs above and below a reference depth. Throughout the analysis, we term the former as surface production (P_1) and the latter as subsurface production (P_2). Based on production distributions inferred from nitrate uptake [*Codispoti et al*., 2013; *Matrai and Apollonio*, 2013] and chlorophyll and production profiles [*Martin et al*., 2010; *McLaughlin and Carmack*, 2010; *Brown et al*., 2015], we chose a reference depth of 20 m (explained in section 4). The subsurface fraction of production is defined as that which occurs below the reference depth

$$\mathrm{Prop}=\frac{P_2}{P_1+P_2}, \tag{1}$$

giving a simple metric that can be related to ambient nitrate and light conditions. Nitrate is dominantly supplied to the euphotic zone through winter mixing [*Tremblay and Gagnon*, 2009; *Popova et al*., 2010; *Codispoti et al*., 2013; *Randelhoff et al*., 2015] and taken up by phytoplankton in summer [*Arrigo et al*., 2008]. We therefore define an annual nitrate inventory (N_{inv}) as the nitrate concentration at the time of maximum mixed layer depth, integrated from the surface to the reference depth. Following previous observational studies [*Codispoti et al*., 2013; *Hill et al*., 2013; *Matrai et al*., 2013; *Randelhoff et al*., 2015], we take the main phytoplankton growth season in the Arctic Ocean to occur between July and September. We then define a solar radiation dose (SRD) as photosynthetically active (400–700 nm) radiation penetrating surface waters through sea ice cover, averaged over July–September and integrated to the reference depth. We use a static reference depth rather than mixed-layer depth, because observations [*Martin et al*., 2010; *McLaughlin and Carmack*, 2010] and our simulation (Figure 1) demonstrate that phytoplankton growth can occur below the mixed layer in summer.

At lower Arctic latitudes (toward 65°N), the phytoplankton growth season may start earlier than July. To test the validity of the July–September interval, we ran an additional analysis covering May–September. This analysis (see supporting information Figure S1) showed that the ability to predict vertical distributions of production declines when the interval is extended to include May and June, justifying the selection of July–September.

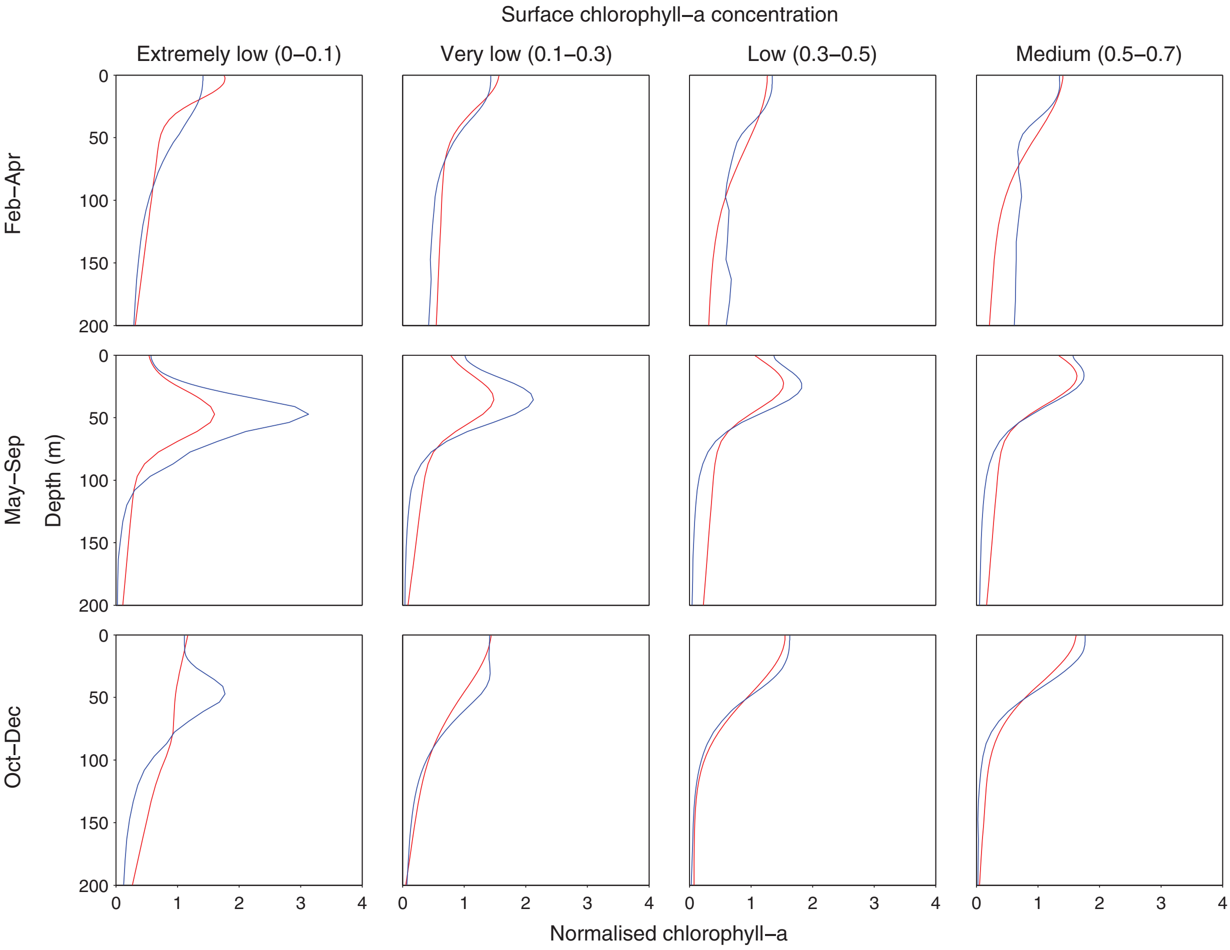

Figure 1. Observed (red) and simulated (blue) Arctic normalized chlorophyll-a profiles, sorted by season and surface chlorophyll concentration. Observations (n = 2403 profiles) span 1954–2007, whereas simulated profiles span 1990–2009. Locations where water depths are <50 m are omitted. Observations cover variable ice conditions but are biased toward open water and summer months; details of the observations can be found in *Ardyna et al.* [2014].

Deepening of production distributions in the projection is presented in terms of deepening chlorophyll and production maxima, where maxima are defined as the depth at which production and chlorophyll profiles are at their water column maximum value.

Surface nitrate depletion is masked at an inventory of 50 mmol m^{-2} to emphasize the spatial correspondence between low surface nitrate waters and production changes—the correspondence arises below this threshold because of the nonlinear dependence of nitrate limitation on ambient nitrate concentrations [*Monod*, 1949].

2.3. Building the Regression Model

We suggest that the vertical structure of Arctic Ocean primary production depends on N_{inv} and SRD. To demonstrate this, we determine how well a multilinear regression model based on the predictors N_{inv} and SRD can predict the spatial map of Prop (equation (1)) that arises from the full simulation. Because our simulation reproduces observed vertical distributions of phytoplankton (Figure 1), a regression model that can accurately predict Prop that arises in the full simulation implies that other variables, such as temperature, are not important in determining vertical production distributions across the Arctic Ocean. The ability of N_{inv} and SRD to predict the vertical distribution of production is tested by building a regression model that is then plotted against the full numerical simulation Prop. Thus, in this analysis, locations where the regression model reproduces the full simulation lie on a 1–1 line. Larger deviations from this line reflect decreasing ability of the linear regression model to reproduce vertical production distributions in the full simulation, possibly either due to nonlinearities in the dependence of production on nitrate and light [*Bergeron and Tremblay*, 2014] or the importance of other variables in setting Prop.

2.4. Direct Temperature Impact on Production

The importance of surface-ocean warming on projected changes in depth-integrated production is testable in the simulation from the temperature dependence of phytoplankton growth rates [*Eppley*, 1972]. The simulated maximum growth rate of phytoplankton is directly dependent on temperature as

$$J_{\max}=V_{\mathrm{p}} * 1.066^{T}, \tag{2}$$

where V_{p} is the maximum growth rate at 0°C [*Eppley*, 1972; *Yool et al.*, 2013]. This maximum growth rate is modulated by nitrate and light limitation such that it is only realized in nitrate and light replete conditions.

3. Results

3.1. Simulation-Observation Chlorophyll Comparison

The simulation reproduces observed Arctic Ocean seasonal chlorophyll distributions (Figure 1). Seasonal increases in light stimulate a spring bloom in nitrate replete surface waters with chlorophyll profiles decreasing with depth according to attenuation of light in the water column (top row). In more oligotrophic waters, surface nitrate depletion by the spring bloom promotes the subsequent development of a shade flora. The subsurface chlorophyll maxima that develop are more pronounced and occur deeper in more oligotrophic waters, a feature captured by the simulation (middle row). In autumn, increased mixing replenishes surface nitrate, and chlorophyll maxima return to surface waters (bottom row), accompanied in ice-free waters by a second bloom [*Ardyna et al.*, 2014]. Deviation of the simulation from observed chlorophyll profiles is restricted to areas with extremely low surface chlorophyll where the model overestimates the strength of summer subsurface chlorophyll maxima and insufficiently homogenizes the vertical chlorophyll distribution during winter mixing (middle left and bottom left plots, respectively).

3.2. Simulation-Observation Nitrate Comparison

Nitrate is depleted in Arctic Ocean summer surface waters [*Codispoti et al.*, 2013], limiting net community production across the Arctic Ocean [*Tremblay et al.*, 2008; *Tremblay and Gagnon*, 2009; *Randelhoff et al.*, 2015]. Here we compare simulated annual-average nitrate to the World Ocean Atlas 2013 (WOA) [*Garcia et al.*, 2014] along a Pacific-Atlantic transect that traverses the Central Basin (Figure 2). Surface nitrate is broadly higher at lower latitudes (toward 65°N) where nitrate is supplied to the Arctic Ocean [*Le Fouest et al.*, 2013; *Torres-Valdés et al.*, 2013] and decreases interiorward as nitrate is removed from surface waters by biological processes and inflowing waters subduct below the halocline [*Hioki et al.*, 2014]. The simulation broadly captures observed nitrate concentrations along the transect, with the exception of the Chukchi shelf where simulated upstream concentrations advected in from the Pacific are too high and observational biases toward summer may also bias the comparison [*Brown et al.*, 2015]. We note that few observations are available for the Central Basin.

3.3. Predicting the Vertical Distribution of Production

A composite of observational time series suggests a consistent seasonal cycle of vertical production distributions across the Arctic Ocean. Supply of nitrate to the euphotic zone across the Arctic Ocean is dominated by entrainment in the winter mixed layer [*Sundfjord et al.*, 2007, 2008; *Tremblay and Gagnon*, 2009; *Codispoti et al.*, 2013; *Randelhoff et al.*, 2015]. Because temperatures are cold and exhibit relatively small vertical variability across the Arctic Ocean [*Steele et al.*, 2001], vertical changes in phytoplankton nitrate uptake rates during the following growing season are determined by light. Therefore, seasonal nitracline deepening rates across the Arctic Ocean may depend on the surface nitrate inventory at the time of maximum mixed-layer depths and solar radiation dose the following summer.

Phytoplankton respond to nitracline deepening by more growth in the water column occurring at depth [*Martin et al.*, 2010; *McLaughlin and Carmack*, 2010; *Bergeron and Tremblay*, 2014]. Therefore, the vertical distribution of production over an annual cycle may be determined by the winter-entrained nitrate inventory and summer solar radiation dose. Spatial maps of simulated subsurface production fraction, nitrate

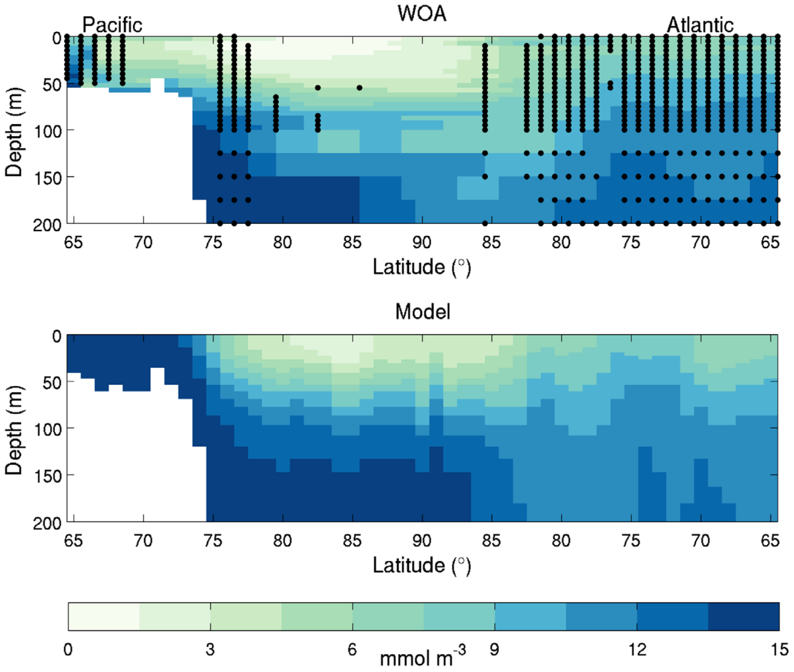

Figure 2. Transect of annual mean (top) observed (World Ocean Atlas) and (bottom) simulated Arctic dissolved inorganic nitrogen in the surface ocean (mmol m^{-3}). The transect runs from Bering Straits to Fram Straits (65°N–90°N at 169°W and 5°W), as shown in Figure 3a. Grid squares containing observations are shown by black dots in the top of the figure (number of observations = 5923). Observation distribution is biased toward lower latitudes (toward 65°N).

inventory, and solar radiation dose demonstrate this (Figure 3). The subsurface fraction of production is higher where the nitrate inventory is lower or solar radiation dose is higher: such as in the Beaufort Gyre and Admunsen Gulf, where stratification and Ekman convergence prevent entrainment of nitrate into surface waters [*Martin et al*., 2010; *McLaughlin and Carmack*, 2010] and our simulation (Figure 3c) and observations [*Tremblay et al*., 2008; *Mundy et al*., 2009; *Martin et al*., 2010] concur that a substantial proportion of annual production happens in subsurface chlorophyll maxima. Conversely, in low light areas, subsurface production is low (Figure 3).

A simple multilinear regression model based on colocated N_{inv} and SRD captures 73% of the simulated variance in the subsurface fraction of annual production (Figure 4). Therefore, the contribution phytoplankton growth at depth makes to depth-integrated annual production is predictable from colocated N_{inv} and SRD.

To examine the spatial variability of simulated vertical production distributions, we split the Arctic Ocean into three geographic regions (Figure 4, inset). First, we delineate inflows as waters exterior of main gateways and the Central Arctic Ocean as interior waters. A third region is then used to show the transformation of water masses as they transit across the Canadian Arctic Ocean from the Pacific inflow to their outflow along the west side of Baffin Bay [*Curry et al*., 2014].

Examining the vertical distribution of production across these three regions then shows the relationship between this subsurface fraction, ice cover, and physical nitrate supply. Around the edge of the Arctic Ocean, ice-free (high SRD, Figure 3b) conditions enable substantial production at depth (Figure 4). Conversely, in the Central Basin and the Chukchi inflow, extensive ice cover (low SRD, Figure 3b) prevents substantial production at depth (Figure 4). SRD and the subsurface fraction increase toward the inflows where ice cover is reduced (Figure 3).

As water masses transit from the Pacific inflow across the Canadian Arctic Ocean, they experience nitrate depletion due to phytoplankton uptake [*Tremblay et al*., 2008] and denitrification [*Yamamoto-Kawai et al*., 2006; *Chang and Devol*, 2009]. Subduction of nitrate replete waters [*Hioki et al*., 2014] and Ekman convergence in the Beaufort Gyre [*McLaughlin and Carmack*, 2010] further reduces $N_{inv.}$

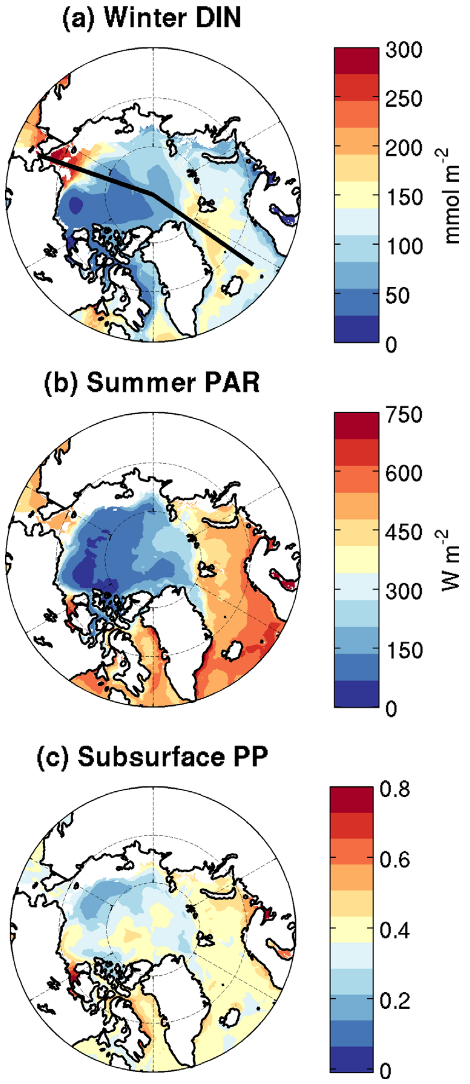

Figure 3. Decade-mean (2000s) simulated (a) winter (month of colocated max mixed layer depth) dissolved inorganic nitrogen (DIN) inventory (N_{inv}, mmol m^{-2}), (b) summer-mean (July–September) solar photosynthetically active irradiance (PAR) dose (SRD, Wm^{-2}), (c) proportion of annual primary production that occurs below 20 m (Subsurface PP). Water depths <50 m are masked in all plots to prevent bias of the subsurface fraction in Figure 3c. The location of the transect plotted in Figure 2 is shown in Figure 3a (black line).

Depletion of N_{inv} in our simulation drives deepening of production maxima, resulting in an increasing subsurface fraction of production as waters move across the Canadian Arctic Ocean (Figure 4). The broad pattern that arises is modulated by ice cover such that the light replete Admunsen Gulf has the highest proportion of production subsurface (Figure 3).

Our simulation demonstrates that reduced N_{inv} causes deepening of production distributions. A higher proportion of annual growth then occurs at depth (>0.5) where light-dependent growth rates are lower. However, under thicker ice, SRD is too low to support net photosynthesis at depth so the subsurface fraction is low (<0.3) despite low N_{inv} (Figure 3).

In the first case, depth-integrated production rates are reduced because surface nitrate depletion necessitates phytoplankton grow at depth where light is lower. In the second case, rates are lower because ice cover reduces light over the entire water column. Therefore, depth-integrated production decreases toward low and high subsurface fractions of production, being maximum at intermediate subsurface fractions. In our simulation, intermediate subsurface fractions correspond to inflows, in agreement with observational-based estimates of depth-integrated production which are also maximum here [*Sakshaug*, 2004; *Arrigo et al.*, 2008; *Pabi et al.*, 2008; *Codispoti et al.*, 2013; *Hill et al.*, 2013].

This analysis suggests that CMIP5 21st-century projections of N_{inv} reductions and SRD increases, that are robust across the ensemble [*Vancoppenolle et al.*, 2013], may cause deepening of production distributions. The impact of increased light over the water column on depth-integrated production would then be offset by reduced light experienced by deeper growth. We now demonstrate this response in the full simulation.

3.4. Phytoplankton Response to an Ice-Free Arctic

The Arctic Ocean is predicted to be ice free by the end of the century [*Boé et al.*, 2009], and perhaps as early as 2054–2058 [*Liu et al.*, 2013]. Physical nitrate supply to surface waters is expected to decrease as Arctic sea ice retreats and light increases [*Vancoppenolle et al.*, 2013].

Here we simulate the onset of a seasonally ice-free Arctic Ocean in the 2050s and a modest reduction in mixed-layer depth from the present day to 2099 (Figure 5a). Unrealistic fluctuations in simulated winter mixed layer depth arise from localized overmixing in the model south of Fram Strait and do not impact Arctic-average N_{inv} (Figure 5b).

Reducing surface nitrate (Figure 5b) induces the expansion of low surface nitrate waters (Figure 6a). Deepening of the nitracline and increased light induces deepening of geographically colocated chlorophyll and production maxima (Figures 5c and 6c) as phytoplankton adjust to the perturbed nitrate and light conditions. Phytoplankton

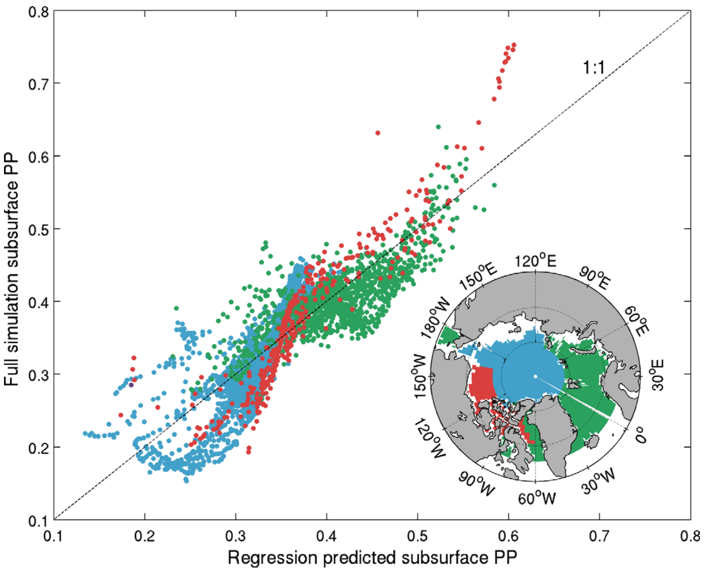

Figure 4. The simulated (2000s) proportion of annual production occurring subsurface (below 20 m) plotted against that predicted by a linear regression model based on N_{inv} and SRD. First, we construct the linear regression model which regresses N_{inv} and SRD to Prop (PropReg = 0.000430 SRD − 0.00120 N_{inv} + 0.355, $R^2 = 0.731$, $p < 0.001$). Data are grouped into three geographical regions: inflows, central Arctic, and the Canadian Arctic, as shown on the inset map. Baffin Bay is split between the Canadian Arctic Outflow to the west and West Greenland Current influenced waters to the east. Water depths <50 m are masked (as in Figure 3) to prevent bias of the subsurface production fraction.

maxima deepen more slowly than the nitracline, resulting in increasingly offset depths which reflect the increase in light limitation with depth. This is in agreement with the observed phytoplankton response to low light at depth in oligotrophic conditions [*McLaughlin and Carmack*, 2010; *Bergeron and Tremblay*, 2014]. Reductions in N_{inv} occur in both Pacific and Atlantic inflows but extremely low inventories (<50 mmol m^2) are only reached in the Atlantic inflow because the decreasing trend starts from a lower present-day inventory here. N_{inv} decreases in both inflows in the simulation because nitrate supply that originates in the subpolar North Atlantic and Pacific decreases in the coming century, in agreement with most CMIP5 models [*Vancoppenolle et al.*, 2013].

Simulated depth-integrated production changes reflect the ability of SRD increases to compensate reduced N_{inv} (Figure 6d). We broadly simulate decreasing production in open water and increasing production within the present ice zone, in agreement with ensemble projections [*Steinacher et al.*, 2010; *Vancoppenolle et al.*, 2013]. This broad pattern is modulated by regional differences in nitrate supply. N_{inv} reductions fully offset SRD increases in the Beaufort Gyre and exceed them downstream where present-day ice cover is thinner and less extensive. Reduced advective nitrate supply to the Siberian shelves exceeds modest SRD increases here.

As the ice retreats and N_{inv} diminishes, SRD increases over the water column are offset by reduced light experienced by deeper phytoplankton growth. Simulated production increases in a future Arctic Ocean are therefore modest. They are 10% at the onset of a seasonally ice-free Arctic Ocean and 30% by the end of the century, with increases occurring solely at depth (Figure 5d).

Phytoplankton metabolic rates are temperature dependent, therefore future Arctic Ocean production changes may be sensitive to ocean warming [*Slagstad et al.*, 2011]. We test the direct impact of sea surface temperature increases on production by using the temperature dependence of simulated phytoplankton growth rates (equation (2)).

We find that despite substantial warming of water flowing into the Arctic Ocean (6–8°C, Figure 7a), direct temperature effects on phytoplankton growth are more modest (40–60%, Figure 7b) compared to SRD and N_{inv} effects across the Arctic Ocean (up to 220%, Figure 6d). Substantial direct temperature-driven increases are restricted to inflows because warmer inflowing surface waters are cooled as they are advected into the Arctic Ocean. Inflowing surface waters where warming occurs generally retain surplus nitrate (Figure 6b) indicating that most of the direct simulated temperature impacts correspond to realized production changes.

4. Discussion

We have shown that vertical production distributions across the Arctic Ocean are governed by local balances in N_{inv} and SRD. N_{inv}-SRD balances that result in low or high subsurface fractions of production lead to low depth-integrated annual production. We have demonstrated that nitrate reductions act to deepen production distributions where light-dependent growth rates are lower, provided light at depth is sufficient to support net growth (Figures 3 and 4). Therefore, CMIP5 projections of reducing N_{inv} [*Vancoppenolle et al.*, 2013] are expected to deepen future production distributions such that increases in SRD due to ice retreat are offset by lower light levels experienced at greater depth (Figures 5 and 6).

In the simulation, low N_{inv} waters are found over the Beaufort Gyre (Figure 6b). Simple process models suggest that sea ice decline will increase Beaufort Gyre convergence [*Davis et al.*, 2014]. Recent convergence has reduced N_{inv} [*McLaughlin and Carmack*, 2010], suggesting that increased convergence under ice retreat may play a role in future N_{inv} reductions in the Beaufort Sea and downstream Canadian Archipelago. Our simulation shows such a change, with some of the largest relative reductions in production arising from convergence in the Beaufort Sea and downstream low N_{inv} waters (Figure 6d).

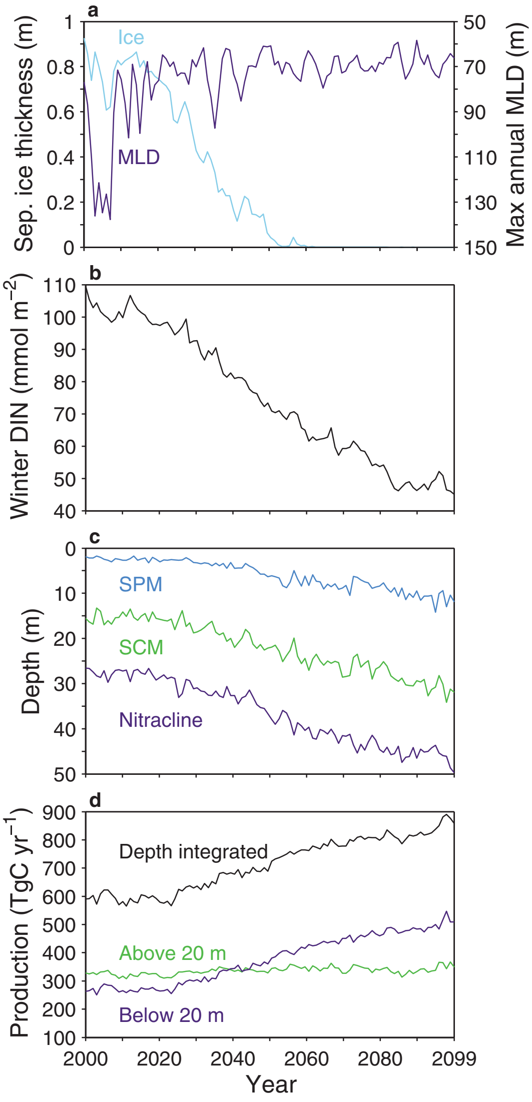

Figure 5. Arctic-average (>65°N) simulated 21st century trends in (a) September ice thickness (ice) and maximum annual mixed layer depth (MLD, m), (b) winter dissolved inorganic nitrogen (DIN) inventory (N_{inv}, mmol m^{-2}), (c) September production maxima (SPM), chlorophyll maxima (SCM), and nitracline depths (m), and (d) annual surface, subsurface and total production (Tg C yr^{-1}).

Large Arctic Ocean production decreases are colocated with September production maxima deepening, except on the Siberian shelves where water depths are too shallow (Figures 6c and 6d). Maxima deepening does not occur across the Arctic Ocean but is localized to extremely low N_{inv} waters. The explanation for this can be found in our analysis of contemporary forcing of phytoplankton distributions by surface nitrate conditions. We have shown that surface nitrate depletion acts to deepen production distributions but may only do so when there is sufficient light to enable production at depth. Therefore, our analysis predicts deepening of production distributions across a broad area of the future Arctic Ocean, verified in the simulation where production increases (Figure 6d) are taken up at depth (Figure 5d). However, production maxima correspond to the depth of minimal nitrate-light colimitation. Since light attenuates exponentially with depth, light limitation increases rapidly with depth and extremely low nitrate concentrations are required to deepen production maxima. For this reason, simulated production maxima deepening is colocated with extremely low surface nitrate concentrations (Figures 6b and 6c).

In elucidating the controls on vertical production distributions, we assumed temperature effects on growth rates are small because vertical temperature gradients in the Arctic Ocean are small. We subsequently demonstrated that this assumption is valid by predicting vertical production distributions with a regression model that neglects temperature (Figure 4). Further, projected depth-integrated production changes are dependent on increases in sea surface temperature (SST) which directly affect growth rates. The contribution of direct temperature effects is shown to be more modest than SRD-N_{inv}-driven changes at the pan-

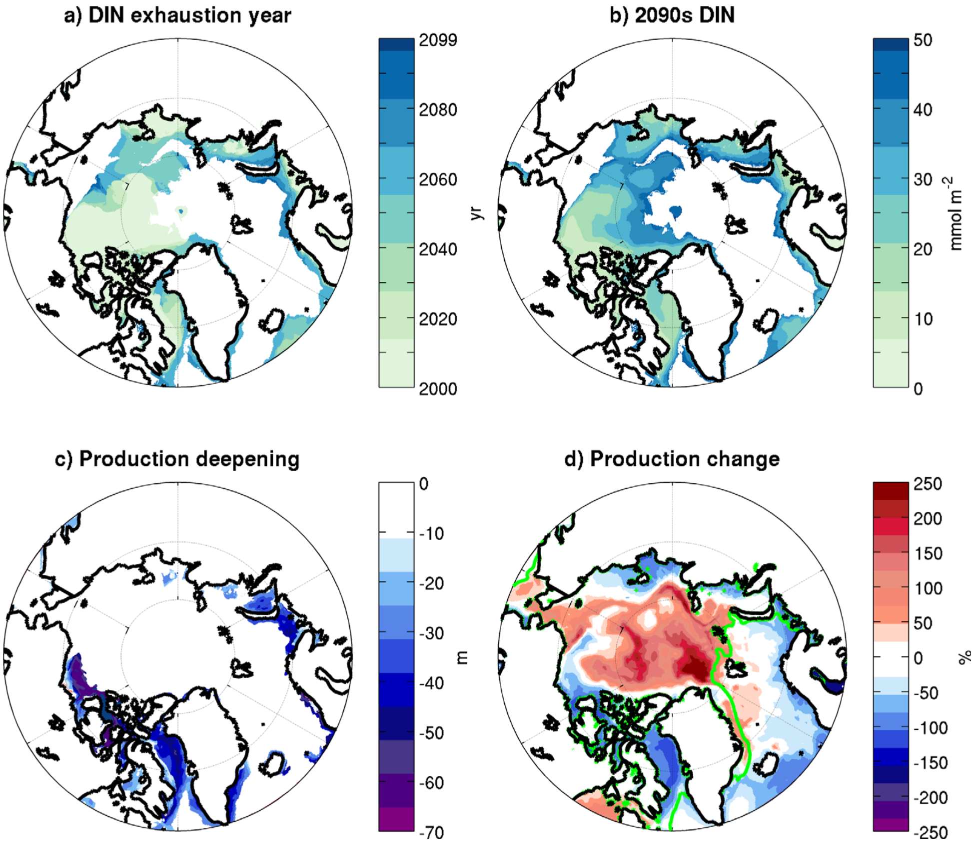

Figure 6. Twenty-first century changes in simulated dissolved inorganic nitrogen and primary production. (a) Onset year at which N_{inv} first drops below 50 mmol m^{-2} (masked areas do not reach this threshold). (b) The 2090s N_{inv} (mmol m^{-2}), masked to only show locations where the inventory is below 50 mmol m^{-2}. (c) The 2090s to 2000s change in September production maxima depth (m) (negative values indicate deepening). (d) The 2090s to 2000s change in annual production (%) with 2000s winter-average (January–March) 95% ice cover contour (green line).

Arctic Ocean scale, failing to compensate N_{inv}-driven reductions in inflows (Figures 6 and 7). We stress that direct temperature effects, as defined here (equation (2)), can only impact production in light and nitrate replete conditions. Therefore, one reason for more modest contributions from direct temperature effects

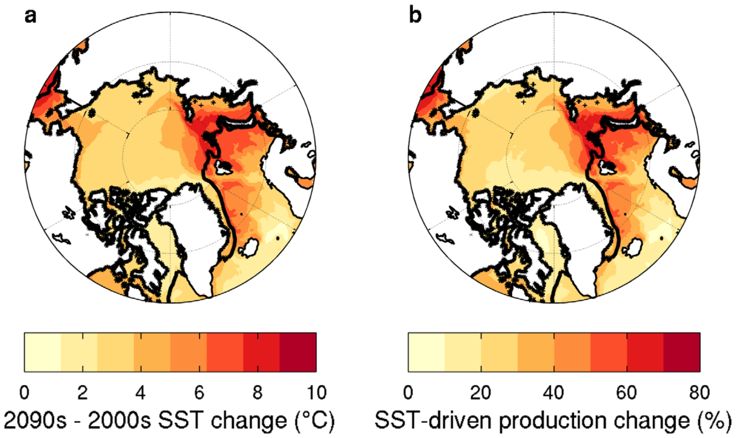

Figure 7. Simulated 2090s to 2000s change in (a) sea surface temperature (SST, °C) and (b) direct temperature-driven production increases (%). The simulated present-day (2000s) winter-average (January–March) 95% ice cover contour is shown (black line).

could be that N_{inv} reductions negate the possibility of SST-driven annual production increases being realized because growth rates may be temperature dependent but annually integrated production increases require available nitrate. In the simulation, SST-driven increases generally occur outside areas where severely limiting nitrate concentrations are projected (Figures 6b and 7b), implying that SST-driven production increases are realized here and are locally important in offsetting N_{inv} reductions in inflows. SST effects on production generally do not overlap with low N_{inv} waters because nitrate is supplied to the surface Arctic Ocean in warm, nitrate replete inflows [*Torres-Valdés et al.*, 2013], which are cooled and depleted of nitrate as they move interiorward into the Arctic Ocean.

We have shown the impact of N_{inv} and SRD on the vertical distribution of production by using a reference depth of 20 m. Now that we have elucidated the impacts of N_{inv} and SRD on the vertical distribution of growth, we can explain what the significance of our choice is. Light limitation increases with depth and nitrate limitation decreases with depth. It is the opposing effects of these limitations that promote deepening of production distributions following exhaustion of surface nitrate in summer (Figures 3 and 4) and enables production maxima to be subsurface in extremely low nitrate conditions (Figure 6). We chose a reference depth based on observed vertical distributions of phytoplankton to highlight these opposing limitations, 20 m being the approximate depth at which the limitations balance.

Therefore, the analysis presented here is not sensitive per se to the reference depth, but at extreme reference depths one of nitrate or light limitation dominates and we end up with the trivial results that occur at the limits. For example, if we chose a very deep reference depth and define SRD and N_{inv} as being integrated from the surface to the reference depth then light limitation will dominate at all locations in the Arctic Ocean. Conversely, if we chose a very shallow reference depth then nitrate limitation dominates. Further, with shallow reference depths Prop (equation (1)) tends toward 1 and with deep reference depths toward 0. Therefore, with deep reference depths, we arrive at the result that light limitation dominates nitrate limitation so growth is restricted to above the reference depth. At shallow reference depths, nitrate limitation dominates so growth is predominantly below the reference depth.

From this, it can be seen that while all reference depths produce consistent and physically sound results, choosing the right reference depth is necessary to see the full impact of nitrate and light limitation on the vertical distribution of Arctic Ocean production.

Models within the CMIP5 ensemble agree on a reduction in N_{inv} contemporary with ice retreat yet disagree on the sign of future production changes [*Vancoppenolle et al.*, 2013]. Our analysis replicates the N_{inv} trend (Figure 5b) and suggests why the current ensemble production projections diverge. Divergence may arise because the model hindcasts generally inadequately reproduce both N_{inv} and SRD [*Vancoppenolle et al.*, 2013], shown here to be central features of Arctic Ocean production dynamics and its anthropogenic perturbation. In particular, models differ in the extent of vertical mixing and most fail to account for production under ice [*Vancoppenolle et al.*, 2013], likely substantial across the ice-covered Arctic Ocean [*Arrigo et al.*, 2012; *Matrai and Apollonio*, 2013; *Arrigo et al.*, 2014]. Differences between models in the magnitude of nitrate reduction trend compound model divergence [*Vancoppenolle et al.*, 2013] but an essential prerequisite to evaluating this divergence will be hindcasts that adequately represent the processes elucidated here.

5. Conclusions

We have used a simulation of Arctic Ocean phytoplankton that reproduces observed chlorophyll and nitrate distributions to show that phytoplankton respond to colocated N_{inv} reductions and SRD increases by deepening of colocated production distributions. The spatial pattern of vertical production distributions (Figure 4) can therefore be related to local nitrate and light conditions (Figure 3).

Because N_{inv} reductions and SRD increases deepen production distributions, CMIP5 ensemble projections of reduced N_{inv} concomitant with ice retreat can be inferred to deepen future production distributions (Figures 5c and 6c). Therefore, light increases due to ice retreat are offset by lower light experienced by deeper production distributions.

Resulting Arctic Ocean production increases are modest, 10% in a seasonally ice-free Arctic, increasing to 30% by the end of the century, and occur at depth (Figure 5d).

Acknowledgments

We gratefully acknowledge the Forum for Arctic Modeling and Observational Synthesis (FAMOS, http://web.whoi.edu/famos/) for providing a forum for stimulating discussion which informed this manuscript. Observational data used in the analysis are available as cited in the manuscript. Model simulation results and code used in the analysis are available on request. The authors gratefully acknowledge the financial support of the Natural Environmental Research Council (NERC). The simulation work was performed as part of the Regional Ocean Modelling project (ROAM; grant NE/H017372/1), part of the NERC UK Ocean Acidification research programme (UKOA). J.L. is funded by a NERC PhD studentship. E.E.P., M.A.S., and A.Y. are supported by NERC National Capability funding. The high-resolution component of this work used the ARCHER UK National Supercomputing Service (http://www.archer.ac.uk). The HadGEM2-ES atmospheric forcing was produced by the UKMO and made available for use in NEMO by Dan Bernie (UKMO). Work to perform HadGEM2-ES simulations was supported by the EU-FP7 COMBINE project (grant 226520).

References

Ardyna, M., M. Babin, M. Gosselin, E. Devred, L. Rainville, and J.-É. Tremblay (2014), Recent Arctic Ocean sea ice loss triggers novel fall phytoplankton blooms, *Geophys. Res. Lett.*, *41*, 6207–6212, doi:10.1002/2014GL061047.

Arrigo, K., G. van Dijken, and S. Pabi (2008), Impact of a shrinking Arctic ice cover on marine primary production, *Geophys. Res. Lett.*, *35*, L19603, doi:10.1029/2008GL035028.

Arrigo, K., P. Matrai, and G. van Dijken (2011), Primary productivity in the Arctic Ocean: Impacts of complex optical properties and subsurface chlorophyll maxima on large-scale estimates, *J. Geophys. Res.*, *116*, C11022, doi:10.1029/2011JC007273.

Arrigo, K., et al. (2012), Massive phytoplankton blooms under Arctic sea ice, *Science*, *336*(6087), 1408–1408, doi:10.1126/science.1215065.

Arrigo, K., et al. (2014), Phytoplankton blooms beneath the sea ice in the Chukchi Sea, *Deep Sea Res., Part II*, *105*, 1–16, doi:10.1016/j.dsr2.2014.03.018.

Arrigo, K. R., and G. L. van Dijken (2015), Continued increases in Arctic Ocean primary production, *Prog. Oceanogr.*, *136*, 60–70, doi:10.1016/j.pocean.2015.05.002.

Bergeron, M., and J.-É. Tremblay (2014), Shifts in biological productivity inferred from nutrient drawdown in the southern Beaufort Sea (2003–2011) and northern Baffin Bay (1997–2011), Canadian Arctic, *Geophys. Res. Lett.*, *41*, 3979–3987, doi:10.1002/2014GL059649.

Bintanja, R., and F. Selten (2014), Future increases in Arctic precipitation linked to local evaporation and sea-ice retreat, *Nature*, *509*(7501), 479–482, doi:10.1038/nature13259.

Boé, J., A. Hall, and X. Qu (2009), September sea-ice cover in the Arctic Ocean projected to vanish by 2100, *Nat. Geosci.*, *2*(5), 341–343, doi:10.1038/ngeo467.

Brown, Z., K. Lowry, M. A. Palmer, G. van Dijken, M. Mills, R. Pickart, and K. Arrigo (2015), Characterizing the subsurface chlorophyll a maximum in the Chukchi Sea and Canada Basin, *Deep Sea Res., Part II*, *118*, 88–104, doi:10.1016/j.dsr2.2015.02.010.

Carmack, E., and D. C. Chapman (2003), Wind-driven shelf/basin exchange on an Arctic shelf: The joint roles of ice cover extent and shelf-break bathymetry, *Geophys. Res. Lett.*, *30*(14), 1778, doi:10.1029/2003GL017526.

Chang, B. X., and A. H. Devol (2009), Seasonal and spatial patterns of sedimentary denitrification rates in the Chukchi Sea, *Deep Sea Res., Part II*, *56*(17), 1339–1350, doi:10.1016/j.dsr2.2008.10.024.

Codispoti, L., V. Kelly, A. Thessen, P. Matrai, S. Suttles, V. Hill, M. Steele, and B. Light (2013), Synthesis of primary production in the Arctic Ocean: III. Nitrate and phosphate based estimates of net community production, *Prog. Oceanogr.*, *110*, 126–150, doi:10.1016/j.pocean.2012.11.006.

Collins, W., et al. (2011), Development and evaluation of an Earth-System model–HADGEM2, *Geosci. Model Dev.*, *4*(4), 1051–1075, doi:10.5194/gmdd-4-997-2011.

Curry, B., C. Lee, B. Petrie, R. Moritz, and R. Kwok (2014), Multiyear volume, liquid freshwater, and sea ice transports through Davis Strait, 2004–10, *J. Phys. Oceanogr.*, *44*(4), 1244–1266, doi:10.1175/JPO-D-13-0177.1.

Davis, P. E., C. Lique, and H. L. Johnson (2014), On the link between Arctic sea ice decline and the freshwater content of the Beaufort Gyre: Insights from a simple process model, *J. Clim.*, *27*(21), 8170–8184, doi:10.1175/JCLI-D-14-00090.1.

Eppley, R. W. (1972), Temperature and phytoplankton growth in the sea, *Fish. Bull*, *70*(4), 1063–1085.

Garcia, H., R. Locarnini, T. Boyer, J. Antonov, O. Baranova, M. Zweng, J. Reagan, and D. Johnson (2014), *World Ocean Atlas 2013, vol. 4, Dissolved Inorganic Nutrients (Phosphate, Nitrate, Silicate)*, A. Mishonov Technical ed., pp. 1–25, US Govern. Print. Off., Washington, D. C.

Giles, K. A., S. W. Laxon, A. L. Ridout, D. J. Wingham, and S. Bacon (2012), Western Arctic Ocean freshwater storage increased by wind-driven spin-up of the Beaufort Gyre, *Nat. Geosci.*, *5*(3), 194–197, doi:10.1038/ngeo1379.

Hill, V., and G. Cota (2005), Spatial patterns of primary production on the shelf, slope and basin of the Western Arctic in 2002, *Deep Sea Res., Part II*, *52*(24), 3344–3354, doi:10.1016/j.dsr2.2005.10.001.

Hill, V., P. Matrai, E. Olson, S. Suttles, M. Steele, L. Codispoti, and R. Zimmerman (2013), Synthesis of integrated primary production in the Arctic Ocean: II. In situ and remotely sensed estimates, *Prog. Oceanogr.*, *110*, 107–125, doi:10.1016/j.pocean.2012.11.005.

Hioki, N., et al. (2014), Laterally spreading iron, humic-like dissolved organic matter and nutrients in cold, dense subsurface water of the Arctic Ocean, *Sci. Rep.*, *4*, 6775, doi:10.1038/srep06775.

Laxon, S. W., et al. (2013), Cryosat-2 estimates of Arctic sea ice thickness and volume, *Geophys. Res. Lett.*, *40*, 732–737, doi:10.1002/grl.50193.

Le Fouest, V., M. Babin, and J.-É. Tremblay (2013), The fate of riverine nutrients on Arctic shelves, *Biogeosci. Discuss.*, *10*(6), 3661–3677, doi:10.5194/bg-10-3661-2013.

Li, W. K., F. A. McLaughlin, C. Lovejoy, and E. C. Carmack (2009), Smallest algae thrive as the Arctic Ocean freshens, *Science*, *326*(5952), 539–539, doi:10.1126/science.1179798.

Liu, J., M. Song, R. M. Horton, and Y. Hu (2013), Reducing spread in climate model projections of a September ice-free Arctic, *Proc. Natl. Acad. Sci. U. S. A.*, *110*(31), 12,571–12,576, doi:10.1073/pnas.1219716110.

Madec, G. (2008), *NEMO Ocean Engine*, Inst. Pierre-Simon Laplace, Paris, France.

Martin, J., J.-É. Tremblay, J. Gagnon, G. Tremblay, A. Lapoussière, C. Jose, M. Poulin, M. Gosselin, Y. Gratton, and C. Michel (2010), Prevalence, structure and properties of subsurface chlorophyll maxima in Canadian Arctic waters, *Mar. Ecol. Prog. Ser.*, *412*, 69–84, doi:10.3354/meps08666.

Martin, J., D. Dumont, and J. Tremblay (2013), Contribution of subsurface chlorophyll maxima to primary production in the Coastal Beaufort Sea (Canadian Arctic): A model assessment, *J. Geophys. Res. Oceans*, *118*, 5873–5886, doi:10.1002/2013JC008843.

Matrai, P., and S. Apollonio (2013), New estimates of microalgae production based upon nitrate reductions under sea ice in Canadian shelf seas and the Canada Basin of the Arctic Ocean, *Mar. Biol.*, *160*(6), 1297–1309, doi:10.1007/s00227-013-2181-0.

Matrai, P., E. Olson, S. Suttles, V. Hill, L. Codispoti, B. Light, and M. Steele (2013), Synthesis of primary production in the Arctic Ocean: I. Surface waters, 1954-2007, *Prog. Oceanogr.*, *110*, 93–106, doi:10.1016/j.pocean.2012.11.004.

McLaughlin, F. A., and E. C. Carmack (2010), Deepening of the nutricline and chlorophyll maximum in the Canada Basin interior, 2003–2009, *Geophys. Res. Lett.*, *37*, L24602, doi:10.1029/2010GL045459.

McLaughlin, F. A., E. C. Carmack, A. Proshutinsky, R. A. Krishfield, C. K. Guay, M. Yamamoto-Kawai, J. M. Jackson, and W. J. Williams (2011), The rapid response of the Canada Basin to climate forcing: From bellwether to alarm bells, *Oceanography*, *24*(3), 146–159.

Monod, J. (1949), The growth of bacterial cultures, *Annu. Rev. Microbiol.*, *3*, 371–394.

Mundy, C., M. Gosselin, J. Ehn, Y. Gratton, A. Rossnagel, D. Barber, J. Martin, J.-É. Tremblay, M. Palmer, and K. Arrigo (2009), Contribution of under-ice primary production to an ice-edge upwelling phytoplankton bloom in the Canadian Beaufort Sea, *Geophys. Res. Lett.*, *36*, L17601, doi:10.1029/2009GL038837.

Pabi, S., G. van Dijken, and K. Arrigo (2008), Primary production in the Arctic Ocean, 1998–2006, *J. Geophys. Res.*, *113*, C08005, doi:10.1029/2007JC004578.

Peterson, B. J., J. McClelland, R. Curry, R. M. Holmes, J. E. Walsh, and K. Aagaard (2006), Trajectory shifts in the Arctic and SubArctic freshwater cycle, *Science*, *313*(5790), 1061–1066, doi:10.1126/science.1122593.

Popova, E., A. Coward, G. Nurser, B. De Cuevas, M. Fasham, and T. Anderson (2006), Mechanisms controlling primary and new production in a global ecosystem model? Part I: Validation of the biological simulation, *Ocean Sci.*, *2*(2), 249–266.

Popova, E., A. Yool, A. Coward, Y. Aksenov, S. Alderson, B. D. Cuevas, and T. Anderson (2010), Control of primary production in the Arctic by nutrients and light: Insights from a high resolution ocean general circulation model, *Biogeosci. Discuss.*, *7*(4), 5557–5620, doi:10.5194/bg-7-3569-2010.

Popova, E., A. Yool, A. Coward, F. Dupont, C. Deal, S. Elliott, E. Hunke, M. Jin, M. Steele, and J. Zhang (2012), What controls primary production in the Arctic Ocean? Results from an intercomparison of five general circulation models with biogeochemistry, *J. Geophys. Res.*, *117*, C00D12, doi:10.1029/2011JC007112.

Proshutinsky, A., R. Bourke, and F. McLaughlin (2002), The role of the Beaufort Gyre in Arctic climate variability: Seasonal to decadal climate scales, *Geophys. Res. Lett.*, *29*(23), 2100, doi:10.1029/2002GL015847.

Rainville, L., and R. A. Woodgate (2009), Observations of internal wave generation in the seasonally ice-free Arctic, *Geophys. Res. Lett.*, *36*, L23604, doi:10.1029/2009GL041291.

Randelhoff, A., A. Sundfjord, and M. Reigstad (2015), Seasonal variability and fluxes of nitrate in the surface waters over the Arctic shelf slope, *Geophys. Res. Lett.*, *42*, 3442–3449, doi:10.1002/2015GL063655.

Riahi, K., S. Rao, V. Krey, C. Cho, V. Chirkov, G. Fischer, G. Kindermann, N. Nakicenovic, and P. Rafaj (2011), RCP 8.5: A scenario of comparatively high greenhouse gas emissions, *Clim. Change*, *109*(1–2), 33–57, doi:10.1007/s10584-011-0149-y.

Sakshaug, E. (2004), Primary and secondary production in the Arctic Seas, in *The Organic Carbon Cycle in the Arctic Ocean*, pp. 57–81, Springer, London, U. K.

Serreze, M. C., M. M. Holland, and J. Stroeve (2007), Perspectives on the Arctic's shrinking sea-ice cover, *Science*, *315*(5818), 1533–1536, doi:10.1126/science.1139426.

Slagstad, D., I. Ellingsen, and P. Wassmann (2011), Evaluating primary and secondary production in an Arctic Ocean void of summer sea ice: an experimental simulation approach, *Prog. Oceanogr.*, *90*(1), 117–131, doi:10.1016/j.pocean.2011.02.009.

Smith, R. (1980), Remote-sensing and depth distribution of ocean chlorophyll, *Mar. Ecol. Prog. Ser.*, *5*, 359–361.

Steele, M., R. Morley, and W. Ermold (2001), PHC: A global ocean hydrography with a high-quality Arctic Ocean, *J. Clim.*, *14*(9), 2079–2087.

Steinacher, M., et al. (2010), Projected 21st century decrease in marine productivity: A multi-model analysis, *Biogeosciences*, *7*(3), 979–1005, doi:10.5194/bg-7-979-2010.

Stroeve, J. C., M. C. Serreze, M. M. Holland, J. E. Kay, J. Malanik, and A. P. Barrett (2012), The Arctic's rapidly shrinking sea ice cover: A research synthesis, *Clim. Change*, *110*(3-4), 1005–1027, doi:10.1007/s10584-011-0101-1.

Sundfjord, A., I. Fer, Y. Kasajima, and H. Svendsen (2007), Observations of turbulent mixing and hydrography in the marginal ice zone of the Barents Sea, *J. Geophys. Res.*, *112*, C05008, doi:10.1029/2006JC003524.

Sundfjord, A., I. Ellingsen, D. Slagstad, and H. Svendsen (2008), Vertical mixing in the marginal ice zone of the northern Barents Sea–Results from numerical model experiments, *Deep Sea Res., Part II*, *55*(20), 2154–2168, doi:10.1016/j.dsr2.2008.05.027.

Timmermann, R., H. Goosse, G. Madec, T. Fichefet, C. Ethe, and V. Duliere (2005), On the representation of high latitude processes in the ORCA-LIM global coupled sea ice–ocean model, *Ocean Modell.*, *8*(1), 175–201, doi:10.1016/j.ocemod.2003.12.009.

Torres-Valdés, S., T. Tsubouchi, S. Bacon, A. C. Naveira-Garabato, R. Sanders, F. A. McLaughlin, B. Petrie, G. Kattner, K. Azetsu-Scott, and T. E. Whitledge (2013), Export of nutrients from the Arctic Ocean, *J. Geophys. Res. Oceans*, *118*, 1625–1644, doi:10.1002/jgrc.20063.

Tremblay, J.-É., and J. Gagnon (2009), The effects of irradiance and nutrient supply on the productivity of Arctic waters: A perspective on climate change, in *Influence of Climate Change on the Changing Arctic and Sub-Arctic Conditions*, pp. 73–93, Springer, London, U. K.

Tremblay, J.-É., K. Simpson, J. Martin, L. Miller, Y. Gratton, D. Barber, and N. M. Price (2008), Vertical stability and the annual dynamics of nutrients and chlorophyll fluorescence in the Coastal, Southeast Beaufort Sea, *J. Geophys. Res.*, *113*, C07S90, doi:10.1029/2007JC004547.

Vancoppenolle, M., L. Bopp, G. Madec, J. Dunne, T. Ilyina, P. R. Halloran, and N. Steiner (2013), Future Arctic Ocean primary productivity from CMIP5 simulations: Uncertain outcome, but consistent mechanisms, *Global Biogeochem. Cycles*, *27*(3), 605–619, doi:10.1002/gbc.20055.

Yamamoto-Kawai, M., E. Carmack, and F. McLaughlin (2006), Nitrogen balance and Arctic throughflow, *Nature*, *443*(7107), 43, doi:10.1038/443043a.

Yool, A., E. Popova, and T. Anderson (2013), Medusa-2.0: An intermediate complexity biogeochemical model of the marine carbon cycle for climate change and ocean acidification studies, *Geosci. Model Dev.*, *6*, 1767–1811, doi:10.5194/gmd-6-1767-2013.

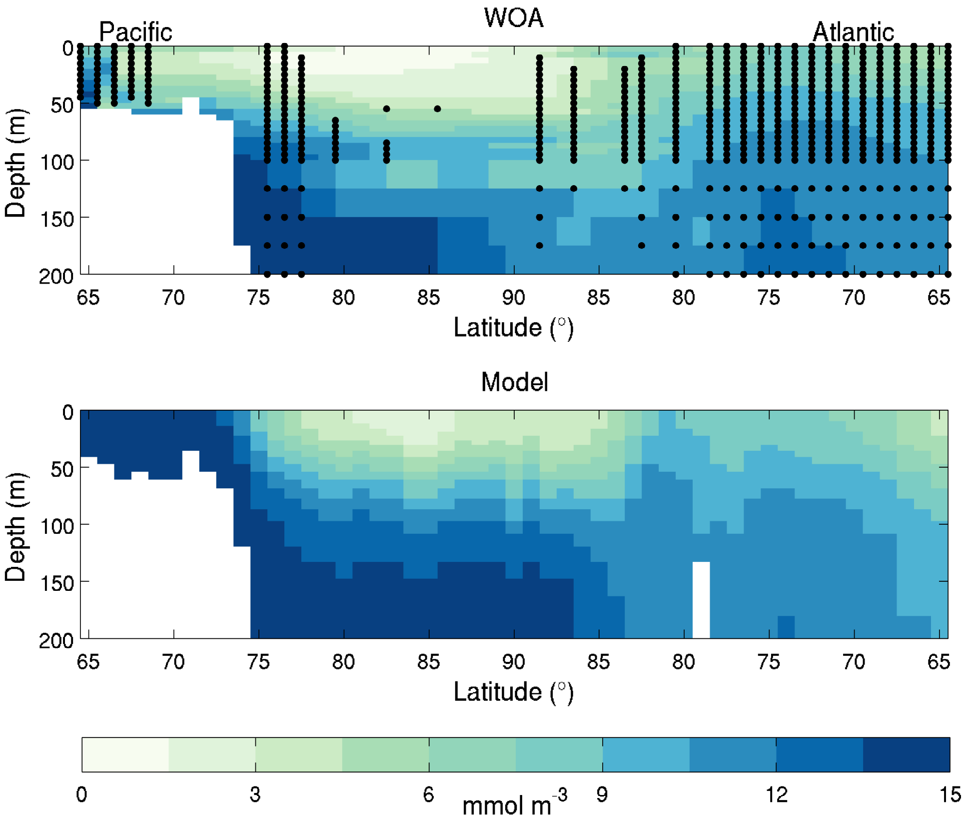

Figure B.1: Repeat of Figure 3.6 except the Atlantic side of the transect is moved from 5°W to 10°E to incorporate more Atlantic inflowing waters. Note the Pacific side remains unchanged.

Reviewer #1 of Lawrence *et al.* (2015) asked why we chose to place the Atlantic side of the DIN transect at 5°W. The selection was made so that the original transect (at 169°W and 5°W) crossed a variety of surface conditions. Here we provide a transect with the Atlantic side further east (10°E) so that it enters Atlantic waters further north, in the inflowing West Spitsbergen Current (WSC), and crosses both the WSC and North Atlantic Current. As in the original (Figure 3.6), the numerical model is not perfect at reproducing observed nitrate distributions (for example, overestimation occurs on the Atlantic side around 82°N and over the Chukchi shelf at 65-75°N on the Pacific side), but it is adequate for our purposes.

APPENDIX C

C1 Simulated production in Chapter 4

In Section 4.6 (Chapter 4), the thesis discusses the model phytoplankton response to an ice-free Arctic. The time evolution of phytoplankton production in the model Arctic over the twenty-first century is plotted in (Figure 4.5d). Three model production trends are shown: production for above 20 m depth, below 20 m depth and integrated over all depths. The plotted trend indicates that model production increases over the twenty-first century, from around 600 TgC yr^{-1} in 2000 to around 860 TgC yr^{-1} by 2099. That figure makes clear that the model increase is driven by increasing amounts of production below 20 m in depth.

The following figure in Section 4.6 (Figure 4.6) provides a map of certain model trends. It plots a different metric from the production profile: the depth of the production maximum (the depth in a given vertical profile at which the rate of production is maximum). This figure in Chapter 4 (Figure 4.6c) indicates a link between nitrate reductions in the model and the depth of production maxima increasing. But it does not map out the changes in total model production, and specifically those that occur below 20 m.

Hence, here we plot a map of the twenty-first century change in production occurring below 20 m depth, the same variable that is plotted in Chapter 4 as a time-series (Figure 4.5d), alongside a map of the same change in total production (reproduced from Figure 4.6d). Side by side, these figures demonstrate that areas where total production increases, also see large increases in the amount of production that occurs below 20 m in depth.

This correspondence is to be expected, since the trend lines plotted in Figure 4.5d indicated that total production increases are driven by production increases below 20 m depth.

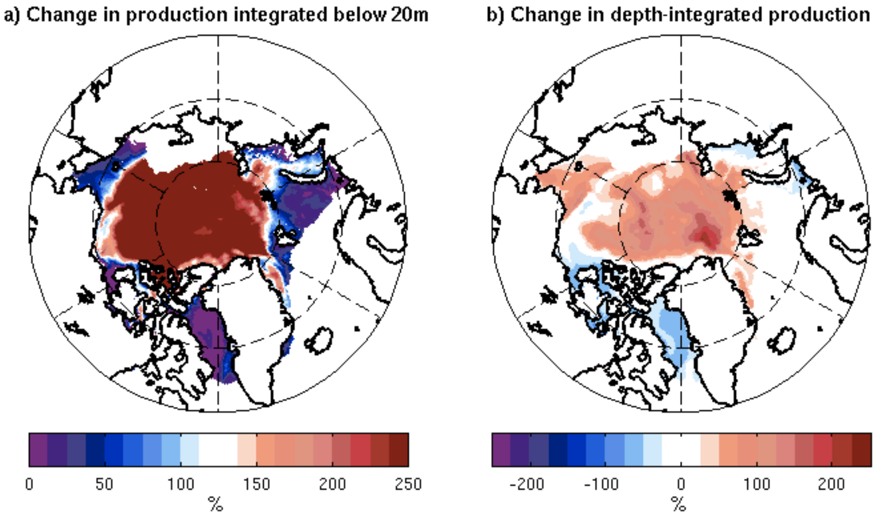

Figure C.1: **(a)** 2090s-2000s change in model 'subsurface' production (that which occurs below 20 m). **(b)** 2090s-2000s change in annual depth-integrated production (%). Panel b is reproduced from Chapter 4. Note the different scales on panels a and b.

References

Aagaard, K., L. Coachman, and E. Carmack, On the halocline of the Arctic Ocean, *Deep Sea Research Part A. Oceanographic Research Papers*, *28*(6), 529–545, 1981.

Aagaard, K., J. Swift, and E. Carmack, Thermohaline circulation in the Arctic Mediterranean seas, *J. Geophys. Res*, *90*(C3), 4833–4846, 1985.

Achterberg, E. P., et al., Natural iron fertilization by the Eyjafjallajökull volcanic eruption, *Geophysical Research Letters*, *40*(5), 921–926, 2013.

Aksenov, Y., S. Bacon, A. C. Coward, and N. P. Holliday, Polar outflow from the Arctic Ocean: A high resolution model study, *Journal of Marine Systems*, *83*(1), 14–37, 2010a.

Aksenov, Y., S. Bacon, A. C. Coward, and A. G. Nurser, The North Atlantic inflow to the Arctic Ocean: High-resolution model study, *Journal of Marine Systems*, *79*(1), 1–22, 2010b.

Aksenov, Y., V. V. Ivanov, A. Nurser, S. Bacon, I. V. Polyakov, A. C. Coward, A. C. Naveira-Garabato, and A. Beszczynska-Moeller, The Arctic circumpolar boundary current, *Journal of Geophysical Research: Oceans*, *116*(C9), 2011.

Antoine, D., J.-M. André, and A. More, Oceanic primary production 2. Estimation at global scale from satellite (Coastal Zone Color Scanner) chlorophyll, *Global biogeochemical cycles*, *10*(1), 57–69, 1996.

Ardyna, M., M. Babin, M. Gosselin, E. Devred, S. Bélanger, A. Matsuoka, and J.-É. Tremblay, Parameterization of vertical chlorophyll a in the Arctic Ocean: Impact of the subsurface chlorophyll maximum on regional, seasonal and annual primary production estimates, *Biogeosciences Discussions*, *10*(1), 1345–1399, 2013.

Ardyna, M., M. Babin, M. Gosselin, E. Devred, L. Rainville, and J.-É. Tremblay, Recent Arctic Ocean sea ice loss triggers novel fall phytoplankton blooms, *Geophysical Research Letters*, *41*(17), 6207–6212, 2014.

Arrigo, K., G. van Dijken, and S. Pabi, Impact of a shrinking Arctic ice cover on marine primary production, *Geophysical Research Letters*, *35*(19), 2008.

Arrigo, K., P. Matrai, and G. van Dijken, Primary productivity in the Arctic Ocean: Impacts of complex optical properties and subsurface chlorophyll maxima on large-scale estimates, *Journal of Geophysical Research*, *116*(C11), C11,022, 2011.

Arrigo, K., D. Perovich, R. Pickart, Z. Brown, G. van Dijken, et al., Phytoplankton blooms beneath the sea ice in the Chukchi Sea, *Deep Sea Research Part II: Topical Studies in Oceanography*, *105*, 1–16, 2014.

Arrigo, K., et al., Massive phytoplankton blooms under Arctic sea ice, *Science*, *336*(6087), 1408–1408, 2012.

Årthun, M., T. Eldevik, L. H. Smedsrud, Ø. Skagseth, and R. Ingvaldsen, Quantifying the influence of Atlantic heat on Barents Sea ice variability and retreat, *Journal of Climate*, *25*(13), 4736–4743, 2012.

Baly, E., The kinetics of photosynthesis, *Proceedings of the Royal Society of London. Series B, Biological Sciences*, *117*(804), 218–239, 1935.

Bates, N., W. Cai, and J. Mathis, The ocean carbon cycle in the western Arctic Ocean: Distributions and air-sea fluxes of carbon dioxide, *Oceanography-Oceanography Society*, *24*(3), 186, 2011.

Beaton, A. D., C. L. Cardwell, R. S. Thomas, V. J. Sieben, F.-E. Legiret, E. M. Waugh, P. J. Statham, M. C. Mowlem, and H. Morgan, Lab-on-chip measurement of nitrate and nitrite for in situ analysis of natural waters, *Environmental science & technology*, *46*(17), 9548–9556, 2012.

Behrenfeld, M. J., and P. G. Falkowski, Photosynthetic rates derived from satellite-based chlorophyll concentration, *Limnology and oceanography*, *42*(1), 1–20, 1997.

Behrenfeld, M. J., A. J. Bale, Z. S. Kolber, J. Aiken, P. G. Falkowski, et al., Confirmation of iron limitation of phytoplankton photosynthesis in the equatorial Pacific Ocean, *Nature*, *383*(6600), 508–511, 1996.

Behrenfeld, M. J., et al., Climate-driven trends in contemporary ocean productivity, *Nature*, *444*(7120), 752–755, 2006.

Beine, H., F. Domine, A. Ianniello, M. Nardino, I. Allegrini, K. Teinilä, and R. Hillamo, Fluxes of nitrates between snow surfaces and the atmosphere in the European high Arctic, *Atmospheric Chemistry and Physics*, *3*(2), 335–346, 2003.

Bekker, A., H. Holland, P.-L. Wang, D. Rumble, H. Stein, J. Hannah, L. Coetzee, and N. Beukes, Dating the rise of atmospheric oxygen, *Nature*, *427*(6970), 117–120, 2004.

Bergeron, M., and J.-É. Tremblay, Shifts in biological productivity inferred from nutrient drawdown in the southern Beaufort Sea (2003-2011) and northern Baffin Bay (1997-2011), Canadian Arctic., *Geophysical Research Letters*, 2014.

Bhatia, M. P., E. B. Kujawinski, S. B. Das, C. F. Breier, P. B. Henderson, and M. A. Charette, Greenland meltwater as a significant and potentially bioavailable source of iron to the ocean, *Nature Geoscience*, *6*(4), 274–278, 2013.

Bishop, J. K., and W. B. Rossow, Spatial and temporal variability of global surface solar irradiance, *Journal of Geophysical Research: Oceans*, *96*(C9), 16,839–16,858, 1991.

Blackman, F. F., Optima and limiting factors, *Annals of Botany*, *19*(74), 281–295, 1905.

Bluhm, B., K. Kosobokova, and E. Carmack, A tale of two basins: An integrated physical and biological perspective of the deep Arctic Ocean, *Progress in Oceanography*, *139*, 89–121, 2015.

Boé, J., A. Hall, and X. Qu, September sea-ice cover in the Arctic Ocean projected to vanish by 2100, *Nature Geoscience*, *2*(5), 341–343, 2009.

Boetius, A., et al., Export of algal biomass from the melting Arctic sea ice, *Science*, *339*(6126), 1430–1432, 2013.

Bopp, L., et al., Multiple stressors of ocean ecosystems in the 21st century: projections with CMIP5 models, *Biogeosciences*, *10*, 6225–6245, 2013.

Bourgault, D., C. Hamel, F. Cyr, J.-É. Tremblay, P. Galbraith, D. Dumont, and Y. Gratton, Turbulent nitrate fluxes in the Amundsen Gulf during ice-covered conditions, *Geophysical Research Letters*, *38*(15), 2011.

Brandt, K., Die Fauna der Ostsee, insbesondere die der Kieler Bucht, *Verhandlungen der Deutschen Zoologischen Gesellschaft*, *7*, 10–34, 1897.

Brandt, K., Life in the ocean, *Annual Report of the Smithsonian Institution for 1900*, pp. 493–506, 1901.

Brandt, K., *Über den Nitratgehalt des Ozeanwassers und seine biologische Bedeutung*, Engelmann, 1915.

Brandt, K. A. H., *Beiträge zur Kenntniss der chemischen Zusammensetzung des Planktons*, vol. 3, 43–90 pp., Joe Somebody, 1898.

Brown, Z., and K. Arrigo, Contrasting trends in sea ice and primary production in the Bering Sea and Arctic Ocean, *ICES Journal of Marine Science: Journal du Conseil*, *69*(7), 1180–1193, 2012.

Brown, Z., K. Lowry, M. A. Palmer, G. van Dijken, M. Mills, R. Pickart, and K. Arrigo, Characterizing the subsurface chlorophyll a maximum in the Chukchi Sea and Canada Basin, *Deep Sea Research Part II: Topical Studies in Oceanography*, *118*, 88–104, 2015.

Brzezinski, M. A., The Si: C: N ratio of marine diatoms: Interspecific variability and the effect of some environmental variables, *Journal of Phycology*, *21*(3), 347–357, 1985.

Brzezinski, M. A., M.-L. Dickson, D. M. Nelson, and R. Sambrotto, Ratios of Si, C and N uptake by microplankton in the Southern Ocean, *Deep Sea Research Part II: Topical Studies in Oceanography*, *50*(3), 619–633, 2003.

Buitenhuis, E. T., T. Hashioka, and C. L. Quéré, Combined constraints on global ocean primary production using observations and models, *Global Biogeochemical Cycles*, *27*(3), 847–858, 2013.

Canfield, D. E., The early history of atmospheric oxygen: homage to Robert M. Garrels, *Annu. Rev. Earth Planet. Sci.*, *33*, 1–36, 2005.

Carder, K., F. Chen, J. Cannizzaro, J. Campbell, and B. Mitchell, Performance of the MODIS semi-analytical ocean color algorithm for chlorophyll-a, *Advances in Space Research*, *33*(7), 1152–1159, 2004.

Carmack, E., and D. C. Chapman, Wind-driven shelf/basin exchange on an Arctic shelf: The joint roles of ice cover extent and shelf-break bathymetry, *Geophysical Research Letters*, *30*(14), 2003.

Carmack, E., and P. Wassmann, Food webs and physical–biological coupling on pan-Arctic shelves: Unifying concepts and comprehensive perspectives, *Progress in Oceanography*, *71*(2), 446–477, 2006.

Chaloner, W., The rise of the first land plants, *Biological Reviews*, *45*(3), 353–377, 1970.

Chang, B. X., and A. H. Devol, Seasonal and spatial patterns of sedimentary denitrification rates in the Chukchi Sea, *Deep Sea Research Part II: Topical Studies in Oceanography*, *56*(17), 1339–1350, 2009.

Codispoti, L., V. Kelly, A. Thessen, P. Matrai, S. Suttles, V. Hill, M. Steele, and B. Light, Synthesis of primary production in the Arctic Ocean: Iii. Nitrate and phosphate based estimates of net community production, *Progress in Oceanography*, *110*, 126–150, 2013.

Cole, H., S. Henson, A. Martin, and A. Yool, Mind the gap: The impact of missing data on the calculation of phytoplankton phenology metrics, *Journal of Geophysical Research: Oceans (1978–2012)*, *117*(C8), 2012.

Collins, W., et al., Development and evaluation of an Earth-system model–HadGEM2, *Geoscientific Model Development*, *4*(4), 1051–1075, 2011.

Comiso, J. C., C. L. Parkinson, R. Gersten, and L. Stock, Accelerated decline in the Arctic sea ice cover, *Geophysical research letters*, *35*(1), 2008.

Conkright, M., T. O'Brien, C. Stephens, R. Locarnini, H. Garcia, T. Boyer, and J. Antonov, *World Ocean Atlas 2001. Volume 6, Chlorophyll*, National Oceanic and Atmospheric Administration, 2002.

Conway, T. M., and S. G. John, Quantification of dissolved iron sources to the North Atlantic Ocean, *Nature*, *511*(7508), 212–215, 2014.

Cowles, T., J. Delaney, J. Orcutt, and R. Weller, The ocean observatories initiative: Sustained ocean observing across a range of spatial scales, *Marine Technology Society Journal*, *44*(6), 54–64, 2010.

Curry, B., C. Lee, B. Petrie, R. Moritz, and R. Kwok, Multiyear volume, liquid freshwater, and sea ice transports through Davis Strait, 2004–10, *Journal of Physical Oceanography*, *44*(4), 1244–1266, 2014.

D'Asaro, E. A., and J. H. Morison, Internal waves and mixing in the Arctic Ocean, *Deep Sea Research Part A. Oceanographic Research Papers*, *39*(2), S459–S484, 1992.

Daufresne, M., K. Lengfellner, and U. Sommer, Global warming benefits the small in aquatic ecosystems, *Proceedings of the National Academy of Sciences*, *106*(31), 12,788–12,793, 2009.

Davis, P. E., C. Lique, and H. L. Johnson, On the link between Arctic sea ice decline and the freshwater content of the Beaufort Gyre: Insights from a simple process model, *Journal of Climate*, *27*(21), 8170–8184, 2014.

De Baar, H. J., J. T. De Jong, D. C. Bakker, B. M. Löscher, C. Veth, U. Bathmann, and V. Smetacek, Importance of iron for plankton blooms and carbon dioxide drawdown in the Southern Ocean, *Nature*, *373*(6513), 412–415, 1995.

de Boyer Montégut, C., G. Madec, A. S. Fischer, A. Lazar, and D. Iudicone, Mixed layer depth over the global ocean: An examination of profile data and a profile-based climatology, *Journal of Geophysical Research: Oceans*, *109*(C12), 2004.

Dickson, R. R., J. Meincke, S.-A. Malmberg, and A. J. Lee, The great salinity anomaly in the northern North Atlantic 1968–1982, *Progress in Oceanography*, *20*(2), 103–151, 1988.

Dutkiewicz, S., M. J. Follows, and J. G. Bragg, Modeling the coupling of ocean ecology and biogeochemistry, *Global Biogeochemical Cycles*, *23*(4), 2009.

Dutkiewicz, S., J. R. Scott, and M. Follows, Winners and losers: Ecological and biogeochemical changes in a warming ocean, *Global Biogeochemical Cycles*, *27*(2), 463–477, 2013.

Dutkiewicz, S., B. Ward, J. Scott, and M. Follows, Understanding predicted shifts in diazotroph biogeography using resource competition theory, *Biogeosciences Discussions*, *11*(19), 5445–5461, 2014.

Dutkiewicz, S., A. Hickman, O. Jahn, W. Gregg, C. Mouw, and M. Follows, Capturing optically important constituents and properties in a marine biogeochemical and ecosystem model, *Biogeosciences*, *12*, 4447–4481, 2015.

Emmerton, C. A., L. F. Lesack, and W. F. Vincent, Nutrient and organic matter patterns across the Mackenzie River, estuary and shelf during the seasonal recession of sea-ice, *Journal of Marine Systems*, *74*(3), 741–755, 2008.

Eppley, R. W., Temperature and phytoplankton growth in the sea, *Fish. Bull*, *70*(4), 1063–1085, 1972.

Fahl, K., and E.-M. Nöthig, Lithogenic and biogenic particle fluxes on the Lomonosov Ridge (Central Arctic Ocean) and their relevance for sediment accumulation: Vertical vs. lateral transport, *Deep Sea Research Part I: Oceanographic Research Papers*, *54*(8), 1256–1272, 2007.

Falkowski, P. G., R. T. Barber, and V. Smetacek, Biogeochemical controls and feedbacks on ocean primary production, *Science*, *281*(5374), 200–206, 1998.

Fasham, M., H. Ducklow, and S. McKelvie, A nitrogen-based model of plankton dynamics in the oceanic mixed layer, *Journal of Marine Research*, *48*(3), 591–639, 1990.

Fer, I., Weak vertical diffusion allows maintenance of cold halocline in the central Arctic, *Atmospheric and Oceanic Science Letters*, *2*(3), 148–152, 2009.

Fernández-Méndez, M., C. Katlein, B. Rabe, M. Nicolaus, I. Peeken, K. Bakker, H. Flores, and A. Boetius, Photosynthetic production in the Central Arctic Ocean during the record sea-ice minimum in 2012, *Biogeosciences*, *12*(11), 3525–3549, 2015.

Ferrari, R., and C. Wunsch, Ocean circulation kinetic energy: Reservoirs, sources, and sinks, *Annual Review of Fluid Mechanics*, *41*(1), 253, 2008.

Field, C. B., M. J. Behrenfeld, J. T. Randerson, and P. Falkowski, Primary production of the biosphere: Integrating terrestrial and oceanic components, *Science*, *281*(5374), 237–240, 1998.

Follows, M. J., S. Dutkiewicz, S. Grant, and S. W. Chisholm, Emergent biogeography of microbial communities in a model ocean, *science*, *315*(5820), 1843–1846, 2007.

Franck, V. M., K. W. Bruland, D. A. Hutchins, and M. A. Brzezinski, Iron and zinc effects on silicic acid and nitrate uptake kinetics in three high-nutrient, low-chlorophyll regions, *Marine Ecology Progress Series*, *252*, 15–33, 2003.

Frey, K. E., D. K. Perovich, and B. Light, The spatial distribution of solar radiation under a melting Arctic sea ice cover, *Geophysical Research Letters*, *38*(22), 2011.

Friedrichs, M. A., et al., Assessing the uncertainties of model estimates of primary productivity in the tropical Pacific Ocean, *Journal of Marine Systems*, *76*(1), 113–133, 2009.

Ganachaud, A., and C. Wunsch, Improved estimates of global ocean circulation, heat transport and mixing from hydrographic data, *Nature*, *408*(6811), 453–457, 2000.

Garcia, H., R. Locarnini, T. Boyer, J. Antonov, O. Baranova, M. Zweng, J. Reagan, and D. Johnson, World Ocean Atlas 2013, Volume 4: Dissolved Inorganic Nutrients (phosphate, nitrate, silicate), *A. Mishonov Technical Ed*, pp. 1–25, 2014.

Gebbing, J., Chemische untersuchungen von meeresboden-, meerwasser und luft-proben der Deutschen Südpolar-Expedition 1901–1903, *E. von Drygalski, Deutsche Südpolar-Expedition*, pp. 75–234, 1909.

Geider, R., H. MacIntyre, and T. Kana, Dynamic model of phytoplankton growth and acclimation: responses of the balanced growth rate and the chlorophyll a: carbon ratio to light, nutrient-limitation and temperature, *Marine Ecology Progress Series*, pp. 187–200, 1997.

Geider, R. J., H. L. Maclntyre, and T. M. Kana, A dynamic regulatory model of phytoplanktonic acclimation to light, nutrients, and temperature, *Limnology and Oceanography*, *43*(4), 679–694, 1998.

Giering, S. L., et al., Reconciliation of the carbon budget in the ocean/'s twilight zone, *Nature*, *507*(7493), 480–483, 2014.

Giles, K. A., S. W. Laxon, A. L. Ridout, D. J. Wingham, and S. Bacon, Western Arctic Ocean freshwater storage increased by wind-driven spin-up of the Beaufort Gyre, *Nature Geoscience*, *5*(3), 194–197, 2012.

Gordon, H. R., and W. McCluney, Estimation of the depth of sunlight penetration in the sea for remote sensing, *Applied optics*, *14*(2), 413–416, 1975.

Gordon, R., J. Martin, and G. Knauer, Iron in north-east Pacific waters, *Nature*, *299*(5884), 611–612, 1982.

Gosselin, M., M. Levasseur, P. A. Wheeler, R. A. Horner, and B. C. Booth, New measurements of phytoplankton and ice algal production in the Arctic Ocean, *Deep Sea Research Part II: Topical Studies in Oceanography*, *44*(8), 1623–1644, 1997.

Gradinger, R., Sea-ice algae: Major contributors to primary production and algal biomass in the Chukchi and Beaufort Seas during May/June 2002, *Deep Sea Research Part II: Topical Studies in Oceanography*, *56*(17), 1201–1212, 2009.

Gran, H. H., *Das Plankton des Norwegischen Nordmeeres von biologischen und hydrographischen Gesichtspunkten behandelt*, [Fiskeridirektoratets havforskningsinstitutt], 1902.

Gran, H. H., *The spring growth of the plankton at Møre 1928-29 and at Lofoten in 1929 in relation to its limiting factors....*, Skrifter utgitt av det Norske Videnskaps-Akademi i Oslo. I. Matematisk-Naturvidenskapelig Klasse, no.5, pp. 1–77, 1930.

Greenfeld, T., and G. Maykut, The optical properties of ice and snow in the Arctic Basin, *Journal ofGlacioloJI*, *18*(80), 1977.

Gruber, N., et al., The argo-oxygen program, *White paper from the Argo Steerring Comité*, *60*, 2007.

Hansell, D. A., and M. J. Follows, Nitrogen in the Atlantic Ocean, *Nitrogen in Marine Environment*, pp. 597–630, 2008.

Hátún, H., A. B. Sandø, H. Drange, B. Hansen, and H. Valdimarsson, Influence of the Atlantic subpolar gyre on the thermohaline circulation, *Science*, *309*(5742), 1841–1844, 2005.

Hedges, S. B., J. E. Blair, M. L. Venturi, and J. L. Shoe, A molecular timescale of eukaryote evolution and the rise of complex multicellular life, *BMC evolutionary biology*, *4*(1), 1–9, 2004.

Hellweger, F. L., E. van Sebille, and N. D. Fredrick, Biogeographic patterns in ocean microbes emerge in a neutral agent-based model, *Science*, *345*(6202), 1346–1349, 2014.

Hensen, V., *Über die bestimmung des planktons oder des im meere treibenden materials an pflanzen und tieren*, Schmidt & Klaunig, 1887.

Hensen, V., Einige ergebnisse der expedition, *Ergebnisse der Plankton-Expedition der Humboldt-Stiftung. IA*, pp. 18–46, 1892.

Hickman, A., S. Dutkiewicz, R. Williams, and M. Follows, Modelling the effects of chromatic adaptation on phytoplankton community structure in the oligotrophic ocean, *Mar. Ecol. Prog. Ser*, *406*, 1–17, 2010.

Hill, V., P. Matrai, E. Olson, S. Suttles, M. Steele, L. Codispoti, and R. Zimmerman, Synthesis of integrated primary production in the Arctic Ocean: Ii. In situ and remotely sensed estimates, *Progress in Oceanography*, *110*, 107–125, 2013.

Hioki, N., et al., Laterally spreading iron, humic-like dissolved organic matter and nutrients in cold, dense subsurface water of the Arctic Ocean, *Scientific reports*, *4*, 6775–6784, 2014.

Holland, M., C. Bitz, and B. Tremblay, Future abrupt reductions in the summer Arctic sea ice, *Geophysical Research Letters*, *33*(23), 2006.

Hopwood, M., S. Bacon, K. Arendt, D. Connelly, and P. Statham, Glacial meltwater from Greenland is not likely to be an important source of fe to the North Atlantic, *Biogeochemistry*, *124*(1-3), 1–11, 2015.

Janout, M. A., J. Hölemann, A. M. Waite, T. Krumpen, W.-J. Appen, and F. Martynov, Sea-ice retreat controls timing of summer plankton blooms in the Eastern Arctic Ocean, *Geophysical Research Letters*, *43(24)*, 12,49312,501, 2016.

Jickells, T., et al., Global iron connections between desert dust, ocean biogeochemistry, and climate, *Science*, *308*(5718), 67–71, 2005.

Jin, M., E. E. Popova, J. Zhang, R. Ji, D. Pendleton, Ø. Varpe, A. Yool, and Y. J. Lee, Ecosystem model intercomparison of under-ice and total primary production in the Arctic Ocean, *Journal of Geophysical Research: Oceans*, *121*(1), 934–948, 2016.

Jones, E., B. Rudels, and L. Anderson, Deep waters of the Arctic Ocean: Origins and circulation, *Deep Sea Research Part I: Oceanographic Research Papers*, *42*(5), 737–760, 1995.

Kahru, M., V. Brotas, M. Manzano-Sarabia, and B. Mitchell, Are phytoplankton blooms occurring earlier in the Arctic?, *Global Change Biology*, *17*(4), 1733–1739, 2011.

Kara, A. B., A. J. Wallcraft, E. J. Metzger, H. E. Hurlburt, and C. W. Fairall, Wind stress drag coefficient over the global ocean, *Journal of Climate*, *20*(23), 5856–5864, 2007.

Karcher, M., J. N. Smith, F. Kauker, R. Gerdes, and W. M. Smethie, Recent changes in Arctic Ocean circulation revealed by Iodine-129 observations and modeling, *Journal of Geophysical Research: Oceans (1978–2012)*, *117*(C8), 2012.

Kenrick, P., and P. R. Crane, The origin and early evolution of plants on land, *Nature*, *389*(6646), 33–39, 1997.

Kirk, J. T., *Light and photosynthesis in aquatic ecosystems*, Cambridge university press, 1994.

Klausmeier, C. A., E. Litchman, T. Daufresne, and S. A. Levin, Optimal nitrogen-to-phosphorus stoichiometry of phytoplankton, *Nature*, *429*(6988), 171–174, 2004.

Klunder, M. B., D. Bauch, P. Laan, H. d. Baar, S. v. Heuven, and S. Ober, Dissolved iron in the Arctic shelf seas and surface waters of the central Arctic Ocean: Impact of Arctic river water and ice-melt, *Journal of Geophysical Research: Oceans (1978–2012)*, *117*(C1), 2012.

Kolber, Z. S., R. T. Barber, K. H. Coale, S. E. Fitzwateri, R. M. Greene, K. S. Johnson, S. Lindley, and P. G. Falkowski, Iron limitation of phytoplankton photosynthesis in the equatorial Pacific Ocean, *Nature*, *371*(6493), 145–149, 1994.

Kump, L. R., and M. E. Barley, Increased subaerial volcanism and the rise of atmospheric oxygen 2.5 billion years ago, *Nature*, *448*(7157), 1033–1036, 2007.

Lalande, C., S. Bélanger, and L. Fortier, Impact of a decreasing sea ice cover on the vertical export of particulate organic carbon in the northern Laptev Sea, Siberian Arctic Ocean, *Geophysical Research Letters*, *36*(21), 2009.

Lam, P. J., and J. K. Bishop, The continental margin is a key source of iron to the HNLC North Pacific Ocean, *Geophysical Research Letters*, *35*(7), 2008.

Lavoie, D., K. Denman, and C. Michel, Modeling ice algal growth and decline in a seasonally ice-covered region of the Arctic (Resolute Passage, Canadian Archipelago), *Journal of Geophysical Research: Oceans*, *110*(C11), 2005.

Laxon, S. W., et al., Cryosat-2 estimates of Arctic sea ice thickness and volume, *Geophysical Research Letters*, *40*(4), 732–737, 2013.

Le Fouest, V., M. Babin, and J.-É. Tremblay, The fate of riverine nutrients on Arctic shelves, *Biogeosciences Discussions*, *10*(6), 3661–3677, 2013.

Lee, S. H., D. Stockwell, and T. E. Whitledge, Uptake rates of dissolved inorganic carbon and nitrogen by under-ice phytoplankton in the Canada Basin in summer 2005, *Polar biology*, *33*(8), 1027–1036, 2010.

Lee, Z., A. Weidemann, J. Kindle, R. Arnone, K. L. Carder, and C. Davis, Euphotic zone depth: Its derivation and implication to ocean-color remote sensing, *Journal of Geophysical Research: Oceans*, *112*(C3), 2007.

Legendre, L., et al., Ecology of sea ice biota, *Polar Biology*, *12*(3-4), 429–444, 1992.

Lenn, Y.-D., et al., Vertical mixing at intermediate depths in the Arctic boundary current, *Geophysical Research Letters*, *36*(5), 2009.

Levine, M. D., C. A. Paulson, and J. H. Morison, Internal waves in the Arctic Ocean: Comparison with lower-latitude observations, *Journal of Physical Oceanography*, *15*(6), 800–809, 1985.

Li, W., F. McLaughlin, C. Lovejoy, and E. Carmack, Smallest algae thrive as the Arctic Ocean freshens, *Science*, *326*(5952), 539–539, 2009.

Lincoln, B. J., T. P. Rippeth, Y.-D. Lenn, M. L. Timmermans, W. J. Williams, and S. Bacon, Wind-driven mixing at intermediate depths in an ice-free Arctic Ocean, *Geophysical Research Letters*, *43*(18), 9749–9756, 2016.

Lique, C., Ocean science: Arctic sea ice heated from below, *Nature Geoscience*, *8*(3), 172–173, 2015.

Liu, J., M. Song, R. M. Horton, and Y. Hu, Reducing spread in climate model projections of a September ice-free Arctic, *Proceedings of the National Academy of Sciences*, *110*(31), 12,571–12,576, 2013.

Lodish, H., D. Baltimore, A. Berk, S. L. Zipursky, P. Matsudaira, and J. Darnell, *Molecular Cell Biology (4th Edition)*, vol. 4, Scientific American Books New York, 2001.

Longhurst, A., S. Sathyendranath, T. Platt, and C. Caverhill, An estimate of global primary production in the ocean from satellite radiometer data, *Journal of Plankton Research*, *17*(6), 1245–1271, 1995.

Lozier, M. S., A. C. Dave, J. B. Palter, L. M. Gerber, and R. T. Barber, On the relationship between stratification and primary productivity in the North Atlantic, *Geophysical Research Letters*, *38*(18), 2011.

Madec, G., *NEMO ocean engine*, Institut Pierre-Simon Laplace (IPSL), 2008.

Margalef, R., Life-forms of phytoplankton as survival alternatives in an unstable environment, *Oceanologica acta*, *1*(4), 493–509, 1978.

Martin, J., J. Tremblay, and N. Price, Nutritive and photosynthetic ecology of subsurface chlorophyll maxima in Canadian Arctic waters, *Biogeosciences*, *9*(12), 5353–5371, 2012.

Martin, J., D. Dumont, and J. Tremblay, Contribution of subsurface chlorophyll maxima to primary production in the coastal Beaufort Sea (Canadian Arctic): A model assessment, *Journal of Geophysical Research: Oceans*, *118*(11), 5873–5886, 2013.

Martin, J., et al., Prevalence, structure and properties of subsurface chlorophyll maxima in Canadian Arctic waters, *Marine Ecology Progress Series*, *412*, 69–84, 2010.

Martin, J. H., and S. Fitzwater, Iron deficiency limits phytoplankton growth in the north-east Pacific subArctic, *Nature*, *331*(3414343), 947–975, 1988.

Martiny, A. C., C. T. Pham, F. W. Primeau, J. A. Vrugt, J. K. Moore, S. A. Levin, and M. W. Lomas, Strong latitudinal patterns in the elemental ratios of marine plankton and organic matter, *Nature Geoscience*, *6*(4), 279–283, 2013.

Matrai, P., and S. Apollonio, New estimates of microalgae production based upon nitrate reductions under sea ice in Canadian shelf seas and the Canada Basin of the Arctic Ocean, *Marine biology*, *160*(6), 1297–1309, 2013.

Matrai, P., E. Olson, S. Suttles, V. Hill, L. Codispoti, B. Light, and M. Steele, Synthesis of primary production in the Arctic Ocean: I. Surface waters, 1954-2007, *Progress in Oceanography*, 2013.

Matsuoka, A., Y. Huot, K. Shimada, S.-I. Saitoh, and M. Babin, Bio-optical characteristics of the western Arctic Ocean: Implications for ocean color algorithms, *Canadian Journal of Remote Sensing*, *33*(6), 503–518, 2007.

Matsuoka, A., P. Larouche, M. Poulin, W. Vincent, and H. Hattori, Phytoplankton community adaptation to changing light levels in the southern Beaufort Sea, Canadian Arctic, *Estuarine, Coastal and Shelf Science*, *82*(3), 537–546, 2009.

Matsuoka, A., V. Hill, Y. Huot, M. Babin, and A. Bricaud, Seasonal variability in the light absorption properties of western Arctic waters: Parameterization of the individual components of absorption for ocean color applications, *Journal of Geophysical Research: Oceans (1978–2012)*, *116*(C2), 2011.

McLaughlin, F. A., and E. C. Carmack, Deepening of the nutricline and chlorophyll maximum in the Canada Basin interior, 2003–2009, *Geophysical Research Letters*, *37*(24), 2010.

McLaughlin, F. A., E. C. Carmack, R. W. Macdonald, and J. K. Bishop, Physical and geochemical properties across the Atlantic/Pacific water mass front in the southern Canadian basin, *Journal of Geophysical Research: Oceans*, *101*(C1), 1183–1197, 1996.

McLaughlin, F. A., E. C. Carmack, A. Proshutinsky, R. A. Krishfield, C. K. Guay, M. Yamamoto-Kawai, J. M. Jackson, and W. J. Williams, The rapid response of the Canada Basin to climate forcing: From bellwether to alarm bells, *Oceanography*, *24*(3), 146–159, 2011.

McPhee, M., A. Proshutinsky, J. H. Morison, M. Steele, and M. Alkire, Rapid change in freshwater content of the Arctic Ocean, *Geophysical Research Letters*, *36*(10), 2009.

Meier, W., F. Fetterer, M. Savoie, S. Mallory, R. Duerr, and J. Stroeve, NOAA/NSIDC Climate data record of passive microwave sea ice concentration, version 2, doi:10.7265/N55M63M1, 2015.

Michaelis, L., and M. L. Menten, Die kinetik der invertinwirkung, *Biochem. z*, *49*(333-369), 352, 1913.

Miller, W. L., and M. A. Moran, Interaction of photochemical and microbial processes in the degradation of refractory dissolved organic matter from a coastal marine environment, *Limnology and Oceanography*, *42*(6), 1317–1324, 1997.

Mills, E. L., *Biological oceanography: An early history, 1870-1960*, Cornell University Press, 1989.

Moore, C., et al., Processes and patterns of oceanic nutrient limitation, *Nature Geoscience*, *6*(9), 701–710, 2013.

Morel, A., B. Gentili, H. Claustre, M. Babin, A. Bricaud, J. Ras, and F. Tieche, Optical properties of the clearest natural waters, *Limnology and oceanography*, *52*(1), 217–229, 2007.

Morel, F., and N. Price, The biogeochemical cycles of trace metals in the oceans, *Science*, *300*(5621), 944–947, 2003.

Morel, F., J. Reinfelder, S. Roberts, C. Chamberlain, J. Lee, D. Yee, et al., Zinc and carbon co-limitation of marine-phytoplankton, *Nature*, *369*(6483), 740–742, 1994.

Morel, F., A. Milligan, M. Saito, and D. Heinrich, Marine bioinorganic chemistry: The role of trace metals in the oceanic cycles of major nutrients, *Treatise on Geochemistry*, *6*, 113–143, 2003.

Morel, F. M., R. J. Hudson, and N. M. Price, Limitation of productivity by trace metals in the sea, *Limnology and Oceanography*, *36*(8), 1742–1755, 1991.

Morison, J., R. Kwok, C. Peralta-Ferriz, M. Alkire, I. Rigor, R. Andersen, and M. Steele, Changing Arctic Ocean freshwater pathways, *Nature*, *481*(7379), 66–70, 2012.

Mundy, C., et al., Contribution of under-ice primary production to an ice-edge upwelling phytoplankton bloom in the Canadian Beaufort Sea, *Geophysical Research Letters*, *36*(17), 2009.

Nathansohn, A., Ueber die bedeutung vertikaler wasserbewegungen für die produktion des planktons im meere, *Abhandlungen der Mathematisch-Physischen Klasse/Koenigl. Saechsischen Gesellschaft der Wissenschaften (Bd. 29*, *1*(5), 1906.

Nathansohn, A., Über die allgemeinen produktionsbedingungen im meere, *Beiträge zur Biologie des Planktons, von HH Gran und Nathansohn. Internationale Revue der gestamten Hydrobiologie*, *1*, 38–72, 1908.

Nelson, N., D. Siegel, and A. Michaels, Seasonal dynamics of colored dissolved material in the Sargasso Sea, *Deep Sea Research Part I: Oceanographic Research Papers*, *45*(6), 931–957, 1998.

Nicolaus, M., C. Katlein, J. Maslanik, and S. Hendricks, Changes in Arctic sea ice result in increasing light transmittance and absorption, *Geophysical Research Letters*, *39*(24), 2012.

Nishioka, J., T. Ono, H. Saito, K. Sakaoka, and T. Yoshimura, Oceanic iron supply mechanisms which support the spring diatom bloom in the Oyashio region, western subArctic Pacific, *Journal of Geophysical Research: Oceans (1978–2012)*, *116*(C2), 2011.

Nurser, A., and S. Bacon, Eddy length scales and the Rossby radius in the Arctic Ocean., *Ocean Science Discussions*, *10*(5), 2013.

Onarheim, I. H., T. Eldevik, M. Årthun, R. B. Ingvaldsen, and L. H. Smedsrud, Skillful prediction of Barents Sea ice cover, *Geophysical Research Letters*, *42*(13), 5364–5371, 2015.

Pabi, S., G. van Dijken, and K. Arrigo, Primary production in the Arctic Ocean, 1998–2006, *Journal of Geophysical Research*, *113*(C8), C08,005, 2008.

Padman, L., and T. M. Dillon, Vertical heat fluxes through the Beaufort Sea thermohaline staircase, *Journal of Geophysical Research: Oceans*, *92*(C10), 10,799–10,806, 1987.

Palmer, M. A., B. T. Saenz, and K. R. Arrigo, Impacts of sea ice retreat, thinning, and melt-pond proliferation on the summer phytoplankton bloom in the Chukchi Sea, Arctic Ocean, *Deep Sea Research Part II: Topical Studies in Oceanography*, *105*, 85–104, 2014.

Parekh, P., M. J. Follows, and E. Boyle, Modeling the global ocean iron cycle, *Global biogeochemical cycles*, *18*(1), 2004.

Peralta-Ferriz, C., and R. A. Woodgate, Seasonal and interannual variability of pan-Arctic surface mixed layer properties from 1979 to 2012 from hydrographic data, and the dominance of stratification for multiyear mixed layer depth shoaling, *Progress in Oceanography*, *134*, 19–53, 2015.

Perovich, D., The changing Arctic sea ice cover, *Oceanography*, *24*, 2011.

Pickart, R. S., L. M. Schulze, G. Moore, M. A. Charette, K. R. Arrigo, G. van Dijken, and S. L. Danielson, Long-term trends of upwelling and impacts on primary productivity in the Alaskan Beaufort Sea, *Deep Sea Research Part I: Oceanographic Research Papers*, *79*, 106–121, 2013.

Pinkel, R., Near-inertial wave propagation in the western Arctic, *Journal of physical oceanography*, *35*(5), 645–665, 2005.

Planquette, H., et al., Dissolved iron in the vicinity of the Crozet islands, Southern Ocean, *Deep Sea Research Part II: Topical Studies in Oceanography*, *54*(18), 1999–2019, 2007.

Platt, T., and S. Sathyendranath, Oceanic primary production: Estimation by remote sensing at local and regional scales., *Science*, *241*(4873), 1613–1620, 1988.

Platt, T., W. Harrison, B. Irwin, E. P. Horne, and C. L. Gallegos, Photosynthesis and photoadaptation of marine phytoplankton in the Arctic, *Deep Sea Research Part A. Oceanographic Research Papers*, *29*(10), 1159–1170, 1982.

Platt, T., C. Caverhill, and S. Sathyendranath, Basin-scale estimates of oceanic primary production by remote sensing: The North Atlantic, *Journal of Geophysical Research: Oceans*, *96*(C8), 15,147–15,159, 1991.

Platt, T., S. Sathyendranath, A. Longhurst, T. Wilson, J. Woods, and T. Takahashi, Remote sensing of primary production in the ocean: Promise and fulfilment [and discussion], *Philosophical Transactions of the Royal Society of London B: Biological Sciences*, *348*(1324), 191–202, 1995.

Plueddemann, A. J., Internal wave observations from the Arctic environmental drifting buoy, *Journal of Geophysical Research: Oceans*, *97*(C8), 12,619–12,638, 1992.

Popova, E., A. Yool, A. Coward, Y. Aksenov, S. Alderson, B. d. Cuevas, and T. Anderson, Control of primary production in the Arctic by nutrients and light: insights from a high resolution ocean general circulation model, *Biogeosciences Discussions*, *7*(4), 5557–5620, 2010.

Popova, E., A. Yool, Y. Aksenov, and A. Coward, Role of advection in Arctic Ocean lower trophic dynamics: A modeling perspective, *Journal of Geophysical Research: Oceans*, *118*(3), 1571–1586, 2013.

Popova, E., et al., What controls primary production in the Arctic Ocean? Results from an intercomparison of five general circulation models with biogeochemistry, *Journal of Geophysical Research: Oceans (1978–2012)*, *117*(C1), 2012.

Proshutinsky, A., R. Bourke, and F. McLaughlin, The role of the Beaufort gyre in Arctic climate variability: Seasonal to decadal climate scales, *Geophysical Research Letters*, *29*(23), 15–1, 2002.

Proshutinsky, A. Y., and M. A. Johnson, Two circulation regimes of the wind-driven Arctic Ocean, *Journal of Geophysical Research: Oceans*, *102*(C6), 12,493–12,514, 1997.

Rabe, B., M. Karcher, U. Schauer, J. M. Toole, R. A. Krishfield, S. Pisarev, F. Kauker, R. Gerdes, and T. Kikuchi, An assessment of Arctic Ocean freshwater content changes from the 1990s to the 2006–2008 period, *Deep Sea Research Part I: Oceanographic Research Papers*, *58*(2), 173–185, 2011.

Rainville, L., and R. A. Woodgate, Observations of internal wave generation in the seasonally ice-free Arctic, *Geophysical Research Letters*, *36*(23), 2009.

Rampal, P., J. Weiss, and D. Marsan, Positive trend in the mean speed and deformation rate of Arctic sea ice, 1979–2007, *Journal of Geophysical Research: Oceans*, *114*(C5), 2009.

Randelhoff, A., A. Sundfjord, and M. Reigstad, Seasonal variability and fluxes of nitrate in the surface waters over the Arctic shelf slope, *Geophysical Research Letters*, 2015.

Redfield, A. C., *On the proportions of organic derivatives in sea water and their relation to the composition of plankton*, University Press of Liverpool James Johnstone memorial volume, 1934.

Regaudie-de Gioux, A., and C. M. Duarte, Temperature dependence of planktonic metabolism in the ocean, *Global Biogeochemical Cycles*, *26*(1), 2012.

Reinfelder, J. R., Carbon concentrating mechanisms in eukaryotic marine phytoplankton, *Annual Review of Marine Science*, *3*, 291–315, 2011.

Resing, J. A., P. N. Sedwick, C. R. German, W. J. Jenkins, J. W. Moffett, B. M. Sohst, and A. Tagliabue, Basin-scale transport of hydrothermal dissolved metals across the South Pacific Ocean, *Nature*, *523*(7559), 200–203, 2015.

Rey, F., Declining silicate concentrations in the Norwegian and Barents Seas, *ICES Journal of Marine Science: Journal du Conseil*, p. fss007, 2012.

Riahi, K., S. Rao, V. Krey, C. Cho, V. Chirkov, G. Fischer, G. Kindermann, N. Nakicenovic, and P. Rafaj, RCP 8.5? A scenario of comparatively high greenhouse gas emissions, *Climatic Change*, *109*(1-2), 33–57, 2011.

Riley, G. A., Factors controlling phytoplankton populations on Georges Bank, *J. mar. Res*, *6*(1), 54–73, 1946.

Rippeth, T. P., B. J. Lincoln, Y.-D. Lenn, J. M. Green, A. Sundfjord, and S. Bacon, Tide-mediated warming of Arctic halocline by Atlantic heat fluxes over rough topography, *Nature Geoscience*, *8*(3), 191–194, 2015.

Rózanska, M., M. Gosselin, M. Poulin, J. M. Wiktor, and C. Michel, Influence of environmental factors on the development of bottom ice protist communities during the winter–spring transition, *Marine Ecology Progress Series*, *386*, 43–59, 2009.

Rudels, B., L. Anderson, and E. Jones, Formation and evolution of the surface mixed layer and halocline of the Arctic Ocean, *Journal of Geophysical Research: Oceans*, *101*(C4), 8807–8821, 1996.

Rudels, B., U. Schauer, G. Björk, M. Korhonen, S. Pisarev, B. Rabe, and A. Wisotzki, Observations of water masses and circulation in the Eurasian Basin of the Arctic Ocean from the 1990s to the late 2000s, *OS Special Issue: Ice-Atmosphere-Ocean interactions in the Arctic Ocean during IPY: the Damocles project*, *9*(1), 147–169, 2013.

Saba, V., et al., An evaluation of ocean color model estimates of marine primary productivity in coastal and pelagic regions across the globe, *Biogeosciences*, pp. 489–503, 2011.

Saito, M. A., G. Rocap, and J. W. Moffett, Production of cobalt binding ligands in a *Synechococcus* feature at the Costa Rica upwelling dome, *Limnology and Oceanography*, *50*(1), 279–290, 2005.

Saito, M. A., T. J. Goepfert, and J. T. Ritt, Some thoughts on the concept of colimitation: three definitions and the importance of bioavailability, *Limnology and Oceanography*, *53*(1), 276–290, 2008.

Sakshaug, E., Primary and secondary production in the Arctic Seas, in *The organic carbon cycle in the Arctic Ocean*, pp. 57–81, Springer, 2004.

Sarmiento, J., N. Gruber, M. Brzezinski, and J. Dunne, High-latitude controls of thermocline nutrients and low latitude biological productivity, *Nature*, *427*(6969), 56–60, 2004a.

Sarmiento, J. L., and N. Gruber, Ocean Biogeochemical Dynamics, 2006.

Sarmiento, J. L., et al., Response of ocean ecosystems to climate warming, *Global Biogeochemical Cycles*, *18*(3), 2004b.

Shaw, W. J., and T. P. Stanton, Vertical diffusivity of the Western Arctic Ocean halocline, *Journal of Geophysical Research: Oceans*, 2014.

Slagstad, D., I. Ellingsen, and P. Wassmann, Evaluating primary and secondary production in an Arctic Ocean void of summer sea ice: an experimental simulation approach, *Progress in Oceanography*, *90*(1), 117–131, 2011.

Slemons, L. O., J. W. Murray, J. Resing, B. Paul, and P. Dutrieux, Western Pacific coastal sources of iron, manganese, and aluminum to the Equatorial Undercurrent, *Global Biogeochemical Cycles*, *24*(3), 2010.

Smith, J. N., F. A. McLaughlin, W. M. Smethie, S. B. Moran, and K. Lepore, Iodine-129, 137Cs, and CFC-11 tracer transit time distributions in the Arctic Ocean, *Journal of Geophysical Research: Oceans*, *116*(C4), 2011.

Stedmon, C., R. Amon, A. Rinehart, and S. Walker, The supply and characteristics of colored dissolved organic matter (CDOM) in the Arctic Ocean: Pan Arctic trends and differences, *Marine Chemistry*, *124*(1), 108–118, 2011.

Steele, M., and T. Boyd, Retreat of the cold halocline layer in the Arctic Ocean, *Journal of Geophysical Research: Oceans*, *103*(C5), 10,419–10,435, 1998.

Steele, M., R. Morley, and W. Ermold, PHC: A global ocean hydrography with a high-quality Arctic Ocean, *Journal of Climate*, *14*(9), 2079–2087, 2001.

Steinacher, M., et al., Projected 21st century decrease in marine productivity: a multi-model analysis, *Biogeosciences*, *7*(3), 2010.

Strass, V. H., and E.-M. Nöthig, Seasonal shifts in ice edge phytoplankton blooms in the Barents Sea related to the water column stability, *Polar Biology*, *16*(6), 409–422, 1996.

Strother, P. K., L. Battison, M. D. Brasier, and C. H. Wellman, Earth/'s earliest non-marine eukaryotes, *Nature*, *473*(7348), 505–509, 2011.

Summons, R. E., L. L. Jahnke, J. M. Hope, and G. A. Logan, 2-Methylhopanoids as biomarkers for cyanobacterial oxygenic photosynthesis, *Nature*, *400*(6744), 554–557, 1999.

Sundfjord, A., I. Fer, Y. Kasajima, and H. Svendsen, Observations of turbulent mixing and hydrography in the marginal ice zone of the Barents Sea, *Journal of Geophysical Research: Oceans (1978–2012)*, *112*(C5), 2007.

Sundfjord, A., I. Ellingsen, D. Slagstad, and H. Svendsen, Vertical mixing in the marginal ice zone of the northern Barents Sea results from numerical model experiments, *Deep Sea Research Part II: Topical Studies in Oceanography*, *55*(20), 2154–2168, 2008.

Sverdrup, H., On conditions for the vernal blooming of phytoplankton, *Journal du Conseil*, *18*(3), 287–295, 1953.

Sverdrup, H. U., The place of physical oceanography in oceanographic research, *Journal of Marine Research*, *14*, 287–294, 1955.

Tagliabue, A., Online Iron Database, `http://pcwww.liv.ac.uk/~{}atagliab/LIV_WEB/Data.html`, [Online; accessed 12-10-2016], 2016.

Tagliabue, A., O. Aumont, and L. Bopp, The impact of different external sources of iron on the global carbon cycle, *Geophysical Research Letters*, *41*(3), 920–926, 2014a.

Tagliabue, A., J.-B. Sallée, A. R. Bowie, M. Lévy, S. Swart, and P. W. Boyd, Surface-water iron supplies in the Southern Ocean sustained by deep winter mixing, *Nature Geoscience*, *7*(4), 314–320, 2014b.

Tagliabue, A., A. R. Bowie, P. W. Boyd, K. N. Buck, K. S. Johnson, and M. A. Saito, The integral role of iron in ocean biogeochemistry, *Nature*, *543*(7643), 51–59, 2017.

Tagliabue, A., et al., Hydrothermal contribution to the oceanic dissolved iron inventory, *Nature Geoscience*, *3*(4), 252–256, 2010.

Taylor, J. R., and R. Ferrari, Shutdown of turbulent convection as a new criterion for the onset of spring phytoplankton blooms, *Limnology and Oceanography*, *56*(6), 2293–2307, 2011.

Thomas, M. K., C. T. Kremer, C. A. Klausmeier, and E. Litchman, A global pattern of thermal adaptation in marine phytoplankton, *Science*, *338*(6110), 1085–1088, 2012.

Timmermann, R., H. Goosse, G. Madec, T. Fichefet, C. Ethe, and V. Duliere, On the representation of high latitude processes in the ORCA-LIM global coupled sea ice–ocean model, *Ocean Modelling*, *8*(1), 175–201, 2005.

Torres-Valdés, S., et al., Export of nutrients from the Arctic Ocean, *Journal of Geophysical Research: Oceans*, *118*(4), 1625–1644, 2013.

Townsend, D. W., M. D. Keller, M. E. Sieracki, and S. G. Ackleson, Spring phytoplankton blooms in the absence of vertical water column stratification, *Nature*, *360*(6399), 59–62, 1992.

Tremblay, J.-É., and J. Gagnon, The effects of irradiance and nutrient supply on the productivity of Arctic waters: a perspective on climate change, in *Influence of Climate Change on the Changing Arctic and Sub-Arctic Conditions*, pp. 73–93, Springer, 2009.

Tremblay, J.-E., C. Michel, K. A. Hobson, M. Gosselin, and N. M. Price, Bloom dynamics in early opening waters of the Arctic Ocean, *Limnology and Oceanography*, *51*(2), 900–912, 2006.

Tremblay, J.-É., K. Simpson, J. Martin, L. Miller, Y. Gratton, D. Barber, and N. M. Price, Vertical stability and the annual dynamics of nutrients and chlorophyll fluorescence in the coastal, southeast Beaufort Sea, *Journal of Geophysical Research: Oceans (1978–2012)*, *113*(C7), 2008.

Tremblay, J.-É., et al., Climate forcing multiplies biological productivity in the coastal Arctic Ocean, *Geophysical Research Letters*, *38*(18), 2011.

Tsubouchi, T., Assembling an Arctic Ocean Boundary Monitoring Array, *Data Science Journal*, *13*(0), PDA72–PDA78, 2014.

Tsubouchi, T., et al., The Arctic Ocean in summer: A quasi-synoptic inverse estimate of boundary fluxes and water mass transformation, *Journal of Geophysical Research: Oceans (1978–2012)*, *117*(C1), 2012.

Tyrrell, T., The relative influences of nitrogen and phosphorus on oceanic primary production, *Nature*, *400*(6744), 525–531, 1999.

Vancoppenolle, M., L. Bopp, G. Madec, J. Dunne, T. Ilyina, P. R. Halloran, and N. Steiner, Future Arctic Ocean primary productivity from CMIP5 simulations: Uncertain outcome, but consistent mechanisms, *Global Biogeochemical Cycles*, *27*(3), 605–619, 2013.

Villar, E., et al., Environmental characteristics of Agulhas rings affect interocean plankton transport, *Science*, *348*(6237), 1261,447, 2015.

von Appen, W.-J., A. Beszczynska-Möller, E. Fahrbach, U. Schauer, and E. Hansen, Long-and short-term variability of currents and hydrography in Fram Strait, in *EGU General Assembly Conference Abstracts*, vol. 16, p. 6682, 2014.

Wang, J., G. F. Cota, and D. A. Ruble, Absorption and backscattering in the Beaufort and Chukchi Seas, *Journal of Geophysical Research: Oceans*, *110*(C4), 2005.

Wang, M., and J. Overland, A sea ice free summer Arctic within 30 years?, *Geophysical Research Letters*, *36*(7), L07,502, 2009.

Warburg, O., Uber die geschwindigkeit der photochemischen kohlensaeurezersetzung in lebenden zellen, *Biochem. Zeit.*, *100*, 230–270, 1919.

Wassmann, P., and M. Reigstad, Future Arctic Ocean seasonal ice zones and implications for pelagic-benthic coupling, *Oceanography*, *24*(3), 220–231, 2011.

Weber, T., and C. Deutsch, Oceanic nitrogen reservoir regulated by plankton diversity and ocean circulation, *Nature*, *489*(7416), 419–422, 2012.

Weingartner, T., K. Aagaard, R. Woodgate, S. Danielson, Y. Sasaki, and D. Cavalieri, Circulation on the north central Chukchi Sea shelf, *Deep Sea Research Part II: Topical Studies in Oceanography*, *52*(24), 3150–3174, 2005.

Westberry, T., M. Behrenfeld, D. Siegel, and E. Boss, Carbon-based primary productivity modeling with vertically resolved photoacclimation, *Global Biogeochemical Cycles*, *22*(2), 2008.

Wheeler, P. A., and M. Gosselim, Active cycling of organic carbon, *Nature*, *380*, 25, 1996.

Whipple, G. C., *Microscopy of drinking-water, 1899*, John Wiley and Sons. New York, 1899.

Williams, R. G., and M. J. Follows, *Ocean dynamics and the carbon cycle: Principles and mechanisms*, Cambridge University Press, 2011.

Woodgate, R. A., K. Aagaard, R. D. Muench, J. Gunn, G. Björk, B. Rudels, A. Roach, and U. Schauer, The Arctic Ocean boundary current along the Eurasian slope and the adjacent Lomonosov Ridge: Water mass properties, transports and transformations from moored instruments, *Deep Sea Research Part I: Oceanographic Research Papers*, *48*(8), 1757–1792, 2001.

Yamamoto-Kawai, M., E. Carmack, and F. McLaughlin, Nitrogen balance and Arctic throughflow, *Nature*, *443*(7107), 43–43, 2006.

Yool, A., E. Popova, and T. Anderson, MEDUSA-2.0: an intermediate complexity biogeochemical model of the marine carbon cycle for climate change and ocean acidification studies, *Geoscientific Model Development*, *6*, 1767–1811, 2013.

Yool, A., E. Popova, and A. Coward, Future change in ocean productivity: Is the Arctic the new Atlantic?, *Journal of Geophysical Research: Oceans*, *120*(12), 7771–7790, 2015.

Zhang, J., R. Lindsay, M. Steele, and A. Schweiger, What drove the dramatic retreat of Arctic sea ice during summer 2007?, *Geophysical Research Letters*, *35*(11), 2008.